Universidade de Aveiro Departamento de Física
2016

António José Sousa de Almeida

Estudos de ressonância magnética de sistemas de spins em nanocristais semiconductores

Magnetic resonance studies of spin systems in semiconductor nanocrystals

Universidade de Aveiro Departamento de Física
2016

António José Sousa de Almeida

Estudos de ressonância magnética de sistemas de spins em nanocristais semiconductores

Magnetic resonance studies of spin systems in semiconductor nanocrystals

Dissertação apresentada à Universidade de Aveiro para cumprimento dos requisitos necessários à obtenção do grau de Doutor em Física, realizada sob a orientação científica do Doutor Rui Nuno Marques Pereira, Investigador Principal do Departamento de Física da Universidade de Aveiro

Apoio financeiro da Fundação Calouste Gulbenkian através do *Prémio de Estímulo à Investigação 2012*.

Apoio financeiro da Fundação para a Ciência e Tecnologia – FCT através da bolsa SFRH / BD / 79223 / 2011.

FUNDAÇÃO CALOUSTE GULBENKIAN

FCT Fundação para a Ciência e a Tecnologia
MINISTÉRIO DA CIÊNCIA, TECNOLOGIA E ENSINO SUPERIOR

W końcu przestałam wiedzieć
czego szukałam tak długo.

Wisława Szymborska

o júri / the jury

president / president

Doutor Rui Luís Andrade Aguiar
Professor Catedrático, Universidade de Aveiro

vogais / examiners comitee

Doutor Martin S. Brandt
Full Professor, Technische Universität Munchen, Walter Schottky Institut, Alemanha

Doutor Mikhail Igorevich Vasilevskiy
Professor Catedrático, Universidade do Minho

Doutor Nicolai Andreevitch Sobolev
Professor Associado, Universidade de Aveiro

Doutor Rui Nuno Marques Pereira
Equiparado a Investigador Principal, Universidade de Aveiro

Doutor João Pedro dos Santos Hall Agorreta de Alpuim
Investigador Associado, Laboratório Ibérico Internacional de Nanotecnologias (INL), Braga

agradecimentos / acknowledgements

Agradeço à Universidade de Aveiro, ao Departamento de Física e ao laboratório associado I3N por terem disponibilizado as condições necessárias ao desenvolvimento deste trabalho. Agradeço também ao Walter Schottky Institüt da Universidade Técnica de Munique por me ter recebido e permitido desenvolver parte deste trabalho nas suas instalações.

Agradeço ao Dr. Rui Nuno Pereira por todo o empenho e dedicação na minha orientação, que foram essenciais para a concretização deste trabalho.

Agradeço ao Prof. Nicolai Sobolev pela ajuda prestada na realização de medidas de ressonância paramagnética.

Agradeço ao Prof. Martin Brandt por me ter acolhido no Walter Schottky Institüt e pela ajuda, motivação e interesse neste trabalho. Agradeço aos meus colegas neste instituto Willi Aigner e Konrad Klein pelo apoio neste trabalho e por terem ajudado a preencher o meu tempo livre enquanto estive em Munique.

Agradeço aos meus colegas do Departamento de Física da Universidade de Aveiro Alexandre Botas, Bruno Falcão, Derese Gugsa, Vânia Freitas e Sandra Correia pela ajuda e convívio.

Agradeço aos meus amigos, em especial ao Alireza Nazaritalooki, à Izabela Miklaszewska, à Helena Zália, à Anabela Paula, ao José Albergaria, pelo apoio e pelos bons momentos que ajudaram a eclipsar as dificuldades inerentes ao percorrer deste caminho.

Agradeço aos meus pais e à minha avó pelo carinho e conselhos, por me terem apoiado incondicionalmente mesmo quando discordaram das minhas decisões, e por nunca me deixarem desistir.

O maior agradecimento ficará sempre para a Malwina e para o destino que nos juntou. Por todas as alegrias e todos os sacrifícios, por acreditar em mim muito mais do que eu próprio, por nunca ter desistido nem me deixado desistir. Por ser a Mulher que deu sentido a este periodo da minha vida. Kocham życie bo dało mi Ciebie... Kocham Ciebie bo – jesteś całym moim życiem.

palavras-chave

Espectroscopia ressonância paramagnética electrónica (RPE), espectroscopia ressonância ferromagnetica (RFM), nanocristais semiconductores, dopagem electrónica, defeitos capturadores de carga, anisotropia magnética.

resumo

Esta tese apresenta um estudo experimental de sistemas de spins fornecidos por dopantes electrónicos e por defeitos capturadores de carga em nanocristais (NCs) semiconductores, por meio de técnicas de ressonância magnética. Aqui, investigámos problemas que têm efeitos limitadores de performance nas propriedades de NCs semiconductores para o seu uso em aplicações tecnológicas. Nomeadamente, estudámos a dopagem electrónica de NCs semiconductores. A dopagem é crítica para controlar o comportamento de semiconductores, que de outra forma seriam isoladores. Investigámos também defeitos capturadores de carga, que podem ter um impacto negativo na conductividade de NCs semiconductores ao capturar portadores de carga em estados electrónicos deslocalizados de NCs. Para além disso, abordámos a origem da anisotropia magnética em NCs de materiais diamagnéticos.

Nesta tese, reportamos investigações usando medidas de ressonância paramagnética electrónica (RPE) quantitativa, dizendo respeito à eficiência de dopagem electrónica de Si NCs com átomos de P e à sua dependência com o ambiente envolvendo os NCs. Das medidas de RPE quantitativas, estimamos eficiências de dopagem nos NCs que são consistentes com a incorporação da maioria dos dopantes P como dadores substitucionais nos NCs. Observamos também que a eficiência de dopagem dos NCs varia em várias ordens de grandeza dependendo do ambiente envolvendo os NCs, devido a uma forte compensação dos dadores por moléculas absorbidas na superfície dos NCs. Usando espectroscopia RPE dependente da temperatura, mostramos também que a energia de ionização dos dopantes P em Si NCs aumenta relativamente ao seu correspondente cristal macroscópico devido a confinamento.

Usamos espectroscopia RPE dependente da temperatura para estudar a interacção entre múltiplos dopantes incorporados num único Si NC e o seu impacto na estrutura electrónica destes NCs. Monitorizámos experimentalmente a interacção de troca em pares de dadores P (dímeros de dadores) em Si NCs através de um desvio da ressonância magnética do seu estado tripleto em relação ao paramagnetismo de Curie. Mostrámos que a interacção de troca entre dadores próximos entre si pode ser bem descrita pela teoria de massa efectiva, permitindo o cálculo de muitas configurações de dopantes e permitindo a consideração de efeitos estatísticos cruciais em conjuntos de nanocristais. Descobrimos que dímeros de dadores induzem estados discretos num NC, e que a sua separação energética difere em até três ordens de grandeza para dímeros colocados aleatoriamente num conjunto de NCs devido a uma enorme dependência da energia de troca na configuração do dímero.

Investigámos também sistemas de spins induzidos por defeitos capturadores de carga e como estes defeitos podem afectar a dopagem de NCs. Identificamos a presença de dois estados de carga de um defeito em NCs

de CdSe usando espectroscopia RPE combinada com a afinação electrónica de NCs através de dopagem com Ag induzida quimicamente. A partir de de RPE foto-induzido, mostramos que estes defeitos têm um papel central na fixação do nível de Fermi em conjuntos de NCs. Através da análise da dependência do sinal de RPE dos defeitos com a concentração de dopantes de Ag, mostramos também que os defeitos actuam como capturadores efectivos de electrões nos NCs. Do RPE dependente da temperatura, estimamos um limite inferior para a energia de ionização dos defeitos estudados. Com base nas características do espectro RPE dos defeitos observados, propomos que está associado a lacunas de Se com o estado paramagnético sendo o estado positivo do defeito.

Para além disso, mostramos que as interacções magnéticas entre spins associados a defeitos nos NCs podem induzir efeitos de anisotropia magnética em conjuntos de NCs que não são esperados acontecer no cristal macroscópico correspondente. Usando espectroscopia de ressonância ferromagnética (RFM) com dependência angular, medimos a anisotropia magnética em conjuntos de aleatórios de NCs de CdSe através da gravação do espectro de ressonância magnética para várias orientações do campo magnético externo. As dependências angulares do campo ressonante são diferente para conjuntos aparentemente similares de NCs de CdSe. Mostramos que a forma e amplitude da variação angular do RFM pode ser bem descrita po um modelo simples que toma em consideração as interacções dipolo-dipolo entre dipolos localizados na superfície dos NCs. Os dipolos na superfície podem originar de ligações pendentes em sítios da superfície que não estão passivados por ligantes. Dos nossos cálculos, descobrimos que para diferentes conjuntos aleatórios de NCs a força da anisotropia magnética induzida por interacções dipolo-dipolo pode tomar valores abrangendo quatro ordens de grandeza, dependendo do arranjo específico dos NCs no conjunto e da distribuição específica dos dipolos na superfície de cada NC. Esta enorme variabilidade pode justificar a disparidade de anisotropias magnéticas observada nas nossas experiências.

keywords

Electron paramgnetic resonance (EPR) spectroscopy, ferromagnetic resonance (FMR) spectroscopy, semiconductor nanocrystals, electronic doping, charge trapping defects, magnetic anisotropy.

abstract

This thesis presents an experimental study of systems of spins provided by electronic dopants and by charge trapping defects in semiconductor NCs, by means of magnetic resonance spectroscopy techniques. Here, we have investigated issues that have performance-limiting effects on the properties of semiconductor NCs for their use in technological applications. Namely, we have studied the electronic doping of semiconductor NCs. Doping is critical to control the behavior of semiconductors, which would otherwise be electrically insulating. We have further investigated charge trapping defects in semiconductor NCs, which can have a negative impact on the conductivity of semiconductor NCs by capturing charge carriers from delocalized electronic states of the NCs. Moreover, we addressed the origin of magnetic anisotropy in NCs of diamagnetic materials.

In this thesis, we report investigations using quantitative electron paramagnetic resonance (EPR) measurements concerning the efficiency of electronic doping of Si NCs with P atoms and its dependence on the environment surrounding the NCs. From quantitative EPR measurements, we estimate doping efficiencies in the NCs that are consistent with the incorporation of most P dopants as substitutional donors in the NCs. We further observe that the doping efficiency of the NCs varies by several orders of magnitude depending on the NCs surrounding environment due to a strong compensation of donors by molecules adsorbed to the NCs surface. Using temperature-dependent EPR spectroscopy, we further show that the ionization energy of P dopants in Si NCs increases with respect to their bulk counterpart due to confinement.

We use temperature-dependent EPR spectroscopy to study the interaction between multiple P dopants incorporated in a single Si NC and its impact on the electronic structure of these NCs. We experimentally probe the exchange interaction in pairs of P donors (donor dimers) in Si NCs via a deviation of their triplet-state magnetic resonance from Curie paramagnetism. We showed that the exchange coupling of closely spaced donors can be well described by effective mass theory, enabling the calculation of many dopant configurations and allowing the consideration of statistical effects crucial in NC ensembles. We find that donor dimers induce discrete states in a NC, and that their energy splitting differs by up to three orders of magnitude for randomly placed dimers in a NC ensemble due to an enormous dependence of the exchange energy on the dimer configuration.

We also investigate systems of spins induced by charge trapping defects and how these defects can affect the doping of NCs. We identify the presence of two charge states of a defect in CdSe NCs using EPR spectroscopy, combined with electronic tuning of NCs via chemically induced Ag doping. From

light-induced EPR, we show that these defects have a central role on Fermi level pinning of NC ensembles. By analyzing the dependence of the EPR signal of the defects on the concentration of Ag dopants, we further demonstrate that the defects act as effective electron traps in the NCs. From temperature-dependent EPR, we estimate a lower limit for the ionization energy of the studied defects. Based on the characteristics of the EPR spectrum of the observed defect, we propose that it is associated to Se vacancies with the paramagnetic state being the positively charged state of the defect.

Moreover, we show that magnetic interactions between spins associated to defects in NCs can induce magnetic anisotropy effects in NCs ensembles that are not expected to occur in their bulk counterpart. Using angular-dependent ferromagnetic resonance (FMR) spectroscopy, we measure the magnetic anisotropy in different random ensembles of CdSe NCs by recording magnetic resonance spectra for various orientations of the external magnetic field. The observed angular dependencies of resonant field are different for apparently similar CdSe NC ensembles. We show that the shape and amplitude of the FMR angular variation can be well described by a simple model that considers magnetic dipole-dipole interactions between dipoles located at the NCs surface. The surface dipoles may originate from dangling bonds on surface sites that are not passivated by ligands. From our calculations, we find that for different random ensembles of NCs the strength of the magnetic anisotropy induced by dipole-dipole interactions may take values spanning four orders of magnitude, depending on the specific arrangement of the NCs in the ensemble and the specific distribution of the surface dipoles in each NC. This huge variability may justify the disparity of magnetic anisotropies observed in our experiments.

Contents

List of Figures

Chapter 1

Introduction

In the last two decades, the scientific community has developed an increasing interest in the growth and characterization of semiconductor nanocrystals (NCs) [24–28]. These materials are few nanometers in scale and show size-specific optical, electronic, and magnetic properties that are not present in their bulk counterpart [24, 25, 29–34]. For example, NCs have large surface-to-volume ratio, can show luminescence when reduced to nanometric dimensions [24], and have a tunable energy band-gap [29]. Moreover, NCs can show novel magnetic phenomena resulting from their reduced dimensions, such as superparamagnetism [35], quantum tunneling of magnetization [36], and enhanced magnetic coercivity [37].

Semiconductor NCs are interesting for a wide range of (opto)electronic applications. These are being explored for use in printable electronics such as thin-film transistors (TFTs) [38], where they display performances comparable to those of TFTs based in bulk semiconductors [39]. Another important application of semiconductor NCs is light-emitting diodes (LEDs), for which NCs offer good optical stability, size-tunable color across the visible spectrum, and color quality rivaling that of state-of-the-art organic LEDs [40]. Semiconductor NCs have also proven suitable for use as light-absorbing materials in photovoltaics [41], in which case devices based on NCs have achieved efficiencies near 8.5% [42]. Semiconductor NCs have also been used for the improvement of thermoelectric power devices [43]. For instance, studies have reported increasing thermopower with decreasing NC size for superlattices of ligand-capped semiconductor NCs [43].

For the integration of semiconductor NCs in many electronic devices, the NCs must possess free carriers that can participate in electrical transport. This task may seem unfeasible because, as in their bulk counterparts, intrinsic semiconductor NCs are insulating at room temperature. However, their conductivity can be enhanced by introducing additional charges through doping [44]. Doped semiconductor NCs have also been used as prototypical systems to study fundamental physical phenomena at the nanoscale, namely the electronic confinement inside the NCs [7,45,46]. Thus, the electronic doping of semiconductor NCs is highly desirable for novel technological applications [47, 48]. To understand and control the electronic doping of semiconductor NCs, some crucial questions need to be clarified. One question concerns doping efficiency of semiconductor NCs, i.e. the extent to which shallow impurity atoms are effectively incorporated in NCs. Another question is whether the ionization energy of dopants in NCs is significantly enhanced due to size-dependent confinement effects, thus affecting the the amount of electrically active dopants at room temperature. Further, it is crucial to understand and assess the influence of defect states localized either within the NCs

volume or at their surface on the concentration of charge carriers that are provided by the dopants. Defects have an important and detrimental role in limiting the performance of NC-based devices [49–52], as they give rise to energy states energetically localized within the NCs energy gap that capture charge carriers from delocalized electronic states of the NCs [53]. Studies have already demonstrated the negative impact of charge trapping defects on the performance of NC-based photovoltaic devices [49, 52, 54–56], which have been reported to induce a reduction of the open circuit voltage and short circuit current of solar cells [49,52,56] and to act as recombination centers that limit the photocurrent extraction from NC-based solar cells [54].

The technological progress in the use of NCs in electronics has also pushed research on their magnetic properties due to e.g. their relevancy in the improvement of magnetic recording media [11], and on the development of novel electronic devices based on the manipulation of electron and hole spins (so-called spintronics) [57]. Ensembles of magnetic NCs have been the subject of intense research for high-density recording media, where superparamagnetic NCs that support stable magnetization reversal can be used as bits for nanorecording and are expected to enable recording densities up to a few Tbit/in^2 [11]. Research has also demonstrated the possibility of recording the magnetic state of NCs via the injection of a spin-polarized current instead of an external magnetic field [58, 59] as in conventional magnetic memories, providing a new way for the development of novel recording media. Magnetic NCs have also proved useful for applications in medicine and biotechnology [60–64]. For example, magnetic NCs functionalized with organic ligands have been shown to enable magnetic resonance imaging (MRI) without harming the targeted organism [61]. Moreover, the sensitivity of MRI can be enhanced by engineering the geometry of magnetic NCs [60]. Magnetic NCs can also be used as therapeutic drug cargos. Drugs can be attached to the NCs surface and released upon application of an AC magnetic field [65]. The applied magnetic field causes the NCs to generate local internal heating and disassemble the bound of between the organic ligands and the NCs surface. Furthermore, heat induction in magnetic NCs by the application of an AC magnetic field can also be used in the treatment of cancer and other diseases by hyperthermia [61–63]. Many of the above mentioned applications rely on the magnetic anisotropy of the NC system. For example, magnetic anisotropy determines the magnetization reversal of the magnetic NCs and thus the stability of the information stored in magnetic storage media fabricated from magnetic NCs [11]. Individual NCs can be magnetically anisotropic [35], but when the NCs are brought together in the form of an ensemble it is necessary to determine and control the overall magnetic anisotropy of the ensemble.

In spite of the fair amount of studies available in the literature concerning the electronic and magnetic properties of NCs ensembles, the role of unpaired spins associated to dopant and defect states on these properties remains little understood. In this thesis, using magnetic resonance techniques we study physical properties induced by spin systems in semiconductor NCs. Magnetic resonance techniques have been widely used to experimentally investigate

materials with unpaired electrons [13, 66, 67]. Before the presentation and discussion of our results, in Ch. 2 we describe the state of the art concerning the topics investigated in this thesis. In this chapter, we overview the major results concerning the electronic doping of semiconductor NCs and the electronic properties of doped semiconductor NCs. Further, we summarize the main results reported in the literature regarding the identification of defects in semiconductor NCs and their effect on the electronic properties of semiconductor NCs. Moreover, we overview the investigations of magnetic anisotropy in NC systems. In Ch. 3 we present a brief description of the setup and theoretical background of the experimental techniques applied in this thesis. This chapter includes a description of the physical principles of electron paramagnetic resonance (EPR) spectroscopy and of the experimental features of this technique. In Ch. 4 we describe the preparation and the basic properties of the different materials investigated, namely intrinsic and P-doped Si NCs, and intrinsic and Ag-doped CdSe NCs. We present the synthesis techniques used to grow these NCs as well as some of their basic structural and morphological properties of used NCs.

In Ch. 5, we describe our work on the doping efficiency of Si NCs and its dependence on the external environment surrounding the NCs, and on the effect of confinement on doping of Si NCs. We experimentally probed the efficiency of doping Si NCs with P donors using electron paramagnetic resonance (EPR) spectroscopy. From quantitative EPR measurements in combination with a statistical model for the random distribution of donors in different NCs on an ensemble, we estimated that the P doping efficiency of these NCs is about 30% and we infer that most P dopants are incorporated at substitutional sites of the NCs lattice and thus act as donors. We also show that the doping efficiency of Si NCs varies by several orders of magnitude depending on their external environment. We relate this effect to charge traps associated to air molecules adsorbed to the NCs surface, which give rise to a strong compensation of donors. We observe that this effect can be reverted by desorbing the molecules from the NCs surface under vacuum. We further experimentally assessed the confinement energy of isolated P donors in Si NCs from the temperature-dependence of their characteristic EPR signal. From this, we provided experimental evidence for a confinement-induced increase of ionization energy of dopants with decreasing NC size.

Moreover, we investigated the interdopant interactions that take place when multiple dopants are incorporated in a single NC, and their effect on the electronic structure of P-doped Si NCs. As described in Ch. 6, we performed temperature-dependent EPR measurements on P-doped Si NCs and observed a deviation from Curie behavior of the temperature dependence of the intensity of the EPR signal associated to exchange coupled donors in the Si NCs. To explain this behavior, we applied a model based on the exchange coupling between pairs of donors (donor dimers) in the P-doped Si NCs. This model uses an effective mass approach, which enables us to take into consideration the random placement of donors in a single NC and within different NCs of an ensemble. Using this model, we find that dimers induce discrete states in a NC and that their EPR signal results from singlet-triplet transitions. The

deviation of the EPR signal due to exchange coupled donors from Curie behavior results from the freezing of coupled donors to their singlet ground state that occurs with decreasing temperature. We further find that, while a dimer induces discrete states in a NC, their energy splitting differs by up to three orders of magnitude for randomly placed dimers in a NC ensemble, due to an enormous dependence of the exchange energy on the dimer configuration. Using the model for exchange coupling of donors in NCs based on effective mass theory, we also predicted the electronic structure of exchange coupled donors in Si NCs with of size between 1 and 10 nm. We inferred a quenching of the intensity of the EPR signal of exchange coupled donors in Si NCs with decreasing NC size, which is more pronounced for smaller NCs. We also predicted that for NCs smaller than ≈2.5 nm, the distribution of exchange energies in a NC ensemble becomes quantized and yields a step-like behavior in the magnetic resonance temperature dependence.

In Ch. 7 we describe our investigations on charge trapping defects in intrinsic and Ag-doped CdSe NCs. Using EPR spectroscopy, we identify the presence of two charge states of a defect from the dependence of the intensity of their EPR signal on the concentration of electronic Ag dopants in the NCs. We demonstrate that these defects act as charge traps in the NCs, since the intensity of the EPR signal associated with these defects decreases by up to 80% with the incorporation of a few n-type Ag dopants per NC. The dependence of the intensity of the EPR signal due to defect traps on the concentration of Ag dopants in the NCs also provided supporting evidence for the mechanism of Ag doping suggested in previous studies [5], according to which Ag atoms behave as n-type dopants at concentrations below 2 Ag atoms per NC, and become p-type dopants for higher Ag concentrations. Using light-induced EPR, we observed an increase in the intensity of the EPR signal of the charge trapping defects under illumination, which indicates that photoexcitation leads to the generation of paramagnetic states in the CdSe NCs. From this, we showed that the charge trapping defects observed in this study cause the pinning of the Fermi level in NCs ensembles. From temperature-dependent EPR measurements, we estimated a lower limit for the ionization energy of the studied defects in CdSe NCs, which we observed to be higher than in the bulk counterpart. We estimated densities of charge trapping defects in the range of $10^{18}-10^{20}$ cm^{-3}, which should be high enough to have a performance-limiting effect in devices based on these NCs. By comparison the g-value of the charge trapping defect observed in our EPR measurements with those reported in the literature for defects in II−VI semiconductors, we assigned the trapping defects to positively charged Se vacancies in the CdSe NCs.

In Ch. 8, we report the observation of magnetic anisotropy in ensembles of isotropically-arranged intrinsic CdSe NCs via angular-dependent ferromagnetic resonance (FMR) spectroscopy. We measured the magnetic anisotropy in different random ensembles of CdSe NCs by recording magnetic resonance spectra for various orientations of the external magnetic field and observe a wide variety of magnitudes of anisotropy for different samples of similar NCs. To clarify if this unexpected behavior results from magnetic impurities in the NCs, we

performed magnetization measurements using a superconducting quantum interference device (SQUID). We obtain saturation magnetization values that are two orders of magnitude higher than those expected if the observed magnetic behavior would origin from impurities in the NCs. We develop a theoretical framework based on the magnetic dipole-dipole interactions between dipoles that are distributed at the surface of the NCs to explain the magnetic anisotropy observed in the ensembles of CdSe NCs. We show that this model can describe well our FMR data. Further, our calculations show that NC ensembles may have magnetic anisotropy with amplitudes spanning four orders of magnitude, depending of the specific arrangement of the dipoles in the NC ensemble. From this huge variability, we justify the disparity of magnetic anisotropy observed in our FMR measurements.

Chapter 2

State of the art

This chapter is divided in four sections. In the first section, we make a brief overview on the concept of doping semiconductor NCs. In the second section, we review the studies published in the literature on electronic doping of semiconductor NCs. In the third section, we review the studies published concerning defects in semiconductor NCs. In the forth section of this chapter, we describe some strategies to enhance and control magnetic anisotropy in ensembles of magnetic NCs. We review the appearance of magnetic anisotropy in two types of ensembles of magnetic NCs: (i) ensembles of NCs ordered with their magnetization easy-axes mutually parallel and (ii) ensembles of NCs randomly stacked in an anisotropic shape.

2.1 Electronic doping of semiconductor nanocrystals

Through the last eight decades, electronic doping of bulk semiconductors has proven to be crucial for the existence and development of most electronic technologies [68]. Semiconductor materials are intrinsically insulating at room temperature [2,68], but the conductivity of these materials can be enhanced by the controlled introduction of charge carriers via a process know as electronic doping. Electronic doping of semiconductors also provides control over the type of charge responsible for the electronic transport through the semiconductor [68]. If electrons are introduced, the semiconductor is said to be n-type. If holes are introduced, the semiconductor is called p-type.

Considering the importance of doping bulk semiconductors for electronic technologies, it is expected that the electronic doping of semiconductor NCs will also be fundamental for their application in future electronic devices. In this chapter, we review the advances attained so far on the electronic doping of semiconductor NCs. We also review current understanding about the electronic properties of doped semiconductor NCs.

2.1.1 Types of electronic doping applied to nanocrystals

Remote doping

The earliest reports on electronic doping of semiconductor NCs described the process of remote doping, i.e. the injection of charge carriers into NCs provided by a molecule or atom attached to the NC surface [69–71]. The process of remote doping of a semiconductor NC is schematized in Fig. 2.1. The spontaneous transfer of charges from adsorbed species into a

semiconductor NC can happen if empty electronic levels are available in the NCs and properly aligned with the occupied levels of the adsorbed molecule. Furthermore, effective remote doping requires the absence of surface or interface states that would accept the transferred charges and prevent them from contributing as free carriers in the semiconductor NC [72].

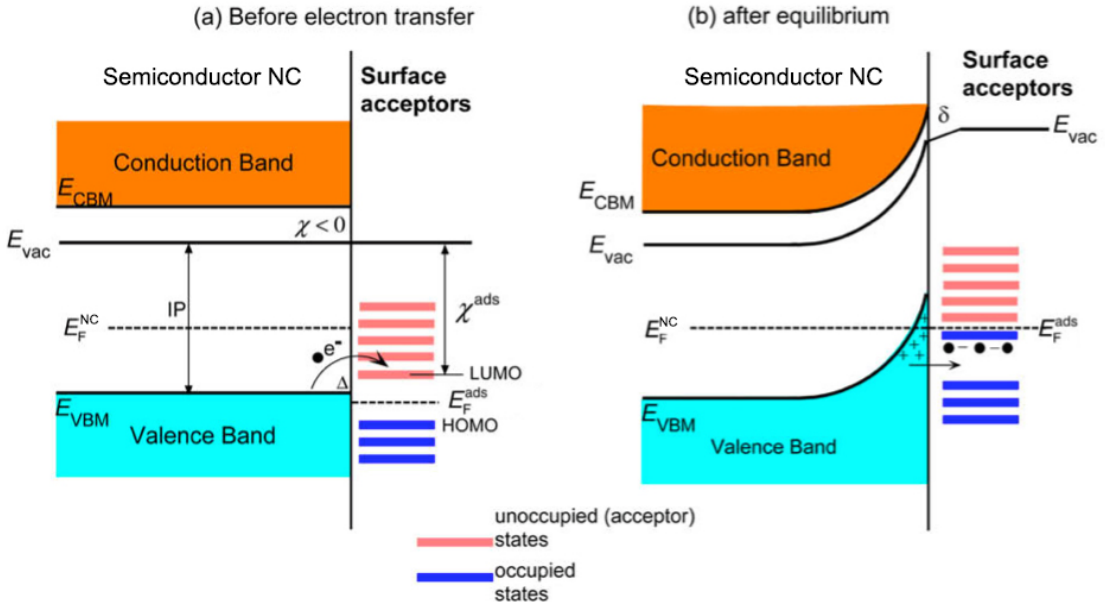

FIGURE 2.1: Schematic energy levels for p-type remote doping process. (a) Before electron transfer from the NC to the surface adsorbed acceptor molecules, the Fermi level of the adsorbates E_F^{ads} is lower than that of the NC E_F^{NC}. Electron transfer is favored from the NC valence band to unoccupied acceptor states localized at the adsorbates. (b) In thermal equilibrium after electron transfer, the Fermi levels of the NC and of the adsorbate are aligned and the NC has a layer of accumulated holes at its surface, with equal amount of compensating electrons in the adsorbates. Adapted from [1].

The first demonstration of remote doping of semiconductor NCs was reported by Shim *et al.*, who showed that CdSe NCs become n-type by injecting electrons into the NCs from sodium biphenyl molecules adsorbed to the NCs surface [69]. Later, Yu *et al.* used remote doping to turn insulating films of CdSe NCs into n-type conducting films [70]. They observed that depositing electron donating potassium atoms on the NCs surface leads to an increase in film conductivity by 12 orders of magnitude. A similar increase in the conductivity of PbSe NCs films was observed when the surface ligands acquired during NC growth were replaced by hydrazine [71]. In this case, exposing as-deposited films of PbSe NCs to hydrazine switches their conductivity from p-type to n-type. The conductivity of hydrazine-treated PbSe NCs films could be reverted to p-type by desorbing the hydrazine molecules from the NC surface. Remote doping of PbSe and PbS NCs was also realized through electron transfer from cobaltocene molecules attached to the NCs surface [73]. This method enabled the injection of

up to eight electrons per NC into the NC band-edge states. Recent investigations have focused on the remote doping of Si NCs by adsorbing strong oxidizing F_4-TCNQ molecules to the NCs surface [74]. These molecules have been used for *p*-type remote doping of diamond [75], graphene [76], and semiconductor polymers [77]. F_4-TCNQ molecules were expected to oxidize the Si surfaces because their electron affinity is larger than the ionization energy of bulk silicon [74]. In Si NCs with adsorbed F_4-TCNQ molecules, *ab initio* electronic structure calculations suggested that NCs with ≈ 1 nm in size have their highest occupied electron state very close to the energy of the lowest unoccupied electron state of the adsorbed molecule [74]. In this situation, the absorbed F_4-TCNQ molecule could oxidize the NC surface and provide a a bridging state for hole transfer between adjacent NCs in *p*-type doped Si NCs networks [74]. The mechanism proposed in this theoretical study was recently questioned by Pereira *et al.*, who observed that *n*-type charge transport in Si NCs films is strongly enhanced by adsorbing F_4-TCNQ molecules at the surface of adjacent NCs [78]. In this study they also performed density functional calculations, which showed that adsorbing F_4-TCNQ molecules to the Si NCs enhances the films conductivity by providing extra electronic connectivity across the NCs and so effectively flattens the electronic potential barrier for electron transfer between adjacent NCs. Remote doping has also been investigated on Cl-terminated Si NCs [79–81]. Studies on Cl-terminated Si NCs capped with hard donor molecules such as ketones and nitriles suggested that the Cl- termination of Si NCs lowers the conduction band level of the NCs so that it becomes an accessible level to interact with the highest occupied molecular orbital of donor molecules adsorbed to the NCs surface [80]. Gresback *et al.* further showed that thin film transistors of Cl-terminated Si NCs with adsorbed hard donor groups of organic solvents show no gating behavior, suggesting degenerate surface doping of the Si NCs [81].

Remote doping is a simple, nondestructive method with promising applications in doping semiconductor NCs [1]. This doping method can be carried out in solution, thereby facilitating large scale development of organic- and nano-electronics [1]. Studies have shown that remote doping with organic molecules can be made stable for several months. For example, films of PbS NCs capped with cobaltocene electron donating molecules were shown to be stable for several months if a thin inorganic passivation layer was applied to the films to reduce trap-mediated loss of charges injected into the NCs from the cobaltocene molecules [73]. In spite of the aforementioned advantages of remote doping, this doping method presents some noteworthy drawbacks. The charge transfer rate from the adsorbed molecule to the NC is quite sensitive to the polarity of the dielectric material surrounding the NCs [82]. Further, depending on the depth of the surface state, surface charges can either interact with the quantum confined orbitals of the NC or be highly localized, not participating in the charge transport process [83]. Some studies have also reported a lack of controllability of the concentration of charge carriers provided by adsorbed molecules [75, 84].

Substitutional doping

Following the preliminary successes achieved on remote doping of semiconductor NCs [69–71], research on the electronic doping of semiconductor NCs has been directed towards substitutional doping. This is the standard method for electronic doping of bulk semiconductors and consists on the replacement of atoms of the NCs lattice by other atoms with different number of valence electrons [68]. The concept of substitutional doping is schematized in Fig 2.2. In the crystal lattice of an undoped semiconductor, which is represented in Fig. 2.2(a), all the valence electrons participate in covalent bonds between neighboring atoms. When an atom from this lattice is replaced by an impurity with one more valence electron than the replaced atom, the extra electron will remain unpaired and loosely bond to the impurity atom; see Fig. 2.2(b). This type of impurity is called a donor because it can provide an electron to the semiconductor conduction band, e.g. by thermal activation. A semiconductor doped with donors will have excess of free electrons and thus will be n-type. Some examples of donors in semiconductors commonly used for electronics include P and As atoms in Si and Ge, and Se atoms in GaAs [4]. In a similar way, if the impurity lacks a valence electron compared with the native atom that it replaces, this impurity takes an electron from the host lattice in order to complete the covalent bonds with its neighbors, thus generating a hole; see Fig. 2.2(c). This impurity can release the bonded hole to the semiconductor valence band and so is called an acceptor. A semiconductor doped with acceptors will have excess free holes and thus will be p-type. Some examples of acceptors in bulk semiconductors include B and Al atoms in Si and Ge, and Cd atoms in GaAs [4].

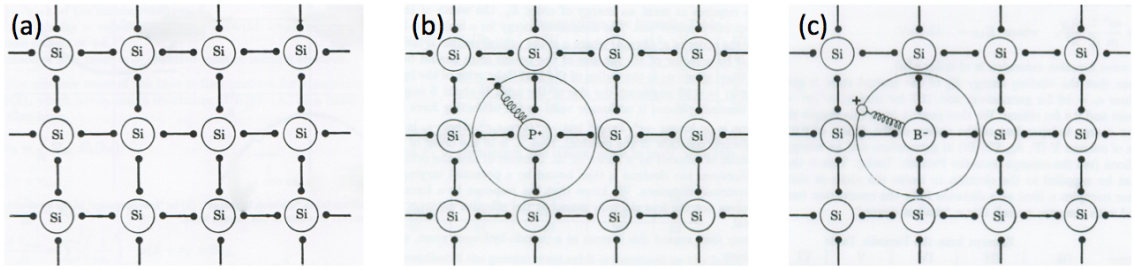

FIGURE 2.2: Scheme illustrating the concept of substitutional doping of semiconductors. Crystal lattice of (a) undoped Si, (b) Si doped with a P donor atom, and (c) Si doped with a B acceptor atom. Adapted from [2].

The introduction of dopants in bulk semiconductors results in the formation of dopant states that lie within a few tens of meV to the corresponding band edge, i.e. the valence band for acceptors and the conduction band for donors [2, 68]; see Fig. 2.3(a) and (b). The dopant state energy, so-called dopant activation energy, corresponds to the energy required to ionize the charge carrier localized at the impurity. The activation energies for some dopants

in some common bulk semiconductors are shown in the table of Fig. 2.3(c). The Fermi level of the semiconductor will also be affected by the presence of donor and acceptor impurities. In n-doped semiconductors, the Fermi level shifts towards the conduction band of the semiconductor, while in p-doped semiconductors, the Fermi level will shift towards the valence

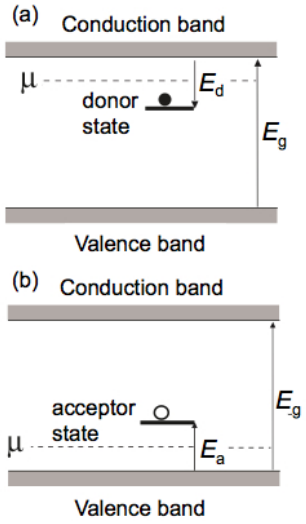

(c) Activation energy for various dopants in some common bulk semiconductors

Semiconductor	Dopant	E_d (meV)	E_a (meV)
Si	P	44	
	As	49	
	B		45
	Al		57
Ge	P	12	
	As	13	
	B		10
	Al		10
GaAs	Se	5	
	Cd		21

FIGURE 2.3: Electronic structure of a semiconductor with a band gap energy E_g and doped with (a) a n-type impurity, which provides a donor state with ionization energy E_d, and (b) a p-type impurity, which provides an acceptor state with energy E_a. In each case, the Fermi level of the doped semiconductor is labelled as μ. (c) Table with the values of donor and acceptor levels for various $n-$ and $p-$type impurities, respectively, in some bulk semiconductors that are commonly used in electronics. Adapted from [3, 4].

band of the semiconductor [2]. Substitutional doping using heterovalent atoms has been demonstrated in a few NC systems. In the following sections, we overview literature reporting the achievements on the substitutional doping of NCs.

2.1.2 Electronic doping of oxide nanocrystals

In one of the earliest reports on the substitutional doping of NCs, Orlinskii *et al.* showed the incorporation of Li dopants in freestanding ZnO NCs produced by a solution-based method [85]. These dopants acted as shallow donors, providing energy levels that were localized in the band gap of the ZnO NCs and close to the NCs conduction band edge. They could probe the confinement of the dopants in small ZnO NCs (up to 4.5 nm in size) using electron nuclear double resonance (ENDOR) via a size dependence of the splitting of the hyperfine signal associated to the interaction between the donor electrons ($S = 1/2$) and their Li nuclei ($I = 3/2$). More recently, it was shown that the incorporation of substitutional Al dopants yields n-type conductivity in films of colloidal ZnO NCs, which makes these films transparent

conductive oxides [86]. The effective incorporation of Al in ZnO NCs was demonstrated by tracking their free electron absorption in the infrared region [86].

Electronic doping has also been investigated in TiO_2 NCs. Substitutional doping of these NCs with N impurities has been reported to improve the photocatalytic activity in the visible-light region of powders and films comprising N-doped TiO_2 NCs by enhancing the decomposition rates of methylene blue under illumination [87–89]. Asahi *et al.* used first-principle calculations and x-ray photoemission spectroscopy to show that N dopants occupy substitutional O sites of TiO_2 NCs, producing intragap energy states near the NCs valence band that can absorb visible light [87]. The presence of these intragap states leads to a narrowing of the NCs band gap, which is very large in intrinsic TiO_2 (3.0-3.2 eV) [87]. A similar observation was done by Spadavecchia *et al.* using optical and electrochemical measurements and computational calculations [90]. From diffuse reflectance measurements, they observed that the introduction of N dopants in the NCs produces intragap states above the NC valence band. This leads to an apparent narrowing of the NC band gap. They also observed the presence of intragap states below the NC conduction band due Ti^{3+} cations associated to O vacancies in the NC. The presence of these O vacancies is expected to be enhanced upon doping the TiO_2 NCs with N, as indicated by theoretical calculations that predicted that N doping of bulk TiO_2 leads to a significant decrease of the energy cost to form oxygen vacancies [91].

2.1.3 Electronic doping of III−V and II−VI nanocrystals

Nanocrystals of III−V and II−VI materials are most commonly produced by solution-based methods [92]. Although the synthesis of NCs doped with *n*- and *p*-type dopants by solution-based methods is not trivial, some progress has recently been reported for NCs of CdSe [5, 93, 94], PbSe [95, 96], and InAs [97, 98]. In the following, we briefly describe some of the recent research regarding the electronic doping of NCs of these materials.

InAs nanocrystals

Considerable advances were made on the electronic doping of InAs NCs [97, 98]. This type of NCs has been doped *n*- and *p*-type, thus enabling the possibility of fabrication of *p*-*n* homojunctions for use in transistors. Bawendi group found that films of intrinsic InAs NCs were *n*-type and attributed this behavior to electron donating states at the NCs surface [97]. But if the as-synthesized InAs NCs were exposed for three hours to a solution of $Cd(Oleate)_2$ with oleylamine and then deposited by drop-casting, the films produced were *p*-type [97]. They proposed that this behavior could result from the substitutional incorporation of Cd acceptor impurities at In sites of the NCs. They also proposed that Cd atoms could be incorporated at the NCs surface, where they would create acceptor states that could passivate surface states with unpaired electrons. In another study, Mocatta *et al.* developed a room-temperature solid-state diffusion method to dope colloidal InAs NCs with Cu and Ag impurities [98]. Using scanning tunneling spectroscopy, they observed shifts in the NCs Fermi level by the

introduction of Cu and Ag impurities. From these measurements, they concluded that Cu and Ag impurities dope InAs NCs *n*- and *p*-type, respectively. In the same study, it was also predicted that interdopant interactions in heavily doped NCs (above 5%) yield the emergence of a confined impurity subband in the NC electronic structure, which seemed to be a behavior parallel to that of bulk semiconductors.

CdSe nanocrystals

Electronic doping of CdSe NCs with substitutional impurities has also been accomplished. Preliminary attempts probed the possibility of producing donor or acceptor states in CdSe NCs by introducing In and Sn impurities [94]. There, the introduction of In and Sn dopants in the CdSe NCs was confirmed by transmission electron microscopy (TEM). It was further observed that the photoluminescence of In- and Sn-doped CdSe NCs exhibited a much steeper temperature dependence than that of undoped CdSe NCs, which provided evidence for the *n*-type behavior for In and Sn doped CdSe NCs. Norris group provided direct evidence for *n*-type doping of CdSe by transport measurements of Al- and In-doped CdSe NCs processed into TFTs [93]. They observed that when Al-doped CdSe NCs were processed into TFTs, enhanced *n*-type transport was observed with a rise in the Fermi level compared to undoped CdSe NCs.

Norris group was also able to dope CdSe NCs with a controlled number of Ag impurities and use them to produce TFTs such as that schematized in Fig. 2.4(a) [5]. Using these devices, they could determine the local voltage in each film at which conduction turned on, since this voltage is directly related to the energy offset between the Fermi level in the film and the conducting states in the NC at zero bias. From this, they could infer the energy level diagram of CdSe NCs for different levels of Ag doping, which is shown in Fig. 2.4(b). The current-voltage curves of the TFTs of Ag-doped CdSe NCs, which are shown in Fig. 2.4(c) for the case of thin films comprinsing 3.6 nm CdSe NCs with different amounts of Ag dopants, show that the films of CdSe NCs conduct when they are positively biased. From this, they inferred that the films of CdSe NCs are *n*-type. From the current-voltage curves shown in Fig. 2.4(c), they extracted the turn-on voltage and the electron mobility as a function of the number of Ag dopants, which are plotted in Figs. 2.4(d) and (e), respectively. The turn-on voltage measured in their films of Ag-doped CdSe NCs showed a shift for different Ag doping concentration, which they associated to changes in the Fermi level of the NCs [see Fig. 2.4(b)]. Accordingly, they proposed that the shifts in the turn-on voltage and electron mobility with Ag doping concentration of the CdSe NCs resulted from a change in the doping behavior with the concentration of Ag dopants in the NCs. For Ag concentrations up to ∼2 Ag/NC, Ag was proposed to be incorporated on interstitial sites of the NCs and behave as an *n*-type dopant [5], leading to a decrease in the turn-on voltage and increase in the electron mobility of the Ag-doped CdSe NCs films. For higher Ag concentrations, it was proposed that the dopants become incorporated on substitutional sites of the NCs and behave as *p*-type dopants

and thus lead to an increase in the turn-on voltage of the films of Ag-doped CdSe NCs and quench of their electron mobility [5].

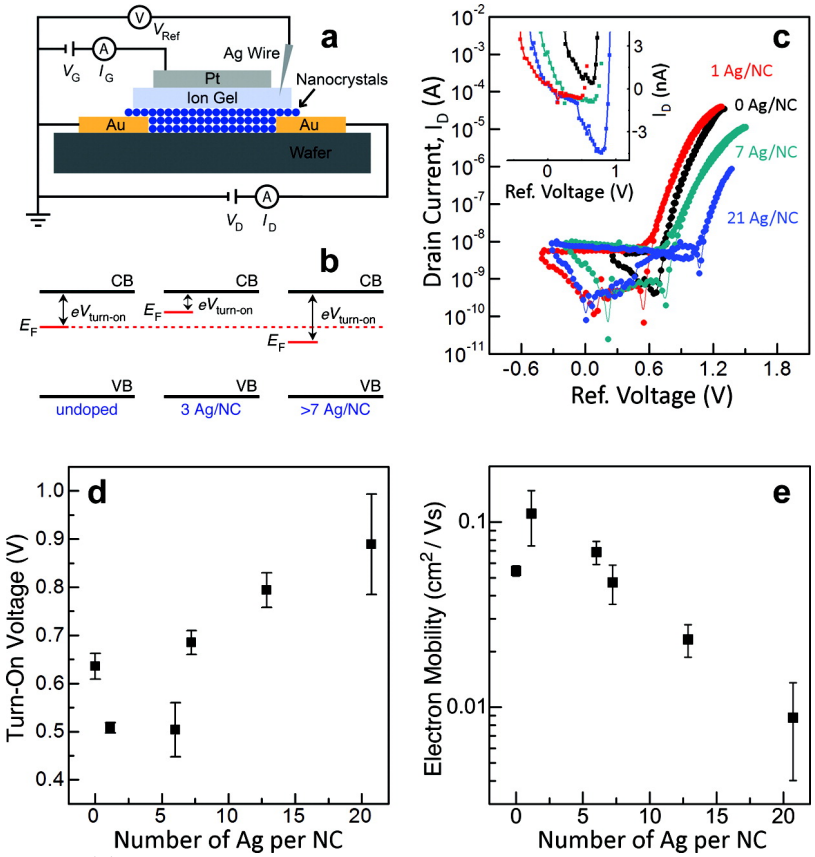

FIGURE 2.4: (a) Schematic cross-section of a thin-film transistor used to characterize the electroncal properties of Ag-doped CdSe NCs. (b) Energy level diagram depicting the relationship between the Fermi level, turn-on voltage, and the conduction band for films of CdSe NCs (undoped, ~ 3 Ag per NC, and > 7 Ag per NC). (c) Absolute value of the drain current versus the reference voltage for 3.6 nm CdSe NCs undoped (black), with 1.0 Ag per NC (red), 7.0 Ag per NC (green), and 21 Ag per NC (blue). (d) Turn-on voltage versus the number of Ag per NC, extracted from data in (c). (e) Electron mobility computed at a gate voltage of 2.5 V versus the number of Ag per NC, extracted from data in (c). Adapted from [5].

PbSe nanocrystals

Very recently, Kang *et al.* reported the doping of PbSe NCs with electronically active impurities [95]. They successfully introduced Ag atoms in PbSe NCs and fabricated field-effect transistors based on these NCs. They examined the temperature-dependent charge transport through the NCs films and from these measurements they found that the incorporation of Ag atoms in the PbSe NCs lowers the Fermi level of the NCs films, which is consistent with *p*-type doping of the PbSe NCs. Furthermore, they observed that the activation energy for

charge transport decreases with the concentration of Ag dopants incorporated into the PbSe NCs. In a succeeding study, Oh *et al.* investigated the effects of introducing excess Pb and Se atoms in PbSe NCs, through thermal evaporation, on the electronic properties of field effect transistors produced with these NCs [96]. There, they reported that the stoichiometric imbalance resulting from the introduction of excess atoms to the NCs lattice lead to unipolar *n*- and *p*-type semiconducting channels for transistors of PbSe NCs prepared with excess Pb and Se, respectively. They further reported that the electron mobilities for the transistors of PbSe NCs prepared with excess Pb were one order of magnitude higher than previously reported in PbSe NCs devices.

2.1.4 Electronic doping of group IV semiconductor nanocrystals

Group IV semiconductor NCs are of particular interest for electronic applications due to the importance of their bulk counterparts, namely Si, in conventional electronics [68]. Nanocrystals of Si have been attracting much research interest over the last decade because of their remarkable electronic, optical, and chemical properties [99–105]. Si NCs combine processing advantages enabled by NCs with the unique features of Si at the nanoscale such as wavelength tunable light emission [106–108] and multiple exciton generation [109]. Si NCs are breaking new ground for applications in light emitting devices [110, 111], solar energy to electricity conversion [112–114], thermoelectric elements [115, 116], cost-efficient large area electronics using printable NC-inks [78, 117–119], and as fluorescent labels for biological sensing, taking advantage of the biocompatibility of silicon [120]. The natural abundance of silicon and its dominant role in microelectronics industry may also facilitate the introduction of Si NCs in commercial products. Si NCs have been synthesized by various techniques, including solid-gas reaction [121], liquid phase synthesis [122, 123], laser pyrolysis of silane [124–127], laser ablation [128], laser vaporization-controlled condensation [129], plasma-enhanced chemical vapor deposition [130], and plasma-assisted decomposition of silane in a flow-through reactor [106, 120, 131, 132]. Among these, plasma-based methods proved to be very efficient in producing high-quality Si NCs with control over diameter in the range from a few nanometers to a few hundred of nanometers [106, 120, 131] and with a very low amount of defects [133]. From these, the microwave-based reactors offer the advantage that they can be scaled up [106], which enables the fabrication of large quantities of high-quality and size-controlled Si NCs for industrial usage. Si NCs have also been successfully synthesized containing *n*- and *p*-type dopant impurities [6, 44, 134–137]. In the following section we will make an overview of the knowledge and the advances attained on the electronic doping of Si NCs.

n-type doping of Si nanocrystals

The synthesis of P-doped Si NCs was first reported in the late 1990's, when Fujii group described a method to produce P-doped Si NCs by simultaneous sputtering of Si, SiO_2 and P_2O_5 and subsequent annealing in N_2 or Ar atmosphere at 1100-1250^{o}C [138, 139]. This

synthesis method yields thin films of P-doped Si NCs embedded in phosphosilicate glass, in which the concentration of P dopants was determined by electron probe microanalysis [138]. To act as an electronic donor, P has to be incorporated on substitutional sites of the Si NCs core. Fujii *et al.* demonstrated this behavior by electron paramagnetic resonance (EPR) experiments via the observation of the EPR line centered at $g = 1.998$, which is a fingerprint of substitutional P in crystalline bulk Si. This line originates from exchange-coupled electrons donated by the P dopant atoms [46]. In addition, they also observed a pair EPR lines with median at $g = 1.998$, which they demonstrate to correspond to the hyperfine structure of non-interacting P donors in the Si NCs [46]. The hyperfine structure of a P donor results from the hyperfine interaction of the donated electron spin ($S = 1/2$) with the nucleus spin ($I = 1/2$) of the P dopant atoms. The hyperfine structure of non-interacting substitutional P donors in crystalline bulk Si is characterized by a magnetic field splitting between the two EPR lines of 4.1 ± 0.1 mT [23,140]. In their measurements, Fuji *et al.* reported that the hyperfine splitting observed in their P-doped Si NCs was much larger than this value and depended strongly on the size of the NCs. They associated this observation to quantum confinement of P donors in the Si NCs [46].

As-synthesized P-doped Si NCs grown by the phase segregation method described above are embedded in a dielectric matrix which prohibits efficient charge transport between Si NCs [46]. More recently, research efforts have been directed towards the synthesis of Si NCs that are non-embedded and non-agglomerated, so-called freestanding Si NCs. Studies have reported a method of synthesis of P-doped Si NCs which relies on the plasma decomposition of silane (SiH_4) in the presence of phosphine (PH_3) precursors [44, 141]. In this system, the doping concentration is adjusted by adding a controlled flow of PH_3. In contrast to the phase segregation synthesis method described above, plasma synthesis of Si NCs yields freestanding NCs and, moreover, it has been scaled to an industrial level to produce high quality and size-controlled P-doped Si NCs [44,106,134,137]. A crucial feature of plasma synthesis approaches is their capacity to produce freestanding NCs of controlled size and with various types of surface functionalization. The first demonstration that P donors participate in the electrical transport through thin films processed from freestanding P-doped Si NCs was reported by Stegner *et al.* [44].

In spite of the successful incorporation of electronically active P donors in Si NCs, it has been observed that the amount of electronically active P donors is much lower than the amount of P atoms incorporated during the NC growth [6, 134]. Stegner *et al.* also studied the surface segregation of P dopants in Si NCs, grown in a flow-through microwave plasma of silane with phosphine used as the precursor of doping during growth, for a wide range of NC sizes (between 3 and 50 nm) and doping level [6]. Using EPR measurements combined with secondary-ion mass spectroscopy (SIMS), they compared the nominal concentration of P atoms $[P]_{nom}$ (defined as the fraction of phosphine in the total flow of precursor gases during growth multiplied by the atomic density of Si $n_{Si} = 5 \times 10^{22}$ cm^{-3}) with the effective

P concentration $[P]_{eff}$ in the NPs measured by SIMS; see Fig. 2.5(a). They found that for as-grown P-doped NCs with a native oxide shell the concentration of P measured by SIMS is approximately equal to the nominal doping concentration, which means that the efficiency of incorporation of P atoms in the NPs is about 100% [6]. This result was obtained for $[P]_{nom}$ between 10^{19} cm^{-3} and 5×10^{20} cm^{-3} and NC diameters ranging from ~ 3 nm to ~ 30 nm. Pi *et al.* also obtained a similar result on P-doped Si NCs with 3.8 nm in size grown in a radio-frequency flow-through plasma reactor via the dissociation of injected silane with phosphine used as a doping precursor [134]. Using inductively-coupled plasma atomic emission (ICP-AES) spectrometry, they observed that only for very high nominal doping concentrations, above 2×10^{21} cm^{-3} the incorporation efficiency of P was found to reduce to 63% [134]. The above studies have also measured $[P]_{eff}$ after the native oxide shell of the P-doped Si NCs has been removed via etching in dilute HF [6, 134]. Using SIMS, Stegner *et al.* found that after HF treatment $[P]_{eff}$ was reduced by a factor of 20, showing that about 95% of the incorporated P atoms are located in the thin outer shell of the NCs that becomes oxidized after these are exposed to air and that is removed with the etching [6]. They associated this observation to the segregation of P atoms to the surface of the NCs during synthesis in the silane plasma, so

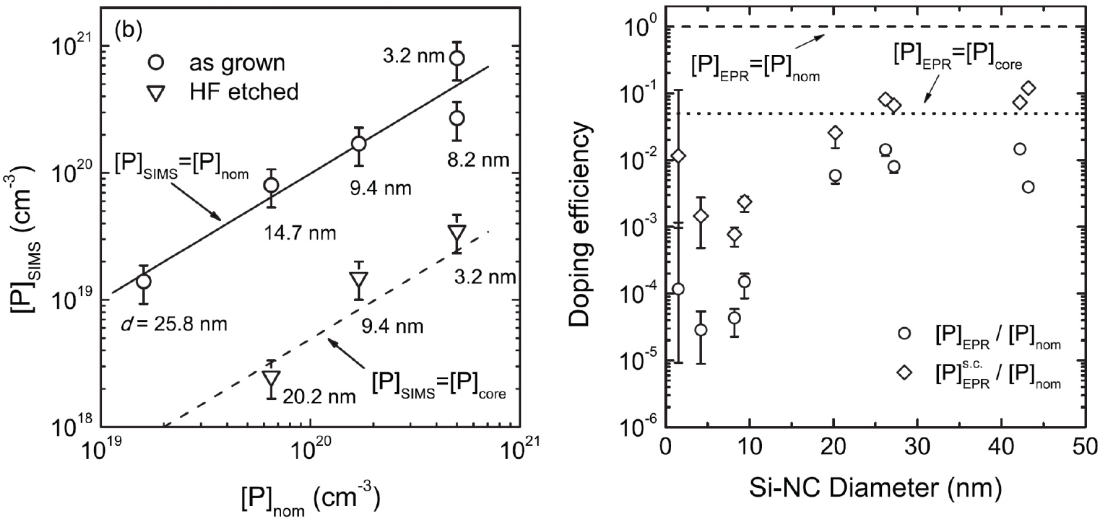

FIGURE 2.5: (a) Measured P concentration ($[P]_{SIMS}$) extracted from SIMS measurements versus $[P]_{nom}$ before (circles) and after (triangles) etching in HF. The data points are labelled with the mean NC diameter of the measured sample. The solid line corresponds to $[P]_{SIMS} = [P]_{nom}$ and the dashed line shows $[P]_{SIMS} = [P]_{nom}/20 \equiv [P]_{eff}$. (b) P doping efficiency determined from the density of spins giving rise to the $g = 1.998$ EPR line in Si NCs (denoted $[P]_{EPR} \equiv [e]$) as a function of NPs diameter. The circles show the measured $[e^-]$ normalized to $[P]_{nom}$ an the diamonds show the same data after correcting for charge compensation of donors by Si-dbs defects ($[P]^{s.c.}_{EPR}$) [6]. The dashed and dotted lines show the cases $[e] \equiv [P]_{EPR} \equiv [P]_{nom}$ and $[e] \equiv [P]_{EPR} \equiv [P]_{eff} \equiv [P]_{core}$, respectively. Adapted from [6].

that only 5% of the P atoms remain in the NCs core. Surface segregation of P atoms has also been observed by Pi *et al.*, in similar experiments involving HF etching of the native surface oxide [134]. However, in their case, the percentage of segregated P was found to be lower (about 80%) than that observed for the Si NCs studied in Ref. [6]. The reason for this difference remains unclear, but was suggested to be related to a somewhat higher temperature to which the P-doped Si NCs are exposed and/or to a longer residence time in the plasma during growth in microwave plasma reactors when compared to RF plasma reactors, which would enhance the diffusion of P atoms to the NCs surface [6].

Studies have also reported the incorporation of P dopants in Si NCs embedded in an oxide matrix, prepared by phase segregation methods [46, 142–147]. Photoluminescence measurements of P-doped Si NCs embedded in SiO_2 estimated the ratio between $[P]_{eff}$ and $[P]_{nom}$, which corresponded to the concentration of P atoms introduced in the films used to produce the Si NCs embedded in SiO_2 [144]. The values of $[P]_{eff}$ were estimated from the quenching of the PL signal, associated with Si dangling bonds (Si-dbs) at the NCs surface, that was observed upon doping the NCs with P. These studies found that $[P]_{eff}/[P]_{nom}$ decreases with increasing $[P]_{nom}$, and associated this observation to the segregation of P dopants to the interface between the NCs and the surrounding matrix, which should become more significant as the P content increases. Further studies on P-doped Si NCs embedded in silicon-oxynitride ($SiO_{0.93}N_{0.22}$) directly assessed $[P]_{eff}$ using three-dimensional atom probe tomography [145]. These studies found that about 20% of the P dopants are incorporated into the Si NCs and that an amount of P atoms corresponding to 30% of $[P]_{nom}$ is located at the interface between the NCs and their surrounding matrix. Studies have also suggested that P dopants can be introduced in Si NCs embedded in a SiO_2 matrix through diffusion of P atoms during thermal annealing at about 1000°C from a spatially separated dopant source, namely a phosphosilicate thin-film with a thickness up to 0.5 nm [148–151]. By combining SIMS and X-ray photoelectron spectroscopy measurements with computational modeling of the experimental data, it was concluded that the incorporation of P dopants into Si NCs is aided by the presence of the SiO_2 matrix surrounding the NCs, which provides a barrier of about 1 eV for the diffusion of P atoms out of the NCs [149, 151]. Further, it was shown that P dopants can be introduced in the Si NCs embedded in SiO_2 at concentrations up to six times the solubility limit of P in bulk Si [151].

Experimental studies on P-doped Si NCs have also investigated the relation between $[P]_{eff}$ and the quantity of donor electrons provided by electrically active P dopants [6, 146, 147]. Magnetic resonance measurements of freestanding P-doped Si NCs showed that donor electrons from substitutional P in the Si NCs may become trapped at defects that introduce mid gap states in the NCs' electronic structure [6]. It was further shown that Si-dbs are a major source of these trap states in Si NCs. These defects were shown to compensate P donors in Si NCs and lead to a reduction of the concentration of electrons $[e^-]$ provided by P donors by about one order of magnitude with respect to $[P]_{eff}$ for NCs with diameters larger than

$\sim$12 nm [6]. In P-doped Si NCs with 4 nm in size and embedded in a SiO_2 matrix, transient current analyzes found that the concentration of carriers $[e^-]$ provided by P dopants for electronic transport within the NCs conduction band was only about 0.12% of $[P]_{nom}$ [146]. This observation was suggested to result from the incorporation of most P dopants in the NCs as interstitial impurities rather than as substitutional donors [146, 147]. Interstitial P dopants in Si NCs are expected to induce deep trap states which cannot donate electrons but provide efficient carrier recombination, based on density functional theory calculations [147].

Experimental studies using electrically detected magnetic resonance (EDMR) observed spin-dependent transport through P donors in the Si NCs [44]. Temperature dependent conductivity measurements we further used to study the influence of P dopants on the electrical conductivity of thin films processed from freestanding P-doped Si NCs [44,137]. They showed that doping Si NCs with nominal P concentrations above 2×10^{19} cm^{-3} yields both an increase in the dark conductivity of the films (up to $5{\times}10^{-8}$ Ω^{-1} cm^{-1} for samples with highest P doping concentration) and a decrease in the temperature dependence of their conductivity [44, 137]. Gresback *et al.* studied the carrier mobility of P-doped Si NCs in field-effect transistors produced from freestanding P-doped Si NCs [81] and observed electron mobilities up to 5×10^{-4} cm^{-2} V^{-1} s^{-1}. Moreover, they observed that the activation efficiency of dopants in Si NCs is quite low, ranging between 10^{-4} and 10^{-2}.

Theoretical studies have also addressed the question of the location of P dopants in Si NCs. *Ab initio* studies suggested that P dopants prefer to occupy sites near the surface of Si NCs [8, 152], because the formation energy of a substitutional P donor is lower near the Si NC surface than at the NCs core [152]. Chan *et al.* further predicted that the dopant impurity formation energy increases with decreasing NC size, suggesting that for very small NCs the dopant atom should be expelled toward the surface [8, 153]. This mechanism was called *self purification* and assumes that thermodynamic equilibrium is established between the NC and its environment and that the dopants are able to diffuse through the NC [47]. Such situation is closer to the growth conditions of NCs produced by phase segregation, in which the NCs are grown by thermal annealing at temperatures above 1000°C during long periods of time. Under these synthesis conditions, the dopants can diffuse from the NCs core towards the NCs surface or the surrounding matrix [47]. Recent studies using density functional theory calculations predicted that P doping of Si NCs does not provide majority charge carriers to Si NCs embedded in SiO_2, because P is expected to introduce a deep donor level with ionization energy of 0.51 eV [147]. It was further predicted P atoms located at the SiO shell surrounding the NCs cannot donate electrons but lead to a decrease of 97% of the energy barrier for electron transfer between neighboring NCs [147].

In Si NCs produced by gas-phase synthesis, a major source of defects is Si-dbs associated to unpassivated sites at the NCs surface [6, 44, 133, 154]. Stegner *et al.* investigated the effect of charge compensation by defects on the P doping efficiency of Si NCs [6]. Using EPR, Stegner *et al.* also detected the presence of silicon dangling bond (Si-dbs) defect at (or close)

to the NCs surface and observed that the amount of these paramagnetic defects ($S = 1/2$) decreases with increasing P doping of the NCs [155]. This indicated that electrons donated by the P dopants are captured at Si-db defects, which become negatively charged ($S = 0$) and thus undetectable in EPR experiments. Stegner *et al.* quantified the density of donor electrons $[e^-]$ provided by the P doping to the Si NCs, using EPR spectroscopy [6]. It was observed that $[e^-]$ is always lower than the concentration of P dopants that can effectively contribute to the doping, as shown in Fig. 2.5(b). Using a statistical model that considered that the probabilities of finding P atoms and surface defects in a NC follow binomial probability distributions, and taking into account the $[P]_{eff}$ measured for each sample with SIMS and the average density of surface defects measured by EPR for undoped Si NCs, Stegner *et al.* showed that for NCs of size larger than 15 nm the difference between $[e^-]$ and $[P]_{eff}$ could be well accounted for by considering the charge compensation by surface defects [6]. Further, they observed that for smaller NCs, doping compensation by surface defects could not alone account for the observed discrepancy between $[e^-]$ and $[P]_{eff}$, see Fig. 2.5(b). Stegner *et al.* suggested that the reduced doping efficiency in smaller NCs could be due to an increase in the number of interface sites, where P does not act as a donor [6]. This number of interface sites increases with decrease NC size and could be further enhanced if P locates preferentially close to the NCs surface.

p-type doping of Si nanocrystals

The p-type doping of Si NCs has been achieved mostly through the incorporation of B atoms on substitutional lattice sites of the Si NCs. The synthesis of B-doped Si NCs is performed in a way identical to that developed for P-doped Si NCs, but with changes in the precursor materials used. B-doped Si NCs embedded in borosilicate glasses have been produced through phase segregation method by using B_2O_3 sputtering targets as the source for B dopants incorporated in the Si NCs [156,157]. In plasma synthesis methods, B-doped Si NCs can also be produced by using SiH_4 and diborane (B_2H_6) as precursor gases [134,137,158]. However, in experiments similar to those performed for P-doped Si NCs, Pi *et al.* have compared the effective concentration of B atoms in the Si NCs using ICP-AES with the nominal boron concentration $[B]_{nom}$ calculated from the gas flow rates of precursor gases used during NC synthesis [134]. The B-doped Si NCs were grown with the same type of RF flow-through plasma reactor as used in the case of P-doped Si NCs, with diborane used as a precursor. In contrast to the case of P doping, Pi *et al.* observed that the efficiency of incorporation of B atoms in the NCs was only 10%, which could be attributed to larger formation energy predicted for substitutional B when compared to that of substitutional P, if there is no lattice relaxation in the doped NCs [152]. However, this result contrasts with that obtained for B-doped Si NCs grown in microwave reactors [137], where the efficiency of doping with B has been found to be 100%, similar to the case of P doping. Regarding the location of B dopants in Si NCs, it is expected that the segregation has a smaller effect on

the doping of Si NCs with B than with P because the segregation coefficient, i.e. the ratio of dopant concentration at the surface to that in the core, of epitaxially-grown Si is much larger for P than for B [159]. Thus, B dopants should have a much stronger tendency to stay in the Si NCs core than at their surface. Theoretical studies have also supported the experimental observation that B dopants tend to be incorporated at the Si NCs core. Ma *et al.* have calculated the formation energy of B in Si NCs [160] and predicted the wavefunction of B dopants has a better chance to extend from the NCs surface to their core when the NC surface is oxidized. This prediction was also confirmed experimentally by Pi *et al.* [134], who studied B doped Si NCs grown with RF plasma [134]. They observed that after exposure of the NCs to air and subsequent removal of the native oxide shell with HF etching, the B concentration increases with respect to that measured for the as-grown NCs, which shows that the surface segregation effect observed for P-doped NCs does not take place in the case of B doping. A similar observation was reported for B-doped Si NCs grown with microwave plasma [137]. Thus, in the case of B dopants in Si NCs, it becomes apparent that the dopant atoms are primarily incorporated in the Si NCs core [134]. Some theoretical studies have focused on the doping efficiency and location of B dopants in Si NCs. Computational studies showed that the formation energy of substitutional B in Si NCs is higher that of substitutional P, indicating that B should be less efficiently incorporated in Si NCs than P [152]. This was experimentally verified by Pi *et al.* [134], who used ICP-AES to analyze the elemental compositions of B-doped Si NCs grown by plasma synthesis.

While the successful incorporation of P donors in the Si NCs could be confirmed by the observation of the above mentioned EPR lines characteristic of P-donors in Si, holes from B acceptors in Si NCs have remained unobserved by EPR even for very high B doping concentrations [161]. Holes from B acceptors in Si are difficult to detect via EPR because of the four-fold degeneracy of the B acceptor ground state, which results in very fast spin relaxation and broadening of their EPR signal [162]. In spite of the difficulties associated to the detection of B acceptors in Si NCs by EPR, studies showed that the incorporation of B dopants in Si NCs can be probed by Raman spectroscopy via the observation of B-related local vibrational modes [137].

The electrical conductivity of B-doped Si NCs has been investigated in several studies. Lechner *et al.* showed that the effect of B-doping on the electrical conductivity of spin-coated films of B-doped NCs is only observable for doping concentrations above 10^{19} cm^{-3} [137]. The electrical conductivity of their as-deposited films of B-doped Si NCs increased linearly with doping concentration but was relatively low (up to 10^{-6} Ω^{-1} cm^{-1} for the samples with highest doping concentration). Gresback *et al.* studied the charge carrier mobility of B-doped Si NCs in field-effect transistors produced from freestanding B-doped Si NCs [81]. They observed hole mobilities in the range of 10^{-6} cm^{-2} V^{-1} s^{-1}.

Co-doping of Si nanocrystals

The co-doping of Si NCs with P and B dopants was initially investigated theoretically by Ossicini *et al.*, who predicted from *ab-initio* calculations that the formation energy of Si NCs simultaneously doped with a B and a P atom was about 1 eV smaller than that of B-doped Si NCs and about 0.7 eV smaller than that of P-doped Si NCs [163–165]. Further, it was predicted that the P and B dopants in co-doped Si NCs tend to occupy nearest neighbors sites inside the NC [166].

Experimentally, Fujii *et al.* have produced co-doped of Si NCs with P and B dopants by the phase segregation method *et al.* [167, 168]. They have reported that Si NCs simultaneously doped with P and B grown by phase segregation synthesis can be removed from their embedding matrix by exposing the as-synthesized NCs matrices to hydrofluoric acid [168]. Furthermore, they report that the isolated NCs can then be dispersed in polar liquids, such as alcohol and water, without functionalization by organic insulating molecules. Without the potential barrier for charge transport introduced by the organic ligands, these NCs may be good candidates to realize high-conductivity NC solids.

Doping of SiGe nanocrystals

In bulk, SiGe can be doped *n*- and *p*-type by the introduction of P [169] and B [170] impurities, respectively, at substitutional sites of the semiconductor lattice. Recently, the group of Kortshagen produced SiGe NCs doped with P and B atoms [171]. In this study, they characterized the structure of P- and B-doped SiGe NCs, showing that P dopants segregate to the NCs surface while B dopants tend to be incorporated in the NC core, as in the case of P- and B-doped Si NCs, respectively. However, the electronic properties of P- and B-doped SiGe NCs remain unstudied.

2.1.5 Electronic properties of doped nanocrystals

In this section we focus on the advances attained in the physical understanding of the electronic properties of doped semiconductor NCs, focusing on the following properties: activation energy of dopants, quantum and dielectric confinements, and interdopant interactions.

Confinement effects

Dopants in NCs are confined to a much smaller volume than in their bulk counterpart. This alters the wave function of the dopant charge carrier from one case to the other. Donors in bulk semiconductors are conventionally described as a hydrogenic impurity, where the donor electron potential energy is given by the Coulomb potential of the singly-charged impurity ion screened by the bulk dielectric constant ϵ_{bulk}. The donor electron ground state envelope-function is the 1s state of a hydrogen-line atom [172], as shown schematically in Fig. 2.6(a). This wave function extends to a large distance from the dopant nucleus. In NCs the wave

function is strongly localized in the NC volume due to the confining potential barrier at the surface of the NC [7]. The donor wave function deviates strongly from the hydrogen-like function due to the influence of the confining potential barrier of the medium surrounding the NC, as schematically shown in Fig. 2.6(b).

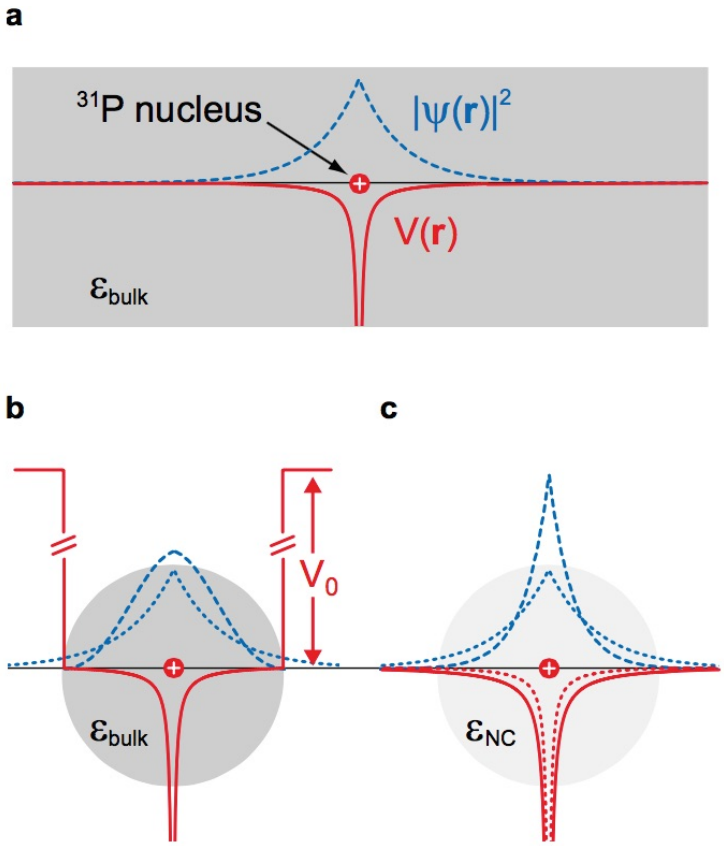

FIGURE 2.6: (a) Hydrogenlike model of a donor impurity in bulk semiconductor. (b) Quantum confinement and (c) dielectric confinement models of a donor impurity in a semiconductor NC. Dashed and solid lines represent electron probability density $|\Psi(r)|^2$ and potential energy $V(r)$, respectively. Dotted lines in (b) and (c) correspond to the bulk situation. Adapted from [7].

Theoretical studies have investigated the effect of confinement on the dopant wave function localization, predicting that the dopant wave function localization within the NC volume increases with decreasing NC size [8,152,173]. Experimentally, magnetic resonance techniques have been very valuable for the study of confinement of donors in semiconductor NCs [7,46,85]. Orlinskii *et al.* used electron nuclear double resonance to probe the wave function of interstitial Li donors in ZnO NCs [85]. They observed that the hyperfine interaction between the donor electron and the Li nucleus, increases when reducing the NC size and associated this effect to the confinement of the Li donors in the ZnO NCs. The hyperfine interaction with P donors

in Si NCs has also been used to study the confinement of P donors in Si NCs [7, 46]. In bulk Si, the hyperfine structure of a P donor consists of two lines separated by 4.2 mT [140]. In P-doped Si NCs, it has been observed that the splitting between the hyperfine lines is larger than in the bulk and increases for smaller NCs [7, 46]. This observation was shown to result from an increase of the donor electron localization in Si NCs due to confinement effects [7, 46]. From the dependence of the hyperfine splitting on the NCs size, Fujii *et al.* showed that the hyperfine splitting for P donors in Si NCs embedded in SiO_2 scales with d_{NC}^{-3}, where d_{NC} is the NC size, which simply corresponds to the dependence of the electron probability density in the center of a spherical potential of infinite height [174]. Studies on the hyperfine interaction for P donors in Si NCs grown by gas phase methods showed that for these NCs the dependence of the hyperfine splitting could be well described by a continuous-medium model that considered both the Coulomb interaction between the donor electron and the positive charge represented by the P nucleus and the confining potential imposed by the NC surface [7]. The screening of the Coulomb interaction was considered via a NC size dependent screening dielectric constant ϵ_{NC} [175–178], which results in a size-dependent localization of the donor state (dielectric confinement), represented in Fig. 2.6(c).

Confinement effects affect the electronic structure of dopants in NCs. Confinement leads to an increase of the NCs band gap with decreasing NC size, thus increasing the depth of the dopant state inside the gap [165]. Further, confinement leads to a shift of the dopant energy level to higher energy when the hydrogenic Bohr radius of the charge carrier localized at the dopant becomes comparable to the size of the NC [165]. The confinement energy may exceed that of Coulomb interaction between the dopant nucleus and the localized charge carrier [179, 180].

The activation energy determines the probability of generating free charge carriers from dopant states in semiconductor NCs. The activation of a dopant in a semiconductor NC comprises (i) the ionization of the dopant in a NC, and (ii) the transfer of the ionized change carrier to an undoped NC [8, 173]. Thus, the activation energy of a dopant in a NC is defined as the difference between the ionization energy of the dopant in the NC and the electron affinity energy of the NC, i.e. the energy gained by adding the ionized electron to an undoped NC [8, 173]. *Ab initio* calculations using density-functional theory have been used to investigate the activation energy of single dopant configurations in NCs [8, 152, 153, 173]. Melnikov *et al.* calculated the ionization, electron affinity, and activation energy of P donors in Si NCs for NC sizes between 0.8 and 2.4 nm [173]. Their calculations suggested that, in contrast to the case of undoped Si NCs, the ionization energy of P-doped Si NCs is independent of the NC size. They further predicted that the activation energy in P-doped Si NCs increases with decreasing NC size. Cantele *et al.* also observed this trend in the ionization energy of P- and B-doped Si NCs [152]. Chan *et al.* calculated the activation energy of P donors in Si NCs with a diameter up to 6 nm for different positions of the donor in the NC [8]. They observed that the calculated activation energies can be described by an effective mass model, which

considers that the donor behaves as an hydrogen-like atom confined in a spherical potential well; see Fig. 2.7.

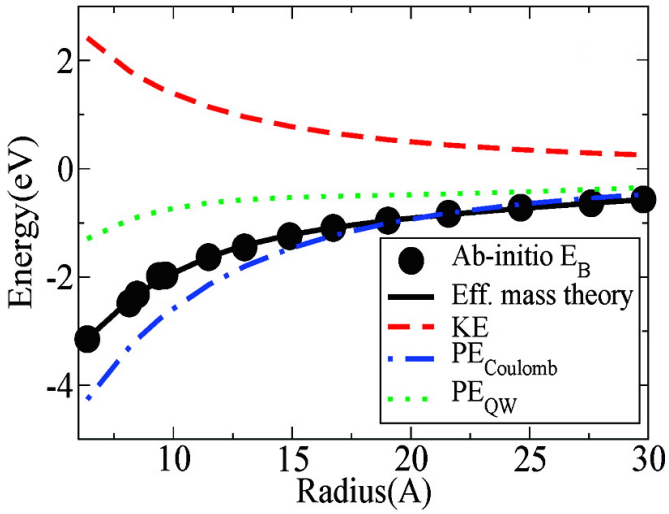

FIGURE 2.7: Activation energy calculated for P-doped Si NCs as a function of the NC radius. Then black dots show the activation energies calculated by *ab initio*. The solid line shows the NC size dependence of the activation energy fitted from effective mass theory, which has contribution from the kinetic energy (KE, red dashed line), the Coulomb interaction between the donor electron and the donor nucleus ($PE_{Coulomb}$, blue dashed and dotted line), and the potential energy due to confinement inside the NC (PE_{QW}, green dotted line). Adapted from [8].

Interdopant interactions

The electronic properties of doped semiconductors are also affected by the interdopant interactions resulting from the overlapping between the wave functions of dopants. For example, in bulk semiconductors, the interaction between many dopants results in closely spaced impurity states that develop into an impurity subband near the respective band edge [181]. Mocatta *et al.* have reported that when doping InAs NCs with *n*- and *p*-type impurities at concentrations above 5%, interdopant interactions yield the emergence of a confined impurity subband in the NCs electronic structure [98].

The presence of multiple dopants in a single Si NC has been demonstrated by EPR for the case of donor electrons from P impurities [6, 44, 142, 182]. These studies reported the observation of a band at $g = 1.998$ which is similar to the EPR resonance attributed to exchange-coupled donors in bulk Si. It was also observed that the intensity of the band associated to exchange-coupled P donors quenches for Si NC sizes below 15 nm [6], and that its temperature dependence shows a deviation from Curie behavior at low-temperatures [6, 142, 182]. These observations cannot be explained solely by the compensation of donors by defects at the NCs surface mentioned above [6,44] and provide an indication that interdopant interactions in NCs should be different from those taking place in bulk semiconductors.

2.2 Defects in semiconductor nanocrystals

Even though doped semiconductor NCs have been proven to be promising materials for future technological applications due to their unique optoelectronic properties, the achievable performance of NC-based devices is currently limited by the presence of defects that act as recombination and trapping centers [27,49–55,183–188]. Electrically active defects give rise to energy states energetically localized within the NC's energy gap that capture charge carriers from delocalized electronic states of the NCs [53]. The presence of trap states reduces the mobility and the diffusion length of charge carriers across films of NCs [54,187]. Trap states can also be centers of fast non-radiative recombination of photogenerated charge carriers [52, 54, 55, 187, 188]. Furthermore, recombination at trap states leads to a quenching of the NCs photoluminescence [55]. Photoluminescence studies also probed the charge carrier diffusion across films of PbS NCs with various surface ligand treatments [54]. There, the authors developed an analytical model of diffusion of charge carriers in 1D and 3D structures that allows the direct extraction of the diffusion length, trap density, mobility and lifetime of charge carriers in the NCs exclusively from optical measurements. Further, they estimated that the diffusion length in PbS NCs-based photovoltaic devices with a power conversion efficiency of 7% is about 80 nm.

A wealth of studies has demonstrated the negative impact of charge traps on the performance of NC-based photovoltaic devices [49, 52, 54–56]. For example, some studies showed that the number and energy of trap states in NCs lead to a reduction of the open circuit voltage and the short circuit current of solar cells [49, 52, 56]. Other studies have shown that charge traps acting as recombination centers limit the photocurrent extraction from NC-based solar cells [54]. Ip *et al.* used transient photovoltage spectroscopy and thermal admittance spectroscopy to investigate the trap state densities in films of PbS NCs [187]. There, they found that the NCs films exhibited a high density of trap states of about 1×10^{17} $\mathrm{cm}^{-3}\mathrm{eV}^{-1}$ near the middle of the NCs band gap. They also produced PbS NCs-based solar cells with a certified efficiency of 7%, whose performance was shown to be limited by electron-hole recombination due to trap states [187].

To develop new strategies for the elimination of trap states from NC-based devices and thus improve their performance, it is crucial to identify the defects responsible for these states and to further understand their impact on electronic properties. However, there have been only a few attempts to identify the origin of charge traps, both experimentally [44, 49–51, 187, 189, 190] and theoretically [187, 191–193]. Some of these studies have suggested the presence of charge traps at the NCs surface [51, 187, 191, 192]. First-principle calculations of CdSe NCs have suggested that charge traps can result from incomplete passivation of the NCs surface [187, 191–193]. Experimental support for these predictions was provided by photoelectron spectroscopy measurements of PbS NCs films, which showed that

passivating the NCs surface with halide ligands leads to a reduction in the number of midgap trap states [51]. However, it has also been proposed that defects in the bulk of the NCs (bulk defects) may give rise to trap states [49, 50, 189], regardless of the quality of the NC's surface passivation. In PbS NCs, trap states were suggested to originate from metal ions in the NC's bulk by comparing the trap capture cross section measured by thermal admittance and deep level transient spectroscopies with the ionic radius of metal ions [49]. Conductivity studies of CdSe/ZnS core/shell NCs observed trap states with an activation energy close to that of Se vacancies in bulk CdSe [50]. In CdS NCs, point defects have been observed by electron paramagnetic resonance (EPR) spectroscopy and assigned to S vacancies by comparison of their g-factor with that reported for S vacancies in bulk ZnS [189]. In spite of these advances, a definite identification of defects in metal-chalcogenide NCs has been elusive and their effect on the performance of devices based on these NCs has remained largely uncharted. Some studies have investigated the role of defects on the transport properties of thin films processed from P-doped freestanding Si NCs using used electrically-detected magnetic resonance (EDMR) [44, 190]. This technique, which is only sensitive to paramagnetic states along the current path, detects transitions between spin states as resonant changes in the conductivity of the NC films [44]. Using EDMR, Stegner *et al.* demonstrated the direct participation of Si-dbs at the NCs surface in the electronic transport through films of Si NCs [44]. They found

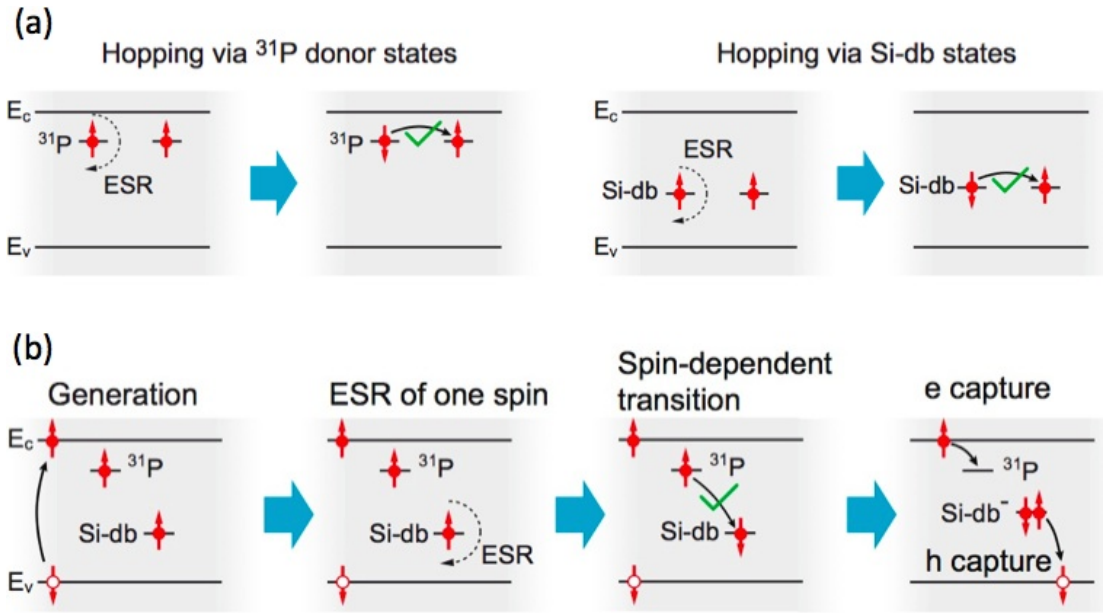

FIGURE 2.8: (a) Spin-dependent hopping through two P donor states (two leftmost panels) and through two NC surface Si-db states (two rightmost panels). (b) Spin-dependent recombination of photogenerated electron and hole at a P donor state and at a NC surface Si-db state, respectively. Adapted from [9].

that the role of NC surface Si-dbs and also P donors on electronic transport depends on the illumination conditions. In the dark transitions between singly occupied electronic states that are forbidden due to the Pauli exclusion principle become allowed via spin flips in one of the states which are induced by electron spin resonance (ESR); see Fig. 2.8(a). Under illumination both P donors and NC surface Si-dbs act as spin-dependent recombination centers for photogenerated electrons and holes, as shown in Fig. 2.8(b). This process leads to a decrease in the charge carrier density in the films of P-doped Si NCs, leading to a quenching of their conductivity.

2.3 Magnetic anisotropy in nanocrystal systems

Many of the applications of ensembles of magnetic NCs rely on magnetic anisotropy to preserve the orientation of magnetization against fluctuations due to e.g. thermal excitation [35]. Magnetic anisotropy describes the dependence of the system internal energy on the direction of its magnetization. In a magnetically anisotropic system, the total magnetization will prefer to be oriented along an easy-axis. From the energetic point of view, the two orientations of the NCs magnetization along the magnetic easy-axis correspond to energy minima, while the orientations along the hard-axis correspond to energy maxima. The energy difference between these energy extrema is called the magnetic anisotropy energy and is shown schematically in Fig. 2.9 as E_{anis}. In individual NCs, magnetic anisotropy can origin from magnetocrystalline anisotropy [194], from an anisotropic shape [195], or from strain [58, 196, 197].

Magnetocrystalline anisotropy results from the spin-orbit interaction between the orbital motion of unpaired electrons and the crystal electric field generated by the valence electrons of the NCs lattice [194]. The magnetic anisotropy has the symmetry of the NC lattice, which can be uniaxial in the case of hexagonal lattices, or cubic in the case of NCs with a cubic crystal lattice.

The magnetic shape anisotropy of a magnetic NC has a magnetostatic origin and results from the presence of magnetic poles on the boundary of a magnetized body. If the NC consists of a single magnetic domain, so-called superparamagnetic NC, these magnetic poles are located at the NC surface. These poles create an internal demagnetizing field, which depends on the geometry of the sample and decreases with increasing distance between poles. The demagnetizing field opposes the direction of magnetization and so it is easier to magnetize a NC in the direction of its largest dimension. The shape of magnetic NCs plays a crucial role in their magnetic anisotropy. For example, studies have shown that ellipsoidal superparamagnetic NCs show increased blocking temperature, which is the temperature below which relaxation time of the NCs magnetic moment becomes comparable to the experimental measurement time so that the NCs magnetic moment appears to be frozen within the time scale

of the measurement [198]. The theory describing the magnetic anisotropy of ellipsoidal superparamagnetic NCs has been described by Stoner and Wohlfarth [195], and the demagnetizing field for a general ellipsoid was calculated by Osborn [199].

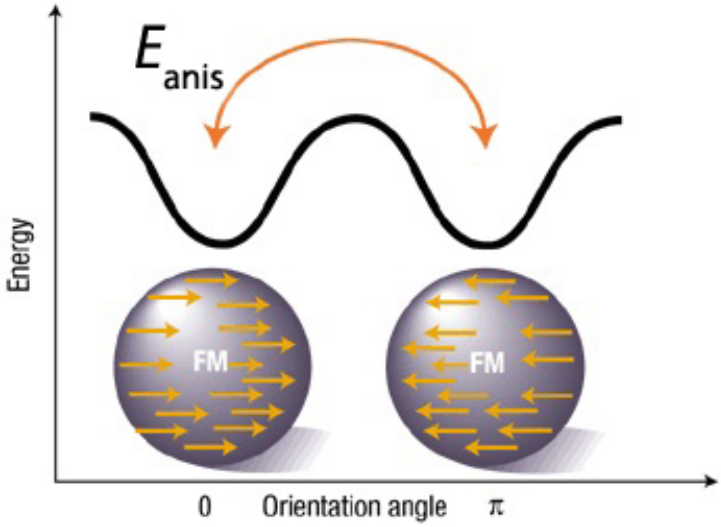

FIGURE 2.9: Plot of the variation of the NC energy with the orientation of an external magnetic field. The NC magnetic anisotropy results from the presence of the energy barrier for magnetization reversal E_{anis}. Adapted from [10].

Magnetic anisotropy can also be induced by strains in the crystalline lattice of a NC. It has been shown that NCs of magnetic alloys annealed under tensile stress show magnetic anisotropy, which results from stress-induced structural distortions of the NC lattice [196, 197]. Strains in the NC lattice can also block the spin precession of magnetic dopants in semiconductor NCs, resulting in magnetically anisotropic NCs [58].

In ensembles of magnetic NCs, magnetic anisotropy can appear if (i) the individual NCs are magnetically anisotropic and at the same time are ordered with their magnetic easy-axes mutually parallel (ensembles of ordered NCs), or (ii) the NCs are randomly stacked in a volume with an anisotropic shape (ensembles of randomly distributed NCs). In the following sections, we will review some recent advances in the study of these two types of NC ensembles.

2.3.1 Ensembles of ordered nanocrystals

As referred above, individual NCs can be magnetically anisotropic. When such NCs are brought together into ensembles, one strategy to retain magnetic anisotropy in the NC ensemble is to arrange the NCs such that the magnetization easy-axis of each NC is parallel to that of the others. One way to achieve such ordering is to use monodisperse magnetic NCs as building blocks for the fabrication of two- and three-dimensional superstructures, so-called superlattices, consisting of NCs arranged in a periodic structure resembling a crystalline lattice [200].

Lithography with photo- or electron beam-active resists has been used to create templates on which magnetic NCs can be adsorbed in the form of a superlattice [201, 202]. Todorovic *et al.* used electron-beam lithography to produce monolayers of equally-spaced nickel nanocylinders with 170 nm in diameter and 2.2 μm in length [202]. These monolayers were produced by selective etching of a AlAs/GaAs substrate coated with a poly(methylmethacrylate) (PMMA) resist. The magnetization easy-axis of each nanocylinder coincides with its long-axes, and so the superstructure displays magnetic anisotropy. The nanocylinders were spaced by 200 nm, which enabled the reading and writing of the magnetization state of individual nanocylinders using a commercial magnetoresistive head. Lithography techniques present limitations, such as the need for complex and costly infrastructures and the slow processing of NC superlattices, which impede their practical application for the mass production of superlattices of magnetic NCs [203].

Superlattices of magnetic NCs can also be fabricated through a process so-called self-assembly. In this process, monodisperse magnetic NCs in a colloidal suspension organize themselves during solvent evaporation because of an imbalance between attractive and repulsive forces acting on the magnetic NCs [200, 204, 205]. Usually, apolar solvents with low dielectric constant are used because electrostatic repulsion and magnetic dipole-dipole interactions between NCs can be neglected [200]. In this situation, attraction between NCs occurs due to attractive Van der Waals forces, which are compensated by steric repulsion between ligands adsorbed to the surface of the each magnetic NC [206]. The ordering of magnetic NCs in superlattices grown via self-assembly strongly depends on the evaporation rate of the solvent. Closely packed glassy films possessing a only short-range order are usually formed if the evaporation rate of a solvent is relatively high [207]. But if the solvent is slowly evaporated, the NCs are mobile enough and have enough time to find their lowest energy sites in a superlattice. For example, it was shown that the formation of superlattices of magnetic NCs is favored by the slow evaporation of solvent with a high boiling at increased temperatures between 50 and 60°C [200].

Self-assembly of colloidal NCs can also be affected by applying an external magnetic field during NC deposition. When the magnetic field was applied in the plane of the substrate during deposition of colloidal NCs, spindle-shaped superlattices grew with their long axes aligned along the external magnetic field [208]. Within these superlattices, individual magnetic NCs were arranged into nearly perfect arrays showing a long-range order. Furthermore, the morphology of two-dimensional superlattices of Co NCs was reported to be influenced by the direction of the external magnetic field applied during NC deposition [209]. If the magnetic field was applied perpendicular to the substrate, uniform two-dimensional ordered hexagonal superlattices were obtained, whereas applying the magnetic field parallel to the substrate led to the formation of stripes of Co NCs.

Thermal annealing can give rise to magnetic anisotropy in superlattices of magnetic NCs by changing the packing symmetry of the NCs in the superlattice. Sun *et al.* prepared

monodisperse FePt NCs that self-assemble into superlattices with face-centered cubic (fcc) symmetry [11]. These superlattices show low magnetic anisotropy, even though each individual NC has a high magnetocrystalline anisotropy. Annealing the as-synthesized fcc superlattices at ≈550°C for 30 minutes induces the rearrangement of the NCs into a face-centered tetragonal superlattice with high magnetic anisotropy. Figure 2.10 shows a TEM image of the as-synthesized and annealed two-dimensional superlattices of FePt NCs. Sun *et al.* showed that these superlattices of FePt NCs can support stable magnetic recording. The highest recording density was obtained in their annealed superlattices of FePt NCs and was equal to 5000 flux changes per mm.

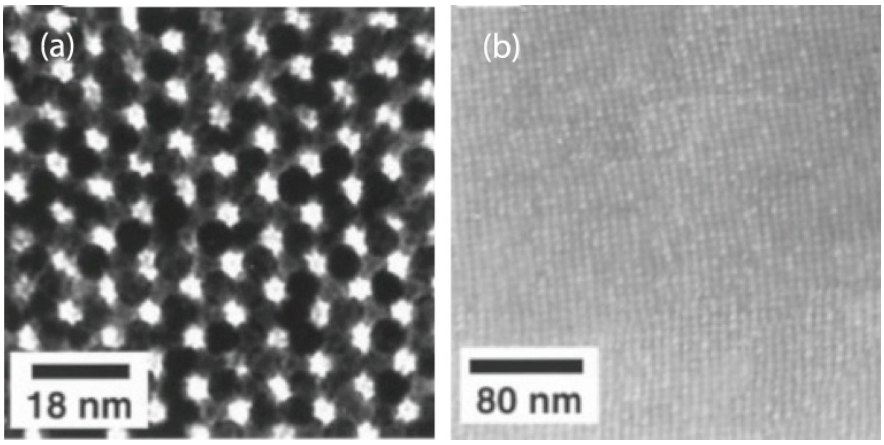

FIGURE 2.10: TEM images of FePT NCs in a two-dimensional superlattice (a) as-deposited from a hexane/octane dispersion and (b) after post-deposition annealing at 560°C. Adapted from [11].

2.3.2 Ensembles of randomly distributed nanocrystals

As we described above, magnetic anisotropy can appear in NC ensembles if the NCs are organized in a superstructure with their magnetization easy-axis mutually parallel. However, ensembles of randomly oriented NCs may also show magnetic anisotropy if the NCs are randomly stacked in a volume with anisotropic shape. Magnetic anisotropy has been observed in thin films of magnetic NCs embedded in an insulating matrix [210–212]. In these NC ensembles, the magnetic anisotropy coincided with the geometry of the film. The easy- and hard-axes of magnetization correspond to the directions of the external magnetic field which were perpendicular and parallel to the film plane, respectively. Magnetic anisotropy has also been observed in chains of magnetic NCs [12, 59, 213, 214]. Noginova *et al.* produced arrays of Fe_3O_4 NCs chains consisting of NCs stacked into nanocolumns which were imprinted in a porous alumina membrane [12]; see Fig. 2.11. Even though the NCs are randomly oriented inside each nanocolumn, these NC ensembles show magnetic anisotropy with magnetization easy-axis coincident with the orientation of the nanocolumns long-axis. Furthermore, Varón *et*

al. observed magnetic anisotropy in linear arrays of NCs [214].

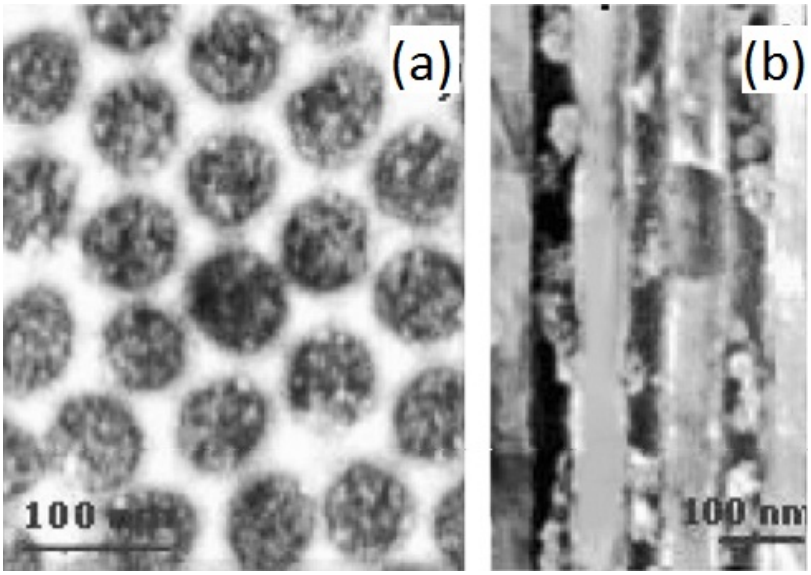

FIGURE 2.11: TEM micrographs of Fe_3O_4 NCs randomly stacked in nanocolumns imprinted in a porous alumina membrane as observed from (a) the top and (b) the side. Adapted from [12].

The magnetic anisotropy of ensembles of NCs randomly stacked in an anisotropic shape has been described within the framework of uniformly finite magnetic bodies with an effective demagnetization tensor having the same symmetry as the NC sample shape [210,212,213,215, 216], in a way similar to that applied for bulk magnetic materials [217]. In early calculations, Dubowik used a mean-field approach to calculate the magnetic anisotropy of heterogeneous magnets consisting of three dimensional arrays of magnetic particles [215]. In this study, he showed that the magnetic anisotropy of these heterogeneous magnets can be well described by a shape-dependent demagnetization field and derived the demagnetization tensor describing the magnetic anisotropy of various arrays of magnetic particles, namely magnetic multilayers, granular films, films comprising arrays of cylindrical particles. Kakazei *et al.* considered an effective demagnetization field to describe the magnetic anisotropy of thin films of Co_xAg_{1-x} NCs probed by ferromagnetic resonance (FMR) [216]. In this technique, the film magnetic anisotropy is obtained form the angular dependence of the resonant magnetic field measured for various orientations of the film with respect to the applied magnetic field. They found that the magnetic anisotropy of their films is well described by the demagnetization fields derived by Dubowik [215] and is affected by the volume fraction of NCs in the film: for low NC volume fractions, the films magnetic anisotropy is well described by the demagnetization field of a films of spherical magnetic particles, while for NC volume fraction factors above a percolation threshold of 0.3, the NCs agglomerate into columnar structures and their magnetic

anisotropy is described by the demagnetization field of a film comprising cylindrical magnetic particles. They further observed that the films magnetic anisotropy increases with the films NC volume fraction. Similar observations were reported by Butera *et al.*, who used FMR measurements to probe the magnetic anisotropy of thin films of Fe NCs sputtered in SiO_2 substrates [212]. They showed that the observed magnetic anisotropy is well described by an effective demagnetization tensor that takes into consideration the shape and the discontinuous nature of their NC films. They also observed that the magnetic anisotropy of their films increases linearly with the volume fraction of Fe incorporated in the SiO_2 substrates.

Some studies considered magnetic dipole-dipole interactions explicitly to link the symmetry of the demagnetization tensor to the shape of the NC ensemble [210, 211, 218]. Tomita *et al.* investigated the role of magnetic dipole-dipole interactions on the magnetic anisotropy of thin films of magnetic Ni NCs embedded in insulating polyimide matrices [210]. From FMR measurements, they observed a signal whose resonant magnetic field shifts when the NC film is rotated from the plane parallel to the external magnetic field to the plane perpendicular to the external magnetic field and that this shift increases from almost 0 G to about 500 G by decreasing the inter-NC spacing (and consequently increasing the NC volume fraction). By comparison between these experimental data and computational simulations of random arrays of Ni NCs interacting via magnetic dipole-dipole interactions, they showed that the magnitude of the shift in the FMR signal of their Ni NCs films is directly associated to the magnetic dipole-dipole interactions between the NCs in the films. Schmool *et al.* performed angular-dependent FMR measurements of discontinuous multilayers of CoFe NCs with layer thicknesses between 7 and 13 Å [211]. Their experimental data provided evidence for a change of coupling regime between NCs in their films from superferromagnetic in thicker NCs films to superparamagnetic in thinner NCs films. They showed that the observed change in NC coupling regime results from magnetic dipole-dipole interactions between the NCs in the films.

Magnetic dipole-dipole interactions have also been proposed to be the origin of other new magnetic phenomena discovered in NC systems [219, 220]. Chen *et al.* observed that the temperature dependence of magnetization of self-assembled binary superlattices consisting of Fe_3O_4 NCs of two different sizes show a single-phase-like behavior that is different from the behavior of phase-separated mixtures of the two types of NCs [219]. Comparing their experimental data with Monte Carlo calculations, they showed that the observed single-phase-like magnetization resulted from the magnetic dipole-dipole interactions between the two types of NCs comprising their superlattices. Puntes *et al.* studied two-dimensional self-assemblies of superparamagnetic Co NCs [220, 221]. In an early study of this group, they observed that magnetic dipole-dipole interactions promote the self-assembly of ferromagnetic Co NCs into closed-loops to minimize the magnetostatic energy [220]. In a more recent study, Puntes *et al.* used magnetic force microscopy to probe the magnetic microstructure of two-dimensional self-assemblies of superparamagnetic Co NCs [221]. They observed the formation of correlated areas of parallel magnetization when the NC volume fraction is higher than 0.7

and associated this behavior to inter-NC magnetic dipole-dipole interactions.

2.4 Conclusions and Outlook

This chapter addressed three major topics. In the first part, we reviewed the advances reported in the literature on the electronic doping of semiconductor NCs and on the study of their electronic properties. The success of semiconductor NCs as technological materials will ultimately depend on our ability to precisely control their behavior through doping. This has prompted several research efforts towards the electronic doping of semiconductor NCs, and progress has already been reported on the electronic doping of NCs of a wealth of materials, namely NCs of oxide materials such as ZnO and TiO_2, compound materials such as PbSe and CdSe, and group IV semiconductors such as Si. With regard to Si NCs, they are of particular interest due to the abundance and non-toxicity of Si, and because bulk Si is the standard material in state-of-the-art electronics [68].

In spite of the advances reported on producing doped semiconductor NCs and understanding their electronic properties, many questions regarding this topic remain unanswered. An issue regarding the electronic doping of semiconductor NCs concerns the role of interdopant interactions on the electronic properties of doped semiconductor NCs. Studies reported a strong reduction of the number of electronically active electrons detected by EPR for NCs smaller than 12 nm and suggested that this observation could result from an inherent difficulty of doping small NCs [6]. However, the observed low efficiency in doping small NCs could also result from the inability of EPR to detect all donor electrons in very small NCs. In a NC, a dopant is confined to a much smaller volume than in the bulk. This alters the wave function of the donor electron from one case to the other: while in the bulk the donor electron wave function extends to a large distance from the donor nucleus, in NCs the donor electron wave function vanishes at the frontiers of the NC. So, in bulk semiconductors the interaction between dopants extends to all the neighboring dopants in the crystal, while in a NC dopants are isolated from neighboring dopants outside the NC. As a consequence, in NCs only interactions between dopants inside the same NC are important and we can have the situation where only two dopants (dimers) interact very strongly, which is not possible in the bulk for the same dopant concentration. In contrast to the situation of single dopants in a NC, the situation of multiple dopants in NCs has remained largely unstudied. The electronic structure of multiple donor electrons in NCs is determined by the exchange coupling between donors, which depends enormously on the relative location of dopants [222, 223]. Thus, for a given number of donor electrons inside a NC, it is necessary to consider all possible dopant configurations to take into account the statistical distribution of dopants. This is a difficult

task for atomistic calculation methods, which are quite useful in the case of single donor electron configurations in NCs [8, 165], and has so far remained unsolved.

The second part of this chapter consisted on a brief overview of the literature concerning the identification of charge trapping defects in semiconductor NCs and the investigation of their impact on the electronic properties of semiconductor NCs. Electrically active defects in semiconductor NCs provide energy states localized within the NCs band gap that capture charge carriers from delocalized electronic states of the NCs, thus leading to reduced mobility and diffusion length of charge carriers across NC systems [54, 187]. For this reason, the presence of defects in semiconductor NCs is a main factor limiting the performance of NC-based devices [27, 49–55, 183–188]. Thus, it is crucial to develop new strategies for the identification and elimination of trap states from NC-based devices in order to improve their performance.

The third part of this chapter concerned studies on the magnetic anisotropy of systems of NCs ensembles. Magnetic anisotropy critically determines the utility of magnetic NCs in new nanomagnetism technologies such as high-density recording media [11] and magnetic resonance imaging [61]. These applications rely on magnetic anisotropy to preserve the orientation of magnetisation against e.g. thermal fluctuations. Magnetic anisotropy has been reported to appear in ensembles of magnetic NCs that are ordered in a superstructure with their magnetization easy-axis mutually parallel. In this case, the magnetic anisotropy of the NC ensemble coincides with the magnetic anisotropy of each individual NC [11]. Magnetic anisotropy can also occur in ensembles of NCs that are randomly stacked in a volume with an anisotropic shape, in which case the magnetic anisotropy of the NC ensemble coincides with the shape of the ensemble. Some studies have linked the observation of magnetic anisotropy in ensembles of NCs randomly stacked in an anisotropic shape to interactions between NCs, namely magnetic dipole-dipole interactions [210–212]. In contrast to the two above mentioned types of NCs ensembles, in ensembles of NCs randomly stacked in an isotropic shape, magnetic anisotropy is not expected to occur. In this PhD thesis, we will aim at clarifying the reason for the observation of this magnetic anisotropy.

In this thesis, we aim at clarifying some of the aforementioned questions by using magnetic resonance techniques, namely EPR and FMR, to study spin states in semiconductor NCs. Accordingly, we use EPR spectroscopy to study the doping efficiency, the confinement, and the interdopant interaction of electrons provided by P donors incorporated in Si NCs. We also use EPR spectroscopy to study charge trapping defects in CdSe NCs. Further, we use FMR spectroscopy to study spin states associated to unpassivated sites of the surface of CdSe NCs, and how the interaction between such states may give rise to magnetic anisotropy in ensembles of randomly stacked CdSe NCs.

Chapter 3

Experimental techniques

In this chapter, we briefly introduce the experimental techniques used in the research presented in this thesis. Most of the experimental data was obtained using magnetic resonance techniques, namely electron paramagnetic resonance (EPR) and ferromagnetic resonance (FMR). In Sec. 3.1, we address the theoretical principles of EPR, its detection, and the basic components of a EPR spectrometer. In Sec. 3.2, we present the theoretical principles specific to ferromagnetic resonance.

Data from complementary experimental techniques were also used in this thesis. Fourier transform infrared spectroscopy (FTIR), which was used to investigate the surface termination of Si NCs, is briefly described in Sec. 3.3. Magnetization measurements to quantify the magnetization of ensembles of CdSe NCs were performed using a superconducting quantum interference device, whose physical principle and setup is briefly presented in Sec. 3.4. X-ray diffraction (XRD) spectroscopy and optical spectroscopy in the UV-Vis range were used to characterize the crystalline structure and optical properties of CdSe NCs. These two techniques are briefly described in Secs. 3.5 and 3.6, respectively. Transmission electron microscopy (TEM), which is presented in Sec. 3.7, was used to assess the shape and size distribution of CdSe NCs and Si NCs.

3.1 Electron paramagnetic resonance

Electron paramagnetic resonance (EPR) is used to experimentally investigate materials with unpaired electrons. For instance, most of the present knowledge about dopants in semiconductor nanocrystals has been obtained from experimental studies based on EPR. In the present thesis, this technique has been applied to study ensembles of P-doped Si NCs in terms of doping efficiency and inter-dopant interactions, and ensembles of CdSe NCs in terms of charge trapping defects and confinement. Therefore, we present in more detail the theoretical background of this experimental technique, which will help us to relate the results obtained from our theoretical approaches with data obtained from experiments.

3.1.1 Physical principles of electron paramagnetic resonance

The basic physics of EPR can be discussed by describing the case of a single electron, which consists of a system with spin $S = 1/2$. In an EPR experiment, this electron is placed in a homogeneous magnetic field B_0, which we define to be aligned along the z-axis. The interaction between this magnetic field and the electron spin can be described by the Hamiltonian

$$\hat{\mathcal{H}}_{\text{Zeeman}}|\psi\rangle = g\beta_e B_0 \hat{S}_z|\psi\rangle \tag{3.1}$$

where g is the Landé factor (or g-factor) and $\beta_e = e\hbar/2m_e$ is the Bohr magneton; here, e and m_e are the electron charge and mass, respectively, and $\hbar$ is the Planck constant divided by 2π . For the situation addressed here of a free electron in vaccuum, the Landé factor is equal to 2.0023 and is conventionally named free electron g-factor g_e. The operator $\hat{S}_z$ is the component of the spin operator $\hat{\mathbf{S}}$ along the z-axis, and $|\psi\rangle$ is an eigenstate of the Hamiltonian $\hat{\mathcal{H}}_{\text{Zeeman}}$. This interaction is called Zeeman interaction and the corresponding eigenstates and eigenenergies for a system with spin $S = 1/2$ are

$$\begin{aligned} |\psi_1\rangle &= |1/2, +1/2\rangle, \quad E_1 = g\beta_e B_0/2 \\ |\psi_2\rangle &= |1/2, -1/2\rangle, \quad E_2 = -g\beta_e B_0/2 \end{aligned} \tag{3.2}$$

These eigenstates are represented in the basis of the common eigenstates of $\hat{\mathbf{S}}$ and S_z. The eigenstates $|S, m_S\rangle$ are characterized by the spin angular momentum quantum number S and their components along the z-axis m_S.

Fig. 3.1 shows the energy scheme of a spin $S = 1/2$ system. There, we see that transitions between the two eigenstates can be triggered by photons when the photon energy $\hbar\omega_{\text{mw}}$ matches the energy level separation ΔE:

$$\hbar\omega_{\text{mw}} = \Delta E = g\beta_e B_0 \tag{3.3}$$

These transitions require a change in the orientation of the electron magnetic moment, i.e. $\Delta m_S = \pm 1$. This reorientation of m_S can only occur if it is caused the electromagnetic resonance. Thus, to make these transitions possible, the microwave field must be polarized such that it has a component perpendicular to B_0. Here, we consider that the microwave field is polarized along the x-axis and is given by $\mathbf{B}_x = B_1 \sin(\omega_{\text{mw}} t)\hat{\mathbf{e}}_x$. The interaction between $\mathbf{B}_x$ and the electron can be described by the following Hamiltonian, $\hat{H}_{\text{ext}}$:

$$\hat{\mathcal{H}}_{\text{ext}} = -\mathbf{B}_x \cdot \hat{\boldsymbol{\mu}} \tag{3.4}$$

where $\hat{\boldsymbol{\mu}}$ is the magnetic dipole moment operator, i.e. $\hat{\boldsymbol{\mu}} = -g\beta_e \hat{\mathbf{S}}$. The total Hamiltonian describing the system is given by $\hat{\mathcal{H}} = \hat{\mathcal{H}}_{\text{Zeeman}} + \hat{\mathcal{H}}_{\text{ext}}$, where $\hat{\mathcal{H}}_{\text{Zeeman}}$ is given by Eq. (3.1)

and $\hat{\mathcal{H}}_{\text{ext}}$ describes the perturbation of the external oscillating microwave field. The first order transition probability can be calculated by applying Fermi's golden rule to the time-dependent Schrödinger equation

$$i\hbar\frac{\partial}{\partial t}|\psi\rangle = \left[\hat{\mathcal{H}}_{\text{Zeeman}}(\mathbf{B}_0) + \hat{\mathcal{H}}_{\text{ext}}\right]|\psi\rangle \tag{3.5}$$

The first order transition rate between states $|\psi_i\rangle$ and $|\psi_j\rangle$ is given by

$$W_{i,j} = \gamma(\omega_{\text{mw}})|\langle\psi_i|\hat{\mathcal{H}}_{\text{ext}}|\psi_i'\rangle|^2 \tag{3.6}$$

where $\gamma(\omega_{\text{mw}})$ is the line shape function. For the system considered above of an isolated $S = 1/2$ system, $\hat{\mathcal{H}}_{\text{ext}} = g\beta_e B_1 \hat{S}_x$.

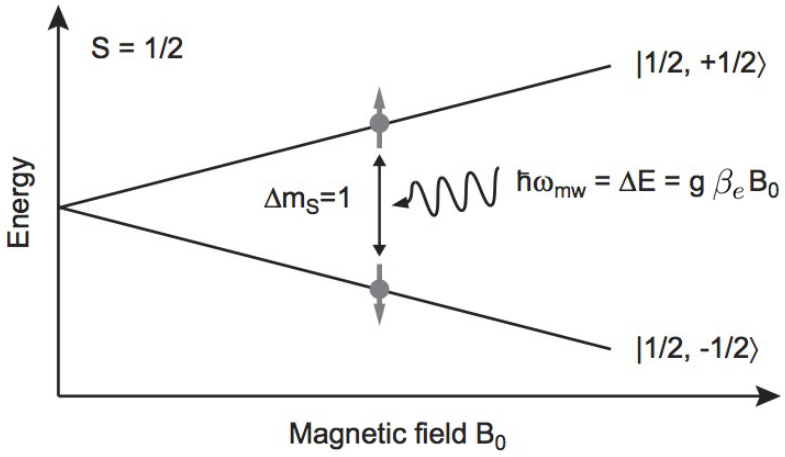

FIGURE 3.1: Energy-level scheme of a spin system with $S = 1/2$ as a function of the external magnetic field B_0. When a microwave field with a frequency ω_{MW} is applied, transitions between the two eigenstates can be induced at a magnetic field where the energy difference ΔE between the two states corresponds to $\hbar\omega_{\text{MW}}$. From [9].

When the spin Hamiltonian includes additional terms besides the Zeeman interaction, the considerations presented above still hold. However, additional selection rules may need to be taken into account. For example, let us consider a system comprising an electron and a nucleus with nuclear spin $I = 1/2$. The Hamiltonian describing this system is

$$\hat{\mathcal{H}}_{\text{nuc}} = g\beta_e B_0 \hat{S}_z + A\hat{\mathbf{S}} \cdot \hat{\mathbf{I}} \tag{3.7}$$

where A is the hyperfine splitting constant. The first term of $\hat{\mathcal{H}}_{\text{nuc}}$ corresponds to the Zeeman interaction with the external magnetic field $\mathbf{B_0}$ and the second term corresponds to the hyperfine interaction between the electron and nucleus spins.

The eigenfunctions of $\hat{H}_{\text{nuc}}$ are expressed in terms of an electron and nucleus spin basis

set $|m_S, m_I\rangle$, corresponding to the electron and nucleus spin quantum numbers m_S and m_I, respectively

$$|+\frac{1}{2},+\frac{1}{2}\rangle \quad |+\frac{1}{2},-\frac{1}{2}\rangle \quad |-\frac{1}{2},+\frac{1}{2}\rangle \quad |-\frac{1}{2},-\frac{1}{2}\rangle \tag{3.8}$$

Using this basis set, the energy matrix of $\langle m_S, m_I|\hat{\mathcal{H}}_{\text{nuc}}|m'_s, m'_I\rangle$ is given by

$$\hat{\mathcal{H}} = \begin{bmatrix} \frac{1}{2}g\beta_e B + \frac{1}{4}A & 0 & 0 & 0 \\ 0 & \frac{1}{2}g\beta_e B - \frac{1}{4}A & \frac{1}{2}A & 0 \\ 0 & \frac{1}{2}A & -\frac{1}{2}g\beta_e B - \frac{1}{4}A & 0 \\ 0 & 0 & 0 & -\frac{1}{2}g\beta_e B + \frac{1}{4}A \end{bmatrix} \tag{3.9}$$

The matrix (3.9) is not diagonal in the basis of functions (3.8). However, we notice that $|+\frac{1}{2},+\frac{1}{2}\rangle$ and $|-\frac{1}{2},-\frac{1}{2}\rangle$ are eigenfunctions of Hamiltonian (3.7). We find the remaining eigenfunctions by diagonalizing the non diagonal sub-matrix,

$$|\alpha\rangle = \cos\omega \cdot |\frac{1}{2},-\frac{1}{2}\rangle + \sin\omega \cdot |-\frac{1}{2},\frac{1}{2}\rangle \tag{3.10}$$

$$|\beta\rangle = -\sin\omega \cdot |\frac{1}{2},-\frac{1}{2}\rangle + \cos\omega \cdot |-\frac{1}{2},\frac{1}{2}\rangle \tag{3.11}$$

with $\omega = \frac{1}{2}\arctan\left(\frac{A}{g\beta_e B}\right)^2$ and eigenvalues

$$U_{|\frac{1}{2},-\frac{1}{2}\rangle} = \frac{1}{2}\sqrt{A^2 + (g\beta_e B)^2} - \frac{1}{4}A \tag{3.12}$$

$$U_{|-\frac{1}{2},\frac{1}{2}\rangle} = -\frac{1}{2}\sqrt{A^2 + (g\beta_e B)^2} - \frac{1}{4}A \tag{3.13}$$

From (3.10) and (3.11) we can see that for high external magnetic fields $\omega \to 0$ and hence we simply obtain $|\alpha\rangle = |+\frac{1}{2},-\frac{1}{2}\rangle$ and $|\beta\rangle = |-\frac{1}{2},+\frac{1}{2}\rangle$, resulting in the four energy states

$$U_{|m_S,m_I\rangle} = m_S g\beta_e B + m_S m_I A \tag{3.14}$$

As in the case of a system with spin $S = 1/2$ presented above, the total Hamiltonian describing the system comprising an electron and a nucleus with nuclear spin $I = 1/2$ is given by $\hat{\mathcal{H}} = \hat{\mathcal{H}}_{\text{nuc}} + \hat{\mathcal{H}}_{\text{ext}}$. We have now to apply $\hat{\mathcal{H}}_{\text{ext}}$ to the eigenfunctions previously found for $S = \frac{1}{2}$ and $I = \frac{1}{2}$. As m_S and m_I are independent quantum numbers, we can consider $|m_S, m_I\rangle = |m_S\rangle|m_I\rangle$. For sufficiently high B we have $g\beta_e B >> |A|$, so the general matrix

elements are

$$\langle m_S, m_I|\hat{\mathcal{H}}_{\text{ext}}|m'_S, m'_I\rangle = g\beta_e B\langle m_S|\hat{S}_x|m'_S\rangle\langle m_I|m'_I\rangle \tag{3.15}$$

For EPR transitions these elements are zero unless $m'_S = m_S \pm 1$ and $m'_I = m_I$. Thus, under high-fide conditions the selection rules for transitions detected in EPR are

$$\Delta m_S = \pm 1 \qquad \Delta m_I = 0 \tag{3.16}$$

Figure 3.2 shows the splitting of energies described and the allowed transitions between different spin states. We note that the Hamiltonian $\hat{\mathcal{H}}_{\text{nuc}}$ described by Eq. (3.7) should also include the nuclear Zeeman interaction term $-g_n\beta_n B_0\hat{I}_z$, where g_n is the nuclear g-factor $\beta_n =$ is the nuclear magneton, and $\hat{I}_z$ is the component of the nuclear spin operator $\hat{\mathbf{I}}$ along the z-axis. However, in most cases the energy contribution of the nuclear Zeeman interaction is negligible on the EPR energy scale. Further, since observed transitions are between levels with the same values of m_I, the nuclear Zeeman energies cancel in computing the EPR transition energies. The selection rules for allowed transitions in EPR given in (3.16) imply the two

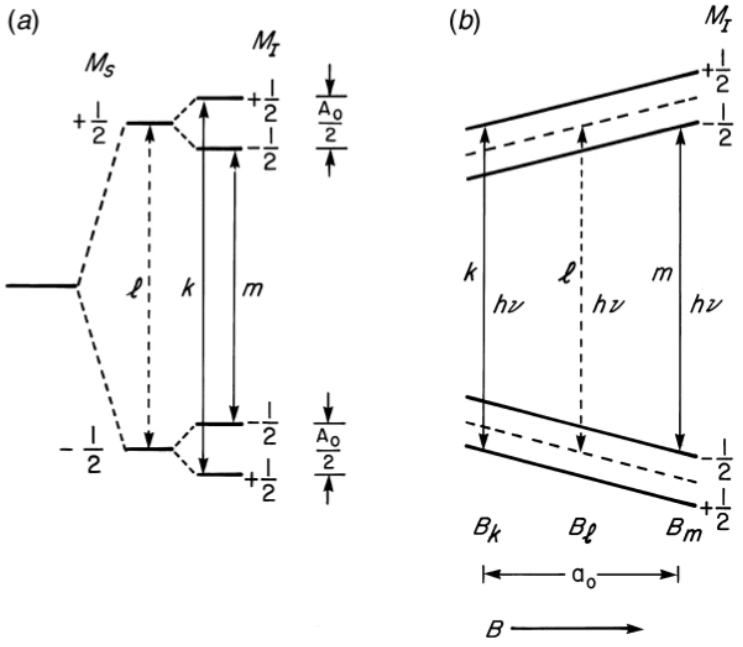

FIGURE 3.2: (a) Splitting of the energy levels corresponding two states of electron spin, $m_S = \pm\frac{1}{2}$. The l line corresponding to transitions allowed in the absence of hyperfine interaction. Both lines k and m correspond to allowed EPR transitions arising from hyperfine interaction $h\nu = g\beta_e \pm \frac{1}{2}A$. (b) Splitting of the energy levels as a function of the applied magnetic field. k and m lines correspond to the transitions induced by $h\nu$ at the resonant fields B_k and B_m. The dashed lines correspond to the energy levels and l transitions in the absence of hyperfine interaction. Adapted from [13].

energy differences

$$\Delta U_1 = U_{\frac{1}{2},\frac{1}{2}} - U_{-\frac{1}{2},\frac{1}{2}} = g\beta_e B + \frac{1}{2}A \tag{3.17}$$

$$\Delta U_2 = U_{\frac{1}{2},-\frac{1}{2}} - U_{-\frac{1}{2},-\frac{1}{2}} = g\beta_e B - \frac{1}{2}A \tag{3.18}$$

In an EPR experiment a constant microwave frequency ω is used while the external magnetic field is swept slowly and the resonant magnetic fields for the transitions (3.17) and (3.18) (represented in Figure 3.2 by k and m, respectively) are

$$B_k = \frac{\hbar\omega}{g\beta_e} - \frac{A}{2g\beta_e} \tag{3.19}$$

$$B_m = \frac{\hbar\omega}{g\beta_e} + \frac{A}{2g\beta_e} \tag{3.20}$$

The hyperfine splitting constant in magnetic-field units, corresponds to the gap between these two EPR signals. For example, the experimental value obtained for a isolated phosphorus donor in bulk Si is $A_{\text{bulk}} = 4.2\,\text{mT}$ [140]. Given the possibility of evaluating A through EPR experiments, investigations have been carried out to study A for P in Si NCs, in particular its dependence with Si NC size [7, 46].

The line shape function for a $S = 1/2$ system can be deduced using a phenomenological classical approach. In a system comprising $S = 1/2$ spins scattered in a volume V, each spin i in the state ψ_i has an individual magnetic moment defined by the expectation values of the corresponding spin operator. The total magnetization $\mathbf{M}$ is given by the volume-normalized sum of the individual magnetic moments

$$\mathbf{M} = \frac{1}{V}\sum_i \mu_i \tag{3.21}$$

where μ_i is the magnetic dipole moment of each spin. The dynamics of this spin system is described by the classical equations of motion of the magnetization vector in a magnetic field $\mathbf{B} = B_0\hat{\mathbf{e}}_z + B_1 \sin(\omega_{\text{MW}}t)\hat{\mathbf{e}}_x$ and so the Bloch equations for a $S = 1/2$ system are given by [13].

$$\begin{aligned}
\frac{dM_x}{dt} &= \frac{g\beta_e}{\hbar}(\mathbf{M}\times\mathbf{B})_x - \frac{M_x}{T_2}\ , \\
\frac{dM_y}{dt} &= \frac{g\beta_e}{\hbar}(\mathbf{M}\times\mathbf{B})_y - \frac{M_y}{T_2}\ , \text{ and} \\
\frac{dM_z}{dt} &= \frac{g\beta_e}{\hbar}(\mathbf{M}\times\mathbf{B})_z + \frac{M_0 - M_z}{T_1}\ .
\end{aligned} \tag{3.22}$$

The terms involving T_1 and T_2 describe an exponential relaxation of the magnetization vector towards its equilibrium value $\mathbf{M}_0$ after it has been driven out of equilibrium by the action of the microwave field $\mathbf{B}_x$. The characteristic relaxation time T_1 is called the spin-lattice relaxation time because when M_z relaxes towards equilibrium, the energy of the spin system is transferred into the host lattice. The components of magnetization along x and y relax with the characteristic time constant T_2 conserving the total energy of the spin system. Thus, T_2 is called spin-spin relaxation time. The equilibrium magnetization $\mathbf{M}_0$ of an ensemble of N spins in thermal equilibrium and in the absence of the oscillating field is given by [13]

$$\mathbf{M}_0 = \frac{1}{2}\frac{N}{V}\tanh\left(\frac{g\beta_e B_0}{2k_B T}\right)\mathbf{e}_z \tag{3.23}$$

The solution of Eqs. (3.22) is a damped precession of the magnetization vector about the magnetic field vector $\mathbf{B}_0$. In a rotating coordinate frame which rotated about the z-axis at the microwave frequency, this solution under steady state conditions is given by [13, 224]

$$\begin{aligned} M_{x\phi} &= -M_0\frac{\omega_0(\omega_0-\omega)T_2^2}{1+(\omega_0-\omega)^2T_2^2+(g\beta_e/\hbar)^2B_1^2T_1T_2}\ , \\ M_{y\phi} &= M_0\frac{\omega T_2}{1+(\omega_0-\omega)^2T_2^2+(g\beta_e/\hbar)^2B_1^2T_1T_2}\ , \text{ and} \\ M_z &= M_0\frac{1+(\omega_0-\omega)^2T_2^2}{1+(\omega_0-\omega)^2T_2^2+(g\beta_e/\hbar)^2B_1^2T_1T_2}\ . \end{aligned} \tag{3.24}$$

where $\omega_0 = \beta_e B_0$, and $M'_{x\phi}$ and $M''_{y\phi}$ are the dynamic transversal magnetizations which are rotating, respectively, in phase and with a phase shift of 90° with respect to $\mathbf{B}_x$, and ϕ is the azimuthal angle of rotation. The relation between the magnetization $\mathbf{M}$ and $\mathbf{B}$ is given by

$$\mathbf{M} = \chi\frac{\mathbf{M}}{\mu_\mathrm{m}} \tag{3.25}$$

where χ is the magnetic susceptibility and $\mu_\mathrm{m} = \kappa\mu_0$ is the permeability of the medium; here μ_0 is the permeability of vacuum and κ is a dimensionless parameter describing the permeability of the medium considered with respect to vacuum. The effects of the oscillating microwave field $\mathbf{B_x}$ are described in terms of dynamic magnetic susceptibilities χ' and χ'' which are given by

$$\chi' = \mu_\mathrm{m}\mu_0 M'_{x\phi}/B_1 = \chi_0\frac{\omega_0(\omega_0-\omega)T_2^2}{1+(\omega_0-\omega)^2T_2^2+(g\beta_e/\hbar)^2B_1^2T_1T_2} \tag{3.26}$$

$$\chi'' = -\mu_\mathrm{m}\mu_0 M''_{y\phi}/B_1 = \chi_0\frac{\omega T_2}{1+(\omega_0-\omega)^2T_2^2+(g\beta_e/\hbar)^2B_1^2T_1T_2} \tag{3.27}$$

where $\chi_0 = \mu_m N_V g^2 \beta_e^2 / 4 K_B T$ is the static magnetic susceptibility. Here T is the temperature of the system and N_V is the system spin volume density. Conventional EPR measures χ' and χ'', which represent the dispersion and power absorption of complex susceptibility $\chi' - i\chi''$, respectively. The microwave power absorbed by the spin system is [13]

$$P(\omega) = \frac{\omega \chi'' B_1^2}{\mu_0 V} \tag{3.28}$$

Under slow adiabatic passage conditions, which are achieved experimentally when the resonance line is passed through a long time compared to T_1 and T_2, the steady state solutions of the Bloch equations given by Eqs. (3.24) are valid. Thus, if B_1 is small so that the microwave field remains a perturbation (non-saturation conditions), the line shape function $\gamma(\omega_0 - \omega)$ can be obtained by substituting Eq. (3.27) in Eq. (3.28):

$$\gamma(\omega_0 - \omega) \propto \frac{\pi \eta_{\text{res}} Q \chi^0 \omega_0 P(\omega)^{1/2}}{(1 + (g\beta_e/\hbar)^2 B_1^2 T_1 T_2)^{1/2}} Y(\omega_0 - \omega), \tag{3.29}$$

where η_{res} is the filling factor and Q is the quality factor of the resonator. The filling factor quantifies the efficiency with which the microwave magnetic field is concentrated in the sample and is proportional to the ratio between the sample volume and the cavity volume [224]. The quality factor is a parameter related to the energy losses in resonator. Some details regarding Q will be given Sec. 3.1.2. $Y(\omega_0 - \omega)$ is a normalized Lorentzian function, which is given by

$$\begin{aligned} Y(\omega_0 - \omega) &= \frac{4 A_{\text{pp}} \Gamma^2}{3\sqrt{3}} \frac{\Gamma}{\Gamma^2 + (\omega - \omega_0)^2} \\ \Gamma &= \frac{(1 + (g\beta_e/\hbar)^2 B_1^2 T_1 T_2)^{1/2}}{T_2} \end{aligned} \tag{3.30}$$

where A_{pp} is the peak-to-peak amplitude. Thus, the Bloch formalism predicts that the EPR lines have a Lorentzian shape, which are homogeneously broadened according to Γ. The intensity of the EPR line I_{EPR} is defined as the area under the corresponding absorption curve. As will become clear in Sec. 3.1.2, in EPR is usually used a modulation-phase-sensitive detection technique that produces first-derivative lines that provide better resolved spectra. For first-derivative Lorentzian shaped EPR lines, I_{EPR} is given by

$$I_{\text{EPR}} = \frac{\pi}{\sqrt{3}} A_{\text{pp}} \Delta B_{\text{pp}}^2 \tag{3.31}$$

where $\Delta B_{\text{pp}} = 2\Gamma/\sqrt{3}$ is the peak-to-peak line width. According to Eq. (3.30), the peak-to-

peak amplitude has the following dependence on $\mathbf{B}_x$:

$$A_{\mathrm{pp}} \propto \frac{\eta_{\mathrm{res}} Q \chi^0 \omega_0 B_1 T_2^2}{(1 + (g\beta_e/\hbar)^2 B_1^2 T_1 T_2)^{3/2}}. \tag{3.32}$$

Thus, under non-saturation conditions, the amplitude of the signal varies linearly with B_1, which according to Eq. (3.28) is proportional to $P(\omega)^{1/2}$. In situations where the microwave field can no longer be regarded as a perturbation and the spin relaxation is not fast enough to keep the spin populations in thermal equilibrium, the EPR signal saturates and decreases proportional to B_1^{-1} [15]. This lead to a loss of resolution and reduction of EPR signal amplitude. It is important to note that not all component of an EPR spectrum have the same microwave power dependence. This may be due to e.g. presence of paramagnetic centers of different origins, variations in the transition moment, or differences in the relaxation rates [14]. In such case, the EPR spectrum has to be recorded at different value of microwave power to optimize or separate various components. The line shape approaches a gaussian shape if it is a superposition of many components. These signals are called *inhomogeneously broadened*.

3.1.2 Experimental setup

A simplified scheme of an EPR spectrometer is shown in Fig. 3.3. In the following, we describe each of the components individually.

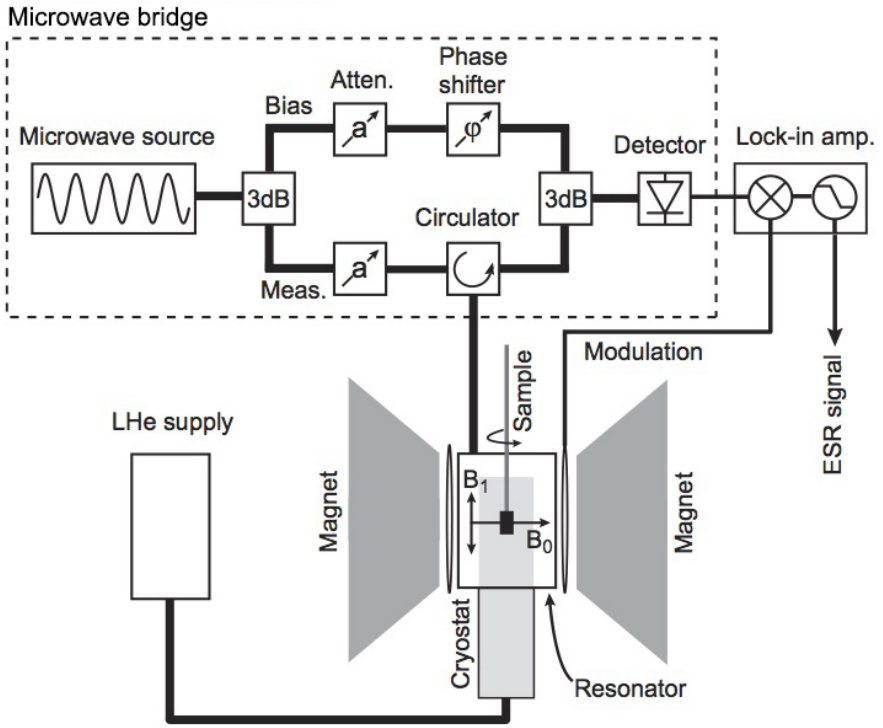

FIGURE 3.3: Schematic representation of a typical EPR spectrometer. From [9].

Resonator

For the generation and detection of EPR in our experiments, the samples are placed in a microwave resonator. This allows for the spatial separation of the magnetic and electrical field components, respectively B_1 and E_1, of the microwave radiation. Further, it allows for an enhancement of the magnetic field amplitude B_1 at the position of the sample. One of the most relevant characteristics of the microwave resonators is their Q factor, which is defined as

$$Q = \nu_{\mathrm{res}}/\Delta\nu \tag{3.33}$$

where ν_{res} is the resonance frequency of the resonator and $\Delta\nu$ is the width of the resonance curve, shown in Fig. 3.4. The Q factor affects the EPR signal intensity as

$$I_{\mathrm{EPR}} \propto \eta_{\mathrm{res}} \times Q \tag{3.34}$$

and is consequently a central parameter for the detection sensitivity of the instrument. The filling factor η_{res} is defined as

$$\eta_{\mathrm{res}} = \frac{\int_{\mathrm{sample}} B_1^2 dV}{\int_{\mathrm{resonator}} B_1^2 dV} \tag{3.35}$$

which is the fraction of the microwave energy stored in the sample with respect to the energy stored in the resonator [224]. From Eqs. (3.34) and (3.35) we can see that I_{EPR} increases with Q and with the sample volume. However, for a fixed resonator, the Q factor decreases with increasing sample volume. Thus, to obtain a maximum I_{EPR} for a given resonator type. the optimum sample volume has to be found. In resonators operating in the X-band frequency range, samples typically have a size corresponding to a tube with $3-5$ mm of inner tube diameter.

An important feature of microwave resonators is the spatial separation of the two field

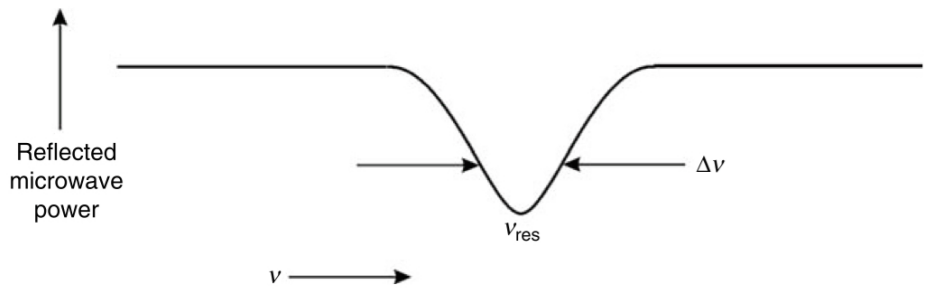

FIGURE 3.4: Reflected microwave power from a resonant cavity. Adapted from [14].

components of an electromagnetic wave. Only the magnetic component B_1 induces a magnetic resonance transition, whereas the E_1 component leads to nonresonant microwave absorption through the electric dipole moments of the sample. This microwave absorption results in a drop of the resonator Q factor and in sample heating. Therefore, EPR resonators are designed to maximize B_1 and minimize E_1 at the sample position. Figure 3.5 shows the spatial distribution of the two field components of an electromagnetic wave inside a rectangular microwave resonator. We used two different types of resonator for our experiments, namely a rectangular TE_{102} (Bruker ER 4102ST) resonator and a cylindrical TM_{110} (Bruker ER 4123SHQE) resonator. The Q factors of these resonators for a sample volume of about 30 mg are 3000 and 25000, respectively.

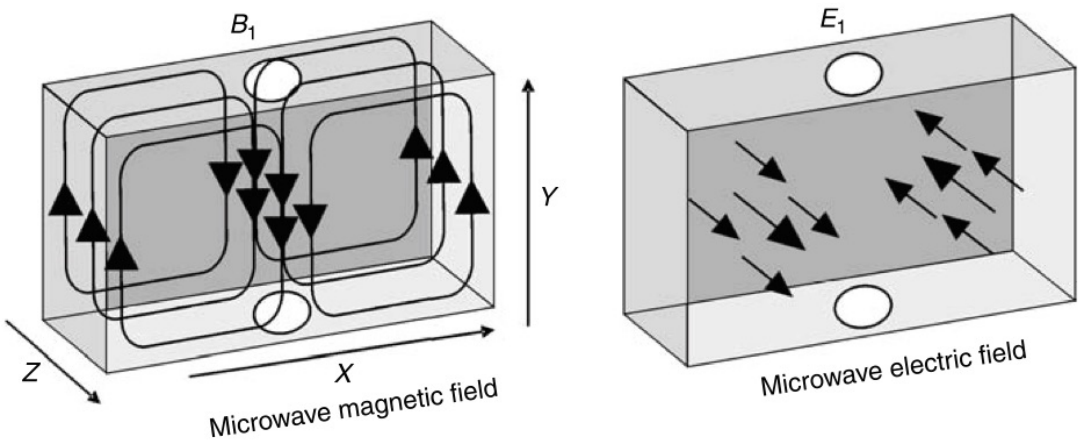

FIGURE 3.5: Spatial distributions of the magnetic ($B1$) and electric (E_1) field components of an electromagnetic wave inside a rectangular TE_{102} resonator. Directions Y and Z correspond to the sample tube axis and the static magnetic field B_0 directions, respectively. Adapted from [14].

Microwave bridge

We used commercial microwave bridges from Bruker operating at X-band (≈9.7 GHz) and Q-band (≈34 GHz) frequencies for the generation and detection of the microwave radiation $\mathbf{B_1}$. The microwave source is stabilized by a Gunn diode with a maximum output power of $P_{\mathrm{MW}}^{\mathrm{max}} = 200$ mW. As shown in Fig. 3.3, after the source the microwave radiation is coupled into two different arms with a 3 dB splitter. Thus, 50% of the microwave power is directed into a so-called reference arm and 50% are directed into the measurement arm.

The reference arm of the microwave bridge applies a bias to the detection diode. This bias can be tuned via an attenuator in the reference arm. Furthermore, the reference arm contains a variable phase shifter to adjust the relative phase between the microwaves coming from the measurement and the reference arms before they pass the 3 dB combiner. This allows to select between the detection of either the absorption or dispersive part of the high frequency dynamic

susceptibility, which are phase-shifted by 90°. In the measurement arm, the microwave power is set by a variable attenuator and guided into the resonator via a circulator. The microwave guide is critically coupled to the resonator, which can be achieved by tuning the resonator with an iris. The critical tuning of the microwave bridge and the resonator implies that there is no reflection of microwaves from the resonator and consequently all the microwave power is coupled into the resonator and dissipated there. When the EPR resonance condition given by Eq. (3.3) is fulfilled for a paramagnetic species in the sample, it will absorb microwave radiation causing a slight detuning of the resonator. In this situation, a small fraction of the microwave radiation entering the resonator is reflected back to the circulator and guided to a high frequency detection diode. However, before entering the detection diode, these microwaves are combined with those in the reference arm by a 3 dB combiner.

One further important component for the functioning of a microwave bridge is the so-called automatic frequency control (AFC). This component modulates the microwave oscillator frequency with a rate of about 80 Hz and an amplitude in the kHz range. For the resonator to absorb all the microwave power coming from the oscillator, the microwave frequency must match the center of the resonator absorption curve (see Fig. 3.4). Whenever the resonator changes its resonance frequency, an error signal is generated at the AFC frequency that is used to correct the oscillator frequency back to the actual resonator frequency.

Magnetic field

The static magnetic field $\mathbf{B_0}$ which induces the Zeeman splitting of the paramagnetic states in the sample is created by an electromagnet. In the EPR setups used in this thesis, the poles of the electromagnets provide a highly homogeneous magnetic field of up to ≈1.5 mT at the position of the sample. The magnetic field is controlled by a magnetic field controller connected to a Hall probe mounted close to the resonator. As shown in Fig. 3.3, $\mathbf{B_0}$ is oriented perpendicular to the microwave magnetic field $\mathbf{B_1}$ and perpendicular to the longitudinal axis of the Suprasil quartz tubes which we use as sample holders. These quartz tubes can be rotated with respect to the magnetic field $\mathbf{B_0}$ for anisotropy measurements. To account for possible offset of the measured magnetic field we regularly performed reference measurements with a 2,2-diphenyl-1-picrylhydrazil (DPPH) sample. This sample shows a single strong resonance at a known g-value of $g = 2.0036$, which can be used for the calibration of $\mathbf{B_0}$.

Lock-in detection

In an EPR experiment, the strength of the absorbed microwave power is very small, which makes the use of lock-in detection fundamental for noise suppression in most experiments [224]. In a lock-in detector, the magnetic field $\mathbf{B_0}$ is modulated at a certain reference frequency, set for the experiments in this thesis to 100 kHz. Experimentally, this is achieved by driving an oscillating current through a pair of coils that are attached to the resonator (see Fig. 3.3). The output signal of the lock-in amplifier is proportional to the Fourier component of the input signal with the frequency of the reference signal.

The principle of lock-in detection is shown in Fig. 3.6. A modulation frequency with amplitude B_{mod} is applied at a certain point in the absorption line. For small B_{mod} compared to the curvature of the absorption line, the response signal is an oscillation with ν_{m} of amplitude I_{lock}. The output amplitude I_{lock} corresponds to the slope of the absorption line at the resonance position. Thus, lock-in detection leads to the measurement of the first derivative $\partial\chi''/\partial B_0$ of the imaginary part of the dynamic high frequency susceptibility χ'' with respect to the magnetic field $\mathbf{B_0}$. If B_{m} is larger than the linewidth of the signal under investigation, the derivative signal will no longer reflect the true line shape and line width of the EPR absorption [224]. For the experiments performed in this work, B_{mod} was set in the range between 0.05 mT and 1 mT.

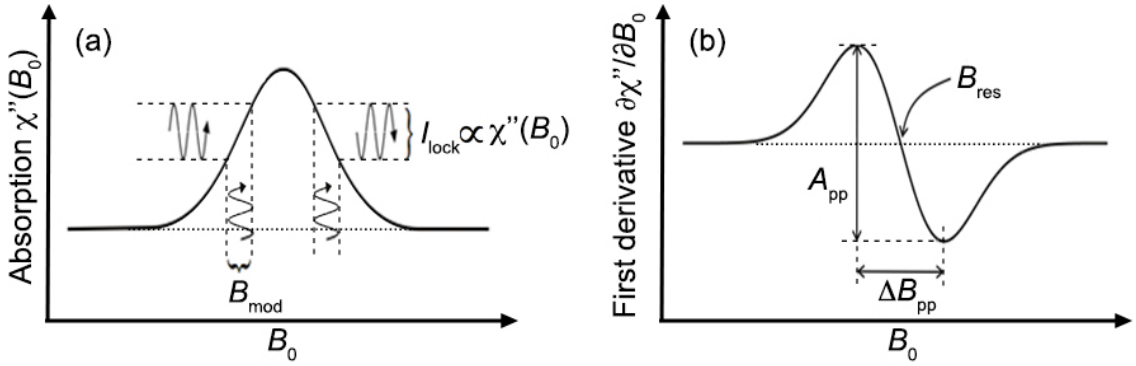

FIGURE 3.6: Schematic representation of (a) resonant microwave absorption and (b) corresponding EPR signal detected with a lock-in amplifier using a magnetic field modulation with amplitude B_{mod}. Also indicated in the figure are the resonant field B_{res}, the peak-to-peak linewidth ΔB_{pp} and the peak-to-peak amplitude A_{pp}. Adapted from [15].

Temperature control

Many of the EPR measurements performed in this work were performed at low temperatures. For example, low temperature measurements are necessary for the study of shallow impurities in Si NCs to keep the donor electrons in their quantum mechanical ground states (bound to their nuclei). To achieve low temperatures in our EPR measurements, we use helium gas flow cryostats that are incorporated in the resonator (see Fig. 3.3). For the X-band measurements performed in this thesis, we used an Oxford ESR 900 cryostat, and for the Q-band measurements, we used an Oxford CF935 continuous flow cryostat. Both cryostats enable the stabilization of the temperature at the sample position inside the resonator between $\approx$ 4 K and $\approx$ 200 K. The temperature is controlled and stabilized by a LakeShore 335 Temperature Controller, which controls the temperature of the system by using a heater coupled to a proportional-integral-derivative (PID) control element.

Photoexcited measurements

Photoexcited EPR measurements could be performed by coupling a light source to the EPR resonator. In this work, such measurements were performed using a rectangular TE_{102} resonator equipped with a transparent window that enables the illumination of the sample, and a white-light high-intensity halogen lamp light source (Thorlabs OSL1-EC) operating at a power of 150 W.

3.1.3 Determination of spin density

The number of specific paramagnetic centers in a sample can be obtained from the experimental EPR spectrum by double numerical integration of the corresponding EPR resonance lines. The spin density quantification can be obtained provided that he EPR spectra are measured in slow adiabatic passage and in absence of saturation. Under these conditions, the area under the EPR absorption peak (see Fig. 3.6) can be used as a direct measure for the number of spins N in the sample. This applies for the case of inhomogenously broadened resonance line, while in the case of bands consisting of overlapping resonance lines from different paramagnetic centers, the corresponding spin densities can only be calculated after the deconvolution of the spectrum via a numerical fitting procedure using a model that is adequate for the spin system investigated. For an absolute quantification of the spin density associated to a certain resonance line, the obtained signal intensity is compared with the value obtained for a reference sample, namely a P-doped Si reference sample with a know density of P donors. The EPR signal intensity is directly proportional to the measurement temperature T, to the modulation amplitude B_{m}, and inversely proportional to the square-root of the power P_{mw} of the microwave radiation **B1**. Thus, the intensities must be normalized by a factor $T/B_{\mathrm{m}}\sqrt{P_{\mathrm{mw}}}$, which compensates for the scaling of the EPR signal intensity with these three experimental parameters.

3.2 Ferromagnetic resonance

Ferromagnetic resonance (FMR) is a technique with which we studied the magnetic anisotropy in NC ensembles. In general, several physical parameters can be obtained with FMR, namely magnetic anisotropy, magnetic moment, Curie temperature, and relaxation mechanisms of the magnetization. The principle and experimental setup of ferromagnetic resonance is similar to that of EPR [224].

In an FMR experiment, the total magnetization of a sample precesses around the direction of the local static magnetic field $B_{\mathrm{eff}} = \mu_0 H_{\mathrm{eff}}$ at the Larmour frequency. However, in a FMR experiment the local magnetic field can be shifted by several Tesla from the value of the externally applied field due to coupling of ferromagnetic atoms by exchange interaction. The

motion of the magnetization vector around its equilibrium position along B_{eff} is described by the Landau-Lifshitz-Gilbert equation of motion [225]

$$\frac{dM}{dt} = -\frac{g\beta_e}{\hbar}\left(M \times B_{\text{eff}}\right) + \frac{\alpha}{M}\left(M \times \frac{dM}{dt}\right), \tag{3.36}$$

where $M = M(T, H)$ denotes the temperature and field dependent magnetization, α is a dimensionless damping parameter. The effective magnetic field B_{eff} is a sum of the external magnetic field, the microwave magnetic field at an angular frequency ω_{MW}, and the anisotropy field. However, the equation of motion of the magnetization vector is expressed in terms of the total free energy density F instead of B_{eff}. The relation between F and B_{eff} is given by

$$dF = \mathbf{B}_{\text{eff}} \cdot d\mathbf{M} \tag{3.37}$$

where the F can expressed as

$$F = F_{\text{Zeeman}} + F_{\text{demag}} + F_{\text{anis}} + F_{\text{exch}}. \tag{3.38}$$

Here, F_{Zeeman} is the Zeeman energy contribution due the external static magnetic field, F_{demag} is the demagnetizing energy of the sample, F_{anis} is the crystallographic magnetic anisotropy energy, which depends on the crystalline structure of the sample, and F_{exch} is the exchange energy. The minimum of the F determines the easy axis of magnetization. From the resonant magnetic field B_{res} and from the peak-to-peak linewidth ΔB_{pp} of a ferromagnetic resonance, it is possible to obtain information about physical parameters of the sample in analysis [226,227]. The magnitude of B_{res} and its dependence on the orientation of the external static magnetic field provides information about the magnetic anisotropy of the sample [228]. The magnitude of ΔB_{pp} yields information about the relaxation rate of the magnetization [228]. In the current work, we use FMR spectroscopy to investigate the observation of magnetic anisotropy in ensembles of intrinsic CdSe NCs capped with organic ligands. We quantify the magnitude of magnetic anisotropy in the ensembles of CdSe NCs by analyzing the dependence of B_{res} on the orientation of the external static magnetic field.

3.3 Fourier-transform infrared spectroscopy

Fourier-transform infrared (FTIR) spectroscopy is mainly used for optical absorption measurements in the middle and far infrared spectra range. This spectroscopy technique exploits the fact that molecules absorb radiation in specific frequencies that are characteristic of their molecular structure. The frequency of the absorbed radiation is determined by e.g. the shape of the molecular potential energy surfaces, the masses of the atoms comprising the

molecule, and the vibrational coupling associated to different bonds of the molecule. FTIR spectrometers use a Michelson interferometer with a moveable mirror to produce an interference pattern. A Michelson interferometer consists in a half-silvered mirror inclined 45 degrees to an incoming beam that acts as a beamsplitter, i.e. reflects half the coherent light hitting it and transmits the other half. Both are collected by mirrors, which reflect the beams, directing them back out the Michelson interferometer. A scheme of such setup is presented in Fig. 3.7. The two beams follow different paths, enabling an interference pattern to occur. By varying the position of one of the mirrors, the interference pattern can be changed.

According to the scheme of Fig. 3.7, we can see that due to the various paths that light can take, only half of the inputed light can be collected on the detector. If the length of the paths taken by the two beams differ in half of the beams wavelength, they will be in opposition of phase when recombined at the beamsplitter and thus cancel each other. However, the translating mirror may be moved, and so the intensity $I(\delta)$ of light transferred to the detector as a function of the path difference (optical delay) will follow the sort of trend shown in Fig. 3.8. This interferogram corresponds to that obtained for a white light source and shows

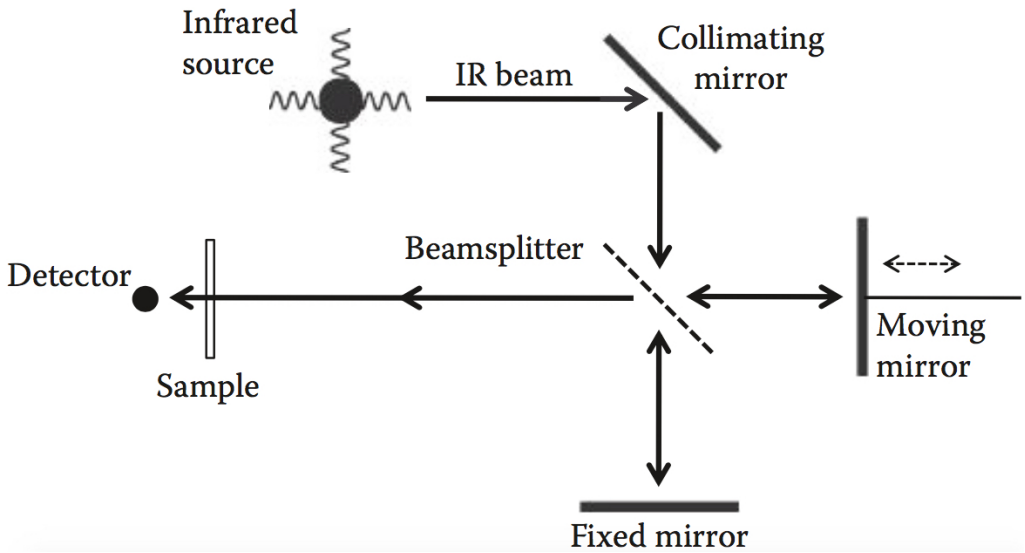

FIGURE 3.7: Schematics of a FTIR spectrometer. From [16].

us that for $\delta = 0$ the intensity of the interferogram is maximum, which indicates that all the radiation is transferred to the detector. The point corresponding to $\delta = 0$ must then be found by aligning the inputed light in order to obtain the maximum value of intensity. This interferogram is then converted in an analyzable spectrum by using the Fourier transform [17]

$$B(\sigma) = \int_{-\infty}^{+\infty} I(\delta)\cos(2\pi\sigma\delta)d\delta \tag{3.39}$$

where $B(\sigma)$ is the spectral power density, and σ is the radiation wavenumber. In practical means, this corresponds to finding the contribution in terms of intensity of each wavenumber to the total intensity of the acquired interferogram and then plot this information as a function of the corresponding wavenumber. This technique presents several advantages over the conventional dispersive spectrometers. One, designated multiplex advantage, is that as all the spectral wavenumbers are measured simultaneously the spectrum can be obtained rather quickly, with the acquisition time depending on the processing capabilities of the spectrometer to calculate the Fourier transform. Another, the Jacquinot advantage is associated with the discards of the use of slits, which attenuate infrared light. This produces a greater output and thus a higher signal/noise ratio.

In this work, FTIR spectroscopy was used to probe the extent to which the silicon oxide (SiO_2) surrounding Si NCs, synthesized by means of the phase segregation technique, is removed upon exposure of the NCs to hydrofluoric acid. This can be probed by FTIR spectroscopy via observation of the vibrational modes characteristic of Si−O−Si bonds of the oxide, as will be shown in Sec. 4.1.3.

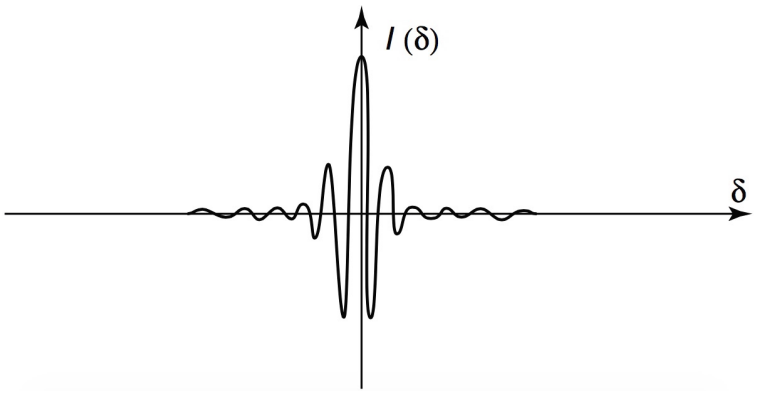

FIGURE 3.8: Example of an interferogram acquired by FITR spectroscopy. From [17].

3.4 Superconducing quantum interference device magnetometry

Superconducting quantum inteference device (SQUID) magnetometry is a method for measuring the static and time-dependent magnetic moment of liquid and solid state sam-

ples at various applied magnetic field and temperatures. Currently SQUID magnetometers provide the most sensitive instrument to measure magnetic moments, with state of the art instruments being capable to measure magnetic moments in the order of 10^{-7} emu [229]. A SQUID consists of a junction in the shape of a ring made of two superconductors separated by two thin insulating layers. A scanning electron microscopy image of a SQUID is shown in Fig. 3.9(a), in which the thin insulating layer separating the two superconductors are indicated by red rectangles. The operating principle of a SQUID is based on the Josephson

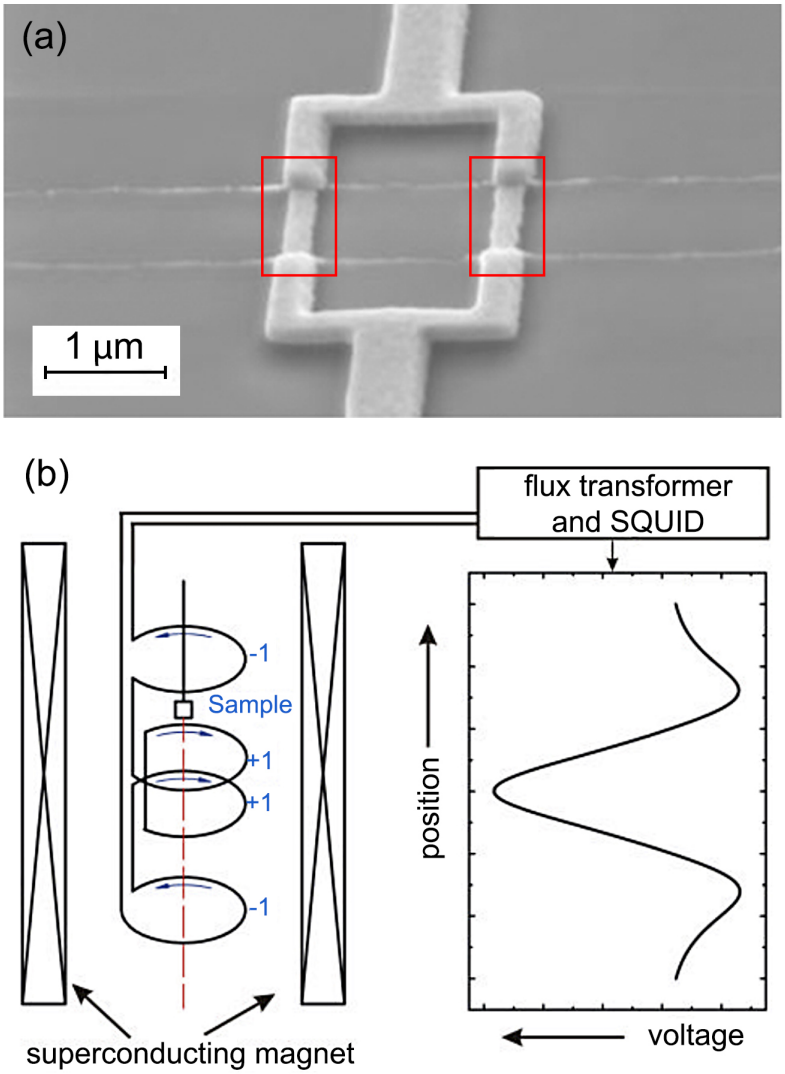

FIGURE 3.9: (a) Scanning electron microscopy image of a superconducting quantum interference device (SQUID). The red rectangles indicate the two thin insulating layers separating the two superconductors. (b) Schematic of a detection coil used in SQUID magnetometer and response signal of an dipole with spin $S = 1/2$ recorded as a function of scan length in a SQUID magnetometer. From [18].

effect. In a SQUID, the insulating layer constitutes a barrier for electron flow. However, if the thickness of the layer separating the two superconductors is sufficiently small to enable the wave function of electrons to spread between the two superconductors, electrons can pass through the two superconductors spontaneously, i.e. without an applied voltage, and establish an electric current. This is the Josephson effect, and the electric current in this junction is a continuous current proportional to the sine of the phase difference between the two superconductors. If a constant electric voltage is applied between the two superconductors, an alternating electric current appears in reaction to phase variations, with a frequency that depends on the applied voltage. Since the phase variation of a superconductor is linked to the magnetic flux, the Josephson effect is very sensitive to applied magnetic fields.

A SQUID magnetometer measures the longitudinal magnetic moment of a sample, i.e. along the direction of the applied magnetic field. The sample space is located within a superconducting detection coil; see Fig. 3.9(b). Centered around the detection coil is the superconducting magnetic capable of producing a uniform constant magnetic field over the entire coil region. The sample is moved vertically through the detection coil. Due to the magnetic moment of the sample, this movement induces an electric current in the detection coils. This current produces a variation is the SQUID output voltage V that is recorded as a function of scan length z, which is shown in Fig. 3.9(b) for the case of a dipole with spin $S = 1/2$. A numerical algorithm then fits the measurement of $V(z)$ to the theoretical curve of an ideal dipole to extract the magnetic moment μ [18].

A characteristic of SQUID magnetometers is that the detection coil is only sensitive to point-like discontinuities in the magnetic flux as the sample is scanned. Thus, samples that are magnetically homogeneous beyond the length of the detector coil (approximately 3 cm) do not contribute to the measured voltage response. Taking this into account, in order to obtain accurate measurements of a sample magnetic moment using SQUID, the sample vertical length must be less than 5 mm.

3.5 X-ray diffraction spectroscopy

X-ray diffraction (XRD) spectroscopy is a technique commonly used to study nanostructured materials such as thin films and superlattices which provides a wide variety of information on the e.g. thickness, crystalline structure, and interfacial properties at the nanometer scale. This technique uses a monochromatic source of X-rays with a wavelength comparable to the interatomic spacing (i.e. in the range of $\sim 0.1 - 100$ Å) to irradiate a sample and a detector is typically moved around the sample to record the directions and intensities of the waves diffracted at the sample, as schematized in Fig. 3.10(a). These X-ray waves can be scattered in all directions by interaction with the sample. If the sample has a crystalline struc-

ture, a regular array of scattered waves is produced. Constructive and destructive interference occurs along different directions as scattered waves are emitted by atoms of different types and at different positions. This interference between diffracted waves originates a diffraction pattern which can be described by the Bragg's law:

$$2d_{hkl} \sin\theta = n\lambda \tag{3.40}$$

where θ is the incident angle, λ is the wavelength of the incident X-ray, n is an integer, and

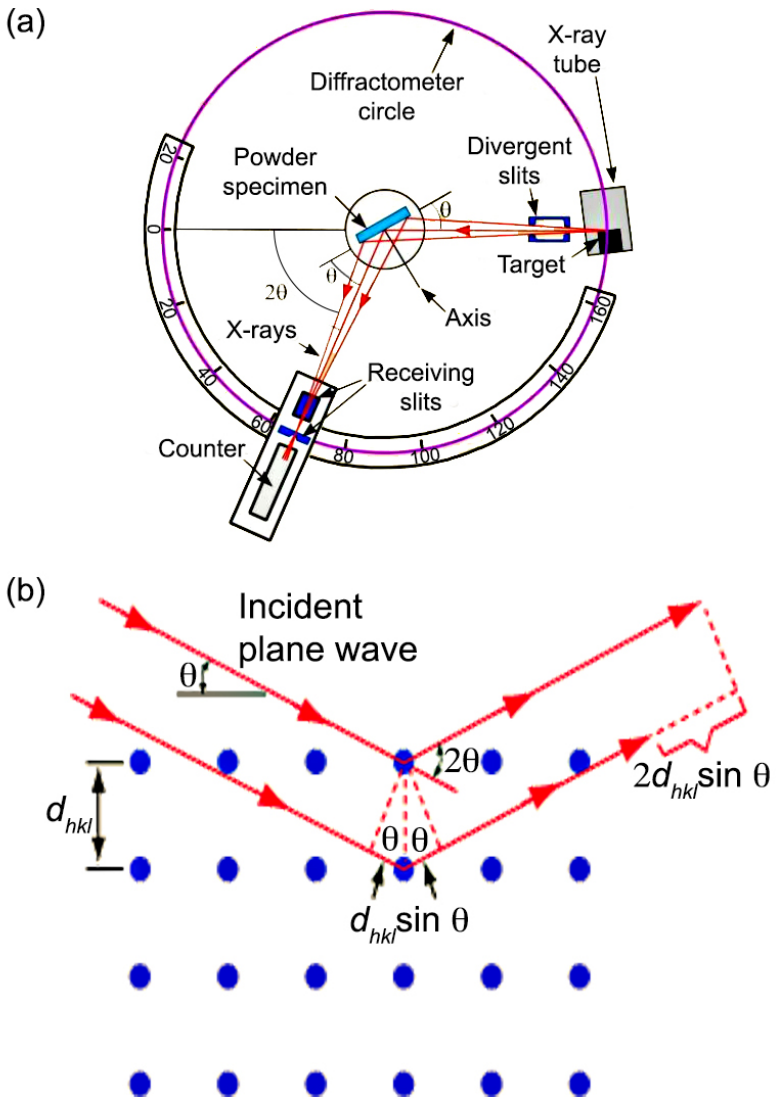

FIGURE 3.10: (a) Schematic of an experimental setup for X-ray diffraction spectroscopy. (b) Scheme illustrating the Bragg law on a crystalline lattice. Adapted from [19].

d_{hkl} is the interatomic spacing between two adjacent planes with Miller indices hkl. The distance d_{hkl} determines the difference in path length for the ray scattered from the top plane and the ray scattered from the bottom plane. Figure 3.10(b) shows that this difference in path lengths is equal to $2d_{hkl}\sin\theta$. Constructive interference occurs when the difference in path length for the top and bottom rays is equal to $n\lambda$. The angle between the reflected and the diffracted beams is always equal to 2θ, as shown in Fig. 3.10(b). This angle can be obtained directly in experimental situations and so the X-ray diffraction spectra are given in terms of 2θ.

A diffraction pattern from a material typically contains many distinct peaks, each corresponding to a different interplanar spacing d_{hkl}. As an example, let us consider the case of a cubic crystal with lattice parameter a_0. In this case, the interplanar spacings d_{hkl} are given by

$$d_{hkl} = \frac{a_0}{\sqrt{h^2 + k^2 + l^2}}. \tag{3.41}$$

From the Bragg law given by Eq. (3.40) we can find that the (hkl) diffraction peak occur at the experimentally measured angle $2\theta_{hkl}$ given by

$$2\theta_{hkl} = 2\arcsin\left(\frac{\sqrt{h^2 + k^2 + l^2}}{2a_0}\right). \tag{3.42}$$

For a sample consisting of a single crystal with a given orientation to the incident X-ray beam, only a few reflections may result because the set of planes with interplanar spacing satisfying the Bragg condition in Eq. (3.40) is limited. However, for a sample comprising many small and randomly-oriented crystallites, such a powder of NCs, one or more crystallite will be in the orientation corresponding to a Bragg angle. Thus, the Bragg condition for all interplanar spacings will be satisfied and reflections from all the crystallites can be observed simultaneously. The information contained in a diffraction pattern can be analyzed through the following three parameters:

- the position of the diffraction maxima, which can be used to infer the crystalline structures existing in the sample;
- the peak intensities, which is given by the area under the peak and is proportion to the relative abundance of the corresponding relative phase in the sample;
- the intensity distribution as a function of diffraction angle, which can be estimated from the full width half maximum of the peak and is proportional to the size of the corresponding crystalline phase.

In the present work, we used XRD spectroscopy to investigate the size, shape, structure,

of CdSe NCs ensembles. We used a Bruker-AXS microdiffractometer to collect winder-angle powder patterns using the Cu-Kα line.

3.6 Optical absorbance spectroscopy in the UV-Vis range

Absorbance spectroscopy is an experimental technique based on measuring the amount of light with a given wavelength absorbed by a sample [230]. When a photon is absorbed by an atom or molecule in the sample, it undergoes a transition from a lower energy state to a higher energy (excited) state, as shown in Fig. 3.11. Absorption occurs only when the photon energy $h\nu$ matches the difference in energy between the two energy levels ΔE:

$$\lambda_{\text{abs}} = \frac{hc_{\text{light}}}{\Delta E} \tag{3.43}$$

where h is the Planck constant, and c_{light} is the velocity of light in vacuum. The type of transition depends on the energy of the photon. In the case of electromagnetic radiation in the UV and visible wavelength range, absorbing a photon promotes one of the valence electrons of the atoms or molecules comprising the sample to a higher energy level.

When the sample absorbs electromagnetic radiation, the number of photons passing through the sample decreases. The measurement of this decrease is defined as absorbance and is commonly used for example to determine the concentration of an absorbing species in solution [230]. The absorbance A of a sample is given by the Beer-Lamber law:

$$A = \log_{10} \frac{I_0}{I} = \alpha z \tag{3.44}$$

where α is the absorption coefficient of the sample, i.e. the fraction of the light intensity that is absorbed per unit length in the sample, z is path length of the light within the sample, A is the absorbance, and I_0 and I are the intensities of the incident light and of the light transmitted through the sample, respectively.

The typical setup of a UV-Vis absorbance spectrometer is schematized in Fig. 3.11. This setup comprises a source of photons, a monochromator for selecting photons with a specific wavelength, a detector for measuring the signal, and a signal processor that displays the signal. This setup comprises a source of electromagnetic radiation, which emits radiation over a broad range of wavelengths. To isolate a single wavelength from the radiation source, a monochromator is used. In a monochromator, a radiation beam enters through an entrance slit and is collected by a collimating mirror. This mirror reflects a parallel beam of radiation to a diffraction grating, which consists of an optically reflecting surface with a large number of parallel grooves. The diffraction grating disperses the radiation and a second mirror focuses

the radiation onto a planar surface containing an exit slit. The monochromatic beam is then split into two equal intensity beams by a half-mirrored device. One beam passes through a cuvette containing a solution of the sample being study in a transparent solvent, and the other beam passes through an identical cuvette containing only the solvent. The intensities of these beams are then measured by a detector and compared. Absorbance spectra are recorded as a function of the wavelength of monochromatic beam passing through the sample.

In this thesis, we used UV-Vis absorbance spectroscopy to characterize the optical properties of CdSe NCs. Our measurements were performed using a Cary 5E UV-Vis-near-infrared spectrophotometer. For these measurements, CdSe NCs were dispersed in hexanes and placed in a 1 cm path length quartz cuvette.

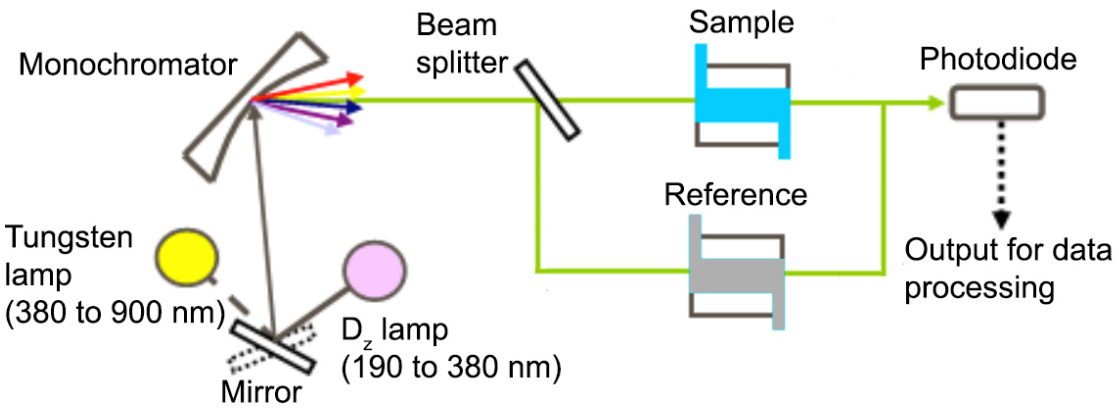

FIGURE 3.11: Schematics of a typical UV-Vis absorbance spectrometer.

3.7 Transmission electron microscopy

Transmission electron microscopy (TEM) is a imaging technique that is commonly used to obtain information on the morphology, composition and crystallography in the scale of a few nanometers, thus being capable of imaging atomic lattice patterns. TEM operates in a similar way to that of an optical microscope but using a beam of electrons instead of visible light. Optical microscopes can reach resolutions of about 200 nm, which is limited by the wavelength of the visible light [231]. TEM uses electrons with De Broglie wavelengths down to a few nanometers, thus enabling much higher resolutions than optical microscopy.

A scheme of a TEM setup is shown in Fig. 3.12. In TEM, a thin sample is irradiated with an electron beam generated by an electron gun. This beam has a uniform current density and comprises electrons that are accelerated by a voltage of 100-300 kV. The electron acceleration voltage is inversely proportional to the De Broglie wavelength of the electrons and so a

higher acceleration voltage provides better resolution to the system. A condenser lens system consisting of three or four lenses is used to vary the illumination aperture and the area of the sample that is illuminated. The condensed beam of electrons is shined through the sample, whose thickness must be smaller than the mean free path of the incident electrons to prevent their absorption by the sample. Incident electrons interact strongly with atoms by elastic and

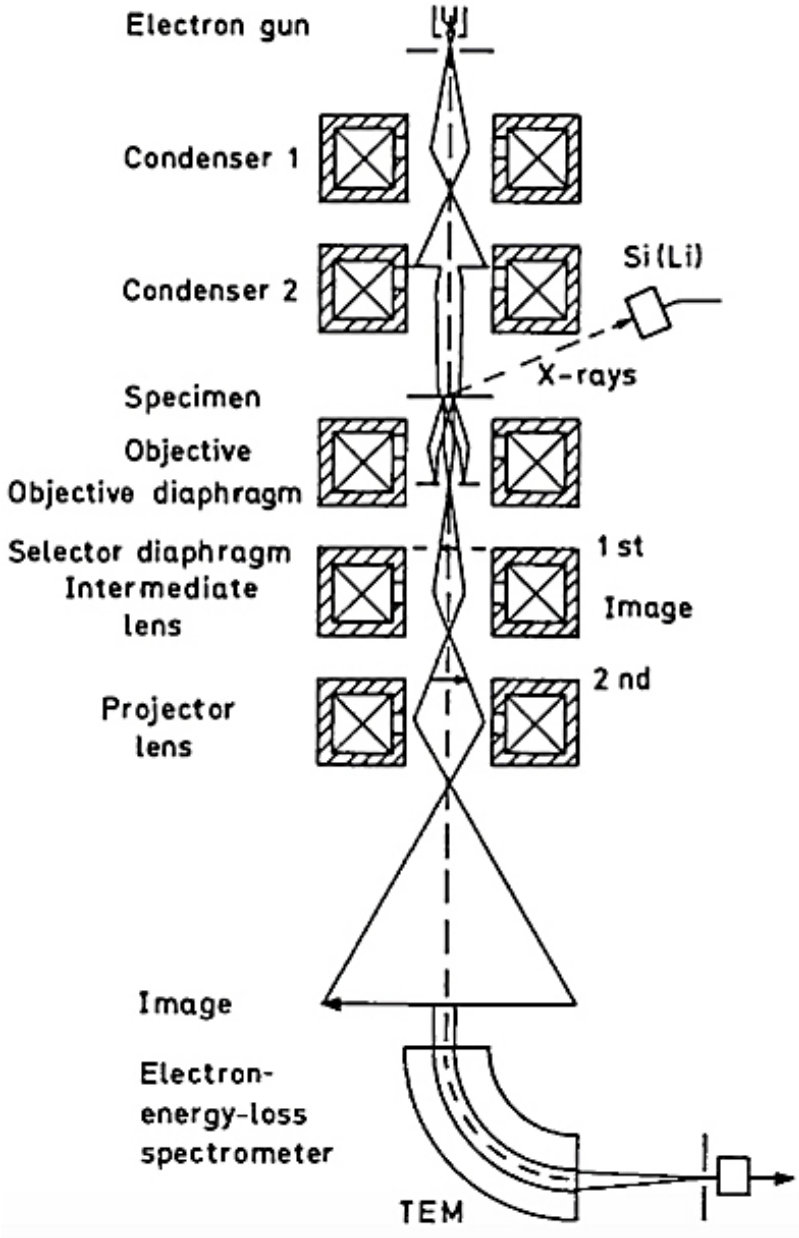

FIGURE 3.12: Scheme of a TEM setup. Adapted from [20].

inelastic scattering. The intensity of the scattering depends on the orientation of the planes of atoms relative to the electron beam. Strongly scattered electrons are deflected away from the direction of the incident beam before being transmitted through the sample. Incident electrons that are transmitted through the sample without being strongly diffracted are sent through several magnification lenses before reaching a detector such a phosphor screen or a CCD camera.

For TEM of CdSe NCs, we used a FEI Tecnai G2 F30 microscope with an acceleration voltage of 300 kV. Each sample was prepared by depositing a drop of dilute dispersion of NCs in hexane onto a 400-mesh carbon-coated copper grid and allowing the solvent to evaporate at room temperature. For TEM of Si NCs, TEM images were used to determine the size distribution of P-doped Si NCs. For this, the NCs must be placed in TEM grids, which can be done by either placing the TEM grids in the reactor chamber for direct deposition of Si NCs or by immersing the TEM grids in very dilute Si NCs dispersions. To determine the NC size distribution, a large amount of TEM images is analyzed with a specialized software [232]. TEM images also provided information about the shape of the NCs and their structural properties, namely the thickness of the NCs oxide shell.

3.8 Brunauer-Emmet-Teller analysis

The Brunauer-Emmet-Teller (BET) analysis is a gas adsorption spectroscopy technique that is based on the fact that the specific surface area S_0 of a powder sample, which is defined as the surface area divided by the mass of the sample, can be determined by measuring the isotherms for the adsorption of gas molecules multilayers on a surface [233]. This relation is given by the following equation

$$\frac{1}{\upsilon[P_0/P-1]} = \frac{C-1}{\upsilon_{\mathrm{m}}C}\cdot\frac{P}{P_0}+\frac{1}{\upsilon_{\mathrm{m}}C} \tag{3.45}$$

where P and P_0 are the equilibrium pressure and saturation pressure, respectively. The saturation pressure is defined as the pressure at which no further gas is adsorbed to the surface upon increasing P. The amount of adsorbed gas is denoted by υ and υ_{m} is the amount of gas forming a monolayer on the surface. Experimentally, P, P_0 and υ are known parameters, while υ_{m} and C are obtained by fitting Eq. (3.45) to the variation of υ as a function of P. From this, it is possible to calculate the surface area of the sample as $S = \upsilon_{\mathrm{m}} N_{\mathrm{A}} \phi$, where N_{A} is the Avogadro constant and ϕ is the adsorption cross section of the gas molecules used for the experiment. Assuming spherical NCs, the average particle diameter d is given by

$$d = \frac{6m}{\rho_{\mathrm{Si}} S} \tag{3.46}$$

where m is the mass of the NC ensemble and $\rho_{\mathrm{Si}} = 2.33$ gcm^{-1} is the mass density of Si.

In this work, the BET analysis was used to determine the average diameter of P-doped Si NCs. A drawback of the BET technique is that it only provides information on the average size of P-doped Si NCs and no information about the size distribution can be deduced from this technique.

Chapter 4

Materials and samples preparation

In this chapter, we summarize the synthesis methods used to fabricate the different materials used in the investigations of this thesis, as well as some of the basic properties of these materials. Section 4.1 addresses the two synthesis methods used to fabricate the P-doped Si NCs, namely the phase segregation method employed by the group of Minoru Fujii at the University of Kobe, Japan, and the gas phase method employed by the group of Harmut Wiggers at the University of Duisburg-Essen, Germany. This section also describes and compares some of the basic properties of the P-doped Si NCs grown by phase segregation and gas phase methods. Finally, this section presents the process used to liberate the P-doped Si NCs produced by phase segregation method from their silicon oxide matrix. Section 4.2 describes the synthesis method used by the group of David Norris at the ETH Zurich to fabricate the intrinsic and the Ag-doped CdSe NCs investigated in this thesis. We also present some of the structural properties of these NCs.

4.1 Phosphorus-doped Si nanocrystals

In this thesis we used Si NCs produced by the phase segregation method yielding Si NCs embedded in amorphous silicon oxide [46, 142, 234], and by the gas-phase method yielding freestanding Si NCs [44, 115, 134]. In the following, we briefly describe these two methods to synthesize P-doped Si NCs, as well as some of the basic properties of the P-doped Si NCs used in this thesis.

4.1.1 Synthesis techniques

Phase segregation method

One of the two methods used to grow Si NCs studied in this thesis was the phase segregation of silicon suboxide (SiO_x) into Si NCs and SiO_2 at high-temperature annealing. This method, which we here call phase segregation method, yields Si NCs embedded in a SiO_2 matrix. The P-doped Si NCs grown by gas phase segregation that we used in this thesis were synthesized by the group of Minoru Fujii at the Kobe University, Japan.

The first step of the phase segregation synthesis of Si NCs consists on growing a Si-rich silicate glass film by the simultaneous sputtering of Si and SiO_2 onto thin stainless steel plates under an Ar gas atmosphere. During sputtering deposition, which is schematized in

Fig. 4.1(a), free electrons are accelerated by an applied voltage and ionize Ar atoms introduced in the sputtering chamber. The Ar ions strike the positively charged targets and extract atoms from them. These atoms are ejected from the targets and are deposited on the substrate to grow a film. The duration of this process determines the thickness of the grown film. In our case, this sputtering deposition process yielded a silicate glass SiO_x with a thickness of about 50 μm. In the second step of phase segregation synthesis, which is schematized in Fig. 4.1(b), the SiO_x films are peeled off the stainless steel plates and annealed in a N_2 atmosphere for 30 minutes at 1100-1250°C [138, 139]. The annealing of the SiO_x films induces the nucleation, growth and crystallization of Si NCs, as is described by the following equation

$$SiO_x \rightarrow \left(1 - \frac{x}{2}\right) Si + \frac{x}{2} SiO_2 \tag{4.1}$$

In this method, the size of the Si NCs can be controlled by the Si concentration in SiO_x and by the annealing temperature. The phase segregation method can be adapted to grow P-doped Si NCs by adding a phosphate target (P_2O_5) to the sputtering process described above. This yield a phosphosilicate thin film with a nominal concentration of P atoms introduced in the films $[P]_{nom}$, which is controlled by changing the P_2O_5 concentration in the phosphosilicate sputtering target. During the annealing step part of the P atoms introduced in the film become incorporated into the Si NCs during their growth. Assuming that the dopants are uniformly distributed in the samples after annealing, the effective concentration of P dopants incorporated within the NCs $[P]_{eff}$ would be equal to $[P]_{nom}$.

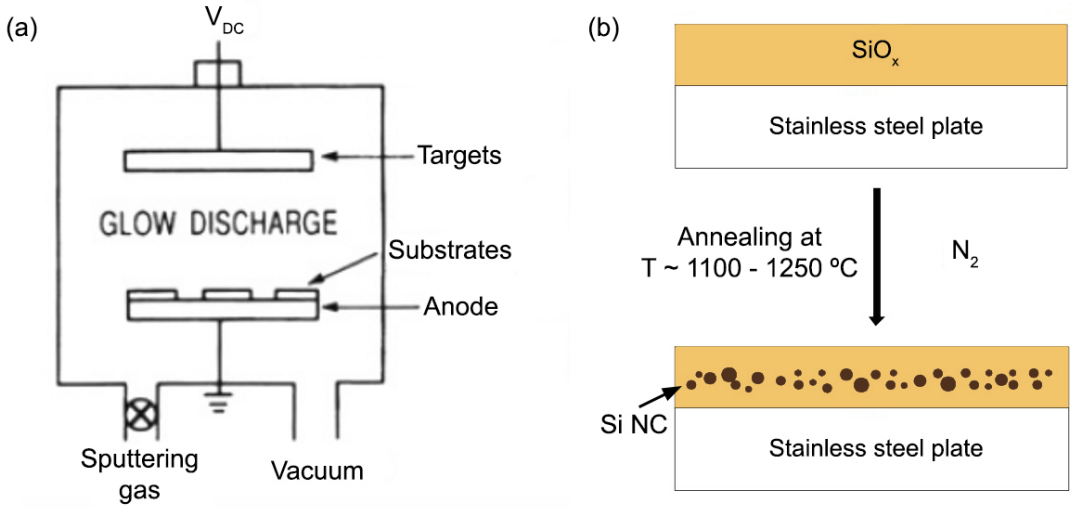

FIGURE 4.1: Schematics showing (a) a setup for sputtering deposition, and (b) the growth of Si NCs embedded in SiO_2 by high temperature annealing. Adapted from [21].

Gas phase method

Gas phase methods for growth of Si NCs in a plasma have been scaled to an industrial level to produce high quality and size-controlled Si NCs [44, 106, 134, 137]. A crucial feature of plasma synthesis approaches is their capacity to produce freestanding NCs with a H-terminated surface and with a controlled size. As referred above, freestanding NCs are much easier to integrate in electronic devices than NCs embedded in a matrix.

In general, gas-phase synthesis of Si NCs relies on the decomposition of silane (SiH_4) in a plasma [131, 235, 236] and the growth of NCs is controlled by their residence time in the plasma [141]. Two types of processes for plasma synthesis of Si NCs have been developed, which differ on the method adopted to control the residence time of the NCs in the plasma. One is the so-called batch method or *digital plasma approach* [136, 235, 237, 238]. In this method NCs are grown in the plasma and, once they reach the desired size, they are extracted from the plasma by injecting pulses of hydrogen gas. The other method, uses a continuous gas flow which drags the particles through the plasma volume [232, 236, 239]. This is simpler than the *digital plasma approach* because it is driven in a steady-state [141]. In the current work, the continuous gas flow method was used to fabricate the freestanding P-doped Si NCs.

A typical reactor for continuous gas flow plasma synthesis of Si NCs is schematized in Fig. 4.2. A mixture of SiH_4 and Ar precursor gases is injected into a quartz tube. Additionally, Ar and H_2 are injected into the quartz tube to tune the reaction kinetics via dilution of

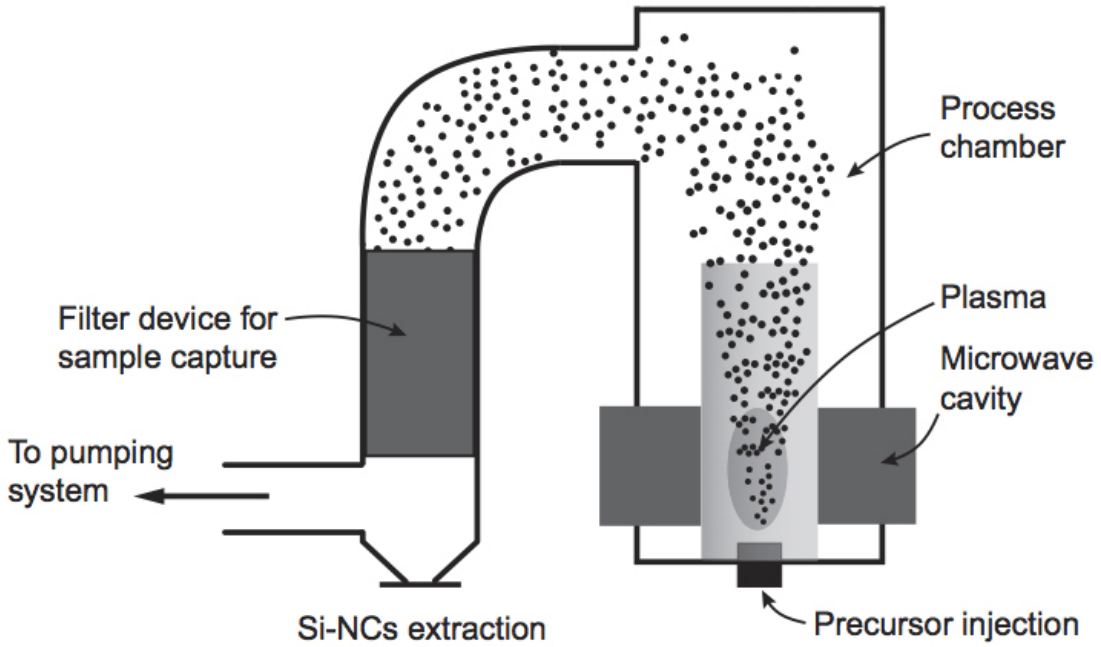

FIGURE 4.2: Schematic drawing of a typical continuous gas flow plasma reactor for the synthesis of P doped Si NCs. Adapted from [9].

the precursor gas and passivation of surfaces and radicals. After the injection region, the quartz tube is passed through a microwave cavity working at a frequency of 2.45 GHz and a microwave power in the range between 1 kW and 2 kW. In this region, the SiH_4 molecules are decomposed into radical silane compounds and ions forming a plasma. From this plasma, the formation of NCs occurs by homogenous nucleation and their growth occurs by coagulation and coalescence as they move along the quartz tube. Afterwards, the particle stream is lead through a filter system which is attached to a vacuum pumping system. After every growth cycle, the filter is purged with N_2 to extract the Si NCs powder.

In gas phase synthesis of Si NCs, P doping can be achieved by adding different amounts of phosphine (PH_3) to the dilute SiH_4 precursor gas injected into the quartz tube. The amount of phosphine added to the precursor gas determines the nominal doping concentration $[P]_{nom}$, which is given by

$$[P]_{nom} = \frac{[PH_3]}{[SiH_4] + [PH_3]} \times n_{Si} \tag{4.2}$$

where $[PH_3]$ and $[SiH_4]$ are the concentrations of PH_3 and SiH_4 precursor gases in the gas flow, and $n_{Si} = 5 \times 10^{22}$ cm^{-3} is the atomic density of Si.

In gas-phase synthesis of P-doped Si NCs, the main process parameters that can be used to control the NC growth are the concentration of precursor gases SiH_4 (and PH_3 in the case of P-doped Si NCs), the overall pressure in the reaction chamber, and the microwave power applied. By tuning these parameters, single crystalline P-doped Si NCs with mean diameter in the range of 4 nm to 50 nm can be grown in a controlled way. The general dependencies between the NC size and the different process parameters are as follows [232]:

- Precursor gases concentration: the average NC size increases with increasing concentration of the precursor gases in the gas flow. Higher precursor gases concentration leads to a higher density of particles in the plasma, resulting in a higher collision rate between the initial Si clusters and thus allowing for a faster growth by coagulation. Typical SiH_4 concentrations are in the range of 0.5% to 20% in Ar;

- Overall reactor pressure: the average NC size increases with increasing overall reactor pressure, for the same reasons as those mentioned for the precursors concentration. In the reactors used by Wiggers group to synthesize Si NCs used in this thesis the overall reactor pressure ranges between 20 and 500 mbar;

- Microwave power: increasing the microwave power increases the temperature in the reaction chamber, which should enhance coagulation. However, the higher temperature increases the flow velocity of particles through the reaction chamber, reducing the residence time of the particles. As a result, the particle size decreases with increasing microwave power.

4.1.2 Basic properties of the P-doped Si nanocrystals

Figures 4.3(a) and (b) show the TEM images of Si NCs synthesized by the phase segregation method. In the case of the Si NCs synthesized by phase segregation method, as-synthesized NCs are embedded in a SiO_2 matrix. In both TEM images of Fig. 4.3 we can see lattice interference fringes, which show that individual Si NCs consist of single crystalline cores with a spherical shape.

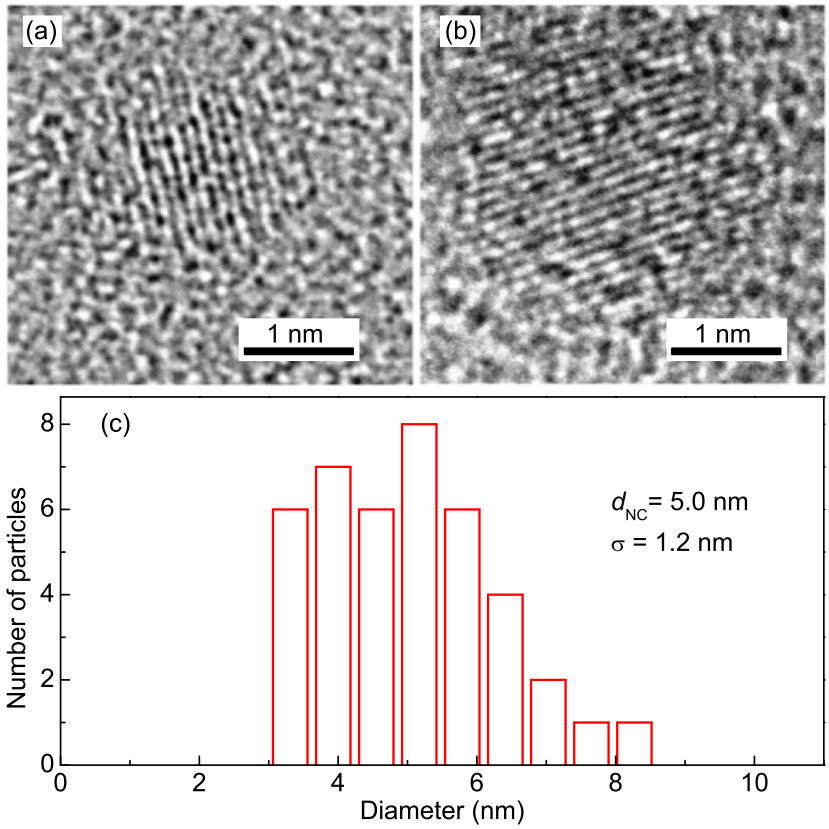

FIGURE 4.3: (a) and (b) TEM images of Si NCs synthesized by the phase segregation method. The lattice fringes correspond to the {111} planes of Si. (c) NC size distribution extracted from the TEM images of the Si NCs.

In this thesis, the size distribution of the samples of P-doped Si NCs grown by phase segregation method has been determined by TEM images like that shown in Fig. 4.3(a) and (b). This distribution is described by a Gaussian function and is shown in Fig. 4.3(c) for the case of an ensemble of Si NCs with a mean diameter of 5.0 nm and standard deviation of $\sigma = 1.2\%$

Figure 4.3(a) shows a TEM image recorded for Si NCs grown by the gas-phase method with a mean diameter of 20 nm and after their exposure to air. In the case of the Si NCs

grown by gas phase method, as-synthesized NCs have a H-terminated surface. This surface oxidizes upon the exposure of the NCs to air and the NCs become surrounded by an SiO_2 shell [6, 119, 240]. Previous studies have shown that the thickness of this oxide shell is 1.4 ± 0.4 nm for NCs with diameters up to 45 nm [6]. In the P-doped Si NCs grown by gas phase method that we used in this thesis, the NCs mean size has been determined by BET analysis. Previous studies using particle mass spectroscopy determined that the diameter of Si NCs grown by gas phase method follows a lognormal characteristic [106,232,236]. This distribution is described by

$$f(d_{\mathrm{NC}}) = \frac{1}{\sqrt{2\pi}\ln(\sigma)d_{\mathrm{NC}}} \exp\left(-\frac{[\ln(d_{\mathrm{NC}}/d_0)]^2}{2[\ln(\sigma)]^2}\right) \tag{4.3}$$

where d_0 is the average NC diameter and σ is the distribution standard deviation. The value of σ is weakly dependent on the NC size, varying from 1.3 to 1.5 [141]. The size distribution for an ensemble of Si NCs with a mean diameter of 3.9 nm grown by gas phase method is shown in Fig. 4.4(b).

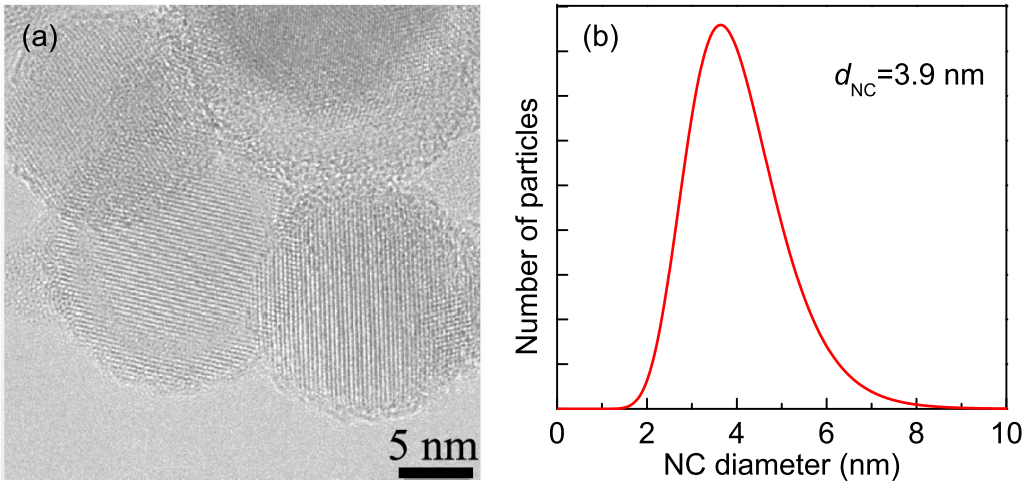

FIGURE 4.4: (a) TEM image of Si NCs synthesized by the gas phase method. (b) Size distributions of P-doped Si NC ensembles with mean diameter d_{NC} =3.9 nm, produced by the gas phase method.

4.1.3 Liberation of Si nanocrystals from oxide matrix

As referred above, P-doped Si NCs grown by phase segregation method are embedded in SiO_2 matrix. These oxide matrix forms a high potential barrier with several nanometers in thickness that suppresses the tunneling of charge carriers between the NCs and prohibits

efficient charge transport among Si NCs [46]. In order to remove the the oxide matrix embedding the NCs, we may treat them with hydrofluoric acid (HF). This process is so-called etching and its effect on the NCs surface is schematized in Fig. 4.5.

To etch Si NCs , the NCs powder is dispersed in an aqueous solution of 46% HF in water, in a proportion of 1.5 mL of HF solution per 20 mg of NC powder. The solution of NCs in HF is stirred for 20 minutes, after which time the embedding silicate matrix is completely dissolved. The solution of etched NCs is transferred to centrifugation vials and centrifuged at 6000 rpm for 2 minutes to separate the HF solution from the NCs. The HF solution is then removed from the vials and the NCs are redispersed in a solvent, usually methanol.

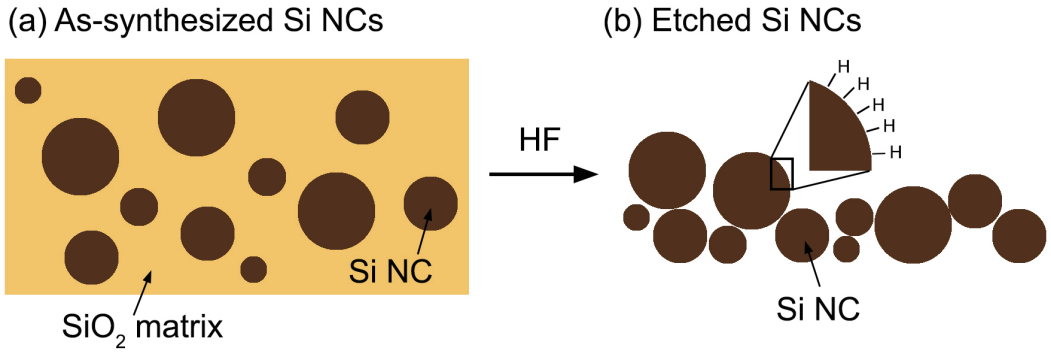

FIGURE 4.5: Schematic of the effect of HF etching on the surface of Si NCs. (a) After HF etching, the Si NCs are covered with a natural oxide which forms a high potential barrier which suppresses transfer of charge carriers between neighboring NCs.(b) After HF etching, the oxide shell is removed and the NCs surface becomes H-terminated. This enables the close contact between neighboring NCs.

We repeated this procedure 3 times. To obtain a dry NCs powder from the solution of etched NCs in methanol, we dried the NCs solution in vacuum for 2 hours.

To confirm that the NCs were successfully etched we prepared films of as-synthesized and of HF-etched Si NCs and measured their FTIR spectra, which are shown in Fig. 4.6. In this figure, we can see that both FTIR spectra show a band at 600 cm^{-1} due to vibrational modes of Si-H bonds at the NCs surface and two bands at 900 cm^{-1} and 2050 cm^{-1} assigned to vibrational modes of Si-H bonds [154, 241]. These spectra also show a signal at 1050 cm^{-1} due to Si-O-Si bonds [154,241]. However, the intensity of this signal observed in the spectrum of HF-etched Si NCs is almost negligible in comparison with that observed in the spectrum of as-synthesized NCs. This observation gives a good indication that the NCs were successfully etched. We note that the FTIR spectrum of HF-etched Si NCs shown in Fig. 4.6 as a black line shows a strong background slope and that the peaks observed in this spectrum have a first derivative-like appearance. These features result from thickness oscillations in the measured sample, which could not be repeated due to shortage of the analyzed material. However,

these features do not affect the position of the observed bands and so our assignment of the peaks associated to Si-H bounds at the surface of etched Si NCs should remain valid.

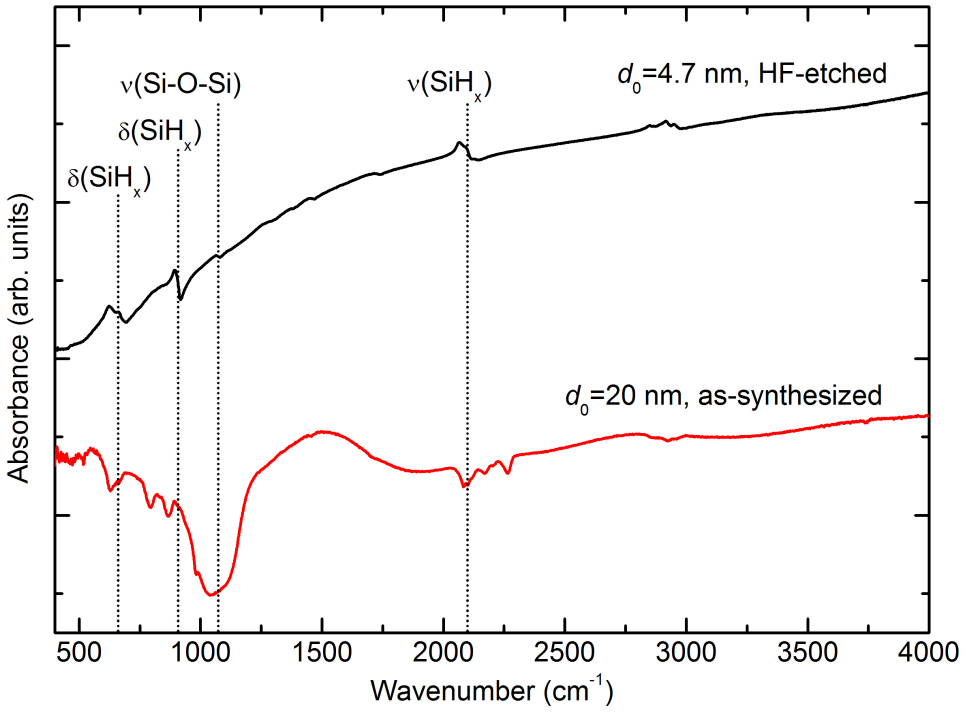

FIGURE 4.6: FTIR spectra of thin films of Si NCs after HF etching with an average size of 4.7 nm (solid line) and of as-synthesized Si NCs with an average size of 20 nm (dashed line). A detailed discussion of the results is given in the text.

4.2 Intrinsic and Ag-doped CdSe nanocrystals

4.2.1 Synthesis of intrinsic CdSe nanocrystals

CdSe NCs were prepared with a modified a procedure developed by Reiss *et al.* to fabricate CdSe/ZnSe core-shell NCs [242]. This procedure is schematized in Fig. 4.7(a)−(e). To prepare intrinsic CdSe NCs with 2.7 nm of diameter, a mixture of CdO (410.0 mg, 3.2 mmol), hexadecylamine (HDA, 18.54 g, 76.8 mmol), n-dodecylphosphonic acid (DDPA, 1.608 g, 6.4 mmol), and tri-n-octylphosphine oxide (TOPO, 8.096 g, 20.9 mmol) precursors was placed in a 100 ml four-neck round-bottom flask. The flask was then degassed under vacuum (<20 mtorr) and purged with dry N_2. This degassing process was repeated at least three times to remove

water and O_2. Afterwards, the mixture was heated at 90 ° while being continuously stirred [see Fig. 4.7(a)]. When this temperature was reached, stirring was stopped and the mixture was heated to 315 °C under N_2. The mixture was then kept at that temperature for nearly 30 minutes until it turned into a colorless solution, as schematized in Fig. 4.7(b). The temperature of the colorless solution was then stabilized at 280 °C, and a mixture of 20 ml of a 0.2 M solution of Se in tri-n-octylphosphine (TOP, 4 mmol) and 0.3 ml of diphenylphosphine (DPP) prepared in a N_2-filled glove box was rapidly injected into the reaction vessel with continuous stirring [see Fig. 4.7(c)], resulting in a temperature drop to 225 °C. The temperature was then quickly raised to 270 °C using a heat gun, and kept at that temperature for 10 minutes to facilitate nanocrystal growth [see Fig. 4.7(d)]. The reaction vessel was cooled to 90 °C and 40 ml of 1-butanol was added to prevent solidification of the reaction mixture [see Fig. 4.7(e)]. The NCs were isolated by addition of methanol to induce flocculation, followed by centrifugation. The resulting precipitate was formed by CdSe NCs with surfaces coated by a mixture of HDA, DDPA, and TOP/TOPO. A scheme of an as-synthesized CdSe NC is shown in Fig. 4.7(f).

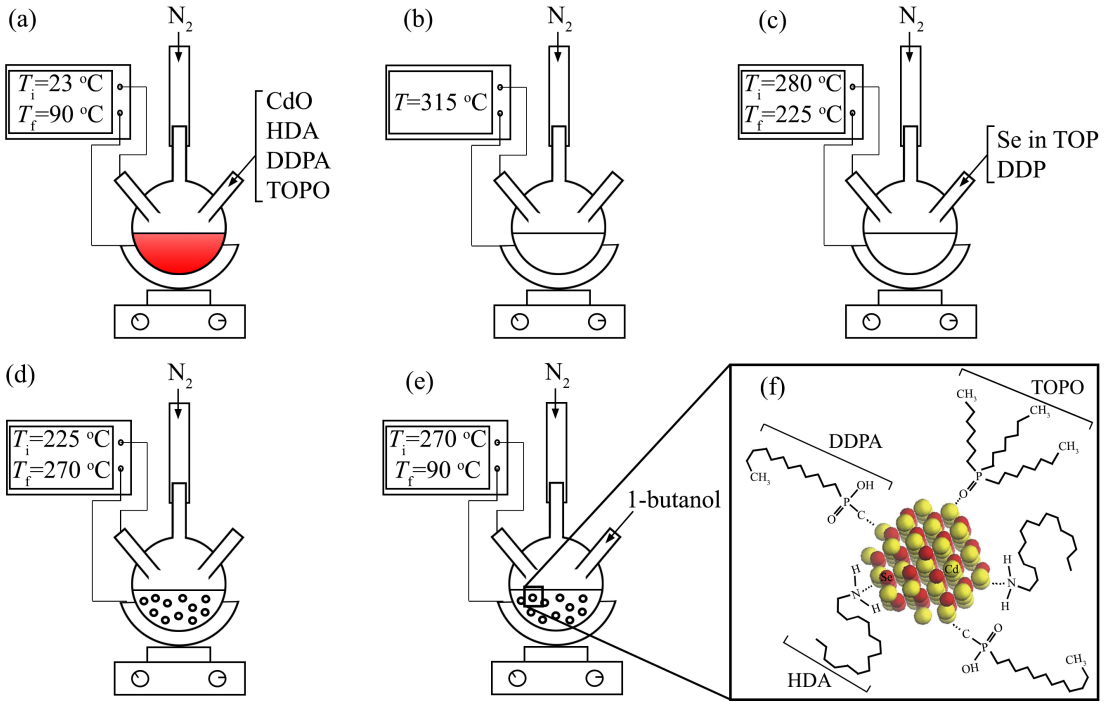

FIGURE 4.7: (a)−(e) Scheme of the synthesis process used to produce intrinsic CdSe NCs. In the steps of this process that involve a change in the temperature of the reaction mixture, the initial and final temperatures are labelled as T_i and T_f, respectively. (f) Scheme of as-synthesized CdSe NCs and of the types of ligands that passivate the NCs surface.

Following the synthesis of the CdSe NCs, several purification steps are performed to remove

excess ligands in the NCs precipitate. The first procedure consists on redispersing the NCs precipitate in hexanes and centrifuging. From this process results a supernatant containing the NCs and a precipitate containing mostly unreacted HDA. This precipitate is redispersed in hexanes and centrifuged again to extract more NCs. This procedure is repeated multiple times until all possible NCs are extracted from the initial precipitate. The purified dispersion is then stored overnight in a freezer at $-20°C$, during which time excess surfactants precipitate out of the dispersion. This precipitate is removed from the dispersion by centrifugation. The further purified dispersion is then filtered through a 0.2 nm polytetrafluoroethylene (PTFE) syringe filter. Then, reagent alcohol is added, and the solution is centrifuged. Multiple iterations (in general two more cycles) of redispersion and precipitation using hexanes and reagent alcohol are performed to obtain pure CdSe NCs. Finally the isolated CdSe NCs are dried under vacuum, dispersed in toluene, filtered through a 0.2 μm PTFE syringe filter to obtain a stable colloidal dispersion. Purified CdSe NCs are stored under ambient conditions until needed.

4.2.2 Ag doping of CdSe nanocrystals

After synthesis of intrinsic CdSe NCs, the incorporation of Ag dopants was achieved by applying a modified cation-exchange procedure [243], in which Ag dopants diffuse into the NCs and/or take the place of cations of the NC structure. Sahu *et al.* showed that this process takes place much faster in NCs than in the bulk by observing that exposing CdSe NCs to Ag cations causes their total or partial conversion to Ag_2Se NCs [5]. To avoid this and attain low concentrations of Ag dopants in the CdSe NCs, TOP was included in the exchange reaction as a surfactant that mediates the incorporation of Ag dopants in the CdSe NCs. A typical cation-exchange reaction consists on heating 6 ml of a 5 mg/ml dispersion of CdSe NCs in toluene to 60 °C in a glass vial with continuous stirring. Then, 1 ml of 0.1 M ethanolic AgNO3 and 1.5 ml of TOP are added to the rapidly stirring dispersion. After 2 minutes the reaction is quenched with 10 ml of ethanol. The precipitated NCs are then isolated by centrifugation and cleaned from unreacted reagents following the procedure described above for the intrinsic CdSe NCs.

4.2.3 Basic properties of intrinsic and Ag-doped CdSe nanocrystals

The CdSe NCs investigated in this work were analyzed by TEM and by X-ray diffractometry to determine their crystallinity and their size distribution. Figure 4.8(a) shows TEM images of intrinsic CdSe NCs with a mean diameter of 4.2 nm, together with their NC size distribution. There, we can see that the NCs have an approximately spherical shape and a narrow size distribution. The X-ray diffraction pattern of these NCs, shown in Fig. 4.9(a) as a black line, exhibits three peaks at approximately 26°, 42°, and 49°. These peaks can be assigned to, respectively, $\langle 111 \rangle$,

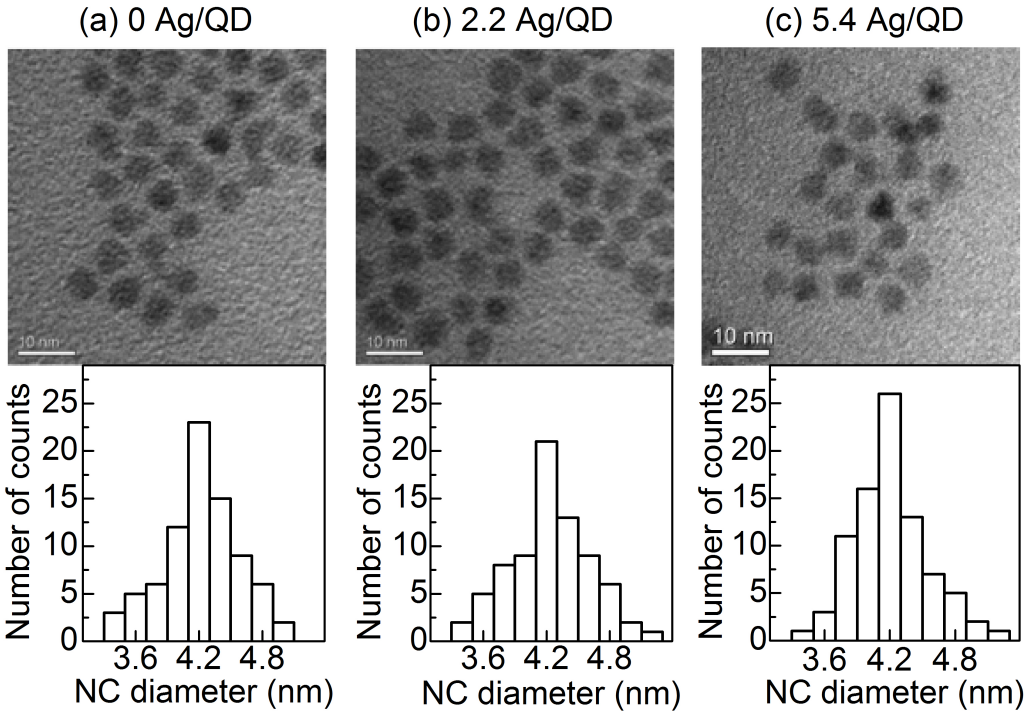

FIGURE 4.8: TEM images and NC size distributions of CdSe NCs with a mean diameter 4.2 nm: (a) undoped, (b) doped with 2.2 Ag per NC, and (c) doped with 5.4 Ag per NC.

$\langle 200 \rangle$, and $\langle 311 \rangle$ reflections of CdSe NCs with a zinc blende structure [244]. The black line in Fig. 4.9(b) shows the absorption spectrum of intrinsic CdSe NCs with a mean diameter of 2.7 nm. This spectrum displays discrete bands at 350 nm, 420 nm, 475 nm and 520 nm. These bands correspond to allowed optical transitions between quantized energy levels of electrons and holes in CdSe NCs. These energy levels can be described by the effective mass model taking into account the mixing of three valence sub-bands due to quantum confinement [245]. The bands observed in the absorption spectrum of intrinsic CdSe NCs thus correspond to the following transitions between energy levels of electrons and holes in the CdSe NCs [246]:

- Band at 350 nm: $3S_{3/2}(\mathrm{h}) \rightarrow 1S(\mathrm{e})$
- Band at 420 nm: $1P_{3/2}(\mathrm{h}) \rightarrow 1P(\mathrm{e})$
- Band at 475 nm: $2S_{3/2}(\mathrm{h}) \rightarrow 1S(\mathrm{e})$
- Band at 520 nm: $1S_{3/2}(\mathrm{h}) \rightarrow 1S(\mathrm{e})$

Further, the absorption spectrum of undoped CdSe NCs, shown in Fig. 4.9(b) as a black line, is similar to that reported previously for undoped CdSe NCs [184, 242, 247].

We also analyzed the effect of Ag doping on the size distribution, crystallinity, and optical absorption spectra of CdSe NCs. Figures 4.8(b) and (c) show the TEM images of CdSe NCs doped with 2.2 and 5.4 Ag dopants per NC, respectively, together with the corresponding NC size distributions. The concentration of Ag dopants in the CdSe NCs prepared for this work was determined in a previous study using inductively

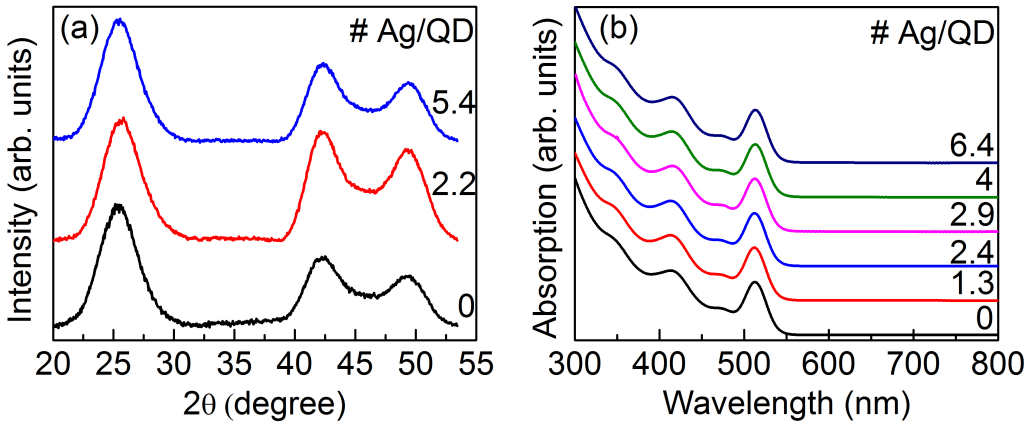

FIGURE 4.9: (a) X-ray diffraction spectra of the CdSe NCs with different concentrations of Ag dopants. (b) Absorption spectra for a series of CdSe NCs doped with different Ag doping concentrations (mean diameter of the CdSe NCs is 2.7 nm).

coupled plasma optical emission mass spectroscopy [5]. Using this technique, the net Ag:Cd:Se concentration was determined and, using the mean size of the NCs, the number of Cd, Se, and Ag atoms per NC can be deduced. We note that after NC synthesis, numerous rounds of cleaning are performed to remove any Ag atoms that are not incorporated in the NCs and so ensure that only those Ag atoms that were incorporated are taken into account. In Figs. 4.8(b) and (c), we can see that there are no significative changes in the size or size distribution of the NCs with doping. From the X-ray diffraction patterns obtained for the same NCs, shown in Fig. 4.9(a) as red and blue lines, we may see that the crystal structure of the NCs remains unchanged upon doping. Further, the absorption spectra of CdSe NCs shown that the energy band gap and optical absorption spectra remain intact after Ag doping; see Fig. 4.9(b). We also quantified the concentration of transition-metal contaminants using inductively coupled plasma-optical emission spectroscopy (ICP-OES). The concentrations of Fe impurities in both intrinsic and Ag-doped CdSe NCs is about 1−2 ppb (i.e. roughly about 1 Fe atom per 2500 NCs), and the concentration of Co and Ni is below the detection limit of the technique (< 0.1 ppb).

Chapter 5

Doping efficiency and confinement of phosphorus dopants in Si nanocrystals

In this chapter, we report our investigations using X-band EPR spectroscopy on the doping efficiency and confinement of donors in P-doped Si NCs that are surrounded by different environments. This chapter is divided as follows: in the first section, we present the EPR spectra of undoped and P-doped Si NCs and identify the EPR lines associated to P donors in Si NCs. We show that the EPR resonances associated to P donors in Si NCs consist on a band due to exchange coupled donor electrons in the NCs, and a pair of lines due to isolated (non-interacting) donor electrons in the NCs. In the second section of this chapter, we present and discuss the EPR spectrum of P-doped Si NCs in different surrounding environments. We compare the obtained EPR spectra with computational fits to discriminate the contributions of different species to the EPR spectra of P-doped Si NCs. From this analysis, we estimate a P doping efficiency of these Si NCs of about 30% and from this we infer that most P dopants are incorporated at substitutional sites of the NCs lattice and thus act as donors. We further find that the doping efficiency of P-doped Si NCs varies by several orders of magnitude depending on the NCs surrounding environment. We associate this effect to air molecules adsorbed to the NCs surface, which give rise to a strong compensation of donors. We find that this process can be reverted by desorbing the molecules from the NCs surface under vacuum. In the third section of this chapter, we perform temperature-dependent EPR measurements of P-doped Si NCs. From the temperature dependence of the intensity of the EPR signal associated to isolated donors in the NCs, we experimentally assess the confinement energy of isolated donors in Si NCs. From this, we provide experimental evidence for the confinement induced increase of ionization energy of dopants with decreasing NC size predicted with *ab-initio* calculations [8, 153, 163, 173]. We also investigate the temperature dependence of the intensity EPR signal associated to exchange coupled donor electrons in Si NCs. We observe that this intensity deviates from Curie behavior at temperatures below 40 K, which indicates that the amount of donors giving rise to the EPR signal due to exchange coupled donors in the NCs quenches with decreasing temperature. We further discuss this observation in the light of previous studies and argue that the exchange interaction between donors in NCs cannot be easily predicted by computation calculations using *ab-initio* methods.

For the investigations conducted in the present chapter, we used Si NCs synthesized by the phase segregation method described in Sec. 4.1.1, with a mean diameter of 5.0 nm. We used undoped Si NCs and P-doped Si NCs with a nominal doping concentration of $[P]_{nom} = 2 \times 10^{20}$ cm^{-3}, which corresponds to the average concentration of P atoms in the PSG films used to produced the Si NC samples (see description in Sec. 4.1.1). In this part of the work we studied P-doped Si NCs in different surrounding environments. We studied P-doped Si NCs embedded in their SiO_2 matrix, which are labeled SiNCs−SiO_2, and freestanding P-doped Si NCs with H-terminated surface obtained by HF etching of the as-synthesized P-doped Si NCs (SiNCs−SiO_2), as described in Sec. 4.1.3. The freestanding P-doped Si NCs with H-terminated surface are labeled SiNCs−H.

5.1 Identification of donor-related EPR lines in phosphorus-doped Si nanocrystals

We start by looking for evidence of P doping of the Si NCs grown by phase segregation method investigated in this thesis. Figure 5.1 shows the EPR spectra measured at 20 K of undoped (black line) and P-doped (red line) SiNCs−SiO_2. There, we see that both samples show a sharp signal at $g = 2.002$ with a peak-to-peak line width of about 0.2 mT. In previous works, this signal was attributed to EX centers at the SiO_2 matrix surrounding the NCs [46, 161, 248]. The EPR spectra of undoped and P-doped Si NCs also show an asymmetric band centered at about 334 mT which appears as an absorption band due to fast passage conditions. As will become clear in Sec. 5.2.1, this band results from Si-dbs at the NCs surface. The EPR spectrum of P-doped Si NCs also shows a line at $g = 1.998$, labelled here as Exch, and a pair of lines with median at $g = 1.998$ and separated by about 10.8 mT, which we label hf(^{31}P). As can be seen in Fig. 5.1, these three lines are absent from the spectrum of undoped Si NCs and thus are associated to P donors in the Si NCs. The Exch line observed in the EPR spectrum of Fig. 5.1 recorded for P-doped Si NCs has a g-value ($g = 1.998$) that is typical for P donor electrons in bulk Si and in Si NCs [6, 22, 23, 44]. Thus, we attribute this line to exchange coupled donor electrons. Further investigations on exchange coupled donor electrons will be described in Chap. 6 of this thesis. The hf(^{31}P) lines should result from the hyperfine interaction between the donor electrons spin ($S = 1/2$) and their ^{31}P nucleus spin ($I = 1/2$) [46]. In P-doped bulk crystalline Si, a hyperfine pair of lines with splitting of 4.2 mT and central g-value at $g = 1.998$ is the characteristic fingerprint of substitutional, isolated P donors [23, 140]. Thus, the hf(^{31}P) signals observed in our NCs should be due to isolated donor electrons in the P-doped Si NCs. However, the splitting of 10.8 mT between the pair of hyperfine lines observed in our P-doped Si NCs is about 2.5 times larger than that observed in P-doped bulk crystalline Si. Experimental studies further showed that the

magnitude of the hyperfine splitting can be used to infer the size of the P-doped Si NCs [7,46]. Comparing the reported size dependence of the hyperfine splitting of P donors in Si NCs [7] with the hyperfine splitting observed in our P-doped Si NCs, we can estimate that the size of our NCs is in the range of $4-5$ nm. This estimation is in very good agreement with the distribution of NC sizes obtained for the P-doped Si NCs studied here, which gives a mean diameter of 5.0 nm.

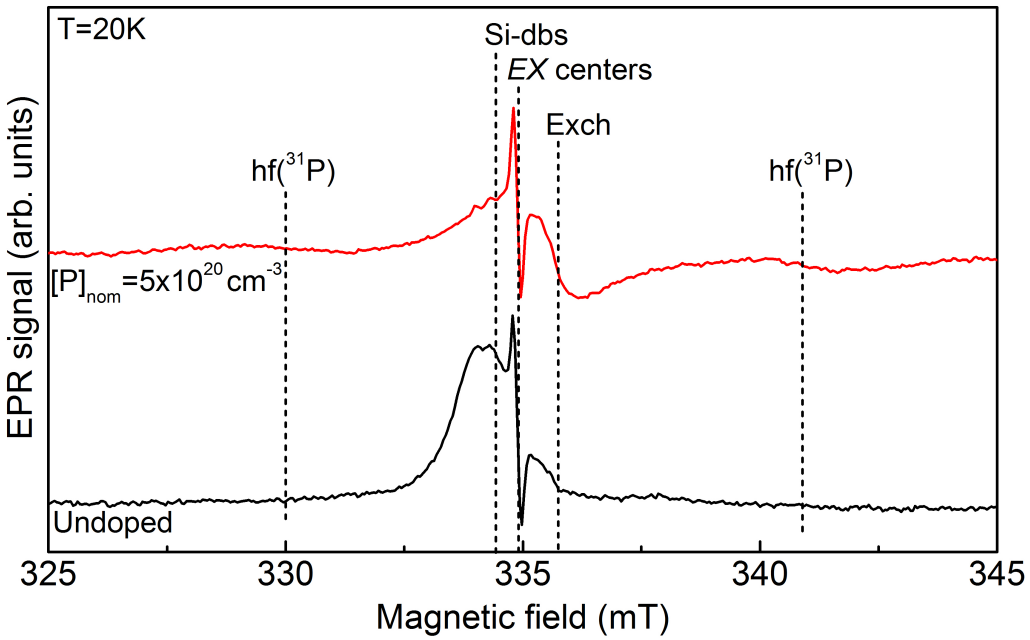

FIGURE 5.1: EPR spectra measured at 20 K of SiNCs$-SiO_2$ that are undoped (black line), and P-doped with $[P]_{nom}=5\times10^{20}$ cm^{-3} (red line).

5.2 Doping efficiency of P-doped Si nanocrystals grown with phase segregation method

5.2.1 Quantitative EPR measurements of P-doped Si NCs

We now focus on the study of the doping efficiency of the P-doped Si NCs. Curve (a) in Fig. 5.2 shows the EPR spectrum obtained for a SiNCs$-SiO_2$ sample. This spectrum can be well described by a computational simulation, shown in Fig. 5.3(a), that takes into account the spectral contributions of (i) the sharp signal located at $g = 2.002$ with a linewidth of

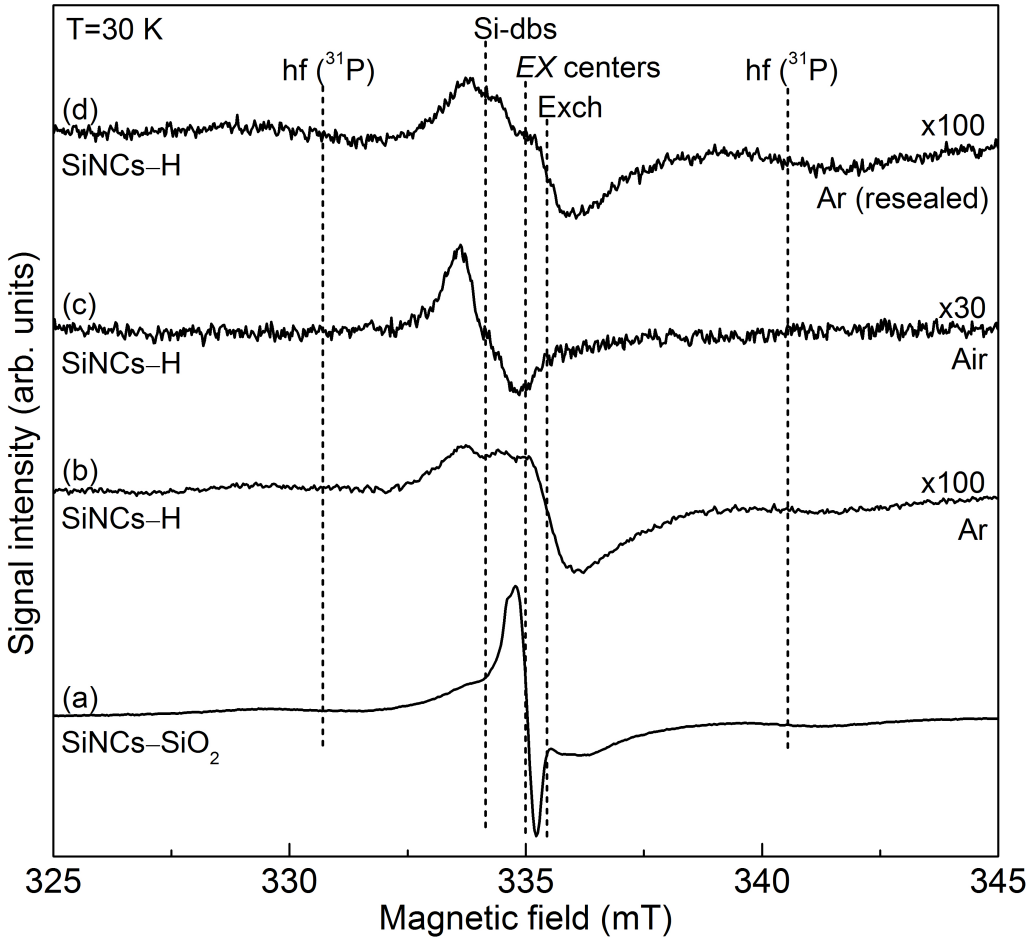

FIGURE 5.2: EPR spectra of (a) SiNCs−SiO_2, (b) SiNCs−H sealed in a Ar atmosphere, (c) SiNCs−H exposed to air, and (d) SiNCs−H resealed in an Ar atmosphere after exposure to air.

0.2. mT, attributed to EX centers at the SiO_2 matrix (green dash dotted line), (ii) an asymmetric band with zero-crossing magnetic field at about 334 mT (blue line), (iii) the Exch line at $g = 1.998$ (pink dashed line), and (iv) the pair of hf(^{31}P lines with median at $g = 1.998$ and separated by about 10.8 mT (purple dotted line). The line shape of (ii) results from the sum of two Lorentzian components and was obtained from the computational simulation of the EPR spectrum of SiNCs−H exposed to air [see Fig. 5.3(c)] which, as will become clear below, only displays the EPR signal associated to Si-dbs.

Curve (b) in Fig. 5.2 shows the EPR spectrum of a SiNCs−H sample, measured in an inert Ar atmosphere. From the computational simulation of this spectrum, shown in Fig. 5.3(b), we can see that the sharp signal at $g = 2.002$ due to EX centers disappears in relation to the

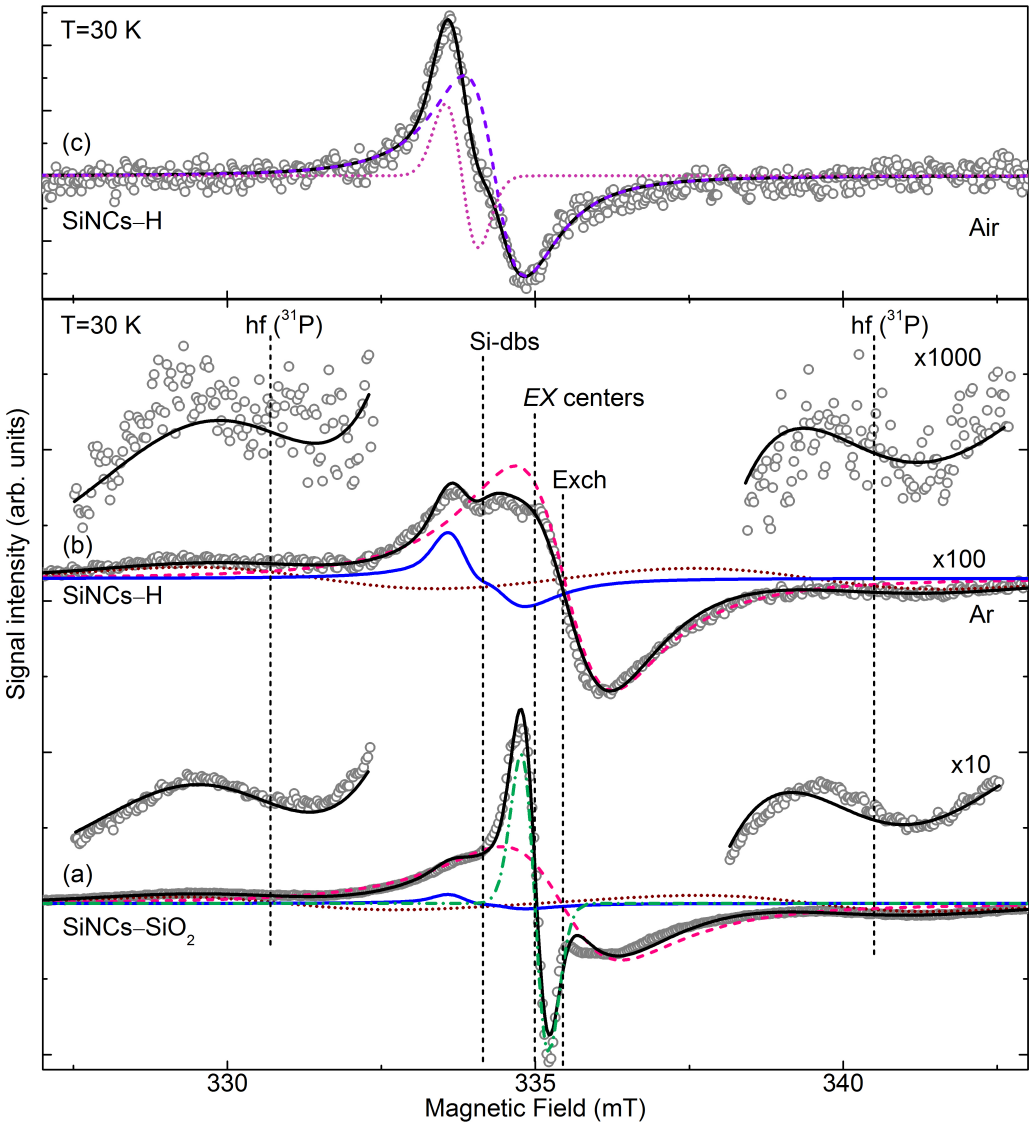

FIGURE 5.3: EPR spectra of (a) SiNCs−SiO_2, (b) SiNCs−H sealed in an Ar atmosphere, and (c) SiNCs−H exposed to air. The EPR spectra are shown together with simulated spectra (black solid line) composed of (i) a resonance at $g = 1.998$ (pink dashed lines), labelled Exch signal, (ii) a resonance at $g = 2.002$ (green dash-dotted line) due to *EX* centers at the SiO_2 matrix surrounding the NCs, (iii) a pair of pair of hf(^{31}P lines with median at $g = 1.998$ and separated by about 10.8 mT (brown dotted line), and (iv) a band at $g = 2.006$ due to Si-dbs (blue solid line) that results from the sum of two Lorentzian lines, which are shown in (c) as purple dashed and pink dotted lines.

EPR spectrum of SiNCs−SiO_2. This observation indicates that the etching procedure successfully removes the SiO_2 matrix surrounding the NCs. Further, in curve (b) of Fig. 5.3 we distinguish the signal due to Si-dbs at the NCs surface and the signals associated to P donors

in the NCs, namely the Exch signal due to exchange coupled donor electrons and the pair of lines hf(^{31}P) due to isolated P donors in the Si NCs.

From the computational fits of the EPR spectra of P-doped Si NCs, we estimate the intensity of the EPR signals due to P donors in the Si NCs by numerical double integration of the corresponding resonance lines. The intensity of the hf(^{31}P) signal I_{hf} is given by the sum of the intensities of the two hf(^{31}P) lines, and the intensity of the Exch signal I_{Exch} is given by the intensity of the signal observed at $g = 1.998$. Figure 5.4 shows I_{Exch} (black circles) and I_{hf} (black triangle) for two sets of SiNCs−SiO_2 and SiNCs−H samples. There we see that the intensity of the signals due to P donors decreases by about two orders of magnitude upon removal of the oxide matrix surrounding the NCs. This observation indicates that the nature of the NCs surface has a strong effect on the doping efficiency of the Si NCs. A reason for this strong decrease may be the depassivation of Si-dbs at the NCs surface upon removal of the SiO_2 matrix surrounding the NCs. Such unpassivated Si-dbs may compensate P donors in the Si NCs and thus quench the EPR signals associated to donor electrons in the P-doped Si NCs. Another reason may be adsorption of residual H_2O and O_2 molecules to the NCs surface that provide trap states for electrons donated by P donors in the Si NCs. The trends of I_{Exch} and I_{hf} displayed in Fig. 5.4 are identical for two sets of samples, which shows the reproducibility of the data.

To further investigate the effect of the nature of the environment surrounding the NCs on the P doping efficiency of Si NCs, we exposed SiNCs−H samples to air by unsealing the samples tube and measured their EPR spectrum. This is shown in curve (c) of Fig. 5.2 for one sample. We can see that the signals due to P donors in the Si NCs disappear upon exposure of the NCs to air and that the EPR spectrum only displays the signal at $g = 2.006$ due to Si-dbs. As shown in Fig. 5.3(c), this signal is asymmetric and can be well described by a sum of two Lorentzian lines. The absence of the EPR signals associated to P donors in Si NCs from the spectrum obtained for the NCs exposed to air indicates that exposure of the NCs to air leads to the compensation of all the P donors incorporated in the Si NCs. After exposure to air, we left the NCs in a vacuum chamber for 20 minutes and then resealed the sample tube under Ar atmosphere. The EPR spectrum measured after resealing the P-doped Si NCs is shown as curve (d) in Fig. 5.2. There, we see that the hf(^{31}P) and the Exch signals attributed to P donors in the Si NCs re-appear. In Fig. 5.4, we can also see that the EPR signals due to P donors in the sample SiNCs−H have a similar intensity before exposure to air and after exposure to air followed by resealing in a Ar atmosphere. This indicates that the observed compensation of P donors in the Si NCs by exposure to air is a reversible process, which may be related to the transfer of donor electrons to air molecules that adsorb to the NCs surface upon their exposure to air. Leaving the NCs in vacuum leads to the desorption of air molecules from the NCs surface and consequent elimination of the trap states that lead to the compensation of P donors. Previous studies showed that the adsorption of air molecules can alter the electrical properties of amorphous Si due to surface charge transfer [249,250]. Recent

studies also reported that the electrical conductivity measured in air of films of H-terminated Si NCs doped with P is about one order of magnitude higher than that of films of undoped H-terminated Si NCs [119]. However, it was further observed that the conductivity of films of P-doped Si NCs decreases exponentially over time and after about four hours of exposure of the films to air the conductivity is about the same as that of undoped Si NCs. Our present results indicate that this effect may be in part caused by the transfer of donor electrons to air molecules that adsorb to the NCs surface upon their exposure to air, which leads to the compensation of donor electrons and makes the P-doped Si NCs effectively undoped.

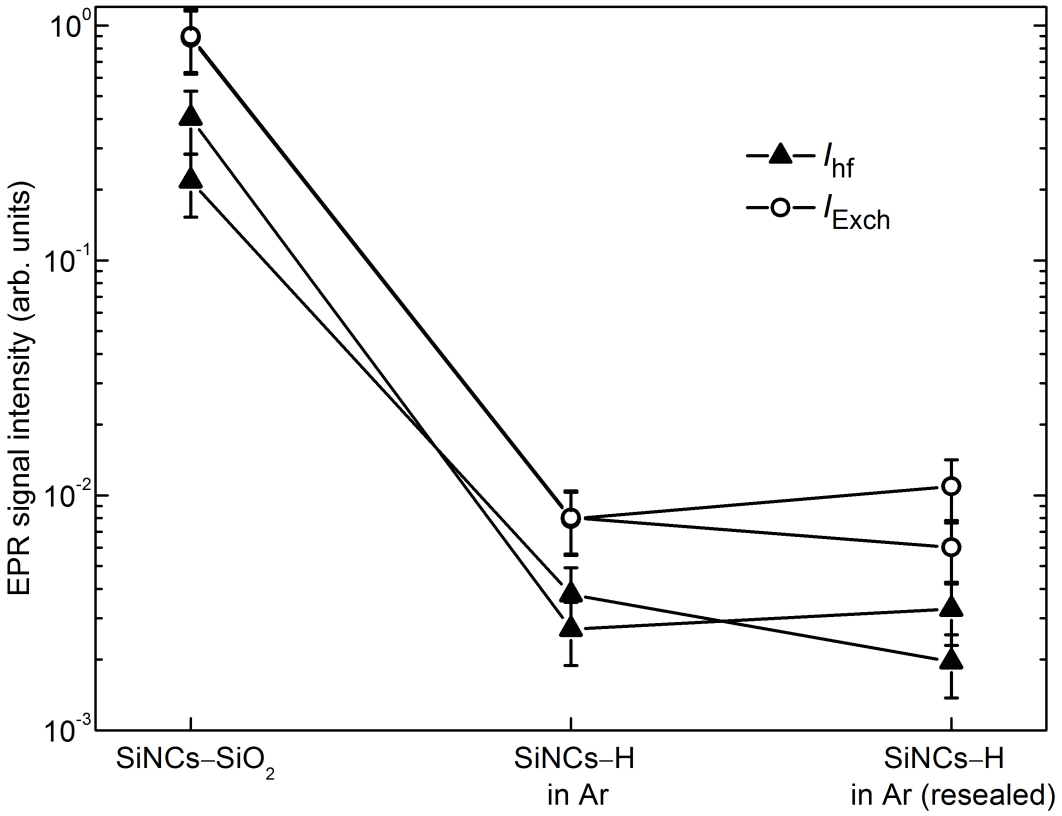

FIGURE 5.4: EPR intensity of the hf(^{31}P) signal (black squares) and of the Exch signal (black dots) observed in the samples of P-doped Si NCs in different surrounding environments.

We have also estimated the density of isolated donors in our P-doped Si NCs by comparing the intensity of the hf(^{31}P) signal (see Fig. 5.4) with that of a known spin standard consisting of a P-doped bulk crystalline Si. From this analysis, we obtained a density of isolated donors of 1.6×10^{18} cm^{-3} in SiNCs−SiO2 and of about 1.1×10^{16} cm^{-3} in SiNCs−H measured in Ar atmosphere. From the density of isolated donor electrons, we can estimate the total amount of donor electrons in our P-doped Si NCs using the statistical analysis presented in the following section.

5.2.2 Statistical distribution of dopants in nanocrystal ensembles

The distribution of dopants in NCs is governed by statistics because dopants are randomly located in different NCs of an ensemble of NCs. Due to the random location of dopants in an NC ensemble, different NCs may have different numbers of donor electrons. For an ensemble of Si NCs with a given density of donor electrons $[e^-]$, we may calculate the probability of finding η donor electrons incorporated in a NC of the ensemble by the binomial distribution:

$$W_x^{N_{\mathrm{NC}}(d_{\mathrm{NC}})}(\eta) = \binom{N_{\mathrm{NC}}(d_{\mathrm{NC}})}{N_{\mathrm{NC}}(d_{\mathrm{NC}}) - \eta} x^{\eta} \, (1-x)^{N_{\mathrm{NC}}(d_{\mathrm{NC}})-\eta} \tag{5.1}$$

where $N_{\mathrm{NC}}(d_{\mathrm{NC}}) = \pi n_{\mathrm{Si}} d_{\mathrm{NC}}^3/6$ is the number of lattice sites in the NCs, and $x = \frac{[e^-]}{n_{\mathrm{Si}}}$ is the relative concentration of donor electrons. Here, $n_{\mathrm{Si}} = 5 \times 10^{22}$ cm^{-3} is the atomic density of bulk crystalline Si. Figure 5.5(a) shows $W_x^{N_{\mathrm{NC}}(d_{\mathrm{NC}})}(\eta)$ for the cases of having 0 to 5 donor electrons in a Si NC as a function of $[e^-]$ for a Si NC diameter $d_0 = 5.0$ nm.

From the calculation of $W_x^{N_{\mathrm{NC}}(d_{\mathrm{NC}})}(\eta)$ using Eq. (5.1), we may calculate the probability p_η that a donor electron is located in a NC with n donor electrons for an NC ensemble with a given $[e^-]$ and with a size distribution $L_{d_0,\sigma}$. Here, d_0 is the average diameter and σ is the width of the diameter distribution. This may be given by

$$p_\eta(\eta, d_0, x) = \sum_{d_{\mathrm{NC}}} L_{d_0,\sigma}(d_{\mathrm{NC}}) \frac{\eta \cdot W_x^{N_{\mathrm{NC}}(d_{\mathrm{NC}})}(\eta)}{\sum_{j=1}^{\infty} j \cdot W_x^{N_{\mathrm{NC}}(d_{\mathrm{NC}})}(j)}. \tag{5.2}$$

Further, $L_{d_0,\sigma}(d_{\mathrm{NC}})$ is the size distribution of the NCs in the ensemble, which for the case of the Si NCs studied in this chapter follows a Gaussian distribution with a mean NC diameter $d_0 = 5.0$ nm and standard deviation of 1.2 nm as described in Sec. 4.1.1. From Eq. (5.1) we can calculate the ensemble density of donor clusters with n donor electrons, which is given by

$$[C_\eta] = [e^-] \times p_\eta/\eta. \tag{5.3}$$

Figure 5.7(c) shows $[C_\eta]$ as a function of $[e^-]$ for $\eta = 1$, $\eta = 2$, and $\eta \geq 2$. From the data shown in this figure, we can see that the density of isolated donor electrons $[C_1]$ that we obtain from EPR corresponds to two possibilities of $[e^-]$. However, only for the highest value of $[e^-]$ the amount of exchange coupled donors in the NCs is higher than that of isolated donors and can result in a Exch signal that is more intense than the hf(^{31}P) signal, as we observe in our EPR measurements (see Fig. 5.4). Thus, from the analysis of Fig. 5.5(b) we estimate a value of $[e^-] \approx 6 \times 10^{19}$ cm^{-3} in SiNCs–SiO_2.

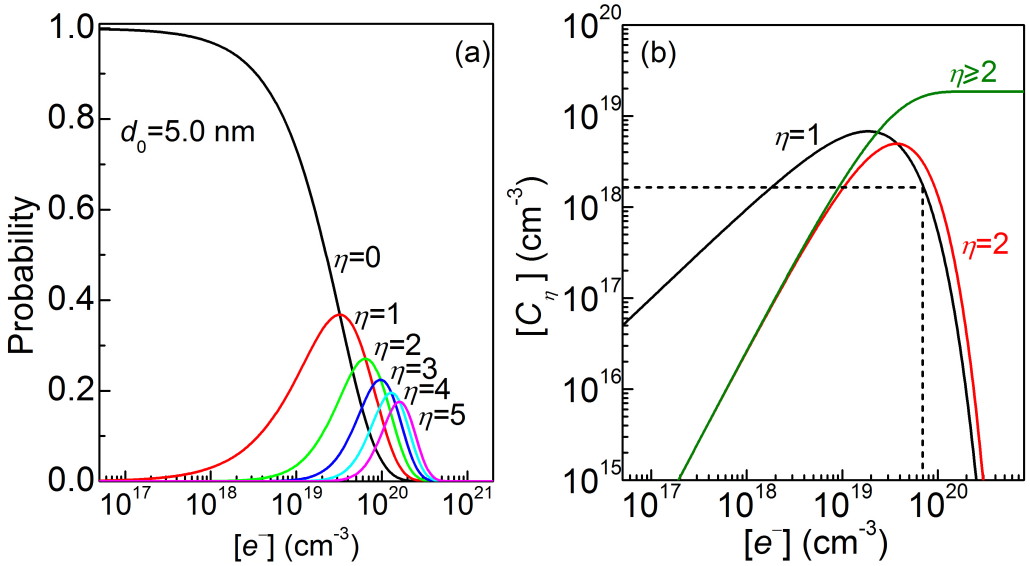

FIGURE 5.5: (a) Binomial distributions for the cases of having $0-5$ donor electrons in a Si NC with diameter of 5.0 nm. (b) Ensemble density of donor clusters with n donor electrons $[C_\eta]$ with $\eta = 1$, $\eta = 2$ and $\eta \geq 2$ as a function of the donor electron density $[e^-]$. This calculation was performed for a NC ensemble with a Gaussian size distribution with average NC size equal to 5.0 nm and $\sigma = 1.2$.

5.2.3 Estimation of doping efficiency in P-doped Si nanocrystals

Comparing the value of $[e^-] \approx 6 \times 10^{19}$ cm^{-3} obtained for SiNCs$-$SiO$_2$ and the nominal doping concentration of these Si NCs $[P]_{nom}$=2×10^{20} cm^{-3}, we infer that the electronic doping efficiency $[e^-]/[P]_{nom}$ is about 30%. This result contrasts with previously reported studies of P-doped Si NCs embedded in SiO$_2$, which estimated that the ratio between (substitutional) P donors providing electrons to the NCs CB and $[P]_{nom}$ was only 0.12% [146]. This low value for the P doping efficiency of Si NCs was proposed to result from the incorporation of P in interstitial sites of the NCs [146]. Our current study indicates that this is not the case, as will become clear below.

Photoluminescence measurements of P-doped Si NCs embedded in SiO$_2$ estimated the ratio between effective density of P dopants incorporated in the NCs $[P]_{eff}$ and the nominal concentration of P dopants $[P]_{nom}$, which corresponded to the concentration of P atoms introduced in the films used to produce the Si NCs embedded in SiO$_2$ [144]. The values of $[P]_{eff}$ were estimated from the quenching of the PL signal, associated to Si dangling bonds (Si-dbs) at the NCs surface, that was observed upon doping the NCs with P. These studies found that $[P]_{eff}/[P]_{nom}$ was about 60% for $[P]_{nom} = 3.3 \times 10^{19}$ cm^{-3} and that it decreased to about 20% as $[P]_{nom}$ was increased to 1.2×10^{20} cm^{-3} [144]. These observations were associated to the segregation of P dopants to the interface between the NCs and the surrounding matrix, which should become more significant as the P content increases. For $[P]_{nom}$ over 1.2×10^{20} cm^{-3}, it was observed that $[P]_{eff}/[P]_{nom}$ increases and reaches about 50% for $[P]_{nom} = 1.7\times10^{20}$ cm^{-3}.

It was suggested that this increase resulted from the introduction at high $[P]_{nom}$ of additional PL quenching centers associated to clusters of P dopants at the NCs interface or to matrix defects rather than from an effective increase in the amount of P dopants incorporated in the NCs [144]. Further studies on P-doped Si NCs embedded in siliconoxynitride ($SiO_{0.93}N_{0.22}$) directly assessed $[P]_{eff}$ using three-dimensional atom probe tomography [145]. These studies reported values of $[P]_{eff} = 4 \times 10^{20}$ cm^{-3} and found that about 20% of the P dopants are incorporated into the Si NCs, thus yielding $[P]_{eff} = 0.2 \cdot [P]_{nom}$. It was further shown that an amount of P atoms corresponding to 30% of $[P]_{nom}$ is located at the interface between the NCs and their surrounding matrix [145]. If we consider the incorporation efficiencies of P dopants in Si NCs embedded in SiO_2 given in Ref. [144], i.e. $20 - 60\%$, we can assume that in our NCs we have $[P]_{eff} = (0.4 \pm 0.2) \cdot [P]_{nom}$. We have $[e^-] = 0.3 \cdot [P]_{nom}$, which means that $[e^-]$ is very close to $[P]_{eff}$. This indicates that nearly all P dopants provide a donor electron, which occurs if P dopants are introduced in the NCs as substitutional impurities. We note that in Ref. [146] the amount of electrons provided by P donors in the NCs was determined by transient current analysis via measuring the voltage dependent ionized carrier density. This method only detects the fraction of donor electrons that are excited to the NCs CB and participate in the current through the NCs network. In contrast, our method detects the amount donor electrons bound to their P atoms. We should should also note at this point that in a very recent work [151], it has been proposed that P atoms may indeed be introduced in Si NCs prepared by phase segregation methods at concentrations higher than the solubility limit of P in bulk Si.

In our SiNCs−H samples measured in Ar, the P doping efficiency decreases drastically to about 0.3%, as can be seen from the decrease by two orders of magnitude of the corresponding value of I_{hf} with respect to that measured for the SiNCs−SiO_2 sample, see Fig. 5.4. Such low electronic doping efficiency is in par with that previously reported for freestanding P-doped Si NCs [6]. A reason for the low doping efficiency observed in the SiNCs−H sample may be an enhancement of charge trap states at the NCs surface upon removal of the NCs surrounding SiO_2 matrix by HF etching. These trap states may result from residual H_2O and O_2 molecules adsorbed at the NCs surface.

5.3 Temperature-dependent EPR measurements of P-doped Si nanocrystals

Figure 6.1(a) shows the X-band EPR spectra recorded for different temperatures of SiNCs−SiO_2, together with the corresponding simulated spectra. In these spectra, we can distinguish the three EPR lines associated to P donors in the Si NCs which were described in Sec. 5.1, namely the Exch line located at $g = 1.998$ (blue dashed line), and the pair of hf(^{31}P)

lines (orange dashed lines) due to the hyperfine interaction between the donor electrons and their P nucleus [23, 140]. Further, the EPR spectra of SiNCs−SiO_2 show a band with zero-

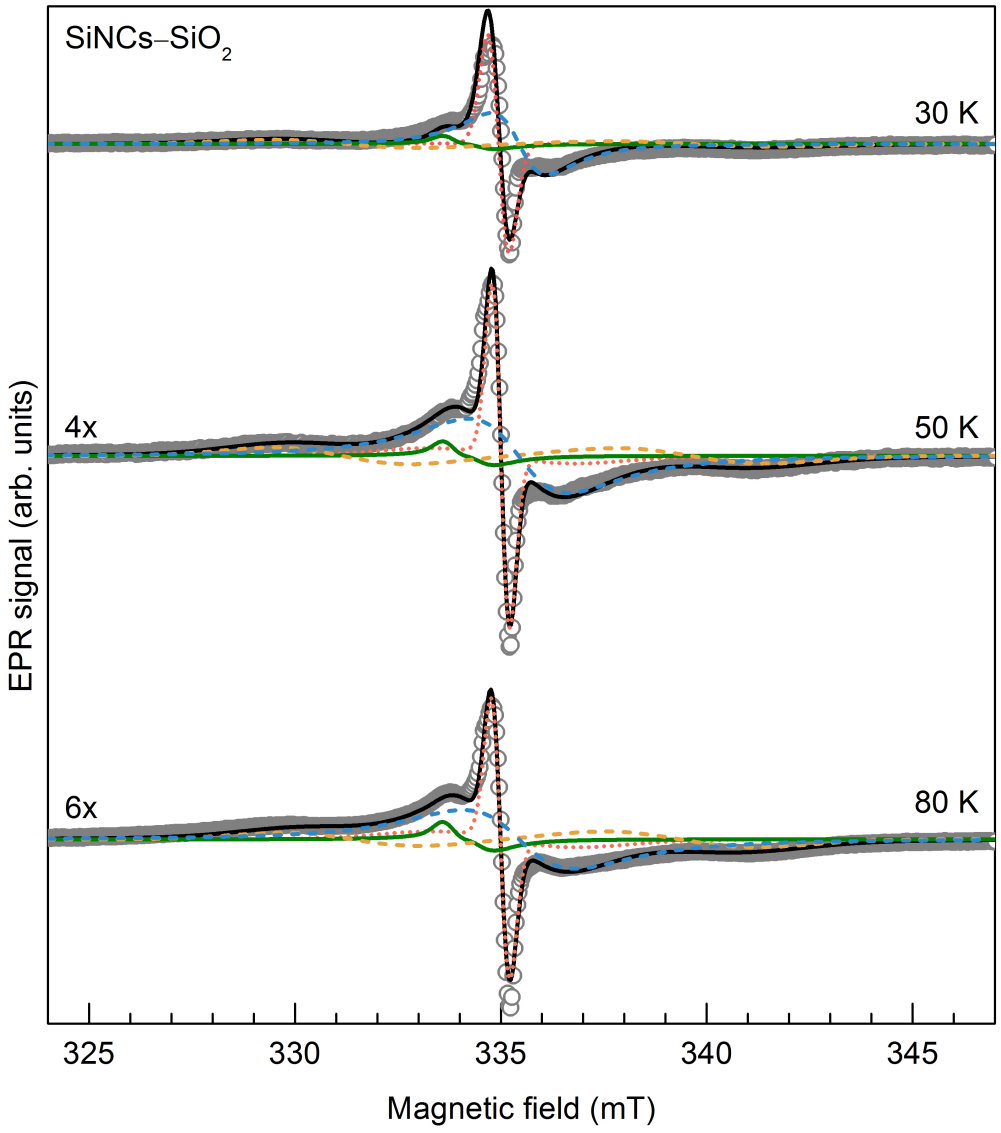

FIGURE 5.6: X-band EPR spectra for P-doped SiNCs−SiO_2 measured at various temperatures. The spectra are shown together with simulated spectra (black solid lines) which are composed of (i) a resonance at $g = 1.998$ (blue dashed lines), labelled Exch signal, (ii) a resonance at $g = 2.002$ (orange dotted lines) due to EX centers at the SiO_2 matrix surrounding the NCs, (iii) a pair of pair of hf(^{31}P lines with median at $g = 1.998$ and separated by about 10.8 mT (yellow dotted lines), and (iv) a band at $g = 2.006$ due to Si-dbs (green solid lines).

crossing magnetic field at about 334 mT (green full line) associated to Si-dbs at the NCs surface, and a sharp band at $g = 2.002$ (red dotted line) associated to EX centers located at the SiO_2 matrix.

5.3.1 Confinement of phosphorus dopants in Si nanocrystals

We have studied the dependence of the EPR intensity of the hf(^{31}P) signal (see Fig. 6.1) observed for the P-doped Si NCs on temperature T. Figure 5.7(a) shows the temperature dependence of $I_{\rm hf}$ measured for a SiNCs$-SiO_2$ sample (blue dots). There we can see that the intensity of the hf(^{31}P) signal scales as T^{-1} between 15 K and 120 K, confirming that this EPR signal displays a Curie behavior within this temperature range. From the temperature dependence of the EPR signal from isolated P donors, we can infer a lower limit for the ionization energy of isolated P donors from their bound ground state to conduction band (CB) states. At 0 K, we have a certain density $n^0_{\rm d,0}$ of donor electrons bound to their isolated P nuclei. As T increases, the donor electrons may be thermally excited to CB states and electrons populate CB states with a density n which is given by [2]

$$n^2 = \frac{N_{\rm c}}{2}\left(n^0_{\rm d,0} - n\right) e^{-E_{\rm d}/k_{\rm B}T} \tag{5.4}$$

where $N_{\rm c} = \left(2\pi m^*_{\rm Si} k_{\rm B} T/h^2\right)^{3/2}$ is the effective density of CB states, $m^*_{\rm Si} = 3(1/0.92m_0 + 2/0.19m_0)^{-1}$ is the electron effective mass and m_0 is the free-electron mass. The maximum density of electrons in the CB is $n^0_{\rm d,0}$, i.e. when all neutral P are thermally excited. Figure 5.7(b) shows $P_+ = n/n^0_{\rm d,0}$, which corresponds to the fraction of P donors that are thermally excited for different values of $E_{\rm d}$ and calculated for $T = 120$ K. In this figure, we see that the onset of P_+ occurs for $E_{\rm d} \approx 240$ meV. From this, we infer that the excitation energy of isolated P donors in P-doped Si NCs is at least 240 meV. This value of $E_{\rm d}$ is significantly higher than that required to ionize a donor electron in bulk crystalline Si (45.6 meV) [251]. Previous theoretical works have predicted that the ionization energy of a single P dopant in a H-terminated Si NC of 4 nm should be about 200 meV due to an increase in the confinement of P donors in the NCs with respect to the bulk [163]. More recent studies using density functional theory calculations predicted that a P donor in a Si NC with 1.5 nm in size and with its surface terminated with OH provides a donor state with an ionization energy of 510 meV [147]. These predictions were supported by X-ray absorption near edge structure spectroscopy measurements of P-doped Si NCs embedded in SiO_2, which were used to show that P dopants could not donate electrons in NCs with 2 to 5 nm in size [147]. Here, using temperature dependent EPR spectroscopy, we estimate a minimum value of about 240 meV for the ionization energy of P dopants in Si NCs with 5.0 nm in size, which is considerably larger than the ionization energy for P dopants in bulk Si. An increase in the dopant ionization energy with respect to that in the bulk counterpart has also been observed in P-doped Si nanowires [252]. There, it was observed that the conductivity of the nanowires decreases

with decreasing wire radius. It was further possible to estimate the dopant ionization energy in the P-doped Si nanowires from the analysis of their experimental data using a model for the size-dependent dopant ionization energy based on the dielectric mismatch between the nanowire and its surroundings [252].

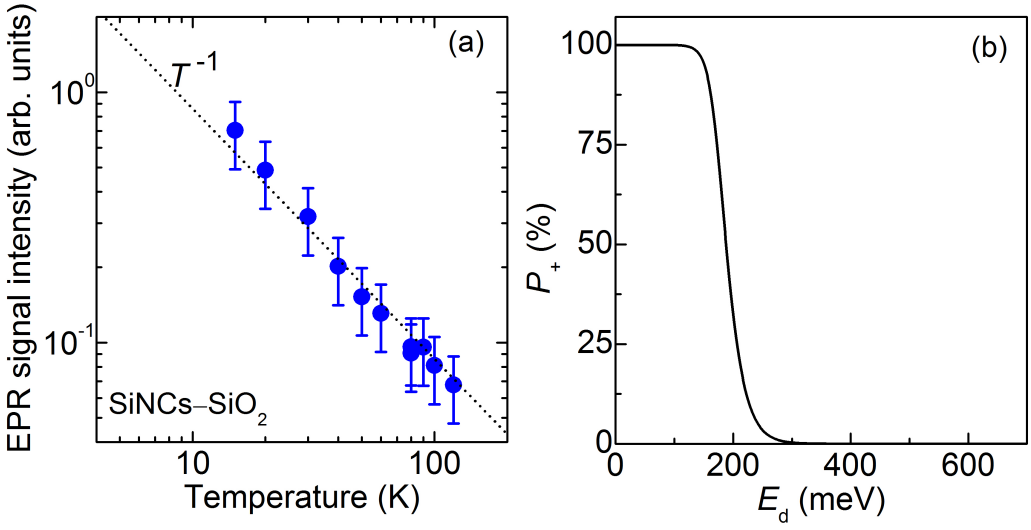

FIGURE 5.7: (a) Temperature dependence of the EPR signal intensity of the pair of hf(^{31}P) signals in SiNCs−SiO_2. (b) Dependence of the fraction of thermally excited P donors P_+ as a function of the excitation energy E_d at a temperature of 120 K.

5.3.2 Exchange interaction of phosphorus donors in Si nanocrystals

We have also studied the temperature dependence of the intensity of the Exch signal I_{Exch} observed for the P-doped Si NCs. Figure 5.8 shows the temperature dependence of I_{Exch} obtained for SiNCs−SiO_2 (red circles) and for SiNCs−H (black squares). There, we can see that, for both samples, the intensity of the Exch signal follows a Curie behavior for temperatures down to 40 K. Below 40 K, the intensity of the Exch signal deviates strongly from Curie behavior. According to the statistical calculations described in Sec. 5.2.2 for the distribution of P donor in the Si NCs studied here, we expect that the signal due to exchange coupled donor electrons results from donor clusters with η larger than 2, taking into account the relative large electron concentration estimated ($[e^-] \approx 6 \times 10^{19}$ cm^{-3}). As can be seen in Fig. 5.5, for this value of $[e^-]$ the density of donor clusters with $\eta > 2$ is much larger than the density of donor dimers, i.e. from Si NCs with only two donor electrons (donor clusters with $\eta = 2$). Therefore, the EPR signal from exchange coupled donor electrons has significant contributions from donor clusters with a wide range of η values, i.e. $\eta = 2$, 3, 4 and so on, for which the electronic structure and its temperature dependence becomes virtually impossible

to predict. However, we expect that the ground state of donor clusters with even number of electrons (η = 2, 4, 6, ...) has zero spin and, therefore, these donor clusters become EPR invisible with decreasing temperature, which is qualitatively compatible with the temperature dependence shown in Fig. 5.8.

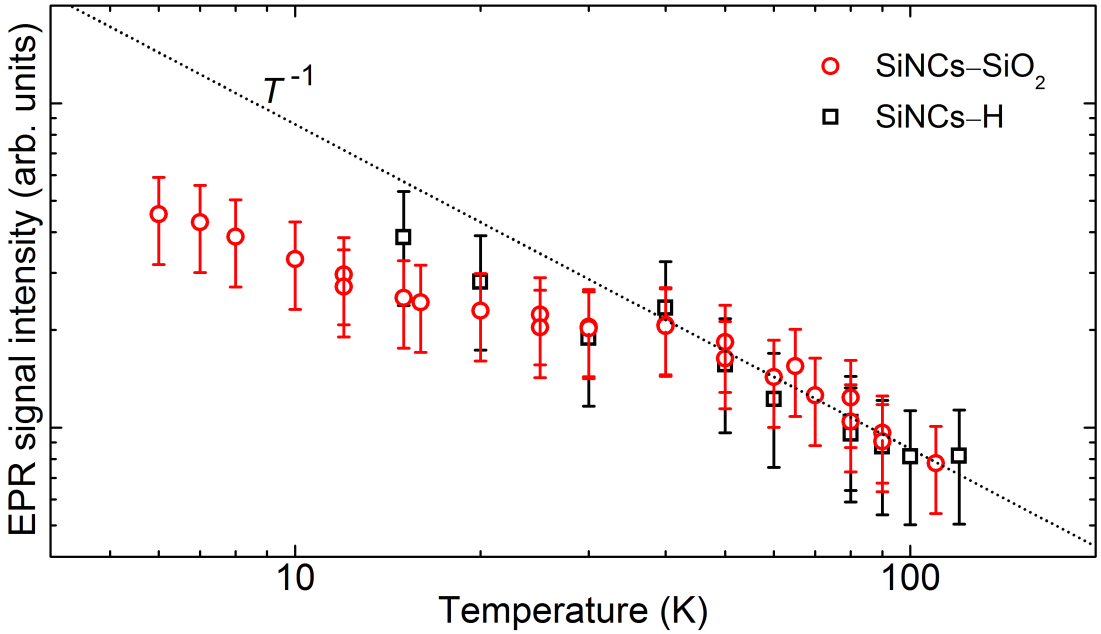

FIGURE 5.8: Temperature dependence of I_{Exch} obtained for SiNCs−SiO_2 (red circles) and for SiNCs−H (black squares).

In contrast to the case of isolated donors in NCs, the situation of having multiple donors in NCs has not been sufficiently analyzed. In part, this is due to the fact that full atomistic modeling methods of electronic structure calculation such as density-functional theory and tight-binding theory, which have been very valuable in the case of a single donor in Si-related materials, become somewhat impracticable in the case of multiple dopants in a NC. For example, density functional-theory has been successfully applied in predicting the properties of single donor and acceptor configurations in Si NCs [8,153,163,173]. Tight-binding theory has been useful in calculating the electronic properties of a single donor electron bound to a single donor impurity [253,254], or a phosphorus pair [255], located in bulk silicon close to a Si−SiO_2 interface. However, the electronic structure of multiple donor electrons in Si NCs is determined by the interdopants exchange coupling, which depends enormously on the relative location of the dopants incorporated in the NCs. Therefore, for a given number of donor electrons inside a NC, one needs to calculate all possible dopant configurations in order to take into account the statistical distribution of dopants, discussed in Sec. 5.2.2. This is a difficult task for atomistic calculation methods applied in the case of single donor electron configurations mentioned above [8, 153, 163, 173, 253–255] where the exchange energy term is not present.

This, for exchange coupled dopants systems, methods requiring less computational power need to be applied. In the following chapter, we present a theoretical framework for the exchange coupling of donors in NCs, which takes into consideration the statistical distribution of dopants in different NCs of an ensemble, and show that this framework can successfully describe the temperature dependence of the Exch signal observed by EPR.

5.4 Conclusion and Outlook

In conclusion, we have quantitatively investigated the compensation and confinement of P donors in Si NCs using EPR spectroscopy. Our analysis started by identifying the EPR signals associated to P donors in Si NCs. In par with previous studies [6,44,46], we successfully observed two EPR signals associated to P donors in Si NCs: an EPR signal at $g = 1.998$ due to exchange coupled donors in the NCs, and a pair of EPR lines with median at $g = 1.998$ and separated by about 10.8 mT that are associated to the hyperfine interaction between the spin ($S = 1/2$) of isolated donor electrons and the ^{31}P nucleus spin ($I = 1/2$).

To investigate the effect of the NCs surrounding environment on the P doping of Si NCs, we studied P-doped Si NCs embedded in SiO_2, and freestanding P-doped Si NCs with an H-terminated surface in an inert Ar atmosphere and in air. Our EPR measurements of P-doped Si NCs indicated that the NCs surrounding environment plays a major role on the doping efficiency of P-doped Si NCs. We observe that the intensities of the EPR lines associated to P donors in the Si NCs decrease by several orders of magnitude when the NCs are removed from their SiO_2 matrix and exposed to air. We associate this observation to charge compensation of P donors in the NCs by traps associated to air molecules adsorbed to the NCs surface. We show that this process can be reverted by desorbing the molecules from the NCs surface under vacuum.

We also determined the doping efficiency of P-doped Si NCs embedded in SiO_2, defined as the ratio between the concentration of donor electrons detected by EPR and the nominal concentration of P dopants introduced in the films used to grow the NCs, which we estimated to be about 30%. Comparing this result with the previously reported incorporation efficiencies of P dopants in Si NCs in the range of 20% to 40% [144, 145], we infer that most P dopants incorporated in the Si NCs that we studied occupy substitutional sites of the NCs lattice and thus behave as donors. We noted that our current result contrasts with that reported in previous studies, which estimated that only about 0.1% of the P dopants introduced in the NCs provide donor electrons [146]. We argue that the disparity between the two results comes from the fact that the experimental technique used in Ref. [146] to quantify the amount of donor electrons in the NCs only enables the detection of the fraction of donor electrons that are excited to the NCs conduction band. In contrast, EPR detects the amount of donor

electrons bound to their P atoms.

We further investigated the temperature dependence of the EPR spectra of P-doped Si NCs. From the temperature dependence of the intensity of the pair of hyperfine lines observed in our EPR spectra, we could assess the confinement of P donors in Si NCs embedded in a SiO_2 matrix. From this, we provide experimental evidence for the predictions made with *ab-initio* calculations, according to which confinement induces an increase in the ionization energy of dopants with decreasing NC size. Moreover, we investigated the temperature dependence of the EPR signal associated to exchange coupled donor electrons in Si NCs. We observed that the intensity of this signal deviates from Curie behavior at low temperatures, which indicates that the amount of spins contributing to the EPR signal due to exchange coupled donors in the NCs quenches at low temperatures. Previous studies have reported similar temperature dependences of the EPR signal due to exchange coupled donors in Si NCs [6, 142,182]. However, the origin of this behavior has remained unexplained. One reason for this comes from the difficulty in using computational simulations based on *ab-initio* methods to predict the behavior of multiple donors in NCs. These methods become impractical in the case of multiple donors in NCs where the statistical distribution of donors in the NCs must be taken into consideration. In the following chapter, we will present a theoretical framework for the exchange coupling of donors in Si NCs, which is based on effective mass approximation and which takes into consideration the random location of donors in NCs. Further, we will show that this method successfully describes the temperature dependence of the EPR signal due to exchange coupled donors under a particular condition (dimers) in Si NCs.

Chapter 6

Interdopant interactions in doped nanocrystals

Dopants in a NC are both confined in a smaller volume than in the bulk counterpart, and are also isolated from dopants in neighboring NCs. This strongly affects the coupling between dopants. In bulk semiconductors, the interactions between multiple dopants result in closely spaced impurity states that develop into an impurity subband near the respective intrinsic band edge [181]. For instance, for P in bulk silicon this impurity subband occurs for doping concentrations above 3.7×10^{18} cm^{-3} [256] and for Ga in bulk Ge occurs for concentrations $>1.8\times10^{17}$ cm^{-3} [257]. For NCs with diameter smaller than 5 nm, at such doping concentrations each NC contains statistically either a single dopant or a pair of dopants with very few exceptions. Therefore, it is expected a very different behavior for NCs with doping concentration in the range at which doping results in an impurity subband in the bulk. For heavily doped NCs, interdopant interactions are essentially limited to those taking place between only a few dopants. This should yield discrete electronic levels in a doped NC and the above mentioned impurity subband model becomes unrealistic. In this chapter, we investigate the electronic structure arising when multiple dopants are incorporated in a single NC, using EPR spectroscopy and ensembles of P-doped Si NCs. In particular, we investigate the exchange coupling between two donor electrons incorporated in a NC.

In the first section of this chapter, we present temperature-dependent Q-band EPR measurements of P-doped Si NCs. We show that Q-band EPR measurements enable a better discrimination of the EPR signal at $g = 1.998$ associated to exchange coupled donors in the P-doped Si NCs. We further monitor the singlet-triplet transition of the exchange coupled donors via the temperature-dependence of the intensity of the $g = 1.998$ signal. We show that this dependence deviates from Curie behavior at low temperatures. In Sec. 6.2, we present the theoretical framework that we used to describe the temperature-dependence of the intensity of the EPR signal at $g = 1.998$. This framework is based on the exchange coupling between pairs of donor electrons (donor dimers) in the P-doped Si NCs. We describe the electronic structure of donor dimers in Si NCs and find that the deviation of the intensity of the EPR signal at $g = 1.998$ from Curie behavior depends on the magnitude of the exchange coupling of the donor dimers. We then quantitatively describe the temperature-dependence of the intensity of the $g = 1.998$ signal and find that our EPR data can be very well described by a model considering the exchange coupling between donor dimers in P-doped Si NCs. We show

that this coupling can be described by effective mass theory, which allow the consideration of the random location of dopants in different NCs of an ensemble of NCs. We perform computational simulations of the exchange coupling energy between donor dimers in NCs and find that this energy differs by up to three orders of magnitude depending on the specific location of donors in a NC.

In the final section of this chapter, we use the theoretical framework for donor dimers in Si NCs to estimate the temperature-dependence of the intensity of the EPR signal at $g = 1.998$ for a range of NC sizes between 1 nm and 10 nm. We start by investigating the conditions of NC size and doping concentration for the dominance of donor dimers in ensembles of NCs and determine if the P-doped Si NCs used in this investigation satisfy these conditions. Our calculations of the temperature-dependence of the intensity of the $g = 1.998$ signal show a quenching for all the NCs sizes investigated, which is more pronounced for smaller NCs. We further predict that in NCs smaller than ∼2.5 nm, the quantization of the distribution of exchange energies in a NC ensemble yields a step-like behavior in the temperature-dependence of the intensity of the EPR signal at $g = 1.998$. We discuss these results in the light of experiments on P-doped Si NCs reported in the literature.

For the investigations conducted in this chapter, we used freestanding P-doped Si NCs grown by the gas phase method described in Sec. 4.1.1, with a mean diameter of 3.9 nm obtained from BET analysis and a lognormal size distribution with standard deviation of $\sigma = 1.3$ [see Sec. 4.1.1] and with $[\mathrm{P}]_{\mathrm{nom}} = 5 \times 10^{20}$ cm^{-3}.

6.1 Temperature-dependent EPR data

Figure 6.1(a) shows the Q-band ($\nu \approx 34$ GHz) EPR spectra recorded at different temperatures for P-doped Si NCs. In these spectra, we can distinguish the Exch signal located at $g = 1.998$ due to exchange coupled donor electrons in the P-doped Si NCs, superimposed to a background signal due to surface Si-dbs. The Q-band EPR spectra of P-doped Si NCs are obtained using relatively high microwave powers, which causes the Si-dbs band to be recorded in the strong saturation condition of rapid passage, resulting in a nonderivative signal (with positive or negative sign) rather than the usual first-derivative shape of unsaturated EPR lines. These experimental conditions enabled a better discrimination of the Exch signal with respect to the Si-dbs band. A low-microwave-power spectrum where the Si-dbs band is recorded in nonsaturation condition is shown in Fig. 6.1(b). At this microwave power, the Exch signal is too small to be visible. In Fig. 6.1, the spectra are compared with the corresponding fits. In Fig. 6.1(a), the shape of the experimental Exch signal was approximated to a sum of two first-derivative Lorentzian lines, with which we could reproduce the line asymmetry observed at the lower T values [6]. As can be seen in Fig. 6.1(a), a good fit to the spectra

is obtained. In Fig. 6.1(b), the Si-dbs band was approximated by a sum of two components, as considered in previous studies [6]. One component, shown in Fig. 6.1(b) as a dotted line, is due to (111)-oriented trivalent Si atoms at the interface between the crystalline core of the Si NCs and their native SiO_2 shell, so-called P_b centers [258,259]. The other signal, shown in Fig. 6.1(b) as a dashed line, is located at $g = 2.0055$ as is typically observed in amorphous and polycrystalline Si and in Si-rich SiO_x [260,261]. In the case of Si NCs, this signal has been attributed to D states located close to the NCs surface [6].

Figure 6.2 shows the dependence of the Exch signal intensity I_{Exch} on T, as computed by

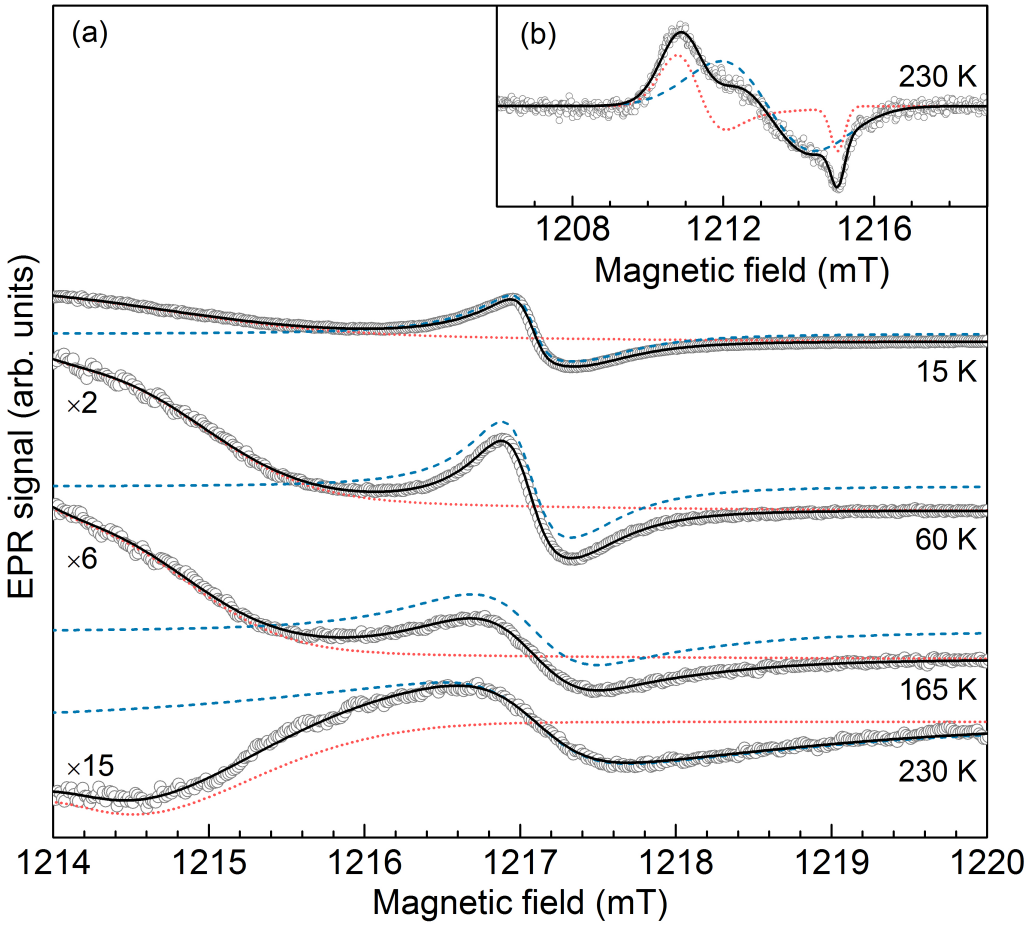

FIGURE 6.1: (a) Q-band EPR spectra measured at T indicated (open dots), together with simulated spectra (solid lines) composed of a resonance at $g = 1.998$ (dashed lines), labeled Exch signal, superimposed to a background (dotted lines). (b) Q-band EPR spectrum recorded under nonsaturation conditions for the Si-dbs signal and simulated spectrum (solid line) with the P_b (dotted line) and D (dashed line) components considered in previous studies [6].

by numerical double integration of the Exch signal obtained from the fits [dashed blue lines in Fig. 6.1(a) and (b)]. In the spectra used to extract I_{Exch} [some of which are shown in Fig. 6.1] the Exch signal was always recorded under nonsaturation conditions, as conscientiously checked with microwave power series experiments. The dependence of I_{Exch} on T strongly deviates from the Curie paramagnetism scaling with T^{-1} [dash-dotted line in Fig. 6.2]. This deviation of I_{Exch} from T^{-1} becomes evident for values of T below ∼100 K. As will become clear in the following sections of this chapter, the deviation of I_{Exch} from Curie behavior observed in P-doped Si NCs should result from the exchange interaction between pairs of donor electrons (donor dimers) in the P-doped Si NCs.

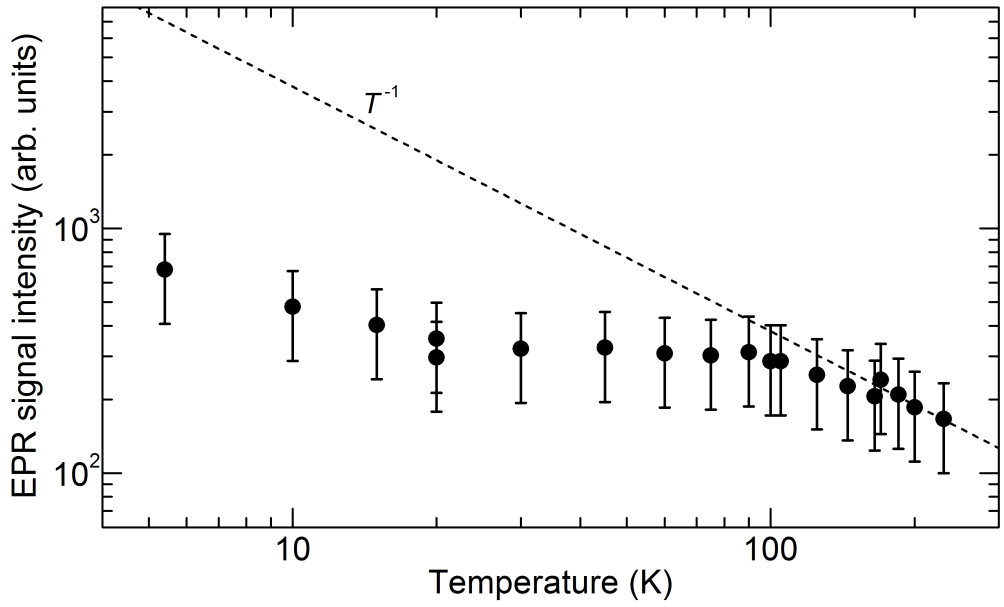

FIGURE 6.2: Temperature dependence of I_{Exch} for P-doped Si NCs.

6.2 Theoretical framework for exchange coupled donor dimers in nanocrystals

To understand the EPR data on P-doped Si NCs presented above, we need to evaluate the effect of the interaction between electrons coupled by exchange interaction to the intensity of the Exch signal. In this section, we make a theoretical overview of the exchange interaction model that we use to describe the interaction between donor electrons in Si NCs for which

the occurrence of pairs is dominant over the occurrence of larger clusters of donors in a single NC. We describe the electronic structure of donor dimers in Si NCs and find that the deviation of the intensity of the EPR signal at $g = 1.998$ from Curie behavior depends on the magnitude of the exchange coupling of the donor dimers. We then quantitatively describe the temperature-dependence of the Exch signal using a model that considers the exchange coupling of donor dimers in P-doped Si NCs that considers the random location of dopants in different NCs on an NC ensemble. We further describe our computational simulations of the exchange coupling energy between donor dimers in NCs.

6.2.1 Statistical distribution of donors in Si nanocrystals

The P-doped Si NCs whose dependence of I_{Exch} on T is shown in Fig. 6.2 have $[\mathrm{P}]_{\mathrm{nom}} = 5 \times 10^{20}$ cm^{-3}. Taking into account the segregation of 95% of the P dopants to the surface region where the native oxide shell is formed [6] (see Sec. 2.1.4), the effective concentration of P donors in the NCs is $[\mathrm{P}]_{\mathrm{eff}} = 2.5 \times 10^{19}$ cm^{-3}. Moreover, previous studies showed that the concentration of donor electrons $[e^-]$ in Si NCs grown by gas phase method is not equal to $[\mathrm{P}]_{\mathrm{eff}}$ due to charge compensation induced by defects at the NCs surface in the form of Si-dbs [6]. These defects provide energy levels within the NCs energy gap below the P donor energy levels. Thus, donor electrons tend to become trapped at the defect levels. This effect leads to a decrease in $[e^-]$ with respect to $[\mathrm{P}]_{\mathrm{eff}}$. Stegner *et al.* developed a statistical calculation for the effect of doping compensation by Si-dbs based on the binomial distribution of P donors and Si-dbs, where the average concentration of Si-dbs is considered to be [Si-db]$= 5.3 \times 10^{11}$ cm^{-3} [6]. We used this statistical distribution to calculate the number of electronically active donor electrons inside our Si NCs, which is given by

$$N_{\mathrm{spins}} = \sum_{j=N_{\mathrm{min}}}^{\infty} \sum_{i=0}^{j-N_{\mathrm{min}}} \left[(j-i) W_{p_{\mathrm{P}}}^{N_{\mathrm{NC}}}(j) W_{p_{\mathrm{db}}}^{S_{\mathrm{NC}}}(i) \right] \tag{6.1}$$

where $W_{p_{\mathrm{P}}}^{N_{\mathrm{NC}}}$ is the binomial probability of finding j P donors in a Si NC with $N_{\mathrm{NC}} = \pi/6 d_{\mathrm{NC}}^3 \cdot n_{\mathrm{Si}}$ lattice sites and p_{P} is the probability of a lattice site to be occupied by P. Similarly, $W_{p_{\mathrm{db}}}^{S_{\mathrm{NC}}}$ is the binomial probability of finding i defects in a Si NC with a surface area $S_{\mathrm{NC}} = \pi d_{\mathrm{NC}}^2$ and a probability p_{db} of finding one Si-db per unit area being given by [Si-db]$\cdot \rho_{\mathrm{Si}}$, where ρ_{Si} is the average Si surface density. As the Exch signal arises from the interaction between donor electrons, the calculation of Eq. (6.1) was performed for at least two P donors in the NC ($N_{\mathrm{min}} = 2$). From the calculation of Eq. (6.1), we can determine $[e^-]$ as $[e^-] = \frac{N_{\mathrm{spins}}}{N_{\mathrm{NC}}} n_{\mathrm{Si}}$. Thus, by considering the compensation of P donors by Si-dbs, the value of $[\mathrm{P}]_{\mathrm{eff}} = 2.5 \times 10^{20}$ cm^{-3} in our P-doped Si NCs is reduced to $[e]^- = 1.4 \times 10^{19}$ cm^{-3}.

From the concentration of donor electrons in P-doped Si NCs $[e^-]$, we can calculate the concentration of donor electron clusters with η electrons $[C_\eta]$ using Eq. (5.3). Fig. 6.3 shows $[C_\eta]$, with $\eta = 1$ (single donors), $\eta = 2$ (donor dimers), and $\eta = 3$, as a function

of $[e^-]$ for $d_0 = 3.9$ nm. There, we see that for situations with $[e^-] \leq 2 \times 10^{19}$ cm^{-3} the density of donor clusters with $\eta \geq 3$ is much smaller than that of single donors and donor dimers. Thus, the EPR spectrum from donor electrons in our P-doped Si NCs with $[e^-] = 1.4 \times 10^{19}$ cm^{-3} should be fully dominated by the spectral contributions from single donors and donor dimers. Specifically, the temperature dependence of I_{Exch} should be fully dominated by the contribution from donor dimers.

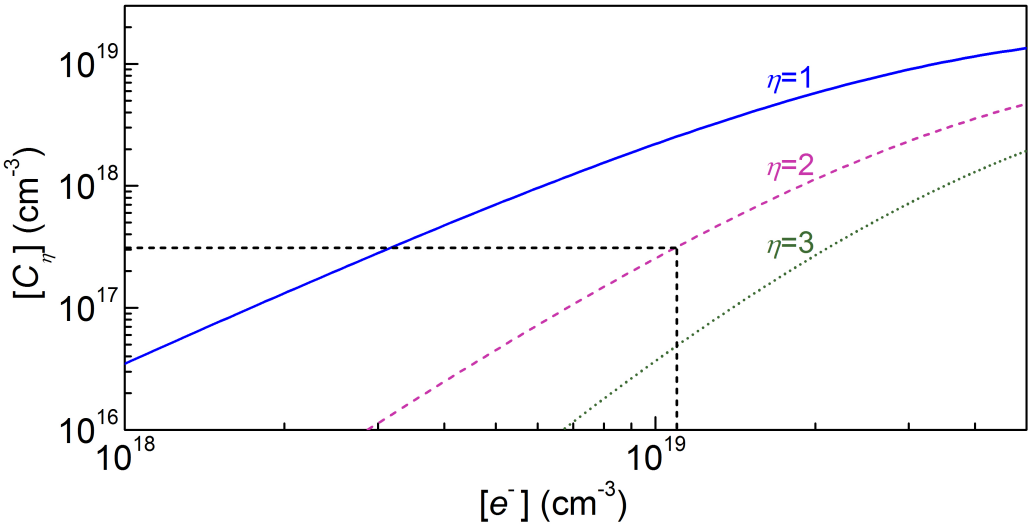

FIGURE 6.3: Concentration of clusters of η donor electrons $[C_\eta]$, with $\eta = 1$ (solid line), $\eta = 2$ (dashed line), and $\eta = 3$ (dotted line), as a function of $[e^-]$ for $d_0 = 3.9$ nm.

6.2.2 Electronic structure of donors in nanocrystals

Single P donors in Si NCs can be described by the effective spin Hamiltonian given by Eq. (3.7) and the corresponding energy level scheme is shown in Fig. 6.4(a). Single donors in Si NCs, from P in Si NCs, would lead to a doublet of hyperfine split lines located at the resonant magnetic fields $B_{a,b} = (h\nu \pm A_{\mathrm{NC}}/2)/(g\beta_e)$, due to transitions a and b in Fig. 6.4(a) [7,44,46]. The nanocrystal hyperfine constant A_{NC} deviates from the bulk value $A_{\mathrm{bulk}} = 4.16$ mT found in bulk Si along a power law dependence [46]

$$A_{\mathrm{NC}} = A_{\mathrm{bulk}} + (\rho/d_{\mathrm{NC}})^{\tau} \tag{6.2}$$

with $\rho = 16.3$ nm and $\tau = 1.6$. The difference between the EPR signal expected for single P donors in Si NCs and the observed Exch signal shows why the later cannot be due to single donors.

To take into consideration the exchange interaction of donor dimers in Si NCs, we consider

the following effective spin hamiltonian [23]:

$$\hat{\mathbf{H}}_{\text{dimer}} = g\beta_e \mathbf{B}\left(\hat{\mathbf{S}}_\mathbf{1} + \hat{\mathbf{S}}_\mathbf{2}\right) + \mathbf{A}\left(\hat{\mathbf{I}}_\mathbf{1}\cdot\hat{\mathbf{S}}_\mathbf{1} + \hat{\mathbf{I}}_\mathbf{2}\cdot\hat{\mathbf{S}}_\mathbf{2}\right) + \mathbf{J}\left(\hat{\mathbf{S}}_\mathbf{1}\cdot\hat{\mathbf{S}}_\mathbf{2}\right) \tag{6.3}$$

where where $\hat{\mathbf{S}}$ and $\hat{\mathbf{I}}$ represent the electron and nuclear spin operators, respectively, and J is the exchange interaction constant. Here, we use the spin state eigenvalues and spin transitions considered by Cullis and Marko (Ref. [23]) for a Hamiltonian like the one in (6.3). The corresponding energy level scheme is shown in Fig. 6.4(b), together with the allowed magnetic resonance transitions $a - d$. The eigenstates are a combination of the states of two coupled nucleus spins with $I = 1/2$, i.e. three symmetric triplet states $|t_{\pm1,0}\rangle$ and an asymmetric singlet state $|s\rangle$ [262], and the singlet $|S\rangle$ and triplet $|T_{\pm1,0}\rangle$ electron-spin states of an electron pair. The eigenenergies of the triplet states $E_T^{0,\pm1}$, and of the singlet states E_S are given by

$$E_T^{0,\pm1} = g\beta_e BM + \frac{1}{2}A_{\text{NC}}M(m_1 + m_2) + \frac{1}{4}J \tag{6.4}$$

$$E_S = -\frac{3}{4}J \tag{6.5}$$

where the quantum number m_i is the electronic spin of the ith donor in the dimer, and M is the z component of the total electronic spin of the donor dimer. Table 6.1 shows the relative transition probability ΔG and transition energies E of transitions a to d indicated in the energy level scheme displayed in Fig. 6.4(b).

TABLE 6.1: Allowed donor pair transitions in P-doped Si NCs. Here, we consider $\nu_e = g\beta_e B$.

Transition	States involved	Relative transition probability (ΔG)	Transition energy E (J)
a	$\|T_{-1}, t_{-1}\rangle \leftrightarrow \|T_0, t_{-1}\rangle$	1	$\nu_e - \frac{1}{2}A_{\text{NC}}$
	$\|T_0, t_{-1}\rangle \leftrightarrow \|T_1, t_{-1}\rangle$	1	$\nu_e - \frac{1}{2}A_{\text{NC}}$
b	$\|T_{-1}, t_1\rangle \leftrightarrow \|T_0, t_1\rangle$	1	$\nu_e + \frac{1}{2}A_{\text{NC}}$
	$\|T_0, t_1\rangle \leftrightarrow \|T_1, t_1\rangle$	1	$\nu_e + \frac{1}{2}A_{\text{NC}}$
c	$\|T_{-1}, s\rangle \leftrightarrow \|T_0, s\rangle$	$\frac{1}{2}\left[1 + J(J^2 + A^2)^{-1/2}\right]$	$\nu_e + \frac{1}{2}(J^2 + A^2)^{1/2} - \frac{1}{2}J$
	$\|T_{-1}, t_0\rangle \leftrightarrow \|T_0, t_0\rangle$	$\frac{1}{2}\left[1 + J(J^2 + A^2)^{-1/2}\right]$	$\nu_e + \frac{1}{2}(J^2 + A^2)^{1/2} - \frac{1}{2}J$
d	$\|T_0, s\rangle \leftrightarrow \|T_1, s\rangle$	$\frac{1}{2}\left[1 + J(J^2 + A^2)^{-1/2}\right]$	$\nu_e - \frac{1}{2}(J^2 + A^2)^{1/2} + \frac{1}{2}J$
	$\|T_0, t_0\rangle \leftrightarrow \|T_1, t_0\rangle$	$\frac{1}{2}\left[1 + J(J^2 + A^2)^{-1/2}\right]$	$\nu_e - \frac{1}{2}(J^2 + A^2)^{1/2} + \frac{1}{2}J$

The ground state of the donor dimer is a singlet $S = 0$. The EPR active triplet states ($S = 1$) can be thermally populated. The EPR spectrum due to transitions within the triplet

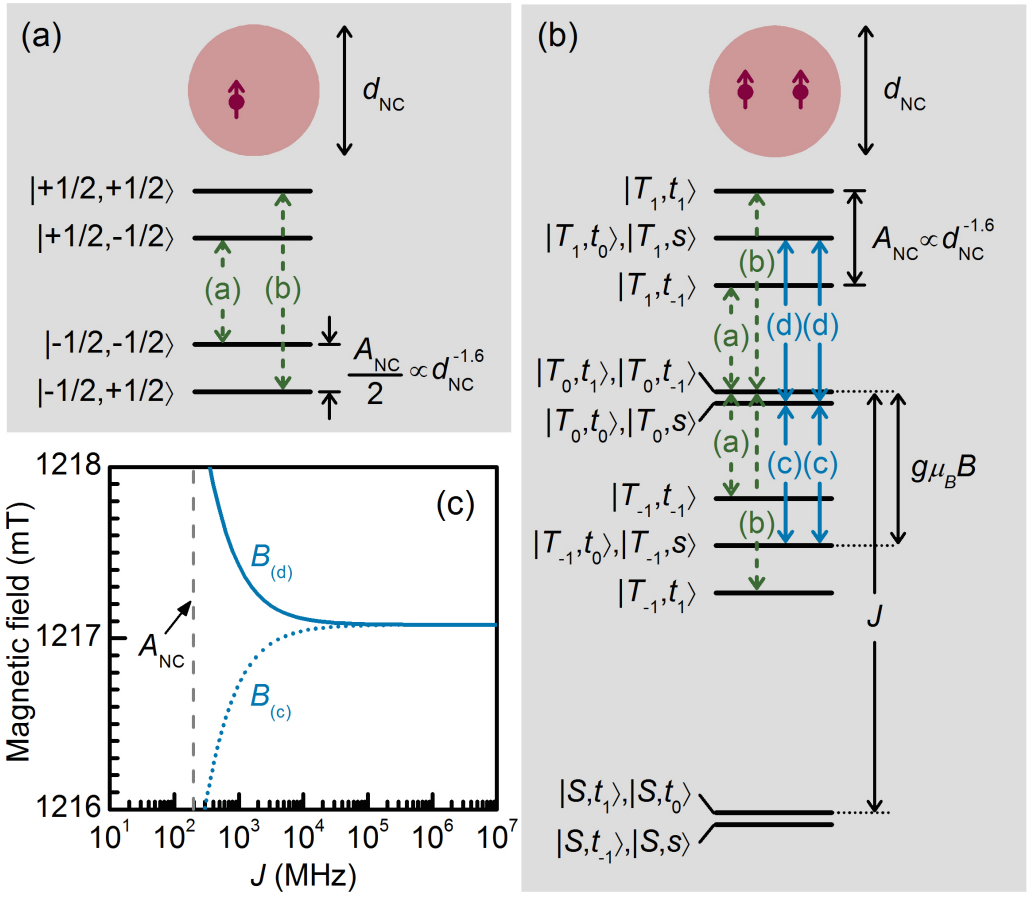

FIGURE 6.4: Energy level scheme for (a) single donors and (b) donor dimers in Si NCs. The first and second quantum numbers of the eigenstates in (a) correspond to electron and nuclear spins, respectively. The eigenstates in (b) are labeled according to the strongly coupled pair states of the limit $J \gg A_{NC}$ [22]. (c) Dependence of the resonant magnetic fields of transitions c and d on the exchange coupling.

states of the dimer is expected to be composed of two sets of resonances: (i) a doublet of lines due to transitions a and b in Fig. 6.4(b), with the same spectral location as the hyperfine doublet of single donors mentioned above, and (ii) resonances associated with transitions c and d in Fig. 6.4(b), with resonant magnetic fields [22]

$$B_{c,d} = \frac{h\nu \mp 1/2\left(J^2 + A_{NC}^2\right)^{1/2} \pm J/2}{g\beta_e} \tag{6.6}$$

Figure 6.4(c) shows the dependence of the magnetic field position of resonances c and d as a function of J for $\nu = 34$ GHz. For sufficiently large J ($J \gg A_{NC}$) [22], the T_0 states are degenerate, and transitions c and d occur at the same magnetic field $B_{c,d} = (h\nu)/(g\beta_e)$. As shall be clear below, the Exch signal observed in our EPR spectra corresponds to these transitions.

We note that the hyperfine doublet lines, from either single donors or donor dimers, are absent from the EPR spectra of P-doped Si NCs grown by gas phase method (see Fig. 6.1), but could be observed in the spectra of P-doped Si NCs grown by phase segregation method (see Fig. 5.6). One reason for this may come from the fact that the P-doped Si NCs grown by gas phase method show a lognormal distribution of NC sizes that is relatively broader than the distribution of NC sizes in the NCs grown by phase segregation method, as can be see in Fig. 6.5, which shows the size distributions for ensembles of Si NCs with a mean diameter of 3.9 nm, grown by the phase segregation method and by the gas phase method. As discussed in Sec. 6.2.2, A_{NC} is proportional to $d_{\mathrm{NC}}^{-1.6}$ [7]. Thus, we associate the absence of the hyperfine line in our conventional EPR spectra of P-doped Si NCs grown by gas phase method to a line broadening induced by the dependence of A_{NC} on d_{NC}. Nonetheless, the hyperfine lines in the P-doped Si NCs grown by gas phase method could be observed in previous studies by means of more sensitive electrically detected EPR techniques [7, 44].

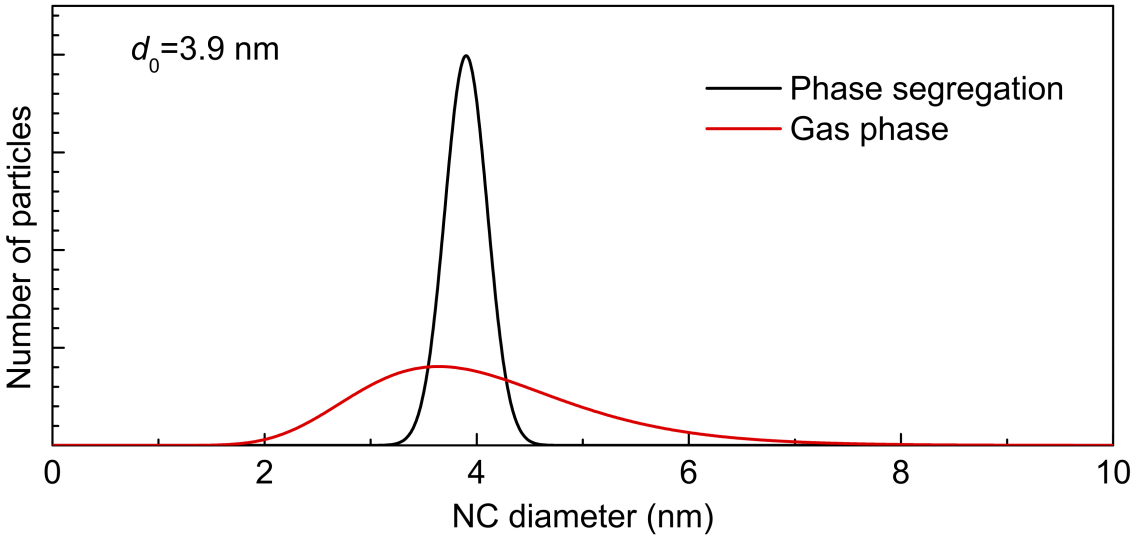

FIGURE 6.5: Size distributions of P-doped Si NCs ensembles with mean diameter d_0 = 3.9 nm, produced by the phase segregation method (black line) and by the gas phase method (red line).

As described above, the amount of dimers thermally excited to triplet states and thus visible by EPR depends on the magnitude of the exchange interaction energy J. In the following, we present the methodology that we used to calculate J for donor dimers in P-doped Si NCs.

6.2.3 Calculation of the exchange interaction energy

To describe the temperature dependence of I_{Exch} associated with the thermal population of the triplet state of donor dimers in Si NCs, we need to calculate the exchange interaction

energy J. To do so, we adopt an expression developed for donor dimers in bulk Si [23], which assumes that each donor wave function is described by the hydrogenic model. However, we introduce modifications appropriate for NCs, which are described below. The equation we use for the exchange energy is

$$\begin{aligned} J(\mathbf{R}) = \frac{1}{4\pi\epsilon_0}\frac{e^2}{\epsilon_{\text{bulk}} a^*_{\text{bulk}}}\left(\sum_{j=1,2,3}\cos\left(\mathbf{k}_j\cdot\mathbf{R}\right)\right)^2 \times \left\{\frac{2}{9}(1+D)\left(1+D+\frac{1}{3}D^2\right)e^{-2D}\right. \\ -\frac{1}{45}\left[\left(\frac{25}{8}+\frac{23}{4}D-3D^2-\frac{1}{3}D^3\right)+\frac{6}{D}\left(1+D+\frac{1}{3}D^2\right)^2(\gamma+\ln D)\right]e^{-2D} \\ \left.-\left[\left(1-D+\frac{1}{3}D^2\right)F(-4D)e^{2D}+2\left(1+D+\frac{1}{3}D^2\right)\left(1-D+\frac{1}{3}D^2\right)F(-2D)\right]\right\}. \end{aligned} \tag{6.7}$$

Here, $\mathbf{R}$ is the separation vector between the two donors of the dimer, $D = |\mathbf{R}|/a^*_{\text{NC}}$, ϵ_0 is the vacuum permittivity, $\gamma = 0.57722$, $F(-y) = \int_y^\infty e^{-z}/z dz$, and $\mathbf{k}_j = 0.85 k_{j,\max}$ are the values of the wave vectors at the conduction band minima in the three mutually perpendicular [100] directions, with $|\mathbf{k}_{j,\max}| = a/\pi$ and $a = 5.43$ Å the Si lattice parameter. For Si NCs, we have to take into account the NC size-dependent Coulomb screening governing the hydrogenic dopant state, which results in a size dependent donor electron wave function localization [7]. To do so, we consider a size-dependent dielectric screening constant ϵ_{NC} parameterized by using a generalization of the Penn model $\epsilon_{\text{NC}}(d_{\text{NC}}) = 1+(\epsilon_{\text{bulk}}-1)/[1+(\alpha/d\text{NC})^l]$ [175–178], with $\alpha = 1.94$ nm and $l = 1.3$ as considered previously in describing the confinement of single donors in NCs [7, 178]. In Eq. (6.7), a^*_{NC} is the effective Bohr radius of a donor electron in the NC $a^*_{\text{NC}} = a_0 \times \epsilon_{\text{NC}} \times m_0/m^*$ [7], where a_0 is the hydrogen Bohr radius, m_0 is the free-electron mass, and $m^* = 3(1/0.92m_0 + 2/0.19m_0)^{-1}$ is the electron effective mass. In our calculations, we considered all possible dimer configurations $\mathbf{R}$ in a spherical NC and calculated explicitly the corresponding values of J from Eq. (6.7). The result of such calculations are the distributions of $|\mathbf{R}|$ and of J, which we denote $N(|\mathbf{R}|)$ and $N(J)$, respectively.

Cullis and Marko performed their calculations for P donors in bulk Si considering relatively low doping concentrations ($< 7\times10^{16}$ donor/cm^3) [23]. These conditions allowed them to neglect interactions between more than two donors and also to use a radial probability distribution which takes advantage of the symmetries given by the bulk nature of the crystal. We have repeated their calculations of $N(J)$ for bulk silicon using our method, which considers all possible configurations of the donor dimers in the crystal, in order to verify the correctness of our own calculation of Eq.(6.7). We used a crystal with a size of 600 nm which is large enough to be considered as a bulk crystal and thus allow us to use the equation of J used by Cullis and Marko [23]. Figure 6.6 compares our results for bulk Si with the data of Ref. [23] and shows that we were able to reproduce the results of Cullis and Marko quite well.

Figure 6.7 shows the distributions $N(|\mathbf{R}|)$ and $N(J)$ that we calculate for a NC ensemble with mean diameter $d_0 = 3.9$ nm and a lognormal size distribution given by Eq. (4.3), with

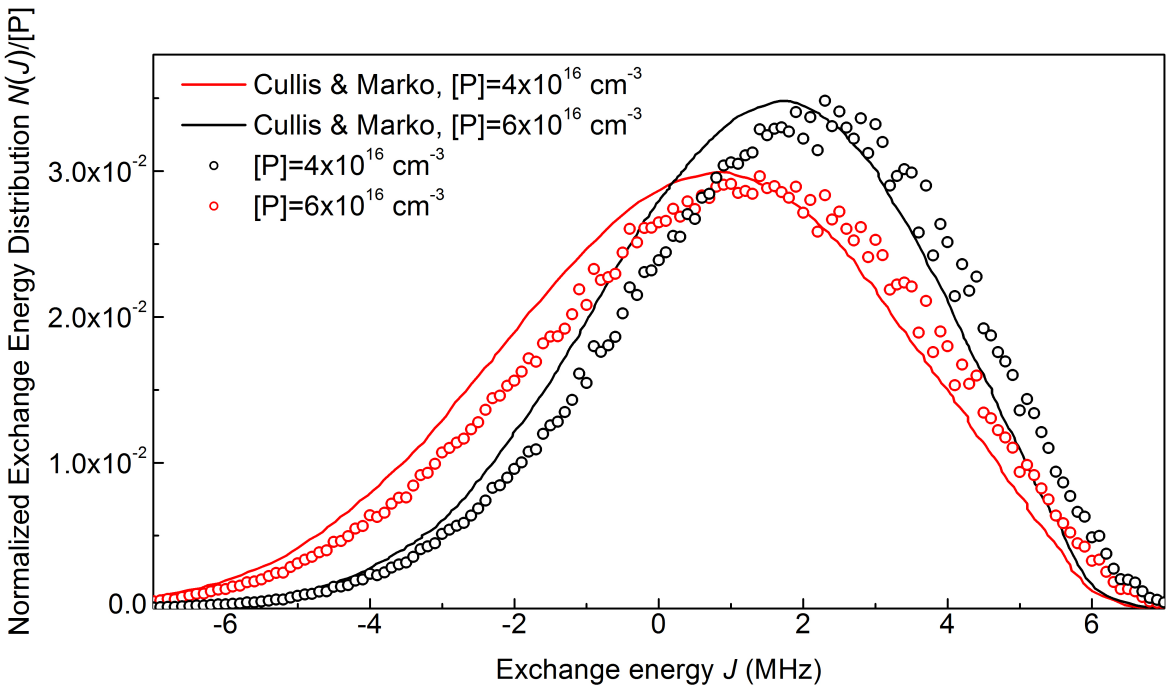

FIGURE 6.6: Exchange energy distribution normalized by the concentration of P donors, obtained for a P-doped Si crystal with [P]= 4×10^{16} cm^{-3} and with [P]= 6×10^{16} cm^{-3}. Points correspond to our data and lines correspond to the data of Cullis and Marko [23].

$\sigma = 1.3$ corresponding to the P-doped Si NCs grown by gas phase method measured in our experiments. As can be seen in this figure, the values of J display quite a broad distribution spanning over about three orders of magnitude, while the distribution of $|\mathbf{R}|$ is relatively narrow, spanning from about 5 to 40 Å. This observation indicates that the magnitude of the exchange coupling interaction between donors in dimers is mainly dependent on the factor $\cos(\mathbf{k}_j \cdot \mathbf{R})$ in Eq. 6.7 [222], leading to J values differing by orders of magnitude for donor dimers with similar $|\mathbf{R}|$. Thus, even in NCs, where allowed values of $\mathbf{R}$ are restricted to a narrow interval, a random donor placement results in quite differing exchange coupling energy strengths. From comparison of the distribution $N(J)$ shown Fig. 6.7(b) and the dependence of the magnetic field position of resonances c and d as a function of J, shown in Fig. 6.4(c), we see that most values of J obtained are above 10^5 MHz, for which the EPR transitions c and d are degenerate and thus result in the single band located at $g = 1.998$.

In the following, we will use the distribution of exchange energies $N(J)$ to estimate the temperature dependence of the intensity of the Exch signal shown in Fig. 6.2.

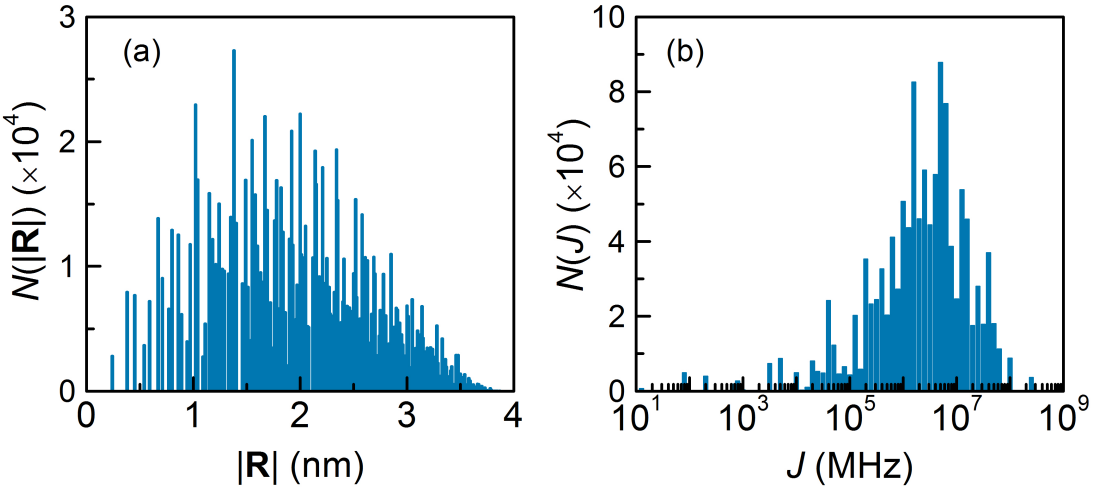

FIGURE 6.7: Calculated distribution of separation distances $|\mathbf{R}|$ and exchange interaction energy J for a Si NC with a diameter of 3.9 nm.

6.2.4 Calculation of the temperature-dependent intensity of the EPR signal due to dimers in P doped Si nanocrystals

The intensity of the Exch signal is proportional to the sum of the occupancy difference $\Delta P(T, J)$ between the states involved in transitions c and d. For each of these transitions, $\Delta P(T, J)$ is given by

$$\Delta P^{|T_0,s\rangle}_{|T_{-1},s\rangle}(T,J) = \Delta G^{|T_0,s\rangle}_{|T_{-1},s\rangle} \frac{e^{-E_{|T_{-1},s\rangle}(J)/k_BT} - e^{E_{|T_0,s\rangle}(J)/k_BT}}{\sum_j e^{-E_j(J)/k_BT}} \tag{6.8}$$

$$\Delta P^{|T_0,t_0\rangle}_{|T_{-1},t_0\rangle}(T,J) = \Delta G^{|T_0,t_0\rangle}_{|T_{-1},t_0\rangle} \frac{e^{-E_{|T_{-1},t_0\rangle}(J)/k_BT} - e^{E_{|T_0,t_0\rangle}(J)/k_BT}}{\sum_j e^{-E_j(J)/k_BT}} \tag{6.9}$$

$$\Delta P^{|T_1,s\rangle}_{|T_0,s\rangle}(T,J) = \Delta G^{|T_1,s\rangle}_{|T_0,s\rangle} \frac{e^{-E_{|T_1,s\rangle}(J)/k_BT} - e^{E_{|T_0,s\rangle}(J)/k_BT}}{\sum_j e^{-E_j(J)/k_BT}} \tag{6.10}$$

$$\Delta P^{|T_0,t_0\rangle}_{|T_1,t_0\rangle}(T,J) = \Delta G^{|T_0,t_0\rangle}_{|T_1,t_0\rangle} \frac{e^{-E_{|T_1,t_0\rangle}(J)/k_BT} - e^{E_{|T_0,t_0\rangle}(J)/k_BT}}{\sum_j e^{-E_j(J)/k_BT}} \tag{6.11}$$

where k_B is the Boltzmann constant. The quantities ΔG for these transitions are given in Table 6.1 and the values of E are given by Eqs. (6.4) and (6.5). We use the distribution of exchange energies $N(J)$ to estimate the temperature dependence of the Exch signal intensity I_{Exch} shown in Fig. 6.1. In this case, we have $A_{\text{NC}} = 198$ MHz. In a first approach, we

considered that all donor dimers in the NC ensemble interact with the same average exchange energy $\langle J \rangle$ which is given by $\langle J \rangle = \sum_i J_i N(J_i) / \sum_i N(J_i)$. From this, we estimate the temperature dependence of the EPR signal as

$$I_{\mathrm{EPR}} = K N_D \Big(\Delta P^{|T_0,s\rangle}_{|T_{-1},s\rangle}(T, \langle J \rangle) + \Delta P^{|T_0,t_0\rangle}_{|T_{-1},t_0\rangle}(T, \langle J \rangle) + \Delta P^{|T_1,s\rangle}_{|T_0,s\rangle}(T, \langle J \rangle) + \Delta P^{|T_0,t_0\rangle}_{|T_1,t_0\rangle}(T, \langle J \rangle) \Big) \tag{6.12}$$

N_D is the number of donor dimers in the sample, and K is the EPR intensity calibration of the spectrometer. The parameter K was obtained using the EPR band from Si-db defects as internal calibration signal. For this, we compared the signal intensity of the Si-dbs in the Q-band spectra recorded with low microwave power in non-saturation condition [see Fig. 6.1(b)] with the density of Si-dbs in the sample (1.8×10^{11} cm^{-2}) determined for the same sample from X-band EPR, where a DPPH spin standard was used as reference. The calculation results are depicted in Fig. 6.8 as a dashed line. As can be seen, this approach cannot give a reasonable description of our experimental data. However, we note that this model does not take into account the distribution $N(J)$ and the lognormal size distribution of the NC ensemble. To consider these, we calculate the dependence of I_{Exch} on T by using the expression

$$I_{\mathrm{EPR}} = K N_D \sum_{d_{\mathrm{NC}}} \sum_J L_{d_0,\sigma}(d_{\mathrm{NC}}) n_{d_{\mathrm{NC}}}(J) \Big(\Delta P^{|T_0,s\rangle}_{|T_{-1},s\rangle}(T, J) + \Delta P^{|T_0,t_0\rangle}_{|T_{-1},t_0\rangle}(T, J) + \Delta P^{|T_1,s\rangle}_{|T_0,s\rangle}(T, J) + \Delta P^{|T_0,t_0\rangle}_{|T_1,t_0\rangle}(T, J) \Big) \tag{6.13}$$

where $L_{d_0,\sigma}(d_{\mathrm{NC}})$ is the normalized lognormal size distribution of our NC ensemble and $n_{d_{\mathrm{NC}}} = N_{d_{\mathrm{NC}}}(J) / \sum N_{d_{\mathrm{NC}}}(J)$. The results of this calculation are shown in Fig. 6.8 as a solid line. There, we see that there is a remarkable agreement between this model and the experimental data. We also performed a calculation where the NC size distribution is neglected by replacing $L_{d_0,\sigma}(d_{\mathrm{NC}})$ with the Kronecker delta $\delta_{d_0,d_{\mathrm{NC}}}$ in Eq. 6.13 (see dotted line in Fig. 6.8). There is no difference between the results of this calculation and those obtained from Eq. (6.13), showing that the relatively narrow size distribution of our NCs does not affect the temperature dependence of I_{Exch}. The slowly varying I_{Exch} is therefore primarily due to the broad distribution of exchange energies possible in an ensemble of donor dimers.

From the vertical alignment between the experimental values of $I_{\mathrm{EPR}}(T)$ and the calculation using Eq. (6.13), we extract the value of N_D, which corresponds to the density of donor dimers $[C_2] = 3 \times 10^{17}$ cm^{-3}. Using the approach described in Sec. 5.2.2, we estimate the density of donor electrons detected by EPR from the value of $[C_2]$ obtained from the fitting of Eq. (6.13) to the experimental values of $I_{\mathrm{EPR}}(T)$. Fig. 6.3 shows the density of cluster of n donor electrons as a function of $[e^-]$ for P-doped Si NCs with $d_{\mathrm{NC}} = 3.9$ nm. In this figure, we can see that the obtained value of $[C_2] = 3 \times 10^{17}$ cm^{-3} corresponds to $[e^-] = 1 \times 10^{19}$ cm^{-3}. This value is remarkably close to the concentration of donor electrons present in the P-doped

Si NCs investigated which we estimated to be 1.4×10^{19} cm^{-3}, as described in Sec. 6.2.1. This confirms that the Exch signal observed in the P-doped Si NCs grown by gas phase method is primarily due to donor dimers.

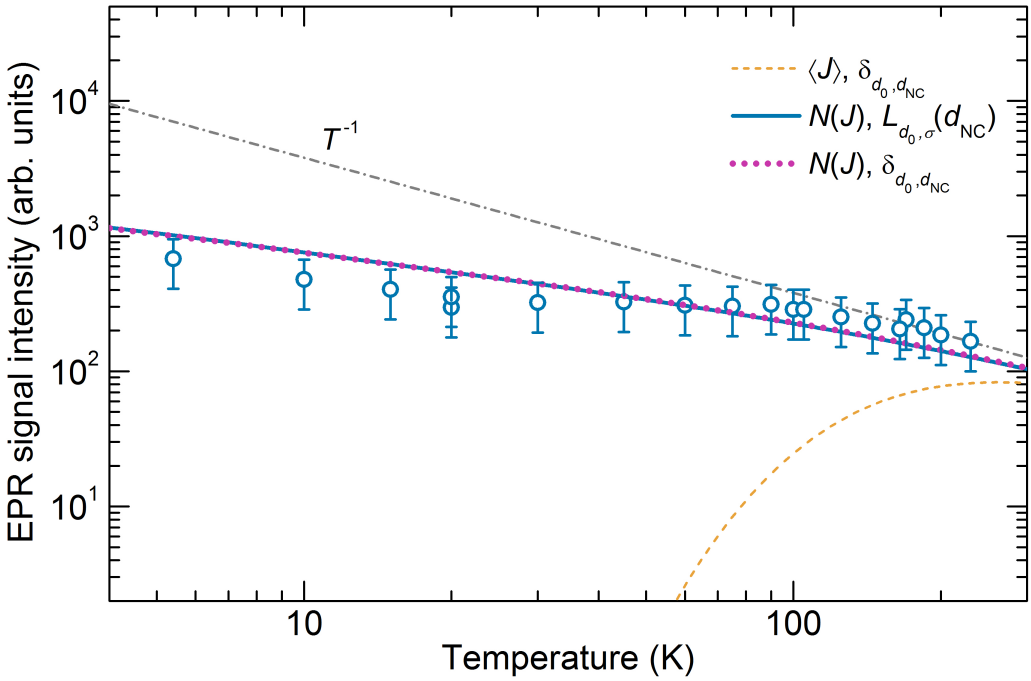

FIGURE 6.8: Temperature dependence of I_{Exch} compared with theoretical estimations based on models described in the text. The first symbol and the second symbol of the labelling of each model indicate, respectively, the distribution of J and distribution of NC size considered in the model. $\delta_{d_0,d_{\mathrm{NC}}}$ is the Kronecker delta.

6.3 Prediction of the exchange coupling of donor dimers in nanocrystals

In this section, we predict the exchange coupling of donor dimers in ensembles of NCs in which most exchange coupled donors are in dimers. We start by establishing the conditions of NC size and doping concentration for which the amount donor dimers in the NC ensemble dominates over the amount of larger clusters of donors. We then use the framework described above for the exchange coupling of donor dimers to calculate the dependence of the intensity of the Exch signal on temperature and on NC size. From our calculations, we infer that the measured deviation of the intensity of the Exch signal from Curie behavior described in the

previous sections should origin from a freezing of the coupled donors to their singlet ground state that occurs with decreasing temperature. Further, we predict a step-like behavior in the temperature dependence of the intensity of the Exch signal for NCs with size smaller than 2.5 nm and relate these results to observations previously reported in the literature.

6.3.1 Conditions for dominance of donor dimers over larger clusters of donors in Si nanocrystals

For the deviation of the intensity of the Exch signal from Curie behavior to be explained by a framework based on the exchange interaction between donor dimers in the NCs, most of the exchange coupled donor electrons in the NCs must be in dimers (i.e. $[C_2] \gg [C_{\eta\geq 2}]$). To determine the conditions for which this situation is verified, we calculated the statistical distribution of dimers in NCs ensembles in the same way as described in Sec. 5.2.2. Figure 6.9 shows the fraction of donor clusters with $\eta = 2$ (donor dimers) in all clusters of exchange coupled donors ($\eta \geq 2$), $[C_2]/[C_{\eta\geq 2}]$, in ensembles of Si NCs covering a broad range of mean

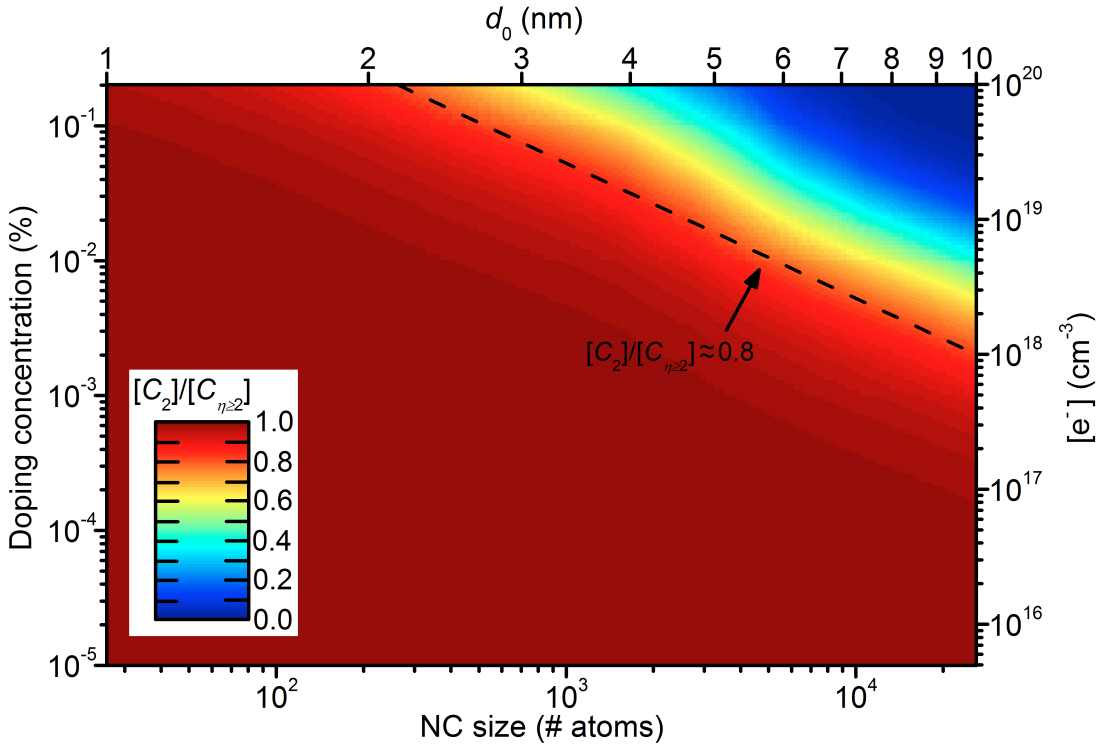

FIGURE 6.9: Dependence of the faction of donor dimers ($\eta = 2$) in all clusters of exchange coupled donors ($\eta \geq 2$) present in a NC ensemble, $[C_2]/[C_{\eta\geq 2}] \equiv [C_2]/\left([e^-]\ \sum_{\eta=2}^{\infty} p_\eta/\eta\right)$, on d_0 and $[e^-]$. d_0 and $[e^-]$ below the dashed line, given by $[e^-] = d_0^{-3} \times 10^{21}$ cm^{-3}, correspond to donor dimer fractions above 80%.

NC sizes d_0 and considering feasible values of $[e^-]$, i.e. $[e^-] < 1 \times 10^{20}$ cm^{-3}. As can be

seen in Fig. 6.9, for donor concentrations $[e^-] \leq d_0^{-3} \times 10^{21}$ cm^{-3}, donor dimers represent at least 80% of all clusters of exchange coupled donors. Thus, in most cases, donor dimers present in the NC ensemble will have a dominant role in determining the behavior of the exchange coupled donors. We note that exceptions to this situation are NC ensembles with simultaneously extremely high doping densities and large d_0.

For a very broad range of $[e^-]$ and d_0, the behavior of exchange coupled donors in Si NCs can, therefore, be established from the properties of the donor dimers. In the following, we use the framework described in the Sec. 6.2.4 to predict the temperature behavior of the Exch signal associated to exchange coupled donors in NC ensembles and its dependence on d_{NC}.

6.3.2 Prediction of the dependence of the EPR signal due to donor dimers in nanocrystals on temperature and on nanocrystal size

Figures 6.10(a)−(c) show the distributions $N(J)$ for d_0 = 1.0, 5, and 7 nm. In these figures, the value of A_{NC} for the corresponding NC size is shown as a dotted line. As can be seen in Fig. 6.10(a)−(c) , the statistically significant values of J are always much larger than A_{NC}. As we discussed in Sec. 6.2.3, this confirms that transitions c and d should be degenerate for the NC sizes shown in Fig. 6.10 and thus should be responsible for the Exch signal observed in the EPR spectra of P-doped Si NCs (see Fig. 6.1).

We now calculate the dependence of I_{Exch} on T and on d_0. For that, we use Eq. (6.13) with $L_{d_0,\sigma}(d_{\mathrm{NC}})$ replaced with the Kronecker delta $\delta_{d_0,d_{\mathrm{NC}}}$. Fig. 6.11(a) shows the calculated temperature dependence of I_{Exch} for d_0 = 1.0, 1.5, 2.5, 5.0, and 10.0 nm. From the figure, we observe that I_{Exch} deviates quite strongly from Curie paramagnetism, scaling as $I_{\mathrm{Curie}} \propto T^{-1}$. This deviation becomes more pronounced with decreasing T and decreasing NC size d_0. A behavior approaching that of Curie paramagnetism is only expected for NCs larger than 5 nm and temperatures well above room temperature. According to our calculations, in the regime close to Curie paramagnetism, the density of exchange coupled donors thermally excited to their triplet states is maximum and independent of T. As T is lowered $I_{\mathrm{EPR}}(T)$ deviates from I_{Curie} due to a decrease in the density of dimers in their triplet (paramagnetic) states. Figures 6.10(d)−(f) show the sum of the occupancy difference $\Delta P(T, J)$ between the states involved in transitions c and d, which is given by the sum of Eqs. (6.8)−(6.11), as a function of J for T = 20 K and T = 300 K. There, we can see that for T = 300 K, $\Delta P(T, J)$ decreases sharply for $J \gtrsim 10^7$ MHz. Exchange coupled donors with $J \gtrsim 10^7$ MHz are frozen in their ground states and, therefore, do not contribute to I_{Exch}. As T is lowered to 20 K, this threshold value of J decreases to $\approx 10^6$ MHz and a smaller number of exchange coupled donors in the ensemble contribute to I_{Exch}. This threshold value of J is independent of the NC size for any given T. Figure 6.11(b) shows the deviation of I_{Exch} from I_{Curie} as a function of d_0 for two different temperatures (T = 20 and T = 300 K). At room temperature, this deviation becomes significant (i.e. $I_{\mathrm{EPR}}/I_{\mathrm{Curie}} \lesssim 0.8$ only for NC ensembles with mean NC sizes below 5 nm. However, at T = 20 K, the value of I_{Exch} already deviates strongly from

I_{Curie} for NCs ensembles with $d_0 \approx 10$ nm in size. We believe that this may in part justify the observed quenching of the Exch signal assigned to exchange coupled donors for NCs with mean size below ≈ 15 nm [6].

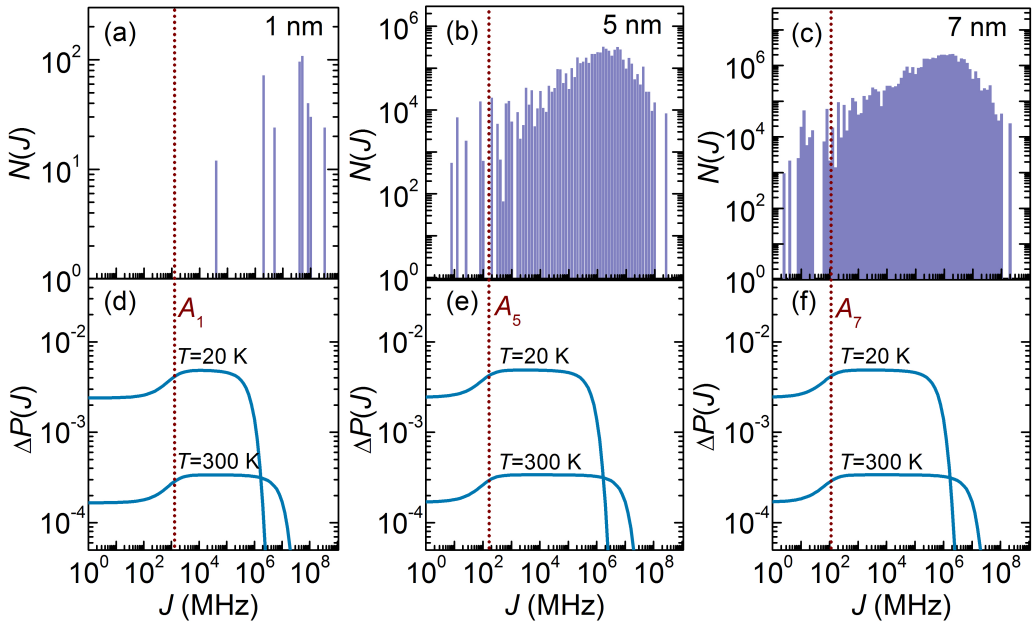

FIGURE 6.10: Distributions of exchange energies J calculated for NCs with $d_0 = 1.0$, 5.0, and 7.0 nm (upper part) and dependency on J of $\Delta P(T, J)$, i.e. the summation over transitions c and d represented in Fig. 6.4(b) of the occupancy differences between states involved in these transitions, calculated for the same NC sizes (bottom part).

Another noteworthy feature of the temperature dependence of I_{Exch} shown in Fig. 6.11(a) is the step-like behavior obtained for the NCs with smaller sizes, e.g., $d_0 = 1.0$ and 1.5 nm. In these cases, we observe that I_{Exch} scales as T^{-1} in some temperature intervals, though it is significantly lower than I_{Curie}. We note that a similar behavior has indeed been observed in the temperature dependence of an EPR band associated with exchange coupled donors in P-doped Si NCs embedded in amorphous SiO_2 films [182]. From our calculations, this behavior occurs for NCs with $d_0 < 2.5$ nm, for which $N(J)$ has a discrete nature. We can understand the origin of this step-like behavior by analyzing Figs. 6.10(a) and (d), which show $N(J)$ and $\Delta P(T, J)$ for $d_0 = 1.0$ nm, respectively. At temperatures decreasing from room temperature to about 100 K, the amount of dimers that contribute to I_{Exch} is somewhat independent of T and I_{Exch} follows a Curie dependence. As the temperature decreases further down to $T = 20$ K, the exchange coupled donors with J between 10^6 and 10^7 MHz become frozen in their ground state ($S = 0$) and no longer contribute to I_{Exch}. At temperatures below

20 K, only the exchange coupled donors with $J \lesssim 4 \times 10^4$ MHz contribute to I_{Exch} and their number is insensitive to T down to 4 K, which results again in a Curie dependence.

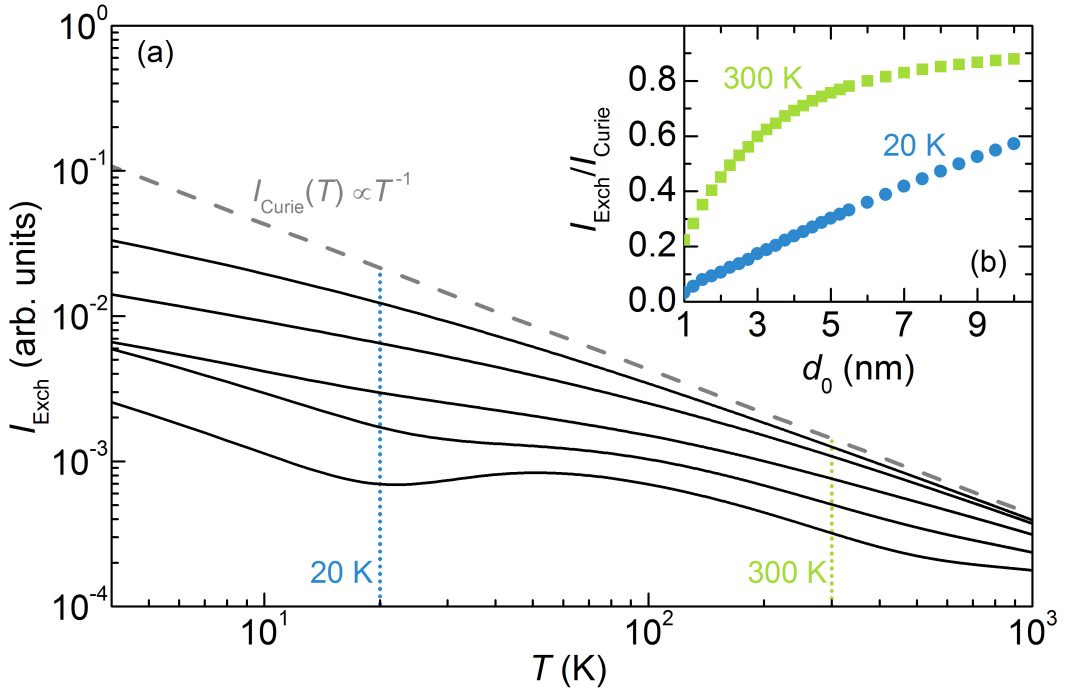

FIGURE 6.11: Temperature dependence of I_{Exch} calculated for Si NCs with d_0 equal to (from bottom to top) 1.0, 1.5, 2.5, 5.0, and 10.0 nm. (b) Deviation of I_{Exch} from I_{Curie}, quantified by the ratio $I_{\mathrm{EPR}}/I_{\mathrm{Curie}}$, as a function of NC size d_0 calculated for $T = 20$ and 300 K.

6.4 Conclusion

In this chapter, we reported the observation of donor dimers in Si NCs via magnetic resonance associated to their triplet state. For this study, we used Q-band EPR spectroscopy, which enabled the observation of EPR signals of exchange coupled donors well separated from background signals of Si-dbs, as opposed to the situation in X-band EPR discussed in Sec. 5.3.2. We showed that the exchange energy J and its distribution can be assessed from the temperature dependence of magnetic resonance spectra. We rationalized our experimental data with calculations of the electronic structure of donor dimers in NCs and of the distribution of exchange energies for an ensemble of NCs with randomly placed dopants. For this, we apply an effective mass approach for calculating the exchange energy. We note that this approach can be generalized to NCs of other materials by taking into consideration the appropriate changes in the material-specific electron effective mass, dielectric constant, values

of the wave vectors at the conduction band minima in the three mutually perpendicular [100] directions. From our calculations we show that, while donor dimers induce discrete states in a NC, their energy splitting differs by up to three orders of magnitude for randomly placed dimers in a NC ensemble, due to an enormous dependence of the exchange energy on the dimer configuration.

We further investigated the electronic structure expected for exchange coupled donors in Si NC ensembles with a broad range of NC sizes and doping concentrations. From statistical calculations we estimated that donor dimers represent most of the exchange coupled donors present in doped Si NCs for a dominant range of doping concentrations, more precisely for $[e^-] \lesssim d_0^{-3} \times 10^{21}$ cm^{-3}. In this regime, the behavior of exchange coupled donors can, therefore, be obtained from the electronic structure of donor dimers in NCs. From this electronic structure, we infer that the measured deviation of the temperature dependence of the magnetic resonance associated with exchange coupled donors in Si NCs from Curie paramagnetism should originate from a freezing of coupled donors to their singlet ground state that occurs with decreasing temperature. Moreover, we find that the deviation from Curie behavior should be stronger for smaller NCs. We further conclude that for very small NCs, with size smaller than 2.5 nm, the temperature dependence of the magnetic resonance displays a step-like behavior, in agreement with recent observation, which results from a quantization from the extreme broadness of the distribution of exchange energies.

Chapter 7

Charge-trapping defects in CdSe nanocrystals

In this chapter, we present our studies on charge trapping defects in CdSe NCs. In the first section of this chapter, we present our EPR spectroscopy measurements of undoped and Ag-doped CdSe NCs performed at room temperature both in the dark and under illumination. We further present temperature dependent EPR measurements of the CdSe NCs. In Sec. 7.2, we start by discussing the origin of the paramagnetic states giving rise to a new EPR signal observed in CdSe NCs. By comparison of the observed EPR signal with those reported in previous studies for paramagnetic defects in II-VI semiconductors, we propose that the observed EPR signal in the CdSe NCs is associated to Se vacancies, with the paramagnetic state being the positively charged state of the defect. We also investigate the effect of the observed defects on the NCs electronic structure. From light-induced EPR measurements of CdSe NCs, we demonstrate that the observed defects have a determinant role in pinning the Fermi level of NCs ensembles. We also analyze the dependence of the intensity of the EPR signal on the amount of electronic Ag dopants in the NCs and show that the defects giving rise to the observed EPR signal in CdSe NCs act as charge traps, since the intensity of the observed EPR signal decreases by up to 80% with the incorporation of a few n-type Ag dopants per NC. Further, we provide evidence for the previously proposed behavior of Ag dopants in CdSe NCs, according to which Ag dopants are n-type donors for concentrations below about 2 Ag atoms per NC (Ag/NC) and become p-type acceptors for higher Ag concentrations [5]. For the studies described in this chapter, we used intrinsic and Ag-doped CdSe NCs with a mean diameter of 2.7 nm, prepared as described in Sec. 4.2. For EPR measurements, a few milligrams of dry NC powder were filled into Suprasil quartz tubes, which were sealed under an inert atmosphere of N_2.

7.1 EPR measurements

The EPR spectrum measured at room temperature for a sample of undoped CdSe NCs is shown in Fig. 7.1(a) (black line). In the EPR spectrum we observe a signal centered at $g = 2.0045 \pm 0.0002$ with a peak-to-peak line width of about 0.8 mT. In order to obtain further information on the paramagnetic states that give rise to this signal, we performed

photoexcited EPR measurements of our CdSe NCs. Figure 7.1(b) compares the EPR spectra measured at room temperature of a sample of undoped CdSe NCs measured in the dark (black line) and under white-light illumination provided by an high-intensity halogen lamp light source (yellow line). We see that the EPR signal measured under illumination is about 3 times more intense than that measured in the dark. In the figure, we also see that the shape of the signal at $g = 2.0045$ observed under illumination is identical to that measured in the dark. We further observed that about 6 hours after ceasing illumination the intensity of the EPR signal returns to that initially measured in the dark, which indicates that the observed response to photoexcitation is reversible. This response to photoexcitation was observed for

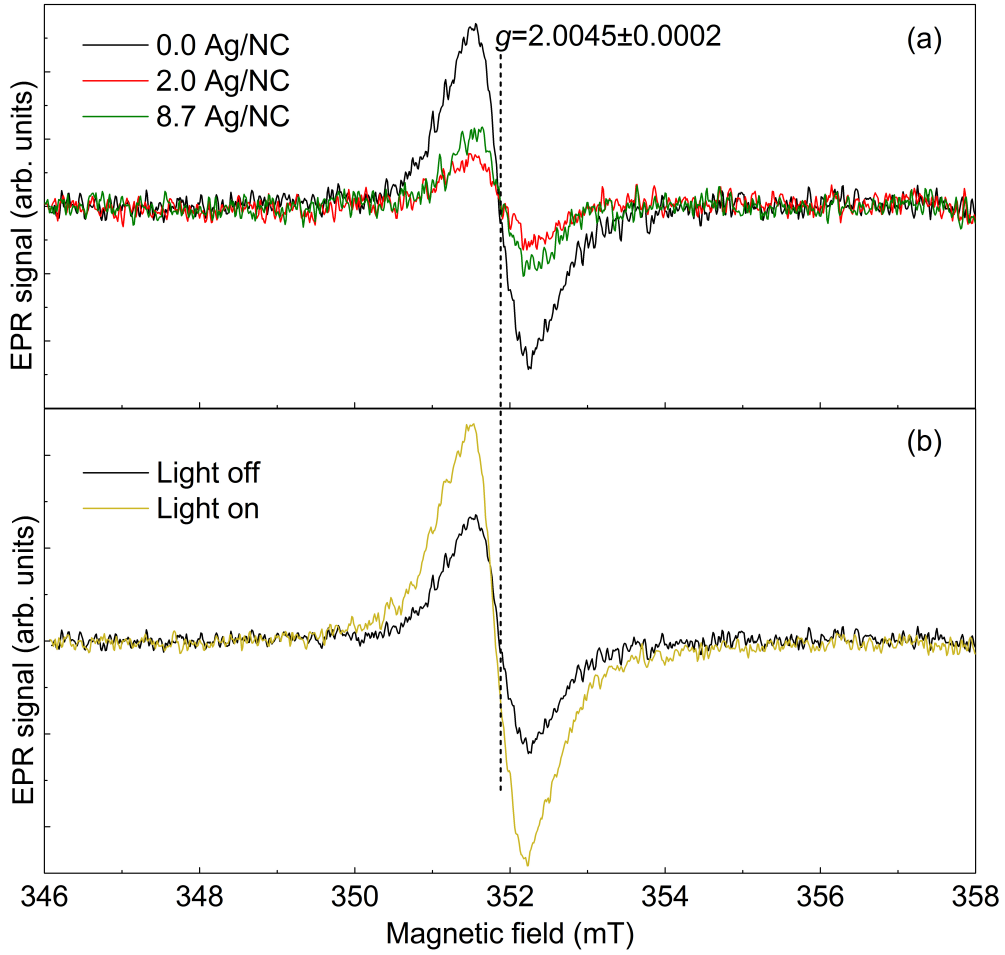

FIGURE 7.1: (a) EPR spectra of undoped and Ag-doped CdSe NCs measured in the dark at room temperature. (b) Comparison between EPR spectra of CdSe NCs (undoped) measured at room temperature in the dark (black line) and under white light illumination (yellow line).

all CdSe NC samples analyzed in this study. The observed increase in the intensity of the EPR signal at $g = 2.0045$ under illumination indicates that photoexcitation leads to the generation of paramagnetic states in the CdSe NCs. This already demonstrates that these states should affect the kinetics of photogenerated charges, such as those involved in photovoltaic devices.

In Fig. 7.2, we show the dependence of the EPR signal at $g = 2.0045$ as a function of temperature T for undoped CdSe NCs with a diameter of 2.7 nm (blue circles) and with a diameter of 5.4 nm (green dots). We see that for both samples the intensity of the EPR signal scales as T^{-1} between 40 K and room temperature, confirming that the EPR signal displays a Curie behavior within this temperature range.

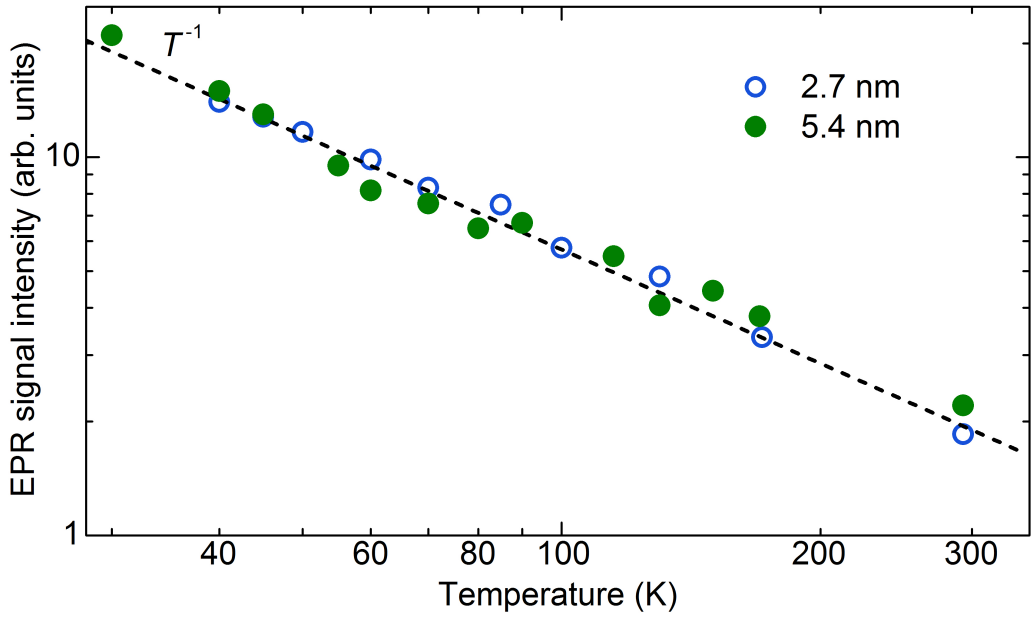

FIGURE 7.2: Temperature dependence of the intensity of the EPR signal at $g = 2.0045$ observed for undoped CdSe NCs with a diameter of 2.7 nm (blue circles) and with a diameter of 5.4 nm (green dots). The dashed line represents a T^{-1} Curie behavior.

The EPR signal at $g = 2.0045$ is also observed in Ag-doped CdSe NCs, but its intensity depends on the concentration of Ag in the samples; see Fig. 7.1(a) (red and green lines). This observation indicates that the density of paramagnetic defects giving rise to the signal at $g = 2.0045$ is affected by the amount of Ag dopants in the NCs. Figure 7.3 shows in more detail the dependence of the intensity of the EPR signal at $g = 2.0045$ on the concentration of Ag dopants as measured for two different sample batches. As can be seen, the intensity of the EPR signal at $g = 2.0045$ decreases with Ag doping and reaches a minimum at ~ 2 Ag dopants per NC (Ag/NC). Above this Ag concentration the intensity of the EPR signal increases with

the Ag concentration.

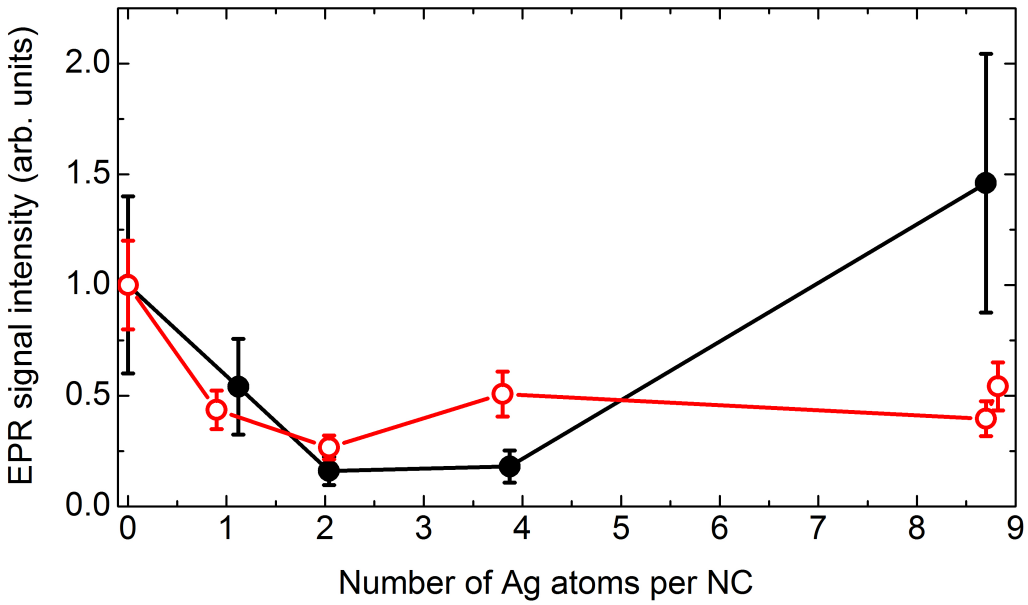

FIGURE 7.3: Intensity of the EPR signal at $g = 2.0045$ as a function of the number of Ag dopants per NC for two sample batches. For each batch, the EPR signal intensity is normalized to the intensity of the corresponding sample of undoped CdSe NCs.

7.2 Discussion

7.2.1 Assignment of the EPR signal at $g = 2.0045$

Firstly, we discuss the origin for the paramagnetic states giving rise to the signal at $g = 2.0045$. Previous studies have identified paramagnetic defects in bulk II-VI semiconductors by EPR. In particular, these investigations have shown that singly charged anion vacancies give rise to isotropic EPR lines near $g = 2$ [263–265]. For example, positively charged S vacancies in ZnS were shown to yield a EPR signal at $g = 2.0034$ with a peak-to-peak line width of 0.05 mT by observing that this signal did not shift when the crystal was rotated around the axis of growth and by detecting the hyperfine structure of the first zinc shell around the anion vacancy [263]. In CdTe, positively charged Te vacancies were shown to yield an EPR signal with an isotropic g-value of $g = 2.000$ and a peak-to-peak line width of 0.4 mT, based on the observation of the resolved isotropic hyperfine interaction of the vacancy with its four nearest Cd neighbors [264]. There is an evident resemblance between the values of g-values reported

in these studies and the value observed in the EPR spectra of our CdSe NCs. This suggests that the EPR signal at $g = 2.0045$ observed in our CdSe NCs is due to positively charged Se vacancies (V_{Se}^{+}) in the NCs. In ZnSe, an EPR signal at $g = 2.0027$ with a peak-to-peak line width of 0.58 mT has also been attributed to positively charged Se vacancies [265], based on the proximity of its g-value to that reported for positively charged anion vacancies in other II-VI materials [263, 264]. Further, a study on CdS NCs capped with poly(methyl 2-methylpropenoate) reported a slightly asymmetric line at $g = 2.004$ with a peak-to-peak line width of 1.5 mT [189]. This EPR signal was also attributed to positively charged S vacancies located at sites on the surface or near the surface of the NCs [189], by comparison with the EPR signal reported for positively charged S vacancies in ZnS [263]. Although the proposed assignment of the defect observed in our EPR spectra of CdSe NCs to positively charged Se vacancies is not completely unambiguous, for the sake of simplicity we will use the label V_{Se}^{+} to refer to the defect giving rise to the observed EPR signal. Should the EPR signal originate from other defect, the discussion presented in the following sections of this chapter remains the same, but applied to the pertinent defect and corresponding charge states.

7.2.2 Electronic structure of charge trapping defects in CdSe nanocrystals

In the following, we investigate the electronic structure of the charge trapping defects in CdSe NCs from the dependence of the observed EPR signal on the concentration of Ag dopants, which is shown in Fig. 7.3. From TEM images recorded for undoped and Ag-doped CdSe NCs, shown in Fig. 4.8, we can see that there are no significant changes in the size or size distribution of the NCs with Ag doping. From the X-ray diffraction patterns obtained for the same NCs, shown in Fig. 4.9(a), we may see that the crystal structure of the NCs remains unchanged upon doping. Further, the absorption spectra of CdSe NCs shows that the energy band gap and optical absorption spectra remain unchanged after Ag doping; see Fig. 4.9(b).

In a previous study, Sahu *et al.* observed that the band-edge peak intensity of the fluorescence of Ag-doped CdSe NCs and the electron mobility of films of these NCs were maximum for Ag concentrations of about 2 Ag/NC [5]. These observations were associated to a change in the doping behavior with the concentration of Ag dopants in the NCs. For Ag concentrations up to ∼2 Ag/NC, Ag was proposed to be incorporated on interstitial sites of the NCs and behave as an n-type dopant [5]. For higher Ag concentrations, it was proposed that the dopants become incorporated on substitutional sites of the NCs and behave as p-type dopants [5]. This behavior of Ag dopants in CdSe NCs is supported by the trend observed by us for the variation of the intensity of the EPR signal of paramagnetic defects with the concentration of Ag dopants, which is shown in Fig. 7.3.

From the analysis of this trend, we may understand the charge trapping mechanism involving the paramagnetic defects in the CdSe NCs. For simplicity, the discussion presented here is made for the situation where the paramagnetic defect observed in EPR corresponds

to V_{Se}^{+}. As described above, we observe a 3-fold increase in the intensity of the EPR signal of paramagnetic defects upon photoexcitation, as shown in Fig. 7.1(b). This observation indicates that in the dark there are two charge states of the defects present in the NCs ensemble, i.e. the positive charge state (observed by EPR) and another charge state that is not observed by EPR (EPR-silent charge state). Moreover, we can conclude that the amount of defects in each of the two charge states is comparable. From this, we infer that the Fermi energy E_F of the NCs ensemble is determined by the populations of the two charge states of the defect (Fermi level pinning). Previous investigations of charge transport of field effect transistors (FETs) made with similar undoped CdSe NCs as those used in this work have concluded that the FETs exhibit n-type behavior [5]. Therefore, the Fermi energy in ensembles of undoped NCs should be located closer to the conduction band (CB) edge than to the valence band (VB) edge. This indicates that the hidden charge state of the defect should be the neutral charge state. In this situation, the Fermi level in the NCs ensemble is then determined by the $V_{Se}^{0/+}$ energy levels of the defects present in the NCs. Here, we consider that the defects are randomly placed in the different NCs of the ensemble and that there are differences in the $V_{Se}^{0/+}$ level of the different defects depending on their specific location within the NC. In practice, this corresponds to a distribution of $V_{Se}^{0/+}$ levels in the ensemble. We represent this

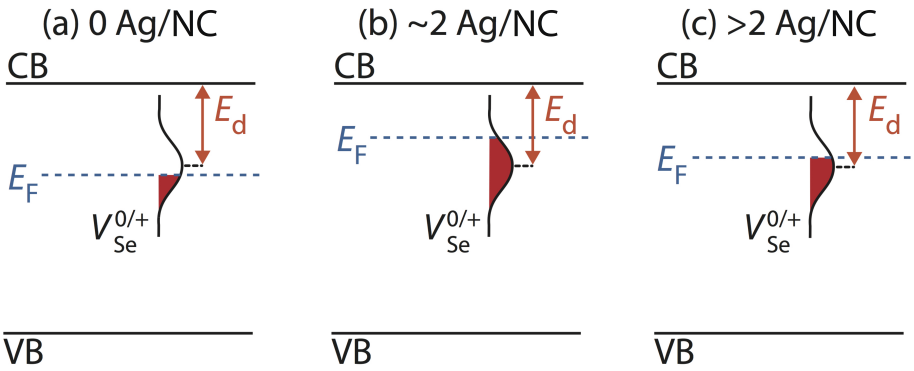

FIGURE 7.4: Scheme of the energy structure of ensembles of CdSe NCs with three Ag doping concentrations: (a) undoped, (b) ~2 Ag/NC, and (c) >2 Ag/NC. In each scheme, the red area under E_F represents the amount of V_{Se}^{0} defects in the NCs ensemble.

distribution with a Gaussian function having a maximum at an energy E_d, as shown in Fig. 7.4(a) for the case of undoped NCs. In this figure, the filled (red) area in the distribution of $V_{Se}^{0/+}$ energies represents the amount of defects in the neutral charge state (invisible by EPR). Using this model, we can describe the dependence of the EPR intensity on the Ag doping. At low doping concentrations (<2 Ag/NC), Ag atoms are expected to act as n-type dopants [5]. As the concentration of Ag increases up to ~ 2 Ag/NC, E_F shifts up in the energy gap and the amount of positively charged Se vacancies decreases; see Fig. 7.4(b). The

result is a quenching of the signal at $g = 2.0045$. At Ag concentrations above 2 Ag/NC, Ag dopants are expected to behave as p-type dopants [5]. In this situation, E_F shifts down in energy; see Fig. 7.4(c). Thus, the amount of positively charged Se vacancies increases, which results in the increase of the intensity of the observed EPR signal.

7.2.3 Estimation of lower limit of ionization energy

Based on conductivity studies, the energy E_d of the transition from the neutral to the positive charge state of V_{Se} defects ($V_{Se}^{0/+}$) in bulk CdSe has been estimated to be 150 meV below the semiconductor CB edge [266]. Further, the presence of V_{Se}^{+} defects has been suggested in CdSe NCs capped with a ZnSe shell [50]. These studies investigated the charge transport and the electroluminescence of diodes containing a layer of CdSe/ZnSe NCs with 6.8 nm in size. In these devices, the authors observed very low electron mobilities. They showed that this effect was due to electron trapping at defects in the NCs, which were present in a density of 8×10^{17} cm^{-3} [50]. From temperature-dependent current-voltage measurements they could estimate that the depth of the electron traps is ∼130 meV below the NCs CB. From comparison between this energy value and that estimated for the ionization energy of V_{Se} defects in bulk CdSe [266], they suggested that the electron trapping states in their CdSe/ZnSe NCs originate from V_{Se}^{+} defects.

The observation of Curie behavior for temperatures at least up to room temperature described in Sec. 7.1 shows that the population of these defects remains constant within this temperature range. Therefore, there is no thermal excitation of the paramagnetic defects up to room temperature. This enables us to infer a lower limit for the energy E_d. At 0 K, we have a certain density of neutral vacancy defects $n_{d,0}^{0}$. As T increases, neutral vacancies may be thermally excited to CB states and electrons populate CB states with a density n which is given by [2]

$$n^2 = \frac{N_c}{2}\left(n_{d,0}^{0} - n\right) e^{-E_d/k_B T} \tag{7.1}$$

where $N_c = \left(2\pi m_{CdSe}^{*} k_B T/h^2\right)^{3/2}$ is the effective density of CB states, $m_{CdSe}^{*} = 0.13 m_0$ is the electron effective mass in bulk CdSe [266]. The density of thermally excited V_{Se}^{+} defects corresponds to n. The maximum of this density is $n_{d,0}^{0}$, i.e. when all neutral defects are thermally excited. Figure 7.5 shows $P_+ = n/n_{d,0}^{0}$, which corresponds to the fraction of thermally excited V_{Se}^{+} defects, as a function of E_d and calculated for $T = 300$ K. In this figure, we see that the onset of P_+ occurs for $E_d \approx 300$ meV. From this, we infer that the energy E_d is at least 300 meV. This low limit for E_d is higher than the previously reported value for the $V_{Se}^{0/+}$ energy level in bulk CdSe of 150 meV as described above [266]. The higher lower limit of E_d observed in the NCs may be due to the effect of confinement. For example, previous theoretical studies on P-doped Si NCs showed that confinement is expected to result in an increase of the dopant excitation energy with respect to that observed in the bulk

counterpart with decreasing NC size [8, 173]. In Sec. 5.3.1 we experimentally showed, using temperature-dependent EPR spectroscopy, that the ionization energy of P donors in Si NCs increased with respect to their bulk counterpart, due to an increase in the confinement of P donors in NCs. The observation of the same lower limit of E_{d} for both NC sizes studied here indicates that the $V_{Se}^{0/+}$ energy level is deeper than the narrowing of the NCs band gap with increasing NC size, which should be about 250 meV narrower for the CdSe NCs with 5.4 nm than for those with 2.7 nm [267]. The lower limit for E_{d} in our CdSe NCs is also higher than the excitation energy estimated in Ref. [50] for Se vacancy defects observed in CdSe/ZnS NCs with 6.8 nm in size. This difference may also be associated to a higher confinement in our CdSe NCs.

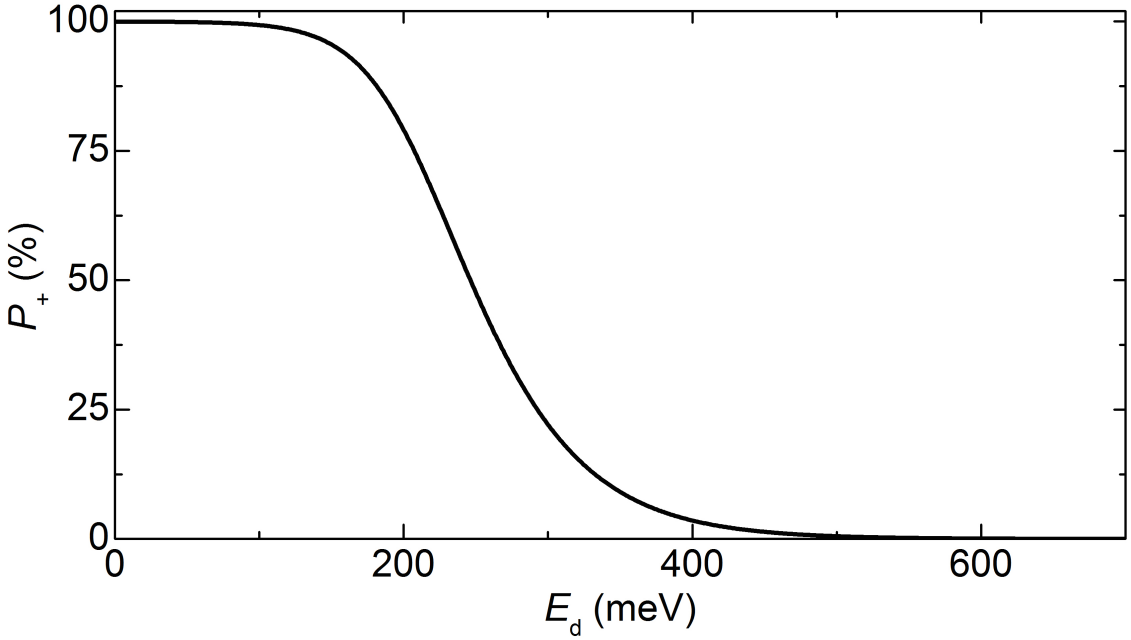

FIGURE 7.5: Dependence of these fraction of vacancy defects in their positive state P_+ as a function of the excitation energy of the defect E_{d} at room temperature.

7.2.4 Defect density in the CdSe nanocrystals and their impact on applications of nanocrystals in devices

Finally, we discuss the impact of the charge trapping defects observed in our study on the application of NCs in devices. In our Ag-doped CdSe NCs, the lowest density of trapping defects observed was $\sim 5 \times 10^{17}$ cm^{-3}. Other studies of the charge transport in films of CdSe NCs used current-voltage measurements to determine the electron mobility and trap density in these films, having estimated trap densities of about $2{\times}10^{16}$ cm^{-3} [186]. These values are very high in comparison to the defect densities necessary to achieve NC-based photovoltaics with efficiencies above 14%, in which the density of traps should be lower than 10^{12} cm^{-3} [56]. The lowest density of charge trapping defects observed in our CdSe NCs

corresponds to approximately 1 defect per 50 NCs. From this value, we can estimate the order of magnitude of the distance l_{trap} that a delocalized electron in a NC film can move without being captured by one of the charge trapping defects investigated here. If we assume that the electron travels in a straight line until it reaches a trapping defect, l_{trap} is at most 100 nm. This value is in par with the l_{trap} ≈80 nm estimated for solar cells of PbS NCs with a power efficiency of 7% [54]. From this discussion, we confirm that the defects observed in our EPR study could have a performance-limiting effect on the electronic properties of devices based on CdSe NCs and that their reduction should have a significant impact on the improvement of the performance of these devices.

7.3 Conclusions

In conclusion, we have observed charge trapping defects in undoped and Ag-doped CdSe NCs using EPR spectroscopy. The observed charge trapping defects are attributed to Se vacancies in the NCs by comparison of the measured EPR signal with those reported in previous studies of paramagnetic defects in II-VI semiconductors. From light-induced EPR measurements we observe a three-fold increase in the intensity of the EPR signal associated to charge trapping defects in the NCs. This observation enabled us to infer that the observed charge trapping defects are present in the NC ensembles in two charge states, which are a charge state visible by EPR and another charge state that is invisible by EPR, and that the amount of defects in each charge state is comparable. From this, we inferred that the Fermi energy of the NCs is determined by the population of the two charge states of the defect.

By combining our EPR measurements with electronic tuning of the NCs via chemically induced Ag doping, we observed that the intensity of the EPR signal due to charge traps depends on the concentration of Ag dopants in the NCs. This observation provides supporting evidence for the mechanism of Ag doping of CdSe NCs suggested in previous studies. Accordingly, Ag dopants are expected to be incorporated at interstitial sites of NCs lattice and behave as donors for dopant concentrations up to ∼2 Ag/NC, while for higher Ag concentrations the Ag dopants are expected to be incorporated at substitutional sites of the NCs lattice an behave as acceptors. Importantly, we show that the defects observed here act as charge traps, since the intensity of the EPR signal associated with these defects decreases by up to 80% with the incorporation of a few n-type Ag dopants per NC.

From the quantification of the EPR signal of charge trapping defects in CdSe NCs, we measure densities of charge trapping defects in the range of $10^{18}-10^{20}$ cm^{-3}. We discussed the impact of the charge trapping defects in the NCs at such densities on the electronic properties of devices based on CdSe NCs. We argued that the measured densities of the charge trapping defects should be high enough to have a performance-limiting effect in devices based on these

NCs [56].

Chapter 8

Magnetic anisotropy in isotropic ensembles of CdSe nanocrystals

In this chapter, we investigate the observation of magnetic anisotropy in ensembles of CdSe NCs randomly stacked in an isotropic shape using FMR spectroscopy. In the first section of this chapter, we describe the observation of angular dependence in the FMR spectra of CdSe NC ensembles, which is a direct evidence of magnetic anisotropy. We complement these data with SQUID measurements, which provide evidence that the observed magnetic anisotropy does not origin from magnetic impurities which could be present in the NC ensembles.

In Sec. 8.2, we present the theoretical framework that we used to rationalize the data from our FMR measurements. We start by calculating the free-energy of an ensemble of randomly distributed magnetic dipoles interacting by magnetic dipole-dipole interactions and show that this interaction should result in an effective magnetic anisotropy. We further show that the magnitude of the magnetic anisotropy of the NCs ensembles can be quantified from the angular dependence of their FMR spectra.

In Sec. 8.3, we describe the computational simulations that we developed to describe the magnetic anisotropy observed in our CdSe NC ensembles. We start by discussing the origin of the magnetic dipoles present in the NC ensembles and argue that these dipoles originate from imperfect NC surface passivation. We then simulated the magnetic dipole-dipole interactions between dipoles that are distributed at the surface of the NCs in an ensemble, and show that these interactions originate values of magnetic anisotropy that are in good agreement with those observed in our FMR measurements.

For the study presented in this chapter, we used undoped CdSe NCs with a diameter of 2.7 nm, which were prepared in the way described in Sec. 4.2. The ensembles of CdSe NCs stacked in an isotropic shape that we used for the current study consist of suprasil quartz tubes filled with a few milligrams of dry NC powder and sealed under an inert atmosphere of N_2. The sample volume corresponds to a cylinder with height approximately equal to the tube diameter. During angular-dependent FMR measurements, the sample tube is rotated around the sample tube axis. For SQUID measurements, the quartz tubes filled with NCs were placed in the center of long plastic tubes.

8.1 Experimental results

In this section, we present the experimental results concerning the magnetic behavior of intrinsic CdSe NCs that we obtained using FMR spectroscopy, complemented with SQUID measurements. Here we report the observation of angular-dependent FMR spectra for ensembles of CdSe NCs. To discard the influence of magnetic impurities on the magnetic anisotropy observed in the CdSe NCs ensembles, we performed SQUID measurements and discussed the obtained results in the light of previous reports of magnetic behavior in CdSe NCs. Finally, we present temperature-dependent FMR measurements of CdSe NCs ensembles, where we observed that the amplitude of the angular dependence of their FMR spectra quenches at low temperatures.

Figure 8.1 shows the FMR spectra recorded at room temperature for two samples of CdSe NCs for various orientations of the external magnetic field **H**. Here, **H** was rotated in the *xy*-

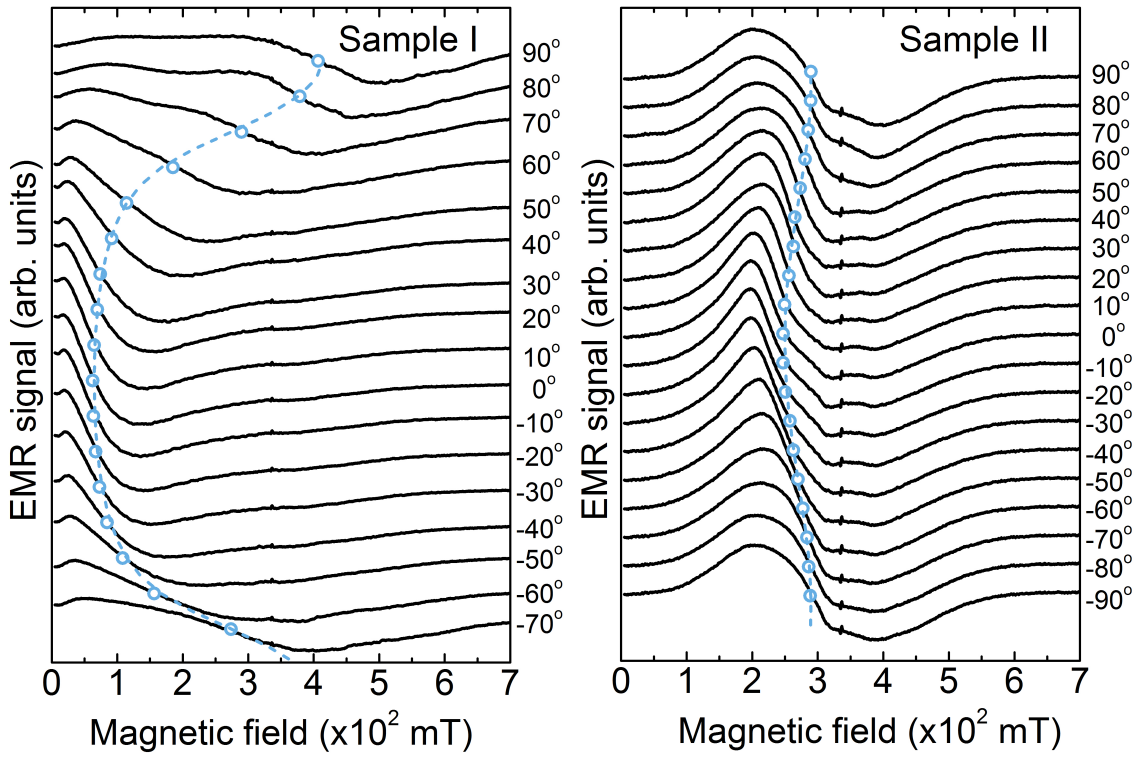

FIGURE 8.1: FMR spectra recorded for two NC samples with **H** at different angles α_H within the *xy*-plane. The open dots indicate the zero-crossing magnetic field H_{res} of the resonance band observed in each spectrum. The dashed lines show the H_{res} angular variation calculated with the model described in the text.

-plane, which is perpendicular to the sample tube axis (z-axis). As can be seen, each FMR spectrum displays a resonance band with a zero-crossing magnetic field $H_{\rm res}$ that depends on the **H** orientation α_H. The location of $H_{\rm res}$ in each spectrum is indicated by the dots in Fig. 8.1. For simplicity, α_H is set with respect to the **H** orientation for which the resonance band displays the lowest $H_{\rm res}$. For sample I, the lowest and highest $H_{\rm res}$ are located at 62 mT (α_H=0°) and ∼400 mT (α_H=90°), respectively. A qualitatively similar angular dependence is observed for sample II, but with a considerably smaller amplitude of variation in $H_{\rm res}$. Sample II also shows the sharp signal at $g = 2.0045$ attributed to charge trapping defects in the CdSe NCs, which was investigated in Ch. 7. The observed angular dependence in FMR spectra is a direct indication of magnetic anisotropy. In our samples, the NC powder was randomly compacted into a volume without shape anisotropy when **H** is rotated within the xy-plane perpendicular to the sample-tube axis. Thus, magnetic anisotropy would not be expected to occur.

To display magnetic resonance, our NCs must contain magnetic dipoles. Recently, both room-temperature ferromagnetism [268–271] and paramagnetism [272] has been reported for CdSe NCs with the surface coated with trioctylphosphine oxide (TOPO) ligands. In fact, ferromagnetism has been recently reported for several types of organic-ligand-capped NCs made of materials which, like CdSe, are diamagnetic in the bulk such as Au [273, 274] and ZnO [275, 276]. In these studies, it was concluded that the magnetic behavior originates from magnetic dipoles located at the NC surface. Figure 8.2 shows magnetization loops measured for four different NC samples. The magnetization curves of our NCs display a saturation at values $M_{\rm s}$=2-6 memu/g and coercivity $H_{\rm c}$ ranging from 20 to 200 mT. No trend is observed in the relation between $M_{\rm s}$ and $H_{\rm c}$. We can rule out that transition-metal contaminants like Fe are the origin of the magnetism of our CdSe NCs. As described in Sec. 4.2.3, we determined from ICP-OES measurements that Fe impurities are present in our CdSe NCs in concentrations of $1-2$ ppb and Co and Ni impurities are present in concentrations below 0.1 ppb. If Fe ($M_{\rm s}$ = 14000 emu/g), Ni ($M_{\rm s}$ = 4000 emu/g), and Co ($M_{\rm s}$ = 12600 emu/g) in quantities of about 1 ppb were the source for the observed magnetization, our samples should display $M_{\rm s} \approx 0.02$ memu/g. This value is at least two orders of magnitude smaller than the values of $M_{\rm s}$ measured in our samples. From magnetization loop measurements, we estimate an average number of magnetic dipoles per NC in the range of $10-30$. The values of magnetization saturation observed for our CdSe NCs are within the range of values (0.2-20 memu/g) reported previously for CdSe NCs [268–271, 277]. The highest values of coercivity observed for our CdSe NCs (200 mT) are above the range of values (5-25 mT) reported for other CdSe NCs [268–271, 277], but are comparable with the values reported for NCs of other diamagnetic materials [273, 278, 279]. There are diverging reports concerning the magnetic properties of CdSe NCs, with some works reporting the observation of ferromagnetism (e.g. Ref. [268]) and other works reporting the observation of paramagnetism (e.g. Ref. [272]). In the specific case of our CdSe NCs, we observe magnetization loops revealing ferromagnetic

behavior, although some of them display smaller coercivity. This shows that samples made of similar NCs can indeed exhibit different behavior. This is in line with the fact that different works, which use CdSe NCs produced in different ways and

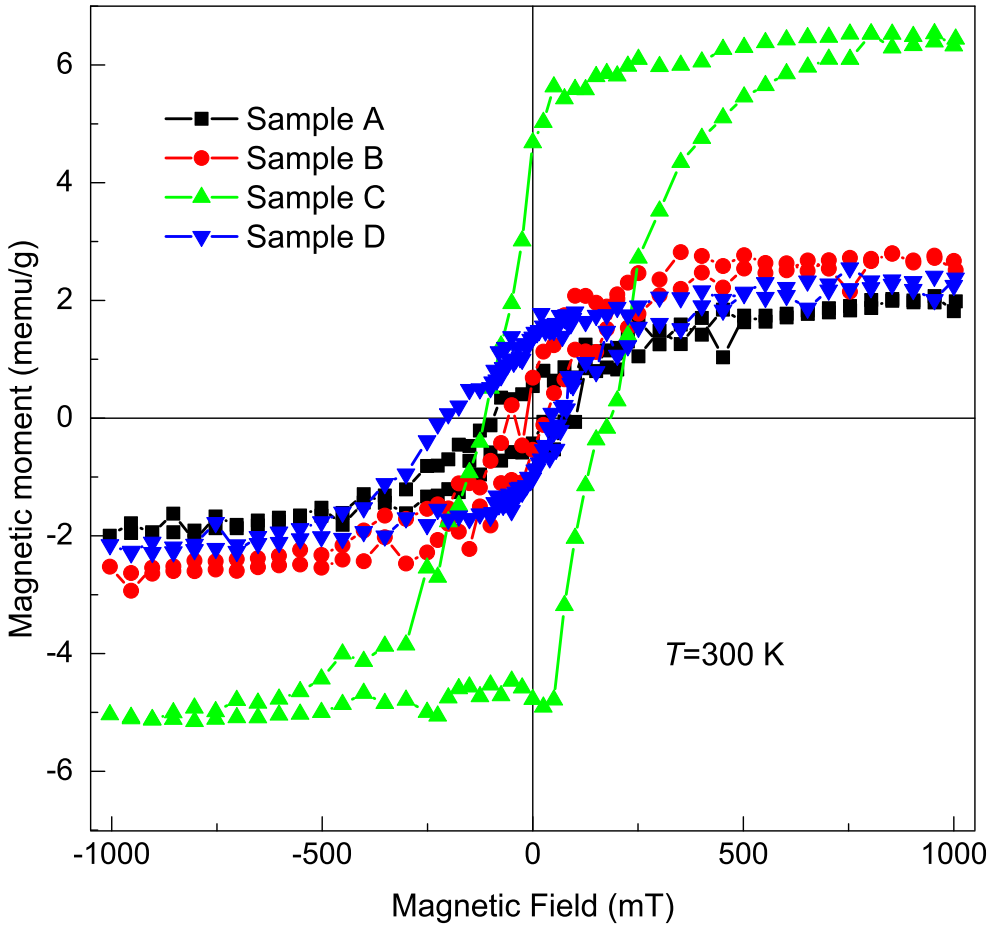

FIGURE 8.2: Magnetization loops measured with SQUID at room temperature for four of the CdSe NC samples analyzed in our study.

therefore with differences in terms of physical properties, report different magnetic behavior and indicates that the magnetic properties of CdSe NCs can be sample dependent. Our goal is not to report the observation of ferromagnetism in CdSe NCs, neither to suggest that CdSe NCs are always ferromagnetic. It is also beyond the scope of our work to explain the origin of the apparent conflicting results published in the literature concerning the magnetic behavior of CdSe NCs. It is possible that both observations are correct, with the appearance of ferromagnetism or paramagnetism being dependent on particular characteristics of the specific CdSe NCs studied in different works, such as surface passivation, geometry and chemistry.

For example, in the case of Au nanoparticles, it has been found that the magnetic properties are strongly dependent on the type of capping agent [280, 281]. Here, we are instead focusing on the description of the shape and amplitude of the observed angular-dependent magnetic resonance. As shall be explained below, this is done using a simple model based on magnetic dipole-dipole interactions between dipoles at the NCs surface. The possible origin of these surface spins will also be briefly discussed below. Importantly, we should note that our model does not require that the system of CdSe NCs is ferromagnetic and can be applied to both ferromagnetic and superparamagnetic systems.

We have also monitored the evolution of the FMR as a function of the measurement temperature. For these measurements, the sample was cooled down to 10 K in the absence of an external magnetic field and the FMR spectra were measured for different orientations of **H** at successively increasing temperatures. Figure 8.3 shows the spectra recorded with sample I for α_H=0° and α_H=90° at temperatures between 10 and 293 K. The FMR band is only observed for temperatures down to about 65 K and below this temperature the band quenches.

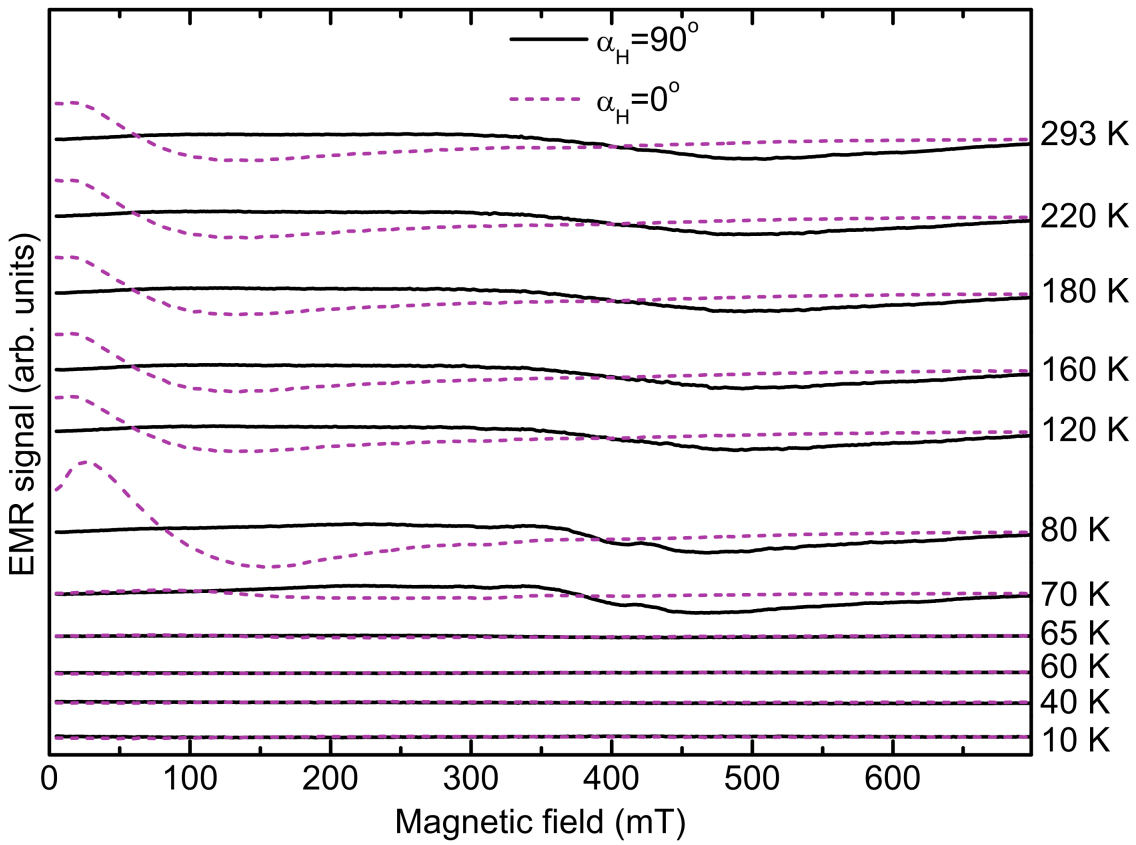

FIGURE 8.3: FMR spectra recorded for sample I at various temperatures for α_H=0° and 90° with **H** in the xy-plane.

The temperature dependence of the FMR spectra will be analyzed further below, in Sec. 8.3.4.

8.2 Theoretical framework

In this section, we describe the theoretical framework that we used to rationalize the magnetic anisotropy observed in our ensembles of CdSe NCs stacked in an isotropic shape. This theoretical framework is based on the magnetic dipole-dipole interactions between magnetic dipoles that are located at the surface of each NC in the ensemble. We show that the magnetic anisotropy in the NC ensembles can be quantified by an effective magnetic anisotropy energy term. We present a method to quantify the magnetic anisotropy of our NC ensembles from their FMR spectra, which uses the resonance equation derived by Suhl and Smit [282,283] together with the effective magnetic anisotropy energy term that describes the effective dipolar interaction between magnetic dipoles in the NC ensemble.

8.2.1 Free-energy of an ensemble of isotropically distributed nanocrystals

In a system consisting of non-interacting magnetic dipoles, each of the dipoles acts independently and the system displays a paramagnetic behavior, which in a powder sample should not show any magnetic anisotropy. However, if the magnetic dipoles interact via magnetic dipole-dipole interactions [221, 284–287], the situation can be rather different. Assuming a system with n_{dip} magnetic dipoles with a magnetic dipole moment m, which are distributed in a volume V, the magnetic free energy density may be given by

$$F = \mathbf{M} \cdot \mathbf{H} + F_{\mathrm{dip}} \tag{8.1}$$

where $\mathbf{M}$ is the total magnetization vector. From the magnetization loop measurements, as well as from measurements reported in Refs. [268–271,277], we can infer that at the observed resonant magnetic fields ($H_{\mathrm{res}} \gtrsim 100$ mT) the magnetization of our NC ensembles is at (or close to) saturation. Thus, we consider that for all resonant fields the dipoles in our samples are collinear and so $\mathbf{M}$ has magnitude $M = n_{\mathrm{dip}} m/V$. The first term in Eq. (8.1) corresponds to the Zeeman interaction and the second term accounts for the magnetic dipole-dipole interactions between the dipoles, which is given by

$$\begin{aligned} F_{\mathrm{dip}} = {} & \frac{\mu_0}{V} \sum_i \sum_{j \neq i} \frac{m^2}{4\pi r_{ij}^3} \times \\ & \left\{ 1 - 3[\sin\alpha_{ij} \cos(\beta_{ij} - \alpha_M) \sin\beta_M - \cos\alpha_{ij} \cos\beta_M]^2 \right\} \end{aligned} \tag{8.2}$$

Here, μ_0 is the vacuum permeability, r_{ij} is the distance between magnetic dipoles i and j, and the angles α_{ij}, β_{ij}, α_M, and β_M are defined in Fig. 8.4(a).

In a first approach, we considered a given number n_{dip} of magnetic dipoles that are randomly distributed in a cylinder with a diameter equal to its height, corresponding to the geometry of our samples. Figures 8.4(b), (c), and (d) show the angular variation of F_{dip} for

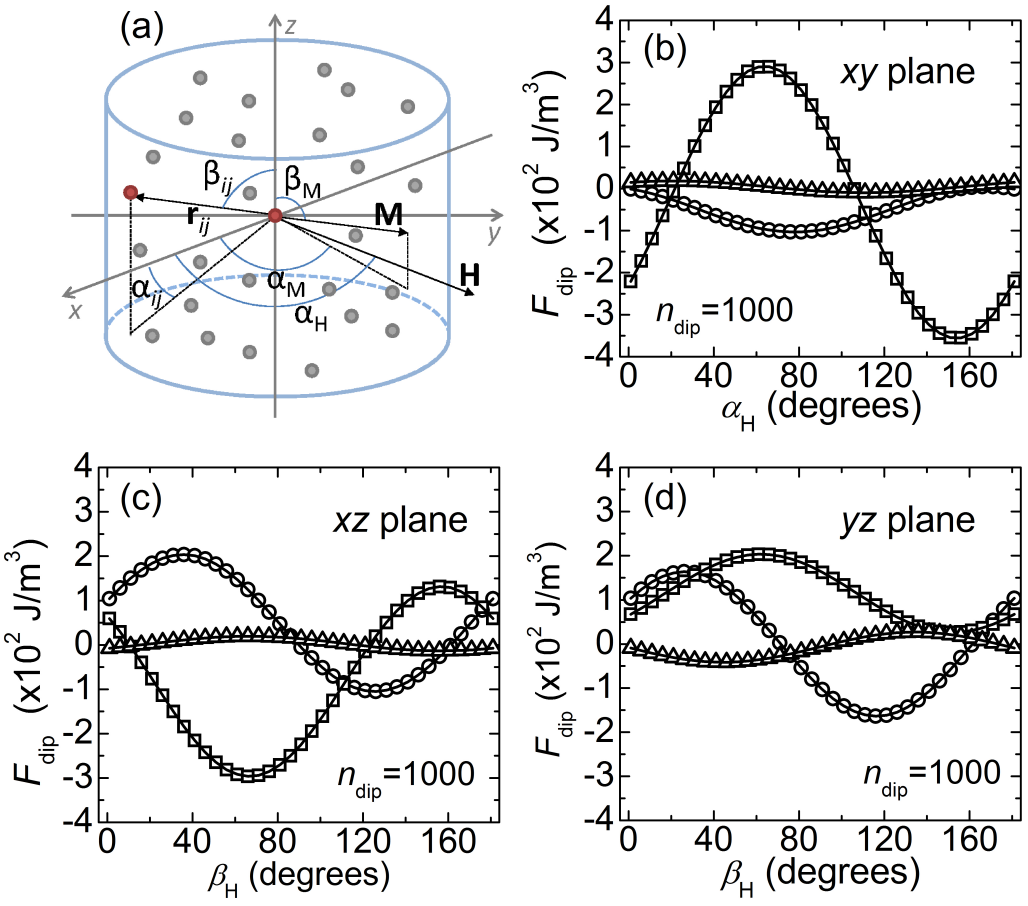

FIGURE 8.4: (a) Coordinate system used to describe **M**, **H**, and the vector $\mathbf{r}_{ij}$ connecting magnetic dipoles i and j. The cylinder and the grey spheres correspond to the sample volume and to magnetic dipoles randomly distributed in that volume, respectively.(b)-(d) Energy F_{dip} calculated for three random arrangements of magnetic dipoles, with n_{dip}=1000, m=1.73μ_{B}, and a density of 2 magnetic dipoles per nm^3, as a function of orientation of **M** within the xy-, xz-, and yz-plane, respectively. The solid lines correspond to fittings using F_{eff} given by Eq. (8.3).

rotation of **M** in the xy-, xz-, and yz-plane, respectively, obtained from three independent calculations, which correspond to three different computer-generated random arrangements of magnetic dipoles with the same n_{dip}. The data shown in these figures is calculated for n_{dip}=1000, a density of magnetic dipoles of 2 dipoles per nm^3, and $m = 1.73\beta_e$,[1]. From

[1]The total magnetic moment of a spin with quantum number S is given by $m = \sqrt{S(S+1)}\beta_e$. Thus, for

the data shown in Figs. 8.4(b), (c), and (d), we observe that in all three calculations F_{dip} displays an angular variation in the three rotation planes. However, the angular variations are quantitatively different for each spatial arrangement of magnetic dipoles. Nonetheless, the calculated data already indicate that the term F_{dip} should result in an effective magnetic anisotropy in a random arrangement of magnetic dipoles. We have found that F_{dip} can always be well parameterized by a simple energy density term of the form

$$F_{\mathrm{eff}} = \frac{\mu_0}{2}\mathbf{M}\cdot\mathbf{U}\cdot\mathbf{M}, \quad \mathbf{U} = \begin{bmatrix} U_{xx} & U_{xy} & U_{xz} \\ U_{yx} & U_{yy} & U_{yz} \\ U_{zx} & U_{zy} & U_{zz} \end{bmatrix} \tag{8.3}$$

where $\mathbf{U}$ is a tensor that describes the effective dipolar interaction in the NC ensemble, with U_{yx}=U_{xy}, U_{zx}=U_{xz}, U_{zy}=U_{yz}, and U_{xx}+U_{yy}+U_{zz}=0. As examples, the results of adjusting Eq. (8.3) to the angular variations of F_{dip} given in Figs. 8.4(b), (c), and (d) are indicated as solid lines in the same figures. As can be seen, an excellent agreement is obtained.

8.2.2 Resonance condition

Our analysis implies that the angular dependence of H_{res} may be obtained from the following resonance equation derived by Suhl and Smit [282, 283]:

$$\left(\frac{\omega}{\gamma}\right)^2 = \frac{1}{M^2\sin^2\beta_M}\left[\frac{\partial^2 F}{\partial^2\beta_M}\frac{\partial^2 F}{\partial^2\alpha_M} - \left(\frac{\partial^2 F}{\partial\beta_M\partial\alpha_M}\right)^2\right] \tag{8.4}$$

From Eq. (8.4), together with the magnetic free energy given by Eq. (8.1) with the quite complex dipolar energy term F_{dip} given simply by Eq. (8.3), we can obtain a general equation for the angular variation of H_{res}, which depends on the elements of $\mathbf{U}$. This is given by

$$\begin{aligned}\left(\frac{\omega}{\gamma}\right)^2 + \frac{1}{4}\{&\sin\beta_{\mathrm{M}}\left[2\sin\beta_{\mathrm{M}}(C\sin(2\alpha_{\mathrm{M}}) + B\cos(2\alpha_{\mathrm{M}})) + 2\cos\beta_{\mathrm{M}}(U_{yz}\sin\alpha_{\mathrm{M}} + U_{xz}\cos\alpha_{\mathrm{M}})\right. \\ &-2H_{\mathrm{res}}\sin\beta_{\mathrm{H}}\cos\Delta] \times [\cos(2\beta_{\mathrm{M}})(A + B\cos(2\alpha_{\mathrm{M}})) + C\cos(2\beta_{\mathrm{M}})\sin 2\alpha_{\mathrm{M}} - \\ &4\sin(2\beta_{\mathrm{M}})(U_{yz}\sin\alpha_{\mathrm{M}} + U_{xz}\cos\alpha_{\mathrm{M}}) + H_{\mathrm{res}}(\sin\beta_{\mathrm{H}}\sin\beta_{\mathrm{M}}\cos\Delta + \cos\beta_{\mathrm{H}}\cos\beta_{\mathrm{M}})] + \\ &[\sin(2\beta_{\mathrm{M}})(C\cos(2\alpha_{\mathrm{M}}) - B\sin(2\alpha_{\mathrm{M}})) + 2\cos(2\beta_{\mathrm{M}})(U_{yz}\cos\alpha_{\mathrm{M}} - U_{xz}\sin\alpha_{\mathrm{M}}) \\ &\left.-2H_{\mathrm{res}}\sin\beta_{\mathrm{H}}\cos\beta_{\mathrm{M}}\sin\Delta]^2\right\} = 0\end{aligned} \tag{8.5}$$

a spin with $S = 1/2$, we have $m = 1.73\beta_e$

For **H** oriented in the xy-plane, this general equation has a negligible dependence on U_{xz} and U_{yz} and, therefore, it can be approximated to

$$\left(\frac{\omega}{\gamma}\right)^2 - \frac{1}{2}\left\{2C\sin(2\alpha_M) + B\cos(2\alpha_M) - H_{\rm res}\cos\Delta\right\}\times \\ \left\{B\cos(2\alpha_M) + 3A + 2[2C\sin(2\alpha_M) + H_{\rm res}\cos\Delta]\right\} = 0 \tag{8.6}$$

where ω=$2\pi\nu$, with ν being the frequency of the applied microwave field, and γ=$2\pi g\mu_{\rm B}/h$. Moreover, h is the Planck constant, Δ=α_H−α_M, and g is the g-factor, which is set equal to 2. The dependence of $H_{\rm res}$ on the orientation of the external magnetic field is determined by the parameters A=$\mu_0 M(U_{xx}$+$U_{yy})$, B=$\mu_0 M(U_{xx}$−$U_{yy})$, and C=$\mu_0 M U_{xy}$. The parameter A gives the shift of the median of the angular variation of $H_{\rm res}$ from H=$h\nu/g\mu_{\rm B}$. The amplitude of this angular variation depends only on B. The parameter C sets the phase of the angular variation of $H_{\rm res}$. The resonance condition in Eq. (8.6) is obtained for the equilibrium orientation of **M**, for which F is minimum ($\partial F/\partial\alpha_M = 0$) [227], which is given by

$$2C\cos(2\alpha_M) - B\sin(2\alpha_M) - 2H_{\rm res}\sin\Delta = 0 \tag{8.7}$$

Overlapped to the spectra sets shown in Fig. 8.1, we plot the fitted angular variations of $H_{\rm res}$ calculated from Eqs. (8.6) and (8.7). As can be seen, the calculations describe quite well our experimental angular variations $H_{\rm res}$. These fits yield the values of A = 191.5 mT and B = 204.6 mT for sample I, and A = 122.6 mT and B = 24.1 mT for sample II. The values of C obtained from these fits are irrelevant and set to C = 0 mT because the phase of our experimental angular variations of $H_{\rm res}$ is set arbitrarily, as mentioned above.

8.3 Computational estimation of magnetic anisotropy in CdSe nanocrystal ensembles

In this section, we present computational simulations on ensembles of CdSe NCs with magnetic dipoles located at the NCs surface. We start by discussing the origin of the magnetic dipoles that give rise to the magnetic anisotropy observed in our ensembles of CdSe NCs. We then describe the method that we developed for the computational simulation of CdSe NC ensembles and show that the results predicted by these simulations are in good agreement with the experimental data obtained by FMR spectroscopy. We finally present a brief discussion of the temperature dependence of the FMR spectra of CdSe NCs ensembles.

8.3.1 Origin of magnetic dipoles in CdSe nanocrystal ensembles

We have shown that the angular variation of the FMR spectra of our samples may be described by a model that considers magnetic dipoles interacting via magnetic dipole-dipole interactions. These interactions may occur between magnetic dipoles at the surface of NCs, where unterminated sites may result in paramagnetic defects with a localized electron spin which has a magnetic dipole moment [288]. In our NCs most of the surface atoms should be passivated with organic ligands, but previous studies showed that only ∼70% of the atoms at the surface of CdSe NCs are passivated by ligands [289, 290]. Thus, in our CdSe NCs with $d_{NC} = 2.7$ nm we expect that about 30 surface atoms remain unpassivated and result in paramagnetic defects that provide the magnetic dipoles in our samples. This amount is consistent with the value of 10-30 magnetic dipoles per CdSe NC estimated above from magnetization loop measurements. We should note that there are differences between the origin of the surface spins considered in Ref. [268] to explain the ferromagnetic behavior of TOPO-capped CdSe NCs and the surface spins considered here to account for the observed anisotropy of the magnetic resonance spectra. In Ref. [268], the surface spins have been associated with charge transfer from surface CdSe atoms to TOPO via Cd-TOPO bonds, similar to the explanation given in other works for the origin of surface spins in thiol-capped Au nanoparticles. [273, 291–294] Here, we associate the spins that lead to the anisotropic magnetic resonance spectra observed in our CdSe NCs with paramagnetic states appearing on surface sites that are not passivated by ligands. It is reasonable to consider that defects are in general more likely to appear at the NCs surface where the periodicity of the lattice is broken, in particular if we consider the very large surface-to-volume ratio of NCs. The formation of defect states on the surface of CdSe NCs has indeed been considered in many experimental and theoretical investigations of CdSe NCs [288, 295–308], including surface paramagnetic centers resulting from incomplete surface passivation as considered here [288, 303–308]. In a very recent paper, it has been theoretically predicted that nonmagnetic CdSe NCs may possess macroscopic magnetic moments associated to the dynamic polarization of dangling-bond spins at the NCs surface [309]. It was further reported that the presence of these magnetic moments successfully explained the experimentally observed low-temperature PL recombination of dark excitons in CdSe NCs. Similar effects have been also reported for the surface of NCs of other materials such as Si (see for example Ref. [310]) and InP (see for example Refs. [308] and [311]). There are clear differences between our experimental observations and those reported in Ref. [268]. Namely, in our case an angular dependent magnetic resonance is observed, whereas no angular variation of magnetic resonance is reported for the CdSe NCs studied in Ref. [268], and a large spread in the values of both saturation magnetization and coercivity is observed for our samples, whereas the CdSe NCs studied in Ref. [268] exhibit well defined values for given NC sizes. These differences indicate that there may be considerable differences in the nature of the spins, and their interactions, between our NCs and the NCs

studied in Ref. [268]. A clear difference between the NCs is related to the surface passivation. In Ref. [268], it was used the original synthesis protocol proposed by Murray et al. [312], where dimethyl cadmium and TOP:Se is injected in boiling TOPO. In the resulting NCs, TOPO binds to surface Cd atoms and TOP binds to surface Se atoms. In our synthesis, however, we also have HDA and DDPA [5, 184, 242]. The DDPA is primarily used to control the nucleation. HDA binds to surface Cd atoms once they are nucleated and while they are growing. HDA is primarily responsible to avoid Ostwald ripening, which is one reason for the robustness of the synthesis method [313]. Thus, in our NCs, TOP binds to surface Se atoms, while Cd-sites are mostly passivated by HDA, plus a small amount of TOPO and DDPA. This difference in surface passivation may result in differences between the surface spins present in our NCs and in the NCs studied in Ref. [268]. As mentioned already above, for the case of Au nanoparticles it has been shown that the magnetic properties are indeed strongly dependent on the capping agent [280, 281].

8.3.2 Computational simulation of CdSe nanocrystal ensembles

To simulate the magnetic dipole-dipole interactions between surface magnetic dipoles in our samples, we generated ensembles of n_{NC} ligand-capped NCs with d_{NC}=2.7 nm. The generated NC ensembles satisfy the following conditions:

- The neighboring NCs in the ensemble are in mutual contact;
- The coverage of the NCs surface by ligands in not complete;
- Regions of the NCs surface with lower ligand coverage should have more magnetic dipoles.

To generate NC ensembles satisfying these conditions, we distribute the NCs in a cylinder with a diameter equal to its height and a volume that corresponds to a volume fraction of NCs equal to 0.2. Each NC in the ensemble is placed with its ligand shell in contact with that of its neighbors. This situation is represented for two neighboring NCs in Fig. 8.5(a). The contact point between NCs is labelled as P. As mentioned above, the ligand coverage of NCs is incomplete. So, we define the thickness of each NC ligand shell at the NC's surface point that is nearest to P, which is indicated in one of the NCs in Fig. 8.5(a) and labelled as P'. For each P', the thickness of the NC ligand shell is picked randomly from the normal distribution shown in Fig. 8.5(b). We set the mean and width of this distribution equal to 0.3 nm. This value is in accordance with previously reported calculations of the potential of mean force for pairs of NCs capped with ligand molecules [314, 315]. In this studies, it was predicted that the equilibrium distance between the centers of NCs capped with ligand molecules always equals $\approx$ 1.25 times the NC diameter. Using these results for the case of the CdSe NCs with 2.7 nm in size that we used here, the separation distance between the surface of two

neighboring CdSe NCs should be equal to 0.3 nm. On the surface of each NC in the ensemble we randomly distribute 10 magnetic dipoles, separated from each others by at least the bond length of CdSe (0.26 nm). This is a conservative estimate for the amount of magnetic dipoles estimated as described above. It is also reasonable to assume that in regions of a NC surface where the ligand shell is thinner, which result from a lower coverage by ligands, the number of surface dipoles is larger. To account for this, we add one magnetic dipole on the NC surface when $d_{\mathrm{lig}} < 0.3$ nm. The extra dipole is placed near the corresponding P', according to a Fisher distribution $P(\mathbf{r}_{\mathrm{dip}}) = C(\kappa) \exp(\kappa \boldsymbol{\zeta} \cdot \mathbf{r}_{\mathrm{dip}})$ [316]. Here, $C(\kappa) = \kappa / 4\pi \sinh \kappa$, $\mathbf{r}_{\mathrm{dip}}$ is the position of the magnetic dipole, and $\boldsymbol{\zeta}$ and κ determine the direction of the maximum and

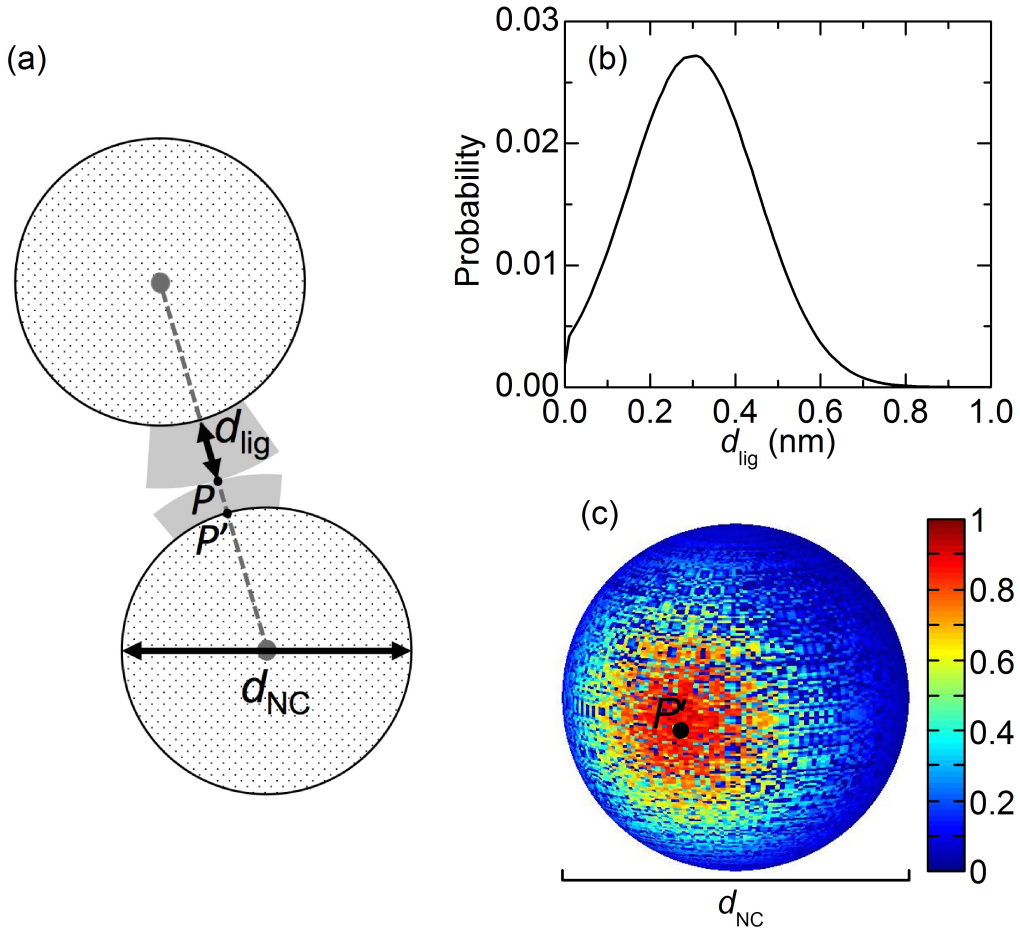

FIGURE 8.5: (a) Scheme of two neighboring ligand-capped NCs in contact with each other at the point P. The grey regions represent the thickness of the ligand shell of each NC at their mutual contact point P. (b) Probability distribution of the ligand shell thickness d_{lig}. (c) Spatial probability distribution $P(\mathbf{r}_{\mathrm{dip}})$ of the extra magnetic dipole that is placed at the NC surface when $d_{\mathrm{lig}} < 0.3$ nm. The maximum of this distribution is located at the point P', which corresponds to the point on the NC surface that is closest to the contact point P.

the width of $P(\mathbf{r}_{\mathrm{dip}})$, respectively. We set $P(\mathbf{r}_{\mathrm{dip}})$ with $\kappa = 3$ and with maximum at the corresponding P'. The used $P(\mathbf{r}_{\mathrm{dip}})$ distribution is shown in Fig. 8.5(c).

8.3.3 Estimation of magnetic anisotropy parameters

We have calculated the distributions of the parameters A and B for different situations of n_{NC}, as described in the following. For each situation, we have generated 2000 different ensembles of NCs. We have calculated F_{dip} for each ensemble, and afterwards we have calculated the elements of the tensor $\mathbf{U}$ for each ensemble by adjusting Eq. (8.3) to F_{dip}. From these elements, we then calculated the parameters A and B for each ensemble. The distributions of these parameters are shown in Fig. 8.6 for sets of 2000 ensembles of NCs with $n_{\mathrm{NC}} = 2$, 10, 20, and 100. There, we see that the distributions of A and B obtained from our calculations span about 4 orders of magnitude and are not significantly dependent on n_{NC}. We note that the experimental values of A and B obtained from the fits shown in Fig. 8.1 (A = 191.5 mT and B = 206.6 mT for sample I, and A =122.6 mT and B =24.1 mT for sample II) are within the ranges of values of A and B obtained from our calculations, for all n_{NC} considered. Figures. 8.6(c) and (d) show the distributions of experimental values of A and B obtained from the FMR spectra of 30 different samples (purple bars). From comparison with the corresponding calculated distributions (black stripped bars), we see that our calculations are in good agreement with the wide distributions of values of A and B observed experimentally.

In ensembles of isotropically-arranged NCs, magnetic anisotropy could be assumed to be negligible since one could expect that for large NC ensembles the angular dependencies of all magnetic dipole interactions in the ensemble statistically average out. This would indeed be the case if the magnitude of the contribution to F_{dip} from all interacting dipoles that are nearest neighbors would be the same. However, this is not the case. Different nearest-neighboring dipoles contribute differently to F_{dip} and this energy term and its angular dependence is dominated by those dipole pairs in the ensemble that are closest to each other. This number is always limited and, therefore, there is not a complete statistical averaging out of the dipole interactions. From our calculations, it becomes apparent that the dipole pairs contributing the most to F_{dip} correspond to pairs where each dipole is located in different NCs and where the inter-dipole distance is in the range of a few angstroms.

Thus, our NC samples correspond to ensembles of interacting NCs, where magnetic dipole-dipole interactions between individual dipoles located in different NCs result in an angular-dependent magnetic energy. In addition, ferromagnetic (exchange) interactions are responsible for the ferromagnetic behavior of the ensembles. These interactions are isotropic in nature and, therefore, cannot contribute to the angular dependence of FMR spectra discussed in this work. The magnitude of the magnetic anisotropy can be large or small depending on the specific statistical arrangement of the strongest interacting dipoles. The broad range of possible inter-NC interaction strengths obtained in our calculations explains the large disparity

of magnetic anisotropies observed in the experiments for different samples of similar NCs.

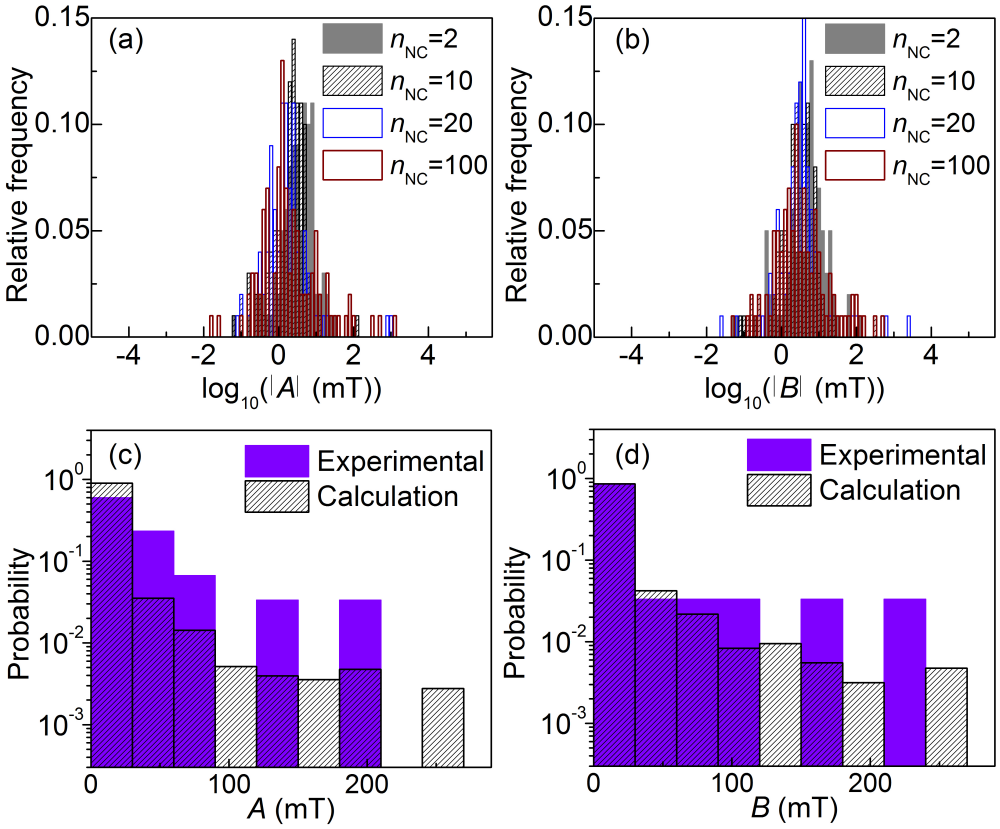

FIGURE 8.6: Distributions of parameters A and B, calculated for 2000 different computer-generated NC ensembles with $n_{\mathrm{NC}} = 2$, 10, 20, and 100. The insets compare the distributions of experimental values of A and B obtained from the FMR spectra with those calculated for NC ensembles with $n_{\mathrm{NC}} = 100$.

8.3.4 Discussion of the temperature-dependence of FMR data for CdSe NC ensembles

In Fig. 8.7(a) is shown the angular dependence of H_{res} recorded for 65, 70, and 293 K. There, we see that the amplitude of the variation of H_{res} decreases with decreasing temperature. In this figure, we also show the corresponding fits of H_{res}, as calculated from Eqs. (8.6) and (8.7). We can see that these fits describe quite well the angular variations of H_{res} measured for different temperatures. In Fig. 8.7(c), we plot the values of A and B obtained from fitting the experimental angular variation of H_{res} as a function of measurement temperature. As can be seen, the two parameters display a similar dependence on temperature. Accordingly, these remain relatively unchanged for temperatures down to 80 K, below which

a decrease is observed. Changes of the parameters $A{=}M(N_{xx}+N_{yy})$ and $B{=}M(N_{xx}-N_{yy})$ with the temperature should be due to changes in the value of M rather than due to changes in N_{xx} and N_{yy}. As we have discussed above, the elements of the tensor $\mathbf{N}$ depend only on the particular arrangement of the NCs in the ensemble. Considering that this arrangement should not change with the temperature, the elements N_{xx} and N_{yy} should be temperature independent. Thus, the experimentally observed temperature variation of A and B [Fig. 8.7(b)] represent the temperature dependence of M in the NC ensemble. We see that M remains approximately constant down to a certain temperature below which a quenching is observed. Similar behavior has been reported for other magnetic NC systems [219, 219, 317]. The M quenching temperature is the blocking temperature, below which the magnetic moments of the NCs are *blocked* during the timescale of the measurement. A blocking temperature of ∼80 K is estimated from our data shown in Fig. 8.7(b), which is within the range of values reported for other magnetic NC systems [219, 317].

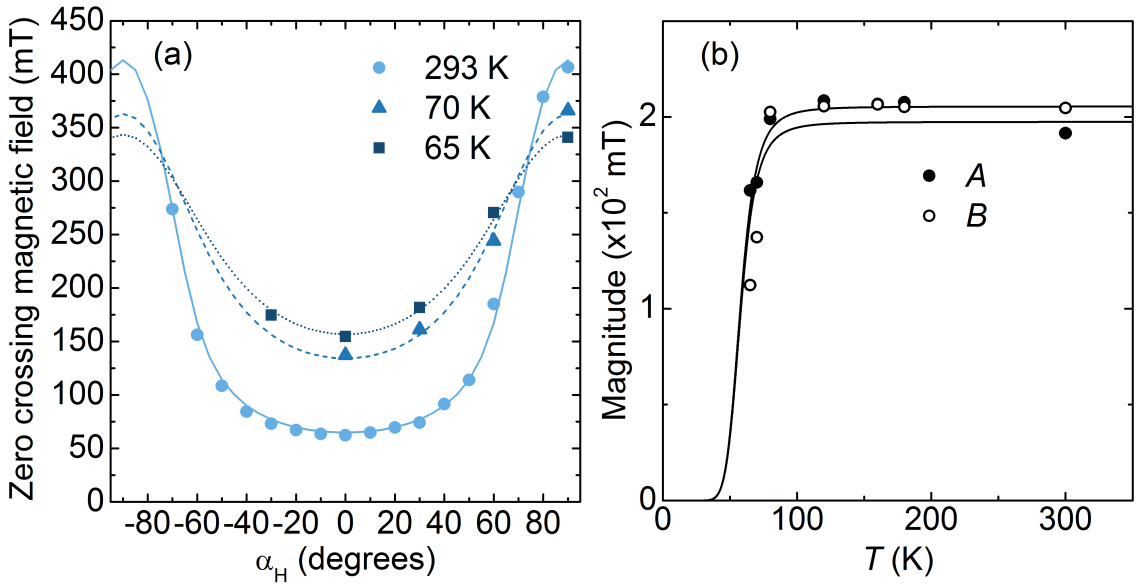

FIGURE 8.7: (a) Angular dependence of H_{res} observed for three different measurement temperatures, together with angular variations fitted with the model described in the text. (b) Temperature dependence of the parameters A and B obtained from the fits. Lines are guides to the eye.

8.4 Conclusions

In this chapter, we investigated the observation of magnetic anisotropy in ensembles of CdSe NCs that are arranged in an isotropic shape. We report the observation of magnetic anisotropy in ensembles of NCs randomly stacked in an isotropic shape using angular-

dependent magnetic resonance. We measured the magnetic anisotropy in different random ensembles of CdSe NCs by recording FMR spectra for various orientations of the external magnetic field. We observe amplitudes of angular variation of resonant magnetic field of up to 350 mT. Moreover, the observed angular dependencies of resonant field are different for apparently similar NC ensembles. We note that the largest magnetic anisotropies observed are close to values reported for ensembles magnetic NCs organized in well-defined anisotropic forms [210, 211].

The NCs in our ensembles are randomly distributed and randomly oriented, and so the observation of magnetic anisotropy is rather unexpected. We show that the shape and amplitude of the magnetic resonance angular dependence can be well described by a simple model that considers magnetic dipole-dipole interactions between dipoles that are randomly distributed over the surface of each NC in the ensemble. The surface dipoles may originate from dangling bonds on surface sites that are not passivated by ligands [288]. In our model, we consider a small number of dipoles on the surface of each NC that depends on the coverage of the NC surface by ligands, which in turn follows a normal distribution. From our calculations, we fund that for different random ensembles of NCs the strength of the magnetic anisotropy induced by dipole-dipole interactions may take values spanning four orders of magnitude, depending on the specific arrangements of the NCs in the ensemble and of the specific distribution of the surface dipoles in each NC. The broad range of possible inter-NC interaction strengths obtained in our calculations explains the large disparity of magnetic anisotropies observed in the experiments for different samples of similar NCs, and may also provide insight into some conflicting results reported for the magnetic anosotropy of expectedly similar nanomaterials [272, 288]. Further, as incomplete NC surface passivation is usually unavoidable, our study shows that magnetic anisotropy may be a general feature of NC systems.

Chapter 9

Summary

This work aimed at experimentally investigating spin systems in semiconductor NCs, which originate from dopants and charge trapping defects. We studied electronic and magnetic properties of spin systems in NCs using magnetic resonance techniques, namely EPR and FMR spectroscopy. With regard to the electronic properties of spin systems in semiconductor NCs, EPR spectroscopy was in part used to quantitatively investigate the doping efficiency and confinement of P-doped Si NCs grown by phase segregation method. We identified two EPR signals attributed to P donors in Si NCs, namely an EPR signal at $g = 1.998$ that is associated to exchange coupled donors in the NCs, and a pair of EPR lines with median at $g = 1.998$ and separated by 10.8 mT that are associated to the hyperfine interaction between the spin of isolated donor electrons and their P nucleus spin. We further identified signals associated to Si-dbs located at the surface of the NCs and to defects located at the SiO_2 matrix that surrounds the as-synthesized P-doped Si NCs grown by phase segregation method. From quantitative EPR measurements of the EPR signal associated to isolated P donors in the Si NCs, we estimated the density of electrons donated by P atoms incorporated in substitutional sites of the Si NCs. We have set up a statistical model to describe the distribution of dopants in NC ensembles. This enabled the determination of the ensemble concentration of donor electrons in the NCs taking into account the concentration of isolated P donors obtained from the intensity of their EPR signal. Comparison of the ensemble concentration of donor electrons with the density of P atoms introduced during synthesis of the Si NCs enabled us to infer that the efficiency of n-type doping of these Si NCs with P impurities is of about 30%. Furthermore, we observed that the donor electron density decreases by at least two orders of magnitude when the NCs are removed from their surrounding SiO_2 matrix and exposed to air. We associate this effect to air molecules adsorbed to the NCs surface, which give rise to a strong compensation of donors. We further find that this process can be reverted by desorbing the molecules from the NCs surface under vacuum.

Temperature-dependent EPR measurements of P-doped Si NCs were used to probe the confinement of P donors in the NCs. From the temperature dependence of the intensity of the pair of hyperfine lines observed in the EPR spectra of P-doped Si NCs grown by phase segregation method, we have shown that the ionization energy of P donors in Si NCs increases with respect to bulk Si. This provides experimental evidence for the predictions made with *ab-initio* methods, according to which confinement induces an increase in the ionization energy of dopants with decreasing NC size.

Temperature-dependent EPR was also used to investigate the interactions between multiple donors introduced in a single NC. For this study, we used Q-band EPR spectroscopy, which enabled a better discrimination of the EPR signal at $g = 1.998$ associated to exchange coupled donor electrons. Further, we used P-doped Si NCs grown by gas phase method with a mean NC size of 3.9 nm and an effective doping concentration $[e^-] = 1.4 \times 10^{19}$ cm^{-3}, which is well above the concentration threshold above which the dopants yield an impurity subband in bulk silicon [256]. We showed that even for such high doping concentrations P donors induce discrete states in the NCs energy band gaps. Using the above-mentioned statistical model that describes the random distribution of donors in NC ensembles, we showed that for the given mean NC size and doping concentration most NCs have statistically one or two dopants. We experimentally measured the exchange coupling interaction between closely-spaced donor pairs (donor dimers) in the NCs by monitoring the singlet-triplet transition of the exchange coupled two electron system formed by the donor dimer via temperature-dependent EPR. This measurement was done by monitoring the deviation of the EPR signal at $g = 1.998$ from Curie paramagnetism. We found that the exchange coupling between donors can be well described by effective mass theory. Our approach allowed us to calculate the net electronic structure of donor dimers in Si NCs by calculating the energy levels for all possible dimer configurations (different interdopant distance and relative positions). We also found that the energy splitting between the singlet and triplet states of the donor dimer differs by up to three orders of magnitude for randomly placed dimers in a NC ensemble, due to an enormous dependence of the exchange energy on the dimer configuration. Moreover, we used the theoretical framework describing the exchange coupling of donor dimers in Si NCs to predict the electronic structure of donor dimers in NC ensembles with a broad range of NC sizes and doping concentrations. From statistical calculations, we determined the range of NC sizes and doping concentrations for which most exchange coupled donors present in the NCs are in the form of dimers. We also predicted the temperature dependence of the intensity of the EPR signal at $g = 1.998$ for NC ensembles in this regime. Our calculations indicate that the deviation of the intensity of the EPR signal at $g = 1.998$ from Curie behavior should be stronger for smaller NCs. We further predict a step-like behavior in the temperature dependence of the intensity of the EPR signal at $g = 1.998$ for NCs with size smaller than 2.5 nm. This last prediction is in agreement with recent experimental observations [182].

We have further used EPR spectroscopy to investigate the charge trapping defects in undoped and Ag-doped CdSe NCs. We observe that these defects give rise to an EPR signal at $g = 2.0045$ with a linewidth of about 0.8 mT. We used chemically-induced Ag doping of the CdSe NCs to tune the electronic structure of the NCs and observed that the intensity of the EPR signal due to defect traps depends on the concentration of electronic Ag dopants in the NCs. This observation provides supporting evidence for the mechanism of Ag doping of CdSe NCs suggested in previous studies [5], according to which Ag dopants are (interstitial) donors at concentrations up to $\approx$2 Ag/NC and (substitutional) acceptors for higher Ag concentra-

tions. We further show that the defects in CdSe NCs observed by EPR act as charge traps because the intensity of the EPR signal associated to these defects decreases by up to 80% with the incorporation of n-type Ag dopants in the NCs. We also performed light-induced EPR measurements of CdSe NCs and observed a three-fold increase in the intensity of the EPR signal associated to charge trapping defects in the NCs. From this, we inferred that the charge trapping defects are present in the NCs in two charge states in a comparable amount and that the Fermi energy of the NCs is determined by the population of the two charge states of the defect. Moreover, we quantified the amount of charge trapping defects in CdSe NCs, having measured densities in the range of $10^{18} - 10^{20}$ cm^{-3}. We argued that such densities of charge trapping defects should be high enough to limit the distance that a delocalized electron can move up to about 100 nm in a NC film without being captured a charge trapping defect. Thus, the defects observed here could have a performance limiting effect in devices based in CdSe NCs. By comparison of the observed EPR signal associated to charge trapping defects with those reported in previous EPR investigations of defects in II−IV semiconductors, we argued that this signal may origin from positively charged Se vacancies in the NCs.

We investigated the observation of magnetic anisotropy in ensembles of isotropically-arranged intrinsic CdSe NCs using FMR spectroscopy. This observation was quite unexpected, considering that in ensembles of isotropically-arranged NCs magnetic anisotropy could be assumed to negligible. By SQUID measurements, we obtained values of magnetic moment that are not compatible with the possibility that the observed magnetic anisotropy origins from magnetic impurities in the NCs ensemble. We developed a theoretical framework to explain the magnetic anisotropy observed in our FMR measurements. First, we considered an ensemble of randomly distributed magnetic dipoles interacting by magnetic dipole-dipole interactions. From computational simulations, we showed that this interaction should result in an effective magnetic anisotropy. Further, we showed that the magnetic anisotropy of an ensemble of magnetic dipoles can be quantified from the angular dependence of their FMR spectra. We then discussed the origin of magnetic dipoles giving rise the magnetic anisotropy observed in our ensembles of CdSe NCs and argued that these dipoles should be associated to NC surface sites that are not passivated by organic ligands. From SQUID measurements of our CdSe NCs, in conjunction with previous estimations of the percentage or surface passivation of CdSe by organic ligands, we estimate that about 30 atoms at the NCs surface remain unpassivated and result in paramagnetic defects that provide the magnetic dipoles in the CdSe NC ensembles. Taking this into account, we performed computational simulations of CdSe NC ensembles with magnetic dipole-dipole interactions between magnetic dipoles located at the NCs surface. From these simulations, we could predict the magnetic anisotropy parameters that describe the angular dependence of the FMR spectra. We found that the predicted values of magnetic anisotropy are in very good agreement with those obtained from our FMR measurements.

In summary, the results presented in this thesis have contributed to the understand-

ing the role of spin systems on electronic and magnetic properties of semiconductor NCs. These materials have a great technological potential in applications, with applications already demonstrated in the fields of e.g. thermoelectrics, electronic devices, and plasmonics. Our investigations in Si NCs and in CdSe NCs have tackled issues that have performance-limiting effects on the properties of NCs, namely the doping efficiency of NCs, the charge trapping by defects in the NCs, and the coupling between dopants when multiple impurities are incorporated in a single NC. We have also focused on describing the appearance of magnetic anisotropy in ensembles of intrinsic CdSe NCs stacked in an isotropic shape. This study may encourage further research on the detection and investigation of the origin of magnetic behavior in NCs of diamagnetic materials. Many of the conclusions described in this thesis have been obtained for specific systems, namely the conclusions on the interdopant interactions between P dopants in Si NCs and the conclusions on the magnetic anisotropy of intrinsic CdSe NCs. However, these findings could be generalized to NCs of other semiconductor materials.

Appendix A

List of Publications

1. **A. J. Almeida**, A. Sahu, A. Riedinger, D. J. Norris, M. S. Brandt, M. Stutzmann, and R. N. Pereira
   "Charge Trapping Defects in CdSe Nanocrystal Quantum Dots"
   J. Phys. Chem. C **120**, 13763 (2016)

2. **A. J. Almeida**, H. Sugimoto, M. Fujii, M. S. Brandt, M. Stutzmann, and R. N. Pereira
   "Doping efficiency and confinement of donors in embedded and free standing Si nanocrystals"
   Phys. Rev. B **93**, 115425 (2016)

3. R. N. Pereira and **A. J. Almeida**
   "Doped semiconductor nanocrystals synthesized in gas-phase plasmas"
   J. Phys. D: Appl. Phys. **48**, 314005 (2015)

4. **A. J. Almeida**, R. N, Pereira, and M. S. Brandt
   "Exchange-coupled dopants in Si quantum dots"
   Appl. Phys. Lett. **101**, 093108 (2012)

5. R. N. Pereira, **A. J. Almeida**, A. R. Stegner, M. S. Brandt, and H. Wiggers.
   "Exchange-Coupled Donor Dimers in Nanocrystal Quantum Dots"
   Phys. Rev. Lett. **108**, 126806 (2012)

Bibliography

[1] W. Chen, D. Qi, X. Gao, and A. T. S. Wee. *Prog. Surf. Sci.*, 84:279, 2009.

[2] H. Sapoval and C. Hermann. *Physics of Semiconductors*. Springer-Verlag, first edition, 1995.

[3] P. Hofmann. *Solid State Physics. An Introduction*. Wiley-VCH Berlin, Berlin, DE, 2008.

[4] W. R. Runyan and S. B. Watelski. *Handbook of Materials and Processes for Electronics*. McGraw-Hill Book Company, New York, 1970.

[5] A. Sahu, M. S. Kang, A. Kompch, C. Notthoff, A. W. Wills, D. Deng, Winterer M., C. D. Frisbie, and D. J. Norris. *Nano Lett.*, 12:2587, 2012.

[6] A. R. Stegner, R. N. Pereira, R. Lechner, K. Klein, H. Wiggers, M. Stutzmann, and M. S. Brandt. *Phys. Rev. B*, 80:165326, 2009.

[7] R. N. Pereira, A. R. Stegner, T. Andlauer, K. Klein, H. Wiggers, M. S. Brandt, and M. Stutzmann. *Phys. Rev. B*, 79:161304(R), 2009.

[8] T. L. Chan, M. L. Tiago, E. Kaxiras, and J. R. Chelikowsky. *Nano Lett.*, 8:596, 2008.

[9] A. R. Stegner. *Shallow dopants in nanostructured and in isotopically engineered silicon*. PhD thesis, Walter Schottky Institut,Technische Universitat Munchen, October 2011.

[10] J. Eisenmenger and I. K. Schuller. *Nat. Mater.*, 2:437, 2003.

[11] S. Sun, C. B. Murray, D. Weller, L. Folks, and A. Moser. *Science*, 287:1989, 2000.

[12] N. Noginova, Yu. Barnakov, A. Radocea, and V. A. Atsarkin. *J. Magn. Magn. Mater.*, 323:2264, 2011.

[13] J. A. Weil, J. R. Bolton, and J. E. Wertz. *Electron Paramagnetic Resonance: Elementary Theory and Practical Applications*. Wiley-Interscience, New York, USA, 1994.

[14] M. Brustolon and E. Giamello, editors. *Electron Paramagnetic Resonance: A Practitionerś Toolkit*. Wiley, 2009.

[15] A. R. Stegner. *Spin-spin interactions of localized electronic states in semiconductors.* PhD thesis, Walter Schottky Institut, Technische Universitat Munchen, 2003.

[16] Brian C. Smith. *Fundamentals of Fourier Transform Infrared Spectroscopy.* CRC Press, Florida, USA, 2011.

[17] Barbara Stuart. *Infrared Spectroscopy: Fundamentals and Applications.* Wiley, Sussex, England, 2004.

[18] S. Bedanta. *Superparamagnetism in magnetic nanoparticle systems.* PhD thesis, Universität Duisburg-Essen, December 2007.

[19] B. D. Cullity. *Elements of X-Ray Diffraction.* Addison-Wesley Publishing Company, Reading, Massachusetts, 1956.

[20] L. Reimer and H. Kohl. *Transmission Electron Microscopy: Physics of Image Formation.* Springer, 2008.

[21] M. Ohring. *Materials Science of Thin Films: Deposition and Structure.* Academic Press, London, UK, 2002.

[22] P. R. Cullis and J. R. Marko. *Phys. Rev. B*, 1:632, 1970.

[23] P. R. Cullis and J. R. Marko. *Phys. Rev. B*, 11:4184, 1975.

[24] A. P. Alivisatos. *Science*, 271:933, 1996.

[25] R. Hanson, L. P. Kouwenhoven, J. R. Petta, S. Tarucha, and L. M. K. Vandersypen. *Rev. Mod. Phys.*, 79:1217, 2007.

[26] M. G. Panthani and B. A. Korgel. *Ann. Rev. Chem. Biomol. Eng.*, 3:287, 2012.

[27] I. J. Kramer and E. H. Sargent. *Chem. Rev.*, 114:863, 2014.

[28] D. A. Hines and P. V. Kamat. *ACS Appl. Mat. Interf.*, 6:3041, 2014.

[29] A. D. Yoffe. *Adv. Phys.*, 51:799, 2002.

[30] S. D. Bader. *Rev. Mod. Phys.*, 78:1, 2006.

[31] A. M. Smith and S. Nie. *Acc. Chem. Res.*, 43:190, 2010.

[32] S. M. Reimann and M. Manninen. *Rev. Mod. Phys.*, 74:1283, 2002.

[33] M. D. Regulacio and M.-Y. Han. *Acc. Chem. Res.*, 43:621, 2010.

[34] M. V. Kovalenko. *ACS Nano*, 9:12, 2015.

[35] S. Bedanta and W. Kleemann. *J. Phys. D: Appl. Phys.*, 42:013001, 2009.

[36] S. Gueron, M. M. Deshmukh, E. B. Myers, and D. C. Ralph. *Phys. Rev. Lett.*, 83:4148, 1999.

[37] S. H. Liou, S. Huang, E. Klimek, R. D. Kirby, and Y. D. Yao. *J. Appl. Phys.*, 85:4334, 1999.

[38] D. L. Klein, R. Roth, A. K. L. Lim, A. P. Alivisatos, and P. L. McEuen. *Nature*, 389: 699, 1997.

[39] A. C. Arias, J. D. MacKenzie ad I. McCulloch, J. Rivnay, and A. Salleo. *Chem. Rev.*, 110:3, 2010.

[40] M. G. Panthani and B. A. Korgel. *Ann. Rev.*, 3:287, 2012.

[41] H. W. Hillhouse and M. C. Beard. *Curr. Opin. Colloid Interface Sci.*, 14:245, 2009.

[42] C. M. Chuang, P. R. Brown, V. Bulovic, and M. G. Bawendi. *Nature Mater.*, 13:796, 2014.

[43] R. Y. Wang, J. P. Feser, J.-S. Lee, D. V. Talapin, R. Segalman, and A. Majumdar. *Nano Lett.*, 8:2283, 2008.

[44] A. R. Stegner, R. N. Pereira, K. Klein, R. Lechner, R. Dietmueller, M. S. Brandt, M. Stutzmann, and H. Wiggers. *Phys. Rev. Lett.*, 100:026803, 2008.

[45] S. B. Orlinskii, J. Schmidt, E. J. J. Groenen, P. G. Baranov, C. M. Donegá, and A. Meijerink. *Phys. Rev. Lett.*, 94:097602, 2005.

[46] M. Fujii, A. Mimura, S. Hayashi, Y. Yamamoto, and K. Murakami. *Phys. Rev. Lett.*, 89:206805, 2002.

[47] D. J. Norris, A. L. Efros, and S. C. Erwin. *Science*, 319:1776, 2008. for a review.

[48] R. N. Pereira and A. J. Almeida. *J. Phys. D: Appl. Phys.*, 48:314005, 2015. For a review.

[49] D. Bozyigit, S. Volk, O. Yarema, and V. Wood. *Nano Lett.*, 13:5284, 2013.

[50] R. A. M. Hikmet, D. V. Talapin, and H. Weller. *J. Appl. Phys.*, 93:3509, 2003.

[51] K. Katsiev, A. H. Ip, A. Fischer, I. Tanabe, X. Zhang, A. R. Kirmani, O. Voznyy, L. R. Rollny, K. W. Chou, S. M. Thon, G. H. Carey, X. Cui, A. Amassian, P. Dowben, and E. H. Sargent. *Adv. Mater.*, 26:937, 2014.

[52] K. W. Kemp, C. T. O. Wong, S. H. Hoogland, and E. H. Sargent. *Appl. Phys. Lett.*, 103:211101, 2013.

[53] A. A. Cordones and S. R. Leone. *Chem. Soc. Rev.*, 42:3209, 2013.

[54] D. Zhitomirsky, O. Voznyy, S. Hoogland, and E. H. Sargent. *ACS Nano*, 7:5282, 2013.

[55] D. A. R. Barkhouse, A. G. Pattantyus-Abraham, L. Levina, and E. H. Sargent. *ACS Nano*, 2:2356, 2008.

[56] I. J. Kramer and E. H. Sargent. *ACS Nano*, 5:8506, 2011.

[57] I. Zutic, J. Fabian, and S. D. Sarma. *Rev. Mod. Phys.*, 76:323, 2004.

[58] C. Le Gall, L. Besombes, H. Boukari, R. Kolodka, J. Cibert, and H. Mariette. *Phys. Rev. Lett.*, 102:127402, 2009.

[59] R. P. Cowburn and M. E. Welland. *Science*, 287:1466, 2000.

[60] G. Zabow, S. Dodd, J. Moreland, and A. Koretsky. *Nature*, 453:1058, 2008.

[61] A. M. Derfus, G. von Maltzahn, T. J. Harris, T. Duza, K. S. Vecchio, E. Ruoslahti, and S. N. Bhatia. *Adv. Mater.*, 19:3932, 2007.

[62] J.-S. Lee, M. V. Kovalenko, J. Huang, D. S. Chung, and D. V. Talapin. *Nat. Nanotechnol.*, 6:348, 2011.

[63] B. Thiesen and A. Jordan. *Int. J. Hyperthermia*, 24:467, 2008.

[64] H. Huang, S. Delikanli, H. Zeng, D. M. Ferkey, and A. Pralle. *Nature Nanotech.*, 5:602, 2010.

[65] C. R. Thomas, D. P. Ferris, J.-H. Lee, E. Choi, M. H. Cho, E. S. Kim, J. F. Stoddart, J.-S. Shin, J. Cheon, and J. I. Zink. *J. Am. Chem. Soc.*, 132:10623, 2010.

[66] O. Yalcin. *Ferromagnetic Resonance − Theory and Applications*. InTech, Rijeka, Croatia, 2013.

[67] B. Aktas and F. Mikailov. *Advances in Nanoscale Magnetism*. Springer, Berlin, Germany, 2007.

[68] S. M. Sze and K. K. Ng. *Physics of Semiconductor Devices*. Joh Wiley & Sons, New York, NY, USA, 2006.

[69] M. Shim and P. Guyot-Sionnest. *Nature*, 407:981, 2000.

[70] D. Yu, C. Wang, and P. Guyot-Siommest. *Science*, 300:1277, 2003.

[71] D. V. Talapin and C. B. Murray. *Science*, 310:86, 2005.

[72] K. J. Rietwyk, Y. Smets, M. Bashouti, S. H. Christiansen, A. Schenk, A. Tadich, M. T. Edmonds, J. Ristein, L. Ley, and C. I. Pakes. *Phys. Rev. Lett.*, 112:155502, 2014.

[73] W. k. Koh, A. Y. Kaposov, J. T. Stewart, B. N. Pal, I. Robel, J. M. Pietryga, and V. I. Klimov. *Sci. Rep.*, 3:2004, 2013.

[74] A. Carvalho, J. Coutinho, M. Barroso, E. L. Silva, S. Öberg, M. Rayson, and P. R. Briddon. *Phys. Rev. B*, 84:125437, 2011.

[75] D.-C. Qi, W. Chen, X. Gao, L. Wang, S. Chen, K. P. Loh, and A. T. S. Wee. *J. Am. Chem. Soc.*, 129:8084, 2007.

[76] W. Chen, S. Chen, D. C. Qi, X. Y. Gao, and A. T. S. Wee. *J. Am. Chem. Soc.*, 129: 10418, 2007.

[77] P. Pingel and D. Neher. *Phys. Rev. B*, 87:115209, 2013.

[78] R. N. Pereira, J. Coutinho, S. Niesar, T. A. Oliveira, W. Aigner, H. Wiggers, M. J. Rayson, P. R. Briddon, M. S. Brandt, and M. Stutzmann. *Nano Lett.*, 14:3817, 2014.

[79] A. Carvalho, S. Öberg, M. Rayson, and M. J. Briddon. *Phys. Rev. B*, 86:045308, 2012.

[80] L. M. Wheeler, N. R. Neale, T. Chen, and U. R. Kortshagen. *Nat. Comm.*, 4:2197, 2013.

[81] R. Gresback, N. J. Kramer, Y. Ding, T. Chen, U. R. Kortshagen, and T. Nozaki. *ACS Nano*, 8:5650, 2014.

[82] Z. Zhou, R. A. Friesner, and L. Brus. *J. Am. Chem. Soc.*, 125:15599, 2003.

[83] D. V. Talapin, J.-S. Lee, M. V. Kovalenko, and E. V. Shevchenko. *Chem. Rev.*, 110: 389, 2010.

[84] J. Ristein. *Science*, 313:1057, 2006.

[85] S. B. Orlinskii, J. Schmidt, P. G. Baranov, D. M. Hofmann, C. M. Donegá, and A. Meijerink. *Phys. Rev. Lett.*, 92:047603, 2004.

[86] R. Buonsanti, A. Llordes, S. Aloni, B. A. Helms, and D. J. Milliron. *Nano Lett.*, 11: 4706, 2011.

[87] R. Asahi, T. Morikawa, and T. Ohwaki. *Science*, 293:269, 2001.

[88] R. Asahi, T. Morikawa, and T. Ohwaki. *Science*, 295:627, 2002.

[89] S. Sato, R. Nakamura, and S. Abe. *Appl. Cat. A: General*, 284:131, 2005.

[90] F. Spadavecchia, G. Cappeletti, S. Ardizzone, M. Ceotto, and L. Falciola. *J. Phys. Chem. C*, 115:6381, 2011.

[91] C. Di Valentin, G. Pacchioni, A. Selloni, S. Livraghi, and E. Giamello. *J. Phys. Chem. B*, 109:11414, 2005.

[92] Y. Yin and A. P. Alivisatos. *Nature*, 437:664, 2005.

[93] A. W. Wills, M. S. Kang, K. M. Wentz, S. E. Hayes, A. Sahu, W. L. Gladfelter, and D. J. Norris. *J. Mater. Chem.*, 22:6335, 2012.

[94] S. Roy, C. Tuinenga, F. Fungura, P. Dagtepe, V. Chikan, and J. Jasinski. *J. Phys. Chem. C*, 113:13008, 2009.

[95] M. S. Kang, A. Sahu, C. D. Frisbie, and D. J. Norris. *Adv. Mater.*, 25:725, 2012.

[96] S. J. Oh, N. E. Berry, J.-H. Choi, E. A. Gaulding, T. Paik, S.-H. Hong, C. B. Murray, and C. R. Kagan. *ACS Nano*, 7:2413, 2013.

[97] S. M. Geyer, P. M. Allen, L.-Y. Chang, C. R. Wong, T. P Osedach, N. Zhao, V. Bulovic, and M. G. Bawendi. *ACS Nano*, 4:7373, 2010.

[98] D. Mocatta, G. Cohen, J. Schattner, O. Millo, E. Rabani, and U. Banin. *Science*, 332: 77, 2011.

[99] L. Pavesi and R. Turan. *Silicon Nanocrystals: Fundamentals, Synthesis and Applications.* Wiley-VCH Verlag GmbH & Co. KGaA, Weinheim, Germany, 2010.

[100] Andrey Rogach. *Semiconductor Nanocrystal Quantum Dots: Synthesis, Assembly, Spectroscopy and Applications.* Springer, Wien, Austria, 2008.

[101] O. Wolf, M. Dasog, Z. Yang, I. Balberg, J. G. C. Veinot, and O. Millo. *Nano Lett.*, 13: 2516, 2013.

[102] N. O'Farrel, A. Houlton, and B. R. Horrocks. *Int. J. Nanomed.*, 4:451, 2006.

[103] S. K. Ray, S. Maikap, W. Banerjee, and S. Das. *J. Phys. D.: Appl. Phys.*, 46:153001, 2013.

[104] L. Shcherbyna and T. Torchynska. *Phys. E*, 51:65, 2013.

[105] F. Priolo, T. Gregorkiewicz, M. Galli, and T. F. Krauss. *Nat. Nanotech.*, 9:19, 2014.

[106] A. Gupta, M. T. Swihart, and H. Wiggers. *Adv. Funct. Mater.*, 19:696, 2009.

[107] R. J. Anthony, D. J. Rowe, M. Stein, J. Yang, and U. Kortshagen. *Adv. Funct. Mater.*, 21:4042, 2011.

[108] D. Jurbergs, E. Rogojina, L. Mangolini, and U. Kortshagen. *Appl. Phys. Lett.*, 88: 233116, 2006.

[109] M. C. Beard, K. P. Knutsen, P. Yu, J. M. Luther, Q. Song, W. K. Metzger, R. J. Ellingson, and A. J. Nozik. *Nano Lett.*, 7:2506, 2007.

[110] K.-Y. Cheng, R. Anthony, U. R. Kortshagen, and R. J. Holmes. *Nano Lett.*, 10:1154, 2010.

[111] K.-Y. Cheng, R. Anthony, U. R. Kortshagen, and R. J. Holmes. *Nano Lett.*, 11:1952, 2011.

[112] S. Niesar, W. Fabian, N. Petermann, D. Herrmann, E. Riedle, H. Wiggers, M. S. Brandt, and M. Stutzmann. *Green*, 1:339, 2011.

[113] C.-Y. Liu, Z. C. Holman, and U. R. Kortshagen. *Nano Lett.*, 9:449, 2009.

[114] C.-Y. Liu, Z. C. Holman, and U. R. Kortshagen. *Adv. Funct. Mater.*, 20:21572164, 2010.

[115] R. Lechner, H. Wiggers, A. Ebbers, J. Steiger, M. S. Brandt, and M. Stutzmann. *Phys. Stat. Sol. (RRL)*, 1:262, 2007.

[116] N. Petermann, N. Stein, G. Schierning, R. Theissmann, B. Stoib, M. S. Brandt, C. Hecht, C. Schulz, and H. Wiggers. *J. Phys. D: Appl. Phys.*, 44:174034, 2011.

[117] Z. C. Holman and U. R. Kortshagen. *Nano Lett.*, 11:2136, 2011.

[118] S. Weiss, R. Körmer, M. P. M. Jank, M. Lemberger, M. Otto, H. Ryssel, W. Peukert, and L. Frey. *Small*, 7:2853, 2011.

[119] R. N. Pereira, S. Niesar, W. B. You, A. F. da Cunha, N. Erhard, A. R. Stegner, H. Wiggers, M.-G. Willinger, M. Stutzmann, and M. S. Brandt. *J. Phys. Chem. C*, 115:20120, 2011.

[120] L. Mangolini and U. Kortshagen. *Adv. Mater.*, 19:2513, 2007.

[121] J. Acker, K. Bohmhammel, E. Henneberg, G. Irmer, I. Röver, and G. Roewer. *Adv. Mater.*, 12:1605, 2000.

[122] J. R. Heath. *Science*, 258:1131, 1992.

[123] R. A. Bley and S. M. Kauzlarich. *J. Am. Chem. Soc.*, 118:12461, 1996.

[124] G. Ledoux, J. Gong, and F. Huisken. *Appl. Phys. Lett.*, 79:4028, 2001.

[125] G. Ledoux, J. Gong, F. Huisken1, O. Guillois, and C. Reynaud. *Appl. Phys. Lett.*, 80: 4834, 2002.

[126] X. Li, Y. He, S. S. Talukdar, and M. T. Swihart. *Langmuir*, 19:8490, 2003.

[127] F. Hua, M. T. Swihart, and E. Ruckenstein. *Langmuir*, 21:6054, 2005.

[128] V. Švrček, T. Sasaki, Y. Shimizu, and N. Koshizaki. *Appl. Phys. Lett.*, 89:213113, 2006.

[129] S. Li, S. J. Silers, and M. S. El-Shall. *J. Phys. Chem. B*, 101:1794, 1997.

[130] P. Roca i Cabarrocas, Th. Nguyen-Tran, Y. Djeridane, A. Abramov, E. Johnson, and G. Patriarche. *J. Phys. D: Appl. Phys.*, 40:2258, 2007.

[131] L. Mangolini, E. Thimsen, and U. Kortshagen. *Nano Lett.*, 5:655, 2005.

[132] Y. Kanemitsu, S. Okamoto, M. Otobe, and S. Oda. *Phys. Rev. B*, 55:R7375, 1997.

[133] R. N. Pereira, D. J. Rowe, R. J. Anthony, and U. Kortshagen. *Phys. Rev. B*, 86:085449, 2012.

[134] X. D. Pi, R. Gresback, R. W. Liptak, S. A. Campbell, and U. Kortshagen. *Appl. Phys. Lett.*, 92:123102, 2008.

[135] Ł. Borowik, K. Kusiaku, D. Deresmes, D. Théron, H. Diesinger, T. Mélin, T. Nguyen-Tran, and P. Roca i Cabarrocas. *Phys. Rev. B*, 82:073302, 2010.

[136] Y. Nakamine, N. Inaba, T. Kodera, K. Uchida, R. N. Pereira, A. R. Stegner, M. S. Brandt, M. Stutzman, and S. Oda. *Jap. J. Appl. Phys.*, 50:025002, 2011.

[137] R. Lechner, A. R. Stegner, R. N. Pereira, R. Dietmueller, M. S. Brandt, A. Ebbers, M. Tricha, H. Wiggers, and M. Stutzmann. *J. Appl. Phys.*, 104:53701, 2008.

[138] M. Fujii, A. Mimura, S. Hayashi, and K. Yamamoto. *Appl. Phys. Lett.*, 75:184, 1999.

[139] A. Mimura, M. Fujii, S. Hayashi, D. Kovalev, and F. Koch. *Phys. Rev. B*, 62:75301, 2000.

[140] G. Feher. *Phys. Rev.*, 114:1219, 1959.

[141] U. R. Kortshagen. *J. Phys. D: Appl. Phys.*, 42:113001, 2009.

[142] K. Sumida, K. Ninomiya, M. Fujii, K. Fujio, S. Hayashi, M. Kodama, and H. Ohta. *J. Appl. Phys.*, 101:033504, 2007.

[143] A. Mimura, M. Fujii, S. Hayashi, D. Kovalev, and F. Koch. *Phys. Rev. B*, 62:12625, 2000.

[144] S. Gutsch, A. M. Hartel, D. Hiller, N. Zakharov, P. Werner, and M. Zacharias. *Appl. Phys. Lett.*, 100:233115, 2012.

[145] H. Gnaser, S. Gutsch, M. Wahl, R. Schiller, M. Kopnarski, D. Hiller, and M. Zacharias. *J. Appl. Phys.*, 115:034304, 2014.

[146] S. Gutsch, J. Laube, D. Hiller, W. Bock, M. Wahl, M. Kopnarski, H. Gnaser, B. Puthen-Veettil, and M. Zacharias. *Appl. Phys. Lett.*, 106:113103, 2015.

[147] D. König, S. Gutsch, H. Gnaser, M. Wahl, M. Kopnarski, J. Göttlicher, R. Steininger, M. Zacharias, and D. Hiller. *Sci. Rep.*, 5:09702, 2015.

[148] M. Perego, C. Bonafos, and M. Fanciulli. *Nanotech.*, 21:025602, 2010.

[149] M. Perego, G. Seguini, and M. Fanciulli. *Surf. Interface Anal.*, 45:386, 2013.

[150] M. Mastromatteo, E. Arduca, E. Napolitani, G. Nicotra, D. De Salvador, L. Bacci, J. Frascaroli, G. Seguini, M. Scuderi, G. Impellizzeri, C. Spinella, M. Perego, and A. Carnera. *Surf. Interface Anal.*, 46:393, 2014.

[151] M. Perego, G. Seguini, E. Arduca, J. Frascaroli, D. D. Salvador, M. Mastromatteo, A. Carnera, G. Nicotra, M. Scuderi, C. Spinella, G. Impellizzeri, C. Lenardi, and E. Napolitani. *Nanoscale*, 7:14469, 2015.

[152] G. Cantele, E. Degoli, E. Luppi, R. Magri, D. Ninno, G. Iadonisi, and S. Ossicini. *Phys. Rev. B*, 72:113303, 2005.

[153] G. M. Dalpian and J. R. Chelikowsky. *Phys. Rev. Lett.*, 96:226802, 2006.

[154] R. N. Pereira, D. J. Rowe, R. J. Anthony, and U. Kortshagen. *Phys. Rev. B*, 83:155327, 2011.

[155] A. R. Stegner, R. N. Pereiraa, K. Klein, H. Wiggers, M.S. Brandt, and M. Stutzmann. *Physica B*, 401-402:541, 2007.

[156] Y. Kanzawa, M. Fujii, S. Hayashi, and K. Yamamoto. *Solid State Comm.*, 100:227, 1996.

[157] M. Fujii, S. Hayashi, and K. Yamamoto. *J. Appl. Phys.*, 83:7953, 1998.

[158] Z. Li, X. Zhang, and G. Han. *Phys. Stat. Sol. (a)*, 207:144, 2010.

[159] J. F. Nutzel and G. Abstreiter. *Phys. Rev. B*, 53:13551, 1996.

[160] J. Ma, S. H. Wei, N. R. Neale, and A. J. Nozik. *Appl. Phys. Lett.*, 98:173103, 2011.

[161] K. Fujio, M. Fujii, K. Sumida, S. Hayashi, M. Fujisawa, and H. Ohta. *Appl. Phys. Lett.*, 93:021920, 2008.

[162] G. Feher, J. C. Hensel, and E. A. Gere. *Phys. Rev. Lett.*, 5:309, 1960.

[163] G. Cantele, E. Degoli, E. Luppi, R. Magri, D. Ninno, G. Iadonisi, and S. Ossicini. *Phys. Rev. B*, 72:113303, 2005.

[164] S. Ossicini, E. Degoli, F. Iori, E. Luppi, R. Magri, G. Cantele, F. Trani, and D. Ninno. *Appl. Phys. Lett.*, 87:173120, 2005.

[165] F.Iori, E. Degoli, R. Magri, I. Marri, G. Cantele, D. Ninno, F. Trani, O. Pulci, and S. Ossicini. *Phys. Rev. B*, 76:085302, 2007.

[166] S. Ossicini, E. Degoli, F. Iori, O. Pulci, G. Cantele, R. Magri, O. Bisi, F. Trani, and D. Ninno. *Surf. Sci.*, 601:2724, 2007.

[167] H. Sugimoto, M. Fujii, K. Imakita, S. Hayashi, and K. Akamatsu. *J. Phys. Chem. C*, 116:17969, 2012.

[168] H. Sugimoto, M. Fujii, K. Imakita, S. Hayashi, and K. Akamatsu. *J. Phys. Chem. C*, 117:6807, 2013.

[169] Y. C. Jeon, T.-J. King, and R. T. Howe. *J. Electrochem. Soc.*, 150:H1, 2003.

[170] T. L. Lin, T. George, E. W. Jones, A. Ksendzov, and M. L. Huberman. *Appl. Phys. Lett.*, 60:380, 1992.

[171] D. J. Rowe and U. R. Kortshagen. *APL Mater.*, 2:022104, 2014.

[172] M. Stutzmann, D. K. Biegelsen, and R. A. Street. *Phys. Rev. B*, 35:5666, 1987.

[173] D. Melnikov and J. R. Chelikowsky. *Phys. Rev. Lett.*, 92:046802, 2004.

[174] J. H. Davies. *The Physics of Low-Dimensional Semiconductors - An Introduction.* Cambridge University Press, Cambridge, UK, 2006.

[175] L. Wang and A. Zunger. *Phys. Rev. Lett.*, 73:1039, 1994.

[176] R. Tsu, L. Ioriatti, J. F. Harvey, H. Shen, and R. A. Lux. *Mater. Res. Soc. Symp. Proc.*, 283:437, 1993.

[177] M. Lannoo, C. Delerue, and G. Allan. *Phys. Rev. Lett.*, 74:3415, 1995. G. Allan, C. Delerue, M. Lannoo, and E. Martin, Phys. Rev. B **52**, 11982 (1995).

[178] S. Öğüt, J. R. Chelikowsky, and S. G. Louie. *Phys. Rev. Lett.*, 79:1770, 1997.

[179] A. P. Alivisatos. *Science*, 271:933, 1996.

[180] A. I. Ekimov, I. A. Kudryavtsev, M. G. Ivanov, and A. L. Efros. *J. Lumin.*, 46:83, 1990.

[181] R. A. Abram, G. J. Rees, and B. L. H. Wilson. *Adv. Phys.*, 27:799, 1978.

[182] K. Murakami, M. Tsujimura, R. Shirakawa, M. Uchida, and N. Fukata. *Jap. J. Appl. Phys.*, 48:081201, 2009.

[183] G. Konstantanos and E. H. Sargent. *Appl. Phys. Lett.*, 91:173505, 2007.

[184] D. V. Talapin, A. L. Rogach, A. Kornowski, M. Haase, and H. Weller. *Nano Lett.*, 1: 207, 2001.

[185] D. Zhitomirsky, I. J. Kramer, A. J. Labelle, A. Fischer, R. Debnath, J. Pan, O. M. Baker, and E. H. Sargent. *Nano Lett.*, 12:1007, 2012.

[186] D. S. Ginger and N. C. Greenham. *J. Appl. Phys.*, 87:1361, 2000.

[187] A. H. Ip, S. M. Thon, S. Hoogland, O. Voznyy, D. Zhitomirsky, R. Debnath, L. Levina, L. R. Rollny, G. H. Carey, A. Fischer, K. W. Kemp, I. J. Kramer, Z. Ning, A. J. Labelle, K. W. Chou, A. Amassian, and E. H. Sargent. *Nat. Nanotech.*, 7:577, 2012.

[188] P. Stadler, B. R. Sutherland, Y. Ren, Z. Ning, A. Simchi, S. M. Thon, S. Hoogland, and E. H. Sargent. *ACS Nano*, 7:5757, 2013.

[189] D. J. Keeble, E. A. Thomsen, A. Stravinadis, I. D. W. Samuel, J. M. Smith, and A. A. R. Watt. *J. Phys. Chem. C*, 113:17306, 2009.

[190] R. N. Pereira, L. Dobaczewski, and B. Bech-Nielsen. *Physica B*, 340-342:803–807, 2003.

[191] O. Voznyy, S. M. Thon, A. H. Ip, and E. H. Sargent. *J. Phys. Chem. Lett.*, 4:987, 2013.

[192] D. Kim, D.-H. Kim, J.-H. Lee, and J. C. Grossman. *Phys. Rev. Lett.*, 110:196802, 2013.

[193] O. Voznyy and E. H. Sargent. *Phys. Rev. Lett.*, 112:157401, 2014.

[194] S. Blundell. *Magnetism in Condensed Matter.* Oxford University Press, New York, 2001.

[195] E. C. Stoner and E. P. Wohlfarth. *Phil. Trans. R. Soc. Lond. A*, 240:599, 1948.

[196] M. Ohnuma, K. Hono, T. Yanai, H. Fukunaga, and Y. Yoshizawa. *Appl. Phys. Lett.*, 83:2859, 2003.

[197] S. J. Kernion, P. R. Ohodnicki Jr., J. Grossman, A. Leary, S. Shen, V. Keylin, J. F. Huth, J. Horwath, M. S. Lucas, and M. E. McHenry. *Appl. Phys. Lett.*, 101:102408, 2012.

[198] C. P. Gibson and K. J. Putzer. *Science*, 267:1338, 1995.

[199] J. A. Osborn. *Phys. Rev.*, 67:351, 1945.

[200] C. B. Murray, C. R. Kagan, and M. G. Bawendi. *Annu. Rev. Mater. Sci.*, 30:545, 2000.

[201] M. H. V. Werts, M. Lambert, J. P. Bourgoin, and M. Brust. *Nano Lett.*, 2:43, 2002.

[202] M. Todorovich, S. Schultz, J. Wong, and A. Scherer. *Appl. Phys. Lett.*, 74:2516, 1999.

[203] S. Landis. *Nano Lithography.* John Wiley & Sons, 2011.

[204] C. P. Collier, T. Vossmeyer, and J. R. Heath. *Annu. Rev. Phys. Chem.*, 49:371, 1998.

[205] V. F. Puntes, K. M. Krishnan, and P. Alivisatos. *Nature*, 370:354, 1994.

[206] N. Buske, H. Sonntag, and T. Gotze. *Colloids Surface*, 12:195, 1984.

[207] M. Hilgendorff. *Bimetallic ferrofluids. In Encyclopedia of Nanoscience and Nanotechnology.* Stevenson Ranch: American Scientific Publishers, first edition, 2004.

[208] C. B. Murray, S. Sun, H. Doyle, and T. Betley. *MRS Bull.*, 26:985, 2001.

[209] M. Giersig and M. Hilgendorff. *Colloids Surface A Physicochem Eng Aspects*, 202:207, 2001.

[210] S. Tomita, K. Akamatsu, H. Shinkai, S. Ikeda, H. Nawafune, C. Mitsumata, T. Kashiwagi, and M. Hagiwara. *Phys. Rev. B*, 71:180414(R), 2005.

[211] D. S. Schmool, R. Rocha, J. B. Sousa, J. A. M. Santos, G. N. Kakazei, J. S. Garitaonandia, and L. Lezama. *J. Appl. Phys.*, 101:103907, 2007.

[212] A. Butera, J. N. Zhou, and J. A. Barnard. *Phys. Rev. B*, 60:12270, 1999.

[213] A. Sugawara and M. R. Scheinfein. *Phys. Rev. B*, 56:R8499, 1997.

[214] M. Varon, M. Beleggia, T. Kasama, R. J. Harrison, R. E. Dunin-Borkowski, V. F. Puntes, and C. Frandsen. *Nat. Sci. Rep.*, 3:1234, 2013.

[215] J. Dubowik. *Phys. Rev. B*, 54:1088, 1996.

[216] G. N. Kakazei, A. F. Kravets, N. A. Lesnik, M. M. P. Azevedo, Y. G. Pogorelov, and J. B. Sousa. *J. Appl. Phys.*, 85:5654, 1999.

[217] T. Iwata. *J. Appl. Phys.*, 39:3094, 1968.

[218] D. S. Schmool and M. Schmalzl. *J. Non-Cryst. Solids*, 353:738, 2007.

[219] J. Chen, A. Dong, J. Chai, X. Ye, Y. Kang, J. M. Kikkawa, and C. B. Murray. *Nano Lett.*, 10:5103, 2010.

[220] V. F. Puntes, K. M. Krishnan, and A. P. Alivisatos. *Science*, 291:16, 2001.

[221] V. F. Puntes, P. Gorostiza, D. M. Aruguete, N. G. Bastus, and A. P. Alivisatos. *Nature Mater.*, 3:263, 2004.

[222] B. Koiller, X. Hu, and S. Das-Sarma. *Phys. Rev. Lett.*, 88:027903, 2001.

[223] C. J. Wellard, C. L. Hollenberg, F. Parisoli, L. M. Kettle, H.-S. Goan, J. A. L. McIntosh, and D. N. Jamieson. *Phys. Rev. B*, 68:195209, 2003.

[224] C. P. Poole. *Electron Spin Resonance: A Comprehensive Treatise on Experimental Techniques*. Dover Publications, Inc., Mineola, New York, USA, 1983.

[225] P. E. Wigen. *Phys. Rev.*, 133:A1557, 1964.

[226] R. Meckenstock, D. Spoddig, K. Himmelbauer, H. Krenn, M. Doi, W. Keune, Z. Frait, and J. Pelzl. *J. Magn. Magn. Mater.*, 240:410, 2002.

[227] S. V. Vonsovskii. *Ferromagnetic Resonance*. Pergamon Press, first edition, 1966.

[228] M. Farle. *Rep. Prog. Phys.*, 61:755, 1998.

[229] J. Clarke. *Sci. Am.*, 271:46, 1994.

[230] Heinz-Helmut Perkampus. *UV-Vis Spectroscopy and Its Applications*. Springer Laboratory, Dusseldorf, Germany, 1992.

[231] O. S. Heavens and R. W. Ditchburn. *Insight Into Optics*. John Wiley & Sons, Inc., 1987.

[232] B. Giesen, H. Wiggers andA. Kowalik, and P. Roth. *J. Nanopart. Res.*, 7:29, 2005.

[233] S. Brunauer, P. Emmet, and E. Teller. *J. Am. Chem. Soc.*, 60:309, 1938.

[234] M. Fujii, Y. Yamaguchi, Y. Takase, K. Ninomiya, and S. Hayashi. *Appl. Phys. Lett.*, 87:211919, 2005.

[235] M. Otobe, T. Kanai, T. Ifuku, H. Yajima, and S. Oda. *J. Non-Cryst. Solids*, 198-200: 875, 1996.

[236] J. Knipping, H. Wiggers, B. Rellinghaus, P. Roth, D. Konjhodzic, and C. Meier. *J. Nanosci. Nanotechnol.*, 4:1039, 2004.

[237] S. Oda. *Adv. Colloid Interfac. Sci.*, 71-72:31, 1996.

[238] T. Ifuku, M. Otobe, A. Itoh, and S. Oda. *J. Appl. Phys.*, 36:4031, 2002.

[239] R. Lechner, H. Wiggers, A. Ebbers, J. Steiger, M. S. Brandt, and M. Stutzmann. *Phys. Status Solidi RRL*, 1:262, 2007.

[240] V. G. Kravets, C. Meier, D. Konjhodzic, A. Lorke, and H. Wiggers. *J. Appl. Phys.*, 97: 084306, 2005.

[241] X. D. Pi, L. Mangolini, S. A. Campbell, and U. Kortshagen. *Phys. Rev. B*, 75:085423, 2007.

[242] P. Reiss, J. Bleuse, and A. Pron. *Nano Lett.*, 2:781, 2002.

[243] D. H. Son, S. M. Hughes, Y. Yin, and A. P. Alivisatos. *Science*, 306:1009, 2004.

[244] T. van Buuren R. W. Meulenberg, K. M. Hanif, T. M. Wile, G. F. Strouse, and L. J. Terminello. *Nano Lett.*, 4:2277, 2004.

[245] A. L. Efros and M. Rosen. *Ann. Rev. Mat. Sci.*, 30:475, 2000.

[246] I. Geissbühler. *Cadmium Selenide Nanocrystals For Specific Interactions With Biomolecules*. PhD thesis, École Polytechnique F´edérale de Lausanne, 2005.

[247] S. L. Cumberland, K. M. Hanif, A. Javier, G. A. Khitrov, G. F. Strouse, S. M. Woessner, and C. S. Yun. *Chem. Mater.*, 14:1576, 2002.

[248] M. Fujii, A. Mimura, S. Hayashi, K. Yamamoto, C. Urakawa, and H. Ohta. *J. Appl. Phys.*, 87:1855, 2000.

[249] M. Tanielian. *Philos. Mag. B*, 45:435, 1982.

[250] C. G. B. Garret and W. H. Brattain. *Phys. Rev.*, 78:3801, 1955.

[251] A. K. Ramdas and S. Rodriguez. *Rep. Prog. Phys.*, 44:1297, 1981.

[252] M. T. Björk, H. Schmid, J. Knoch, H. Riel, and W. Riess. *Nature Nanotech.*, 4:103, 2009.

[253] R. Rahman, C. J. Wellard, F. R. Bradbury, M. Prada, J. H. Cole, G. Klimmeck, and L. C. L. Hollenberg. *Phys. Rev. Lett.*, 99:036403, 2007.

[254] R. Rahman, G. P. Lansberger, S. H. Park, J. Verduijn, G. Klimmech, S. Rogge, and L. C. L. Hollenberg. *Phys. Rev. B*, 80:165314, 2009.

[255] R. Rahman, S. H. Park, G. Klimmeck, and L. C. L. Hollenberg. *Nanotechnology*, 22: 225202, 2011.

[256] T. F. Rosenbaum, K. Andres, G. A. Thomas, and R. N. Bhatt. *Phys. Rev. Lett.*, 45: 1723, 1980.

[257] K. M. Itoh, E. E. Haller, J. W. Beeman, W. L. Hansen, J. Emes, L. A. Reichertz, E. Kreysa, T. Shutt, A. Cummings, W. Stockwell, B. Sadoulet, J. Muto, J. W. Farmer, and V. I. Ozhogin. *Phys. Rev. Lett.*, 77:4058, 1996.

[258] E. Pointdexter, P. Chaplan, B. Deal, and R. Razouk. *J. Appl. Phys.*, 52:879, 1981.

[259] A. Stesmans and V. V. Afanas'ev. *J. Appl. Phys.*, 83:2449, 1998. and references therein.

[260] M. Stutzmann and D. K. Biegelsen. *Phys. Rev. B*, 40:9834, 1989.

[261] E. San Andrés, A. del Prado, I. Mártil, G. Gonz'alez, F. L. Matrínez, D. Bravo, F. J. López, and M. Fernández. *Vacuum*, 67:525, 2002.

[262] D. Jerome and J. M. Winter. *Phys. Rev.*, 134:A1001, 1964.

[263] J. Schneider and A. Rauber. *Solid State Commun.*, 5:779, 1967.

[264] B. K. Meyer, P. Omling, E. Weigel, and G. Muller-Vogt. *Phys. Rev. B*, 46:15135, 1992.

[265] S. D. Setzler, M. Moldovan, Z. Yu, T. H. Meyers, N. C. Giles, and L. E. Halliburton. *Appl. Phys. Lett.*, 70:2274, 1997.

[266] *Landolt-Bornstein Numerical Data and Functional Relationships in Science and Technology, New Series.* New York, 16 April 2004.

[267] S. Baskoutas and A. F. Terzis. *J. Appl. Phys.*, 99:013708, 2006.

[268] M. S. Seehra, P. Dutta, S. Neeleshwar, Y.-Y. Chen, C. L. Chen, S. W. Chou, C. C. Chen, C.-L. Dong, and C.-L. Chang. *Adv. Mater.*, 20:1656, 2008.

[269] S. B. Singh, M. V. Limaye, S. K. Date, and S. K. Kulkarni. *Chem. Phys. Lett.*, 464: 208, 2008.

[270] B. S. Singh, M. V. Limaye, S. K. Date, S. Gokhale, and S. K. Kulkarni. *Phys. Rev. B*, 80:235421, 2009.

[271] S. Singh, M. C. Rath, A. K. Singh, T. Mukherjee, O. D. Jayakumar, A. K. Tyagi, and S. K. Sarkar. *Rad. Phys. Chem.*, 80:736, 2011.

[272] Robert W. Meulenberg, Jonathan R. I. Lee, Scott K. McCall, Khalid M. Hanif, Daniel Haskel, Jonathan C. Lang, Louis J. Terminello, and Tony van Buuren. *J. Am. Chem. Soc.*, 131:6888, 2009.

[273] P. Crespo, R. Litran, T. C. Rojas, M. Multigner, J. M. de la Fuente, J. C. Sanchez-Lopez, M. A. Garcia, A. Hernando, S. Penades, and A. Fernandez. *Phys. Rev. Lett.*, 93:087204, 2004.

[274] J. S. Garitaonandia, M. Insausti, E. Goikolea, M. Suzuki, J. D. Cashion, N. Kawamura, H. Ohsawa, I. G. de Muro, K. Suzuki, F. Plazaola, and T. Rojo. *Nano Lett.*, 8:661, 2008.

[275] M. A. Garcia, J. M. Merino, E. Fernandez Pinel, A. Quesada, J. de la Venta, M. L. Ruiz Gonzalez, G. R. Castro, P. Crespo, J. Llopis, J. M. Gonzalez-Calbet, and A. Hernando. *Nano Lett.*, 7:1489, 2007.

[276] H. Peng, H. J. Xiang, S.-H. Wei, S.-S. Li, J.-B. Xia, and J. Li. *Phys. Rev. Lett.*, 102: 017201, 2009.

[277] S. Kumar, S. Kumar, N. K. Verma, and S. K. Chakarvarti. *J. Mater. Sci: Mater Electron*, 22:901, 2011.

[278] M. A. Munoz-Marquez, E. Guerrero, A. Fernandez, P. Crespo, A. Hernando, R. Lucena, and J. C. Conesa. *J. Nanopart. Res.*, 12:1307, 2010.

[279] A. Sundaresan, R. Bhargavi, N. Rangarajan, U. Siddesh, and C. N. R. Rao. *Phys. Rev. B*, 74:161306(R), 2006.

[280] H. Hori, Y. Yamamoto, T. Iwamoto, T. Miura, T. Teranishi, and M. Miyake. *Phys. Rev. B*, 69:174411, 2004.

[281] P. de-la Presa, M. Multigner, J. de-la Venta, M. A. García, and M. L. Ruiz-González. *J. Appl. Phys.*, 100:123915, 2006.

[282] H. Suhl. *Phys. Rev.*, 97:555, 1955.

[283] J. Smit and G. Beljers. *Philips Res. Rep.*, 10:113, 1955.

[284] V. Russier, C. Petit, J. Legrand, and M. P. Pileni. *Phys. Rev. B*, 62:3910, 2000.

[285] T. Fried, G. Shemer, and G. Markovich. *Adv. Mater.*, 13:1158, 2001.

[286] Q. Song and Z. J. Zhang. *J. Am. Chem. Soc.*, 126:6164, 2004.

[287] C. R. Vestal, Q. Song, and Z. J. Zhang. *J. Phys. Chem. B*, 108:18222, 2004.

[288] S. Neeleshwar, C. L. Chen, C. B. Tsai, Y. Y. Chen, C. C. Chen, S. G. Shyu, and M. S. Seehra. *Phys. Rev. B*, 71:201307(R), 2005.

[289] J. E. B. Katari, V. L. Colvin, and A. P. Alivisatos. *J. Phys. Chem.*, 98:4109, 1994.

[290] J. Taylor, T. Kippeny, and S. J. Rosenthal. *J. Clus. Sci.*, 12:571, 2001.

[291] P. Dutta, S. Pal, M. S. Seehra, M. Anand, and C. B. Roberts. *Appl. Phys. Lett.*, 90: 213102, 2007.

[292] P Zhang and T. K. Sham. *Phys. Rev. Lett.*, 90:213102, 2007.

[293] H. Häkkinen, R. N. Barnett, and U. Landman. *Phys. Rev. Lett.*, 82:3264, 1999.

[294] A. Hernando, P. Crespo, and M. A. Garcia. *Phys. Rev. Lett.*, 96:057206, 2006.

[295] M. G. Bawendi, P. J. Carrol, W. L. Wilson, and L. E. Brus. *J. Chem. Phys.*, 96:946, 1992.

[296] V. N. Soloviev, A. Eichhöfer, D. Fenske, and U. Banin. *J. Am. Chem. Soc.*, 123:2354, 2001.

[297] S. Xu, A. A. Mikhailovsky, J. A. Hollingsworth, and V. I. Klimov. *Phys. Rev. B*, 65: 045319, 2002.

[298] J. E. Bowen-Katari, V. L. Colvin, and A. P. Alivisatos. *J. Phys. Chem.*, 98:4109, 1994.

[299] M. Nirmal, C. B. Murray, and M. G. Bawendi. *Phys. Rev. B*, 50:2293, 1994.

[300] M. Jones, S. S. Lo, and G. D. Scholes. *Proc. Natl. Acad. Sci.*, 106:3011, 2009.

[301] M. A. Hines and P. Guyot-Sionnest. *J. Phys. Chem.*, 100:468, 1996.

[302] S. W. H. Eijt, A. T. van Veen, H. Schut, P. E. Mijnarends, A. B. Denison, B. Barbiellini, and A. Bansil. *Nature Mater.*, 5:23, 2005.

[303] A. Puzder, A. J. Williamson, F. Gygi, and G. Galli. *Phys. Rev. Lett.*, 92:217401, 2004.

[304] A. C. Carter, C. E. Boulding, K. M. Kemmer, M. I. Bell, J. C. Woicik, and S. A. Majetich. *Phys. Rev. B*, 55:13822, 1997.

[305] M. Kuno, J. K. Lee, B. O. Dabbousi, F. V. Mikulec, and M. G. Bawendi. *J. Chem. Phys.*, 106:9869, 1997.

[306] S. Pokrant and K. Whaley. *Eur. Phys. J. D*, 6:255, 1999.

[307] X. Wang, L. Qu, J. Zhang, X. Peng, and M. Xiao. *Nano Lett.*, 3:1103, 2003.

[308] E. Poles, D. C. Selmarten, O. I. Mićić, and A. J. Nozik. *Appl. Phys. Lett.*, 75:971, 1999.

[309] A. Rodina and A. L. Efros. *Nano Lett.*, 15:4214, 2015.

[310] R. N. Pereira, S. Niesar, H. Wiggers, M. S. Brandt, and M. S. Stutzmann. *Phys. Rev. B*, 88:155430, 2013.

[311] H. Fu and A. Zunger. *Phys. Rev. B*, 56:1496, 1997.

[312] C. B. Murray, D. J. Norris, and M. G. Bawendi. *J. Am. Chem. Soc.*, 115:8706, 1993.

[313] S. J. Rosenthal, J. McBride, S. J. Pennycook, and L. C. Feldman. *Surf. Sci. Rep.*, 62: 111, 2007.

[314] P. Schapotschnikow and T. J. H. Vlugt. *J. Chem. Phys.*, 131:124705, 2009.

[315] P. Schapotschnikow, R. Pool, and T. J. H. Vlugt. *Nano Lett.*, 8:2930, 2008.

[316] R. Fisher. *Proc. R. Soc. Lond. A*, 217:295, 1953.

[317] L. Zhang and Y. Zhang. *J. Magn. Magn. Mater.*, 321:L15, 2009.